

GEOLOGICA ULTRAIECTINA

Mededelingen van de
Faculteit Geowetenschappen
Universiteit Utrecht

No. 230

**Seismic anisotropy inside the Earth
from a model space search approach**

Caroline Beghein

Promotor: Prof.Dr. R. D. van der Hilst
Department of Seismology
Faculty of Geosciences
Utrecht University
The Netherlands
and :
Department of Earth, Atmospheric, and Planetary Sciences
Massachusetts Institute of Technology
USA
Co-promotor: Dr. J. Trampert
Department of Seismology
Faculty of Geosciences
Utrecht University
The Netherlands

Members of the dissertation committee:

Prof.Dr. C. Spiers
Faculty of Geosciences
Utrecht University

Prof.Dr. A. Forte
GEOTOP
Université de Québec à Montréal

Prof.Dr. M. Cara
Institut de Physique du Globe de Strasbourg

Prof.Dr. J.-P. Montagner
Institut de Physique du Globe de Paris

**Seismic anisotropy inside the Earth
from a model space search approach**

**Seismische anisotropie in de aarde door
middel van een zoekalgoritme in de
model ruimte**

(met een samenvatting in het Nederlands)

PROEFSCHRIFT

TER VERKRIJGING VAN DE GRAAD VAN DOCTOR
AAN DE UNIVERSITEIT UTRECHT
OP GEZAG VAN DE RECTOR MAGNIFICUS, PROF. DR. W.H. GISPEN,
INGEVOLGE HET BESLUIT VAN HET COLLEGE VOOR PROMOTIES
IN HET OPENBAAR TE VERDEDIGEN
OP VRIJDAG 3 OCTOBER 2003 DES MIDDAGS TE 14:30 UUR

DOOR

Caroline Beghein

Geboren op 22 mei 1975, te Rocourt, België

Promotor: Prof.Dr. R. D. van der Hilst
Department of Seismology
Faculty of Geosciences
Utrecht University
The Netherlands
and :
Department of Earth, Atmospheric, and Planetary Sciences
Massachusetts Institute of Technology
USA
Co-promotor: Dr. J. Trampert
Department of Seismology
Faculty of Geosciences
Utrecht University
The Netherlands

The research described in this thesis was carried out at:
Faculty of Geosciences
Vening Meinesz Research School of Geodynamics
Utrecht University
Budapestlaan 4
3584 CD Utrecht
The Netherlands

<http://www.geo.uu.nl/Research/Seismology/>

ISBN: 90-5744-090-3

*C'est ce que nous pensons déjà connaître
qui nous empêche souvent d'apprendre*

*It is often what we think we already
know that prevents us from learning*
(Free translation from French to English)

Claude Bernard, French philosopher, 1813-1878

Contents

1	Introduction and Outline	11
1.1	Anisotropy : generalities	11
1.2	Method employed and motivation	13
1.3	Outline	16
2	Theoretical background	19
2.1	Free oscillations of a non-rotating spherically symmetric Earth model	19
2.2	Perturbation of a reference Earth model	22
2.2.1	Rotation and ellipticity	23
2.2.2	Aspherical structure : general case of the elastic tensor	24
2.2.3	Particular case of an isolated multiplet	28
2.3	Limit towards surface waves	39
2.3.1	Synthesizing seismograms	39
2.3.2	High frequency limit	41
2.4	Conclusion	44
3	P and S tomography using normal mode and surface wave data with a Neighbourhood Algorithm	47
3.1	Introduction	48
3.2	Data and parameterization	49
3.3	Results	53
3.3.1	Sampling and appraisal	53
3.3.2	Shear and compressional wave velocity models and error bars	61
3.4	Conclusion	70
4	Radial anisotropy in mantle reference models	73
4.1	Introduction	74
4.2	Data	75
4.3	Parameterization and method	77
4.4	Results	78
4.5	Discussion and conclusion	85

5	Probability density functions for radial anisotropy in the uppermost mantle	87
5.1	Introduction	88
5.2	Data and parameterization	91
5.3	Method	93
5.4	Results	94
5.5	Discussion and conclusion	112
6	Probability density functions for radial anisotropy in the upper 1200 km of the mantle	115
6.1	Introduction	116
6.2	Method	116
6.3	Data	117
6.4	Parameterization	118
6.5	Retrieving anisotropy, velocity and density anomalies	119
6.6	Results	120
6.7	Discussion and conclusion	131
7	Azimuthal anisotropy down to 1200 km depth from Love wave overtone measurements	133
7.1	Introduction	133
7.2	Data and method	134
7.3	Results	135
7.4	Concluding remarks	138
8	Inner core anisotropy	139
8.1	Introduction	139
8.2	Parameterization	141
8.3	Data	143
8.4	Results	144
	8.4.1 Inversions	144
	8.4.2 Model space search	146
8.5	Conclusion	150
	Summary and Conclusions	151
	Bibliography	155
A	Strain tensor in generalized coordinates	163
B	Generalized spherical harmonics	165
C	Wigner 3-j symbols	167
D	Wigner 3-j symbols : recursion relations for even $l + l' + s$	169

Samenvatting (Summary in Dutch)	173
Résumé (Summary in French)	177
Acknowledgments	181
Curriculum Vitae	183

Chapter 1

Introduction and Outline

For theoretical and computational convenience, the Earth has long been modelled as an isotropic medium for wave propagation. It was assumed that the speed of seismic waves is not affected by the direction of propagation. There is, however, considerable evidence of seismic anisotropy at different depths and different scales throughout the Earth, which can provide insight into Earth's dynamic processes. Since computational power has greatly increased during the last decades, it has now become possible to account for seismic anisotropy in tomographic modelling. Current methods to map seismic anisotropy inside the Earth are often based on the inversion of seismological data but these inversions can be highly non-unique, yielding discrepancies among the models produced in different studies. Since detection of seismic anisotropy is of great importance for the understanding of mantle mineralogy and deformation processes that take place inside the Earth, it is necessary to better understand tomographic models and the origin of the differences among them. In this thesis, we aimed to study seismic anisotropy in a more robust and systematic way than in previous studies, using a novel technique that describes better the model space and the complete ensemble of solutions, with reliable uncertainty estimates.

1.1 Anisotropy : generalities

While mineral physics and geology are involved in the investigation of anisotropy at a microscopic scale, seismology can be used to study large-scale anisotropy (typically $1 - 10^4$ kilometres). The simplest case of anisotropy, called transverse isotropy, can be described by only five independent elastic coefficients. It occurs when the elastic medium presents a symmetry axis. In seismology, it is referred to as radial anisotropy when the symmetry axis points in the vertical (radial) direction. Azimuthal anisotropy refers to variations of seismic wave velocities perpendicular to the symmetry axis. These two kinds of anisotropy can be detected from seismological data. Body waves present the advantage of providing a very good lateral resolution, but heterogeneities are difficult to locate at

depth. On the contrary, normal modes and surface waves enable to locate heterogeneities at depth but they have a weak lateral resolution (several thousands kilometres).

Azimuthal anisotropy was first detected from the azimuthal dependence of P_n waves in the oceanic lithosphere, beneath the Pacific Ocean (Hess, 1964). Shear-wave splitting, or birefringence, is also commonly used to infer azimuthal anisotropy. It is the most unambiguous evidence of seismic anisotropy as the two directions of polarization of the waves have different arrival times. Azimuthal anisotropy can also be derived from the azimuthal dependence of the local phase velocity of Rayleigh and Love waves that occurs in the presence of slightly anisotropic material (Smith and Dahlen, 1973). Surface waves are not only well suited to study azimuthal anisotropy, but also to study radial anisotropy in the uppermost mantle. The observation of radial anisotropy is, however, indirect. Discrepancies between isotropic Rayleigh and Love phase velocity maps (Anderson, 1961) can strongly be reduced by introducing radial anisotropy in the uppermost mantle. PREM (Dziewonski and Anderson, 1981) was the first reference model to include this kind of anisotropy in the top 220 km of the Earth. These two manifestations of surface wave anisotropy were reconciled by Montagner and Nataf (1986) with a general form of the anisotropy. The presence of seismic anisotropy in the Earth can also be investigated with normal modes, but their use is not as widespread as the use of shear wave splitting or surface waves. So far, their most extensive usage in the framework of seismic anisotropy has been to study inner core anisotropy (e.g. Woodhouse et al. (1986); Li et al. (1991); Tromp (1993, 1995b); Durek and Romanowicz (1999); Romanowicz and Bréger (2000)).

Although the presence of both radial and azimuthal anisotropy is commonly accepted in the uppermost mantle, their depth extent and lateral variations are still not clear. Radial anisotropy for both P-waves and S-waves was found by Montagner and Kennett (1996) down to 1000 km depth and in the lowermost mantle, in a new reference model. Regional studies of shear-wave splitting were also interpreted in terms of radial anisotropy in the transition zone beneath Fiji-Tonga (Chen and Brudzinski, 2003) and in the top of the lower mantle (Wookey et al., 2002), that is beneath the upper mantle transition zone. Azimuthal anisotropy in the transition zone was recently inferred by Trampert and van Heijst (2002) from the azimuthal dependence of Love wave overtone measurements. Numerous observations of anisotropy in the D'' layer have been reported in regional studies (Vinnik et al., 1989; Kendall and Silver, 1996) but it has never been observed in the rest of the lower mantle even though mantle minerals are known to be highly anisotropic at these depths and temperatures (Chen et al., 1998; Wentzcovitch et al., 1998). Intrinsically anisotropic minerals can, indeed, lead to the observation of seismic anisotropy, but only if several conditions are fulfilled. For instance, there has to be an efficient mechanism orientating the crystals in order to preserve large scale anisotropy, and a strain field, such as mantle flow, deformation or accretion, must also be present (e.g. McNamara et al. (2002) and Tommasi (1998)). In addition, the amount of anisotropy detected depends on the percentage of intrinsically anisotropic minerals in mantle rocks. The absence of seismic anisotropy in the bulk of the lower mantle could therefore be interpreted in term of superplastic flow, as proposed by Karato (1995), since preferred alignment of miner-

als is not possible in deformation by diffusion creep. However, the presence of seismic anisotropy in the lower mantle cannot be ruled out but it could have remained undetected with body waves because of their poor depth resolution. Normal modes provide better vertical resolution and would be more suited to investigate this matter. This has not been done yet.

Interpreting observations pertaining to seismic anisotropy is generally difficult. It is now commonly accepted that the mechanism producing seismic anisotropy in the uppermost mantle is the lattice-preferred orientation (LPO) of olivine crystals (Karato, 1989). Olivine has, indeed, a high intrinsic anisotropy and shows a high degree of alignment in an ambient stress field. The observation of large scale seismic anisotropy at shallow depths is commonly explained as a preferred orientation of the [100] crystallographic axis of olivine crystals by tectonic processes. The interpretation of seismic anisotropy at other depths is more difficult. In the asthenosphere, it is often taken as a manifestation of present day convective flow, as opposed to “frozen-in” anisotropy at shallower depths (see, for instance, Simons et al. (2002); Gaboret et al. (2003); Becker et al. (2003)). The detection of seismic anisotropy should, however, not be taken as a direct estimation of mantle flow as the fast axis of the anisotropy is not necessarily aligned with the flow direction. Ribe (1987) demonstrated that flow direction and LPO are only simply related in a few places : above subducted slabs, beneath the lithosphere and in boundary layers. Montagner (1998) therefore proposed to associate the layers of the mantle where seismic anisotropy is observed with boundary layers. Further complications can also arise from the water content of olivine-rich crystals, since it can modify the relation between flow geometry and seismic anisotropy (Jung and Karato, 2001). Another possible source of seismic anisotropy is shape-preferred orientation (SPO) of (isotropic) secondary phases in a host material that has different elastic properties than the inclusions. This includes the anisotropic distribution of melt (as it probably occurs in the crust) and laminated structure. If the alignment is horizontal, radial anisotropy, but not azimuthal anisotropy, can be detected. SPO of melt inclusions was proposed by Kendall and Silver (1996) as an explanation for the observed $V_{SH} > V_{SV}$ in D”, but the origin of lowermost mantle anisotropy is still matter of debate. SPO could also be invoked to explain the observed $V_{SH} > V_{SV}$ in the upper lower mantle (Montagner and Kennett, 1996; Wookey et al., 2002).

1.2 Method employed and motivation

Seismologists usually model the structure of the Earth by solving a set of linear or linearized equations relating geophysical observables to some model parameters. A common way of finding a solution that provides a good fit to the data is by minimizing a cost function (e.g. by minimizing a χ^2 misfit and/or a model norm term). However, the solution to these problems is inherently non-unique as there are typically fewer linearly independent equations than the number of unknowns. This is due to uneven sampling of the Earth (the inverse problem is said to be ill-posed). In addition, even when the problem is not ill-posed, errors in the data tend to propagate and to be magnified through the inverse

operator (the problem is then ill-conditioned), causing instabilities in the solution. From a mathematical point of view, zero eigenvalues are responsible for the ill-posedness of the problem, and small or zero eigenvalues imply ill-conditionedness. They also imply the existence of a model null-space and a data null-space. By definition, the data null-space is the part of the data space that cannot be explained by any model. The components of the data that lie in this data null-space correspond to errors in the data and errors in the operator that describes the physical problem. The model null-space is the part of the model space that is not constrained by the data used and, therefore, it does not affect the data fit. Damped least-squares inversions give a way to find a solution to an inverse problem by minimizing a cost function. It implies the introduction of a trade-off parameter that compromises between minimizing the data misfit and the size of the model. A more general regularisation of the problem can also be imposed to deal with the null-spaces. Its introduction allows us to find a stable solution, i.e. a model that is not too sensitive to errors in the data. Imposing a regularisation can also be seen as a way to reduce the ensemble of possible models, or to choose a particular solution among all the models compatible with the data.

Several levels of regularisation, implicit and explicit, are involved when solving inverse problems (Trampert, 1998). The physical variables used to describe the Earth are, strictly speaking, continuous functions of position, and should be expanded in a complete set of basis functions. The choice of these basis functions should not matter as long as the expansion is complete. However, for practical reasons, they have to be truncated and this implies some level of implicit regularisation. More implicit regularisation is introduced through the choice of the cost function. Choosing a cost function implies choosing norms for the data space and for the model space. The choice of these norms is arbitrary and consists in some kind of implicit *a priori* information. Explicit regularisation is introduced through the choice of a reference model, a trade-off parameter and the data and model covariance matrices.

Despite the choice of data errors, norms and model parameterization, the solution of inverse problems can still be highly non-unique. Indeed, in seismology, discrepancies among different models are often observed, and sometimes they can be large. These differences are not necessarily constrained by the data, but they can be due to the presence of a model null-space (Deal et al., 1999). Comparisons of tomographic mantle P and S models can be found in Ritzwoller and Lavelly (1995) and Becker and Boschi (2002) and the influence of regularisation on density and velocity models was investigated by Resovsky and Ritzwoller (1999a,c). Null-spaces are quite significant in highly underdetermined inverse problems and can cause strong non-Gaussian behaviour in the distribution of likely models (see, for instance, the problem of resolving 3-D density anomalies in the mantle (Resovsky and Trampert, 2003) or finding models of inner core anisotropy that fit different kinds of data, as shown in Chapter 8 of this thesis). Due to the assumptions (smoothness, Gaussian statistics, etc) introduced in the regularisation, an inversion only explores a small part of the model null-space. Hence, inversions with different regularisations can include different components of the model null-space and produce discrepancies

among the solutions. One common way of decreasing the model null-space is by jointly inverting independent data sets (e.g. the joint inversion of seismic and geodynamic data by Forte et al. (1994)). If available, independent physical information introduced in the inversion (for instance, via a prior model covariance matrix) can also help reducing the size of the model null-space, but this is not always possible.

As explained above, in traditional inversions ill-posed problems are regularized by introducing *a priori* information on the model space, and it usually implies that the model space is assumed to have a Gaussian distribution near a chosen starting model. However, even if they are linear, ill-posed problems can be characterized by several minima in the cost function (Tikonov and Arsenin, 1977), as opposed to well-posed linear problems which have, typically, one clear global minimum. For well-posed linear problems, usual inversion methods, as well as Monte Carlo and genetic algorithms, will find the same solution. In the case of linear (or linearized) ill-posed problems, the Gaussian hypothesis imposed on the model space may produce solutions that depend strongly on the starting model. The method employed in this thesis offers a way to characterize the model space better and to give a complete description of resolution, trade-offs and uncertainties on the model parameters. We used the Neighbourhood Algorithm (NA) (Sambridge, 1999a,b), a direct search approach from which robust information on Earth's properties can be obtained without having to introduce unnecessary *a priori* information on the model space. We can thus deal with ill-posed problems without assuming *a priori* Gaussian statistics for the model space.

The NA explores the whole model space (within selected boundaries), including the null-space, and provides information on its approximate topology, that is, it identifies regions of relatively low and relatively high misfit, associated with high and low likelihoods, respectively. It differs from traditional inversion techniques as it gives an overview of all the models compatible with the data rather than choosing one by some subjective regularisation. It also differs from usual direct search approaches by characterizing the whole range of models contained in the model space instead of searching for one "best" solution by optimization of a cost function (e.g. steepest gradient method, etc). Not only does the NA explore the model space by sampling different regions, which is what usual direct search approaches do, it also gives posterior probability density functions (PPDFs) for all model parameters, as explained below. The departure of these PPDFs from a Gaussian distribution can be used as a diagnostic of the degree of ill-posedness, hence of the topology of the model null-space. Another advantage of mapping the model space concerns error analysis. Most linearized inversions give, indeed, a posterior model covariance smaller or equal to the prior covariance by construction (Tarantola, 1987). If the cost function to be minimized has a large valley, that is if there is a large model null-space, the posterior covariance can be seriously underestimated, depending on the prior covariance (Trampert, 1998). We consider the width of the valley in the cost function as a realistic representation of the error bars in the absence of true physical prior information.

The NA is composed of two-stages. The first stage consists of the survey of the model space to identify the "good" data fitting regions. It makes use of a geometrical construct,

the Voronoi cells, to drive the search towards the best data-fitting regions while continuing to sample a relatively wide variety of different models. The use of the Voronoi cells makes this algorithm self-adaptative : with a good choice of some tuning parameters, one can explore the complete model space, and there is always a possibility to escape from a local minimum. It also has the advantage of being able to sample several promising regions simultaneously. During this survey, the sampling density increases in the surroundings of the good models without losing information on the models previously generated (even the “bad” ones). The distribution of misfit obtained in the first stage is used to approximate the real posterior probability density function. An importance sampling of this distribution is then performed in the second stage of the NA to generate a “resampled ensemble” that follows the approximate PPD. This resampled ensemble is then integrated numerically to compute the likelihood associated with each model parameter (also called 1-D marginals), the covariance matrix and two-dimensional marginal PPDFs. The 2-D marginals can be used to infer the trade-offs between two variables. The same information can be deduced from the correlation matrix if a Gaussian approximation of the model space can be made. The likelihoods obtained for the various model parameters give a powerful tool to estimate true resolution and uncertainties, since they characterize the entire ensemble of models compatible with the data.

From these likelihoods, one can also test different hypothesis, such as the probability of anisotropy or the probability of positive (or negative) velocity or density anomalies at a given depth, the probability of correlation between two variables, etc. The distributions of density and velocities obtained can be employed to test models of composition. Independent data sets can be used to “filter” the likelihoods and hence reduce the range of possible models. This is an alternative to joint inversions as a way to decrease the size of the model null-space. Compatibility between two data sets can also be examined with this method. The main drawback of the NA lies in the limited number of model parameters that can be explored. It is, however, well suited for normal mode problems and can be applied to phase velocity maps. In these cases, the inverse problem is easily separable into spherical harmonics and the NA can solve individual inverse problems for each spherical harmonic coefficient.

1.3 Outline

In Chapter 2, the concepts underlying normal mode theory and the splitting of normal modes are revisited, and several of the key-equations employed in this thesis are given.

Chapter 3 presents the first application of the Neighbourhood Algorithm to a large scale tomographic problem. This study consisted in searching the model space for P and S tomographic models of the entire mantle, using normal mode data and fundamental normal mode Rayleigh wave phase velocity maps. The search was limited to degree two structure, since the main purpose of this work was to establish the applicability of the NA to mantle tomography, with real data (synthetic tests were performed by Resovsky and Trampert (2002)). In Chapter 3, the reader can also examine examples of posterior one-

dimensional and two-dimensional marginals. Explanations on how to choose the tuning parameters required in each stage of the NA are also given in this chapter.

In Chapter 4, we aimed to determine the likelihood of radial anisotropy in reference mantle models. The NA was applied to a large set of normal mode frequency shift measurements and degree zero phase velocity maps for fundamental and higher mode Rayleigh and Love waves. We obtained likelihoods and uncertainties for radial anisotropy and density perturbations in different layers of the mantle.

Chapter 5 focusses on establishing the robustness of traditional inversion results for lateral variations of radial anisotropy within the top 220 km of the mantle. The data employed here are fundamental Love and Rayleigh wave phase velocity maps expanded into spherical harmonics.

In Chapter 6, we extended the study of Chapter 5 to 1200 km depth, adding overtone Love and Rayleigh wave phase velocity maps. To reduce the number of unknown parameters, we used the models obtained in the previous chapter to correct the data for the effect of the uppermost mantle.

Chapter 7 deals with azimuthal anisotropy (down to 1200 km depth), inferred from the $2\text{-}\Psi$ component of Love wave phase velocity maps constructed with overtone measurements.

Finally, Chapter 8 is a study of inner core anisotropy, in which the NA was applied to the most recent measurements of anomalously split normal modes. The models obtained from normal modes only can also explain all independent travel-time data, which removes a longstanding controversy arisen from the use of the two kinds of data.

Chapter 2

Theoretical background

This chapter reviews the main equations that describe Earth's free oscillations. It is, however, not necessary to understand all theoretical developments described here to read the other chapters because a reminder of the equations used is given in each chapter. In a first section, we consider the equations that govern the free oscillations of a spherical Earth model in hydrostatic equilibrium under self-gravitation. The second section deals with the splitting of Earth's normal modes due to rotation, ellipticity and asphericities. The effect of a general perturbation to the elastic tensor is examined, first in the most general case, and second in the particular case of an isolated multiplet. Equations for radial anisotropy and isotropy are also given. Finally, the equation relating phase velocities and anisotropy is rederived by taking the limit towards surface waves. For more details, the reader is referred to Dahlen (1972, 1973); Dahlen and Smith (1975); Woodhouse and Dahlen (1978); Tanimoto (1986); Mochizuki (1986); Dahlen and Tromp (1998).

2.1 Free oscillations of a non-rotating spherically symmetric Earth model

Let us first consider a model of the Earth which is in mechanical equilibrium under self-gravitation. This model is supposed to be spherically symmetric, not rotating and perfectly elastic. Let \mathbf{x} be the position of a point in this static equilibrium, measured in an inertial reference frame whose origin coincides with the centre of mass of the Earth's model. The equilibrium state is described by the mass density $\rho_0(\mathbf{x})$, the gravitational potential field $\Phi_0(\mathbf{x})$ and the initial static stress tensor $\mathbf{T}_0(\mathbf{x})$, which are related to one another through the following equilibrium equations:

$$\nabla^2 \Phi_0(\mathbf{x}) = 4\pi G \rho_0(\mathbf{x}) \quad (2.1)$$

$$\rho_0(\mathbf{x}) \nabla \Phi_0(\mathbf{x}) = \nabla \cdot \mathbf{T}_0(\mathbf{x}) \quad (2.2)$$

$$\hat{\mathbf{n}} \cdot \mathbf{T}_0(\mathbf{x}) = \mathbf{0} \quad (2.3)$$

The first equation is Poisson's equation and the second is the momentum equation. The last equation is valid at the outer surface ∂V of the Earth model, which is assumed to be traction-free. The unit vector $\hat{\mathbf{n}}$ is the unit outward normal to the surface ∂V at point \mathbf{x} and G is the gravitational constant.

The Earth undergoes elastic-gravitational oscillations if its equilibrium position is disturbed by external forces. These free oscillations correspond to infinitesimal time-dependent displacements $\mathbf{s}(\mathbf{x}, t)$ of a material particle \mathbf{x} , whose position in a lagrangian reference frame can be written as $\mathbf{r}(\mathbf{x}, t) = \mathbf{x} + \mathbf{s}(\mathbf{x}, t)$. As in Dahlen and Tromp (1998), \mathbf{r} denotes a fixed position in space (Eulerian approach) and \mathbf{x} denotes the position of a moving particle (Lagrangian reference frame). The oscillations are accompanied by infinitesimally small perturbations $\rho_1(\mathbf{r}, t)$ in density, $\Phi_1(\mathbf{r}, t)$ in the gravitational potential and $\mathbf{T}^{E1}(\mathbf{r}, t)$ in the stress tensor. The Eulerian Cauchy stress $\mathbf{T}^E(\mathbf{r}, t)$ (with $\mathbf{T}^E(\mathbf{r}, t) = \mathbf{T}_0 + \mathbf{T}^{E1}(\mathbf{r}, t)$) measures a force $d\mathbf{f}^E$ per unit deformed oriented surface-area $\hat{\mathbf{n}}^t d\Sigma^t$ (Dahlen and Tromp, 1998) :

$$d\mathbf{f}^E = \hat{\mathbf{n}}^t d\Sigma^t \cdot \mathbf{T}^E \quad (2.4)$$

The first Piola-Kirchhoff stress tensor $\mathbf{T}^{PK}(\mathbf{r}, t)$ (Malvern, 1969) is defined as the measure of a force $d\mathbf{f}^E$ per unit undeformed oriented surface-area $\hat{\mathbf{n}}^0 d\Sigma^0$:

$$d\mathbf{f}^E = \hat{\mathbf{n}}^0 d\Sigma^0 \cdot \mathbf{T}^{PK} \quad (2.5)$$

Earth's free oscillations are also accompanied by an increment $\mathbf{T}^{PK1}(\mathbf{r}, t)$ in the first Piola-Kirchhoff stress tensor.

To first order, we can write $\rho_1(\mathbf{r}, t) \simeq \rho_1(\mathbf{x}, t)$ and $\Phi_1(\mathbf{r}, t) \simeq \Phi_1(\mathbf{x}, t)$. The linearized equations of motion for an elastic-gravitational mode are then given by (Dahlen and Tromp, 1998) :

$$\rho_0 \left(\frac{\partial^2 \mathbf{s}}{\partial t^2} + \nabla \Phi_1 + \mathbf{s} \cdot \nabla \nabla \Phi_0 \right) = \nabla \cdot \mathbf{T}^{PK1} \quad (2.6)$$

$$\nabla^2 \Phi_1 = 4\pi G \rho_1 \quad (2.7)$$

$$\rho_1 = -\nabla \cdot (\rho_0 \mathbf{s}) \quad (2.8)$$

Equation 2.6 is the linearized momentum equation, 2.7 is the linearized Poisson's equation and equation 2.8 is the linearized continuity condition. It can be shown (Hooke's law, see Dahlen and Tromp (1998)) that the incremental first Piola-Kirchhoff stress tensor is given by

$$\mathbf{T}^{PK1} = \mathbf{\Lambda} : \nabla \mathbf{s} \quad (2.9)$$

or

$$T_{ij}^{PK1} = \Lambda_{ijkl} \frac{\partial s_l}{\partial x_k} \quad (2.10)$$

where the sums over k and l are implicit (Einstein's convention). The tensor Λ is the sum of an elastic tensor \mathbf{C} and terms depending upon the initial stress \mathbf{T}_0 :

$$\Lambda_{ijkl} = C_{ijkl} + \frac{1}{2}(T_{ij}^0\delta_{kl} + T_{kl}^0\delta_{ij} + T_{ik}^0\delta_{jl} - T_{jk}^0\delta_{il} - T_{il}^0\delta_{jk} - T_{jl}^0\delta_{ik}) \quad (2.11)$$

If the initial stress tensor is isotropic, $T_0(\mathbf{r}) = -p_0(\mathbf{r})\mathbf{I}$ at every point in its equilibrium configuration (\mathbf{I} is the identity matrix). Equation 2.11 is then

$$\Lambda_{ijkl} = C_{ijkl} - p_0(\delta_{ij}\delta_{kl} - \delta_{jk}\delta_{il}) \quad (2.12)$$

The elastic tensor has the following symmetries : $C_{ijkl} = C_{klij} = C_{jikl} = C_{ijlk}$, which brings the number of independent elastic coefficients to 21 in an arbitrary anisotropic medium. In the particular case of transverse isotropy only five of these coefficients are independent, and in the case of isotropy this number reduces to two. The form of elastic tensor for an isotropic medium is :

$$C_{ijkl} = \lambda\delta_{ij}\delta_{kl} + \mu(\delta_{ik}\delta_{jl} + \delta_{il}\delta_{jk}) \quad (2.13)$$

where μ and λ are the well-known Lamé parameters. Transverse isotropy is the most general case of anisotropy for a spherically symmetric Earth model (see Section 2.2.3).

For solutions of the type $\mathbf{s}(\mathbf{x}, t) = \mathbf{s}(\mathbf{x})e^{i\omega t}$ and $\Phi_1(\mathbf{x}, t) = \Phi_1(\mathbf{x})e^{i\omega t}$, the Fourier transform of equation 2.6 gives

$$\rho_0(-\omega^2\mathbf{s} + \nabla\Phi_1 + \mathbf{s}\cdot\nabla\nabla\Phi_0) = \nabla\cdot\mathbf{T}^{\mathbf{PK1}} \quad (2.14)$$

The boundary conditions for Φ_1 at all boundaries may be written

$$[\Phi_1]_{\pm}^{\pm} = 0 \quad (2.15)$$

$$[\hat{\mathbf{n}}\cdot((4\pi\mathbf{G})^{-1}\nabla\Phi_1 + \rho_0\mathbf{s})]_{\pm}^{\pm} = 0 \quad (2.16)$$

For \mathbf{s} and $\mathbf{T}^{\mathbf{PK1}}$, the boundary conditions require careful considerations. Details are given in Woodhouse and Dahlen (1978) and Dahlen and Tromp (1998).

To compute the eigenfrequencies and eigenfunctions of such a model (spherically symmetric, non-rotating, elastic and (transversely) isotropic), the system of linearized equations, composed by equations 2.7, 2.8, 2.10, 2.14, 2.12, and the associated boundary conditions, needs to be solved. Dahlen and Tromp (1998) present three different ways to convert these equations into an equivalent system of coupled scalar equations : (1) making use of Rayleigh's principle; (2) using a generalized spherical harmonic representation of the tensor fields; (3) seeking separable eigensolutions of the system of equations. It can further be shown that these scalar equations separate into two sets of completely decoupled equations. Thus, this type of Earth model (e.g. PREM (Dziewonski and Anderson, 1981)) has two distinct types of normal modes : the spheroidal modes and the toroidal modes. They are characterized by three integers : an overtone number n , an angular order l , both varying between zero and infinity, and an azimuthal order m , which takes $2l + 1$ values between $-l$ and l . They are called fundamental modes if $n = 0$ and overtones

otherwise. The angular order is related to their frequency of vibration. At fixed n , the higher l , the higher the frequency. A spheroidal mode, denoted ${}_nS_l$, has an associated particle displacement (or eigenfunction) given by

$${}_n\mathbf{s}_l^m(\mathbf{r}) = \hat{\mathbf{e}}_{\mathbf{r}} {}_nU_l(\mathbf{r})Y_l^m(\theta, \phi) + {}_nV_l(\mathbf{r}) \nabla_1 Y_l^m(\theta, \phi) \quad (2.17)$$

A toroidal mode ${}_nT_l$ has an eigenfunction of the form

$${}_n\mathbf{s}_l^m(\mathbf{r}) = -{}_nW_l(\mathbf{r}) \hat{\mathbf{e}}_{\mathbf{r}} \times \nabla_1 Y_l^m(\theta, \phi) \quad (2.18)$$

$\nabla_1 = \hat{\mathbf{e}}_{\theta} \frac{\partial}{\partial \theta} + \hat{\mathbf{e}}_{\phi} (\sin \theta)^{-1} \frac{\partial}{\partial \phi}$, and $Y_l^m(\theta, \phi)$ are fully normalised complex spherical harmonic (Edmonds, 1960) in a spherical coordinate system $\mathbf{r} = (r, \theta, \phi)$ whose origin is at the centre of the Earth. Functions $U(r)$, $V(r)$ and $W(r)$ are the radial eigenfunctions. Since vertical motion occurs in spheroidal modes and not in toroidal modes, spheroidal modes alter the shape of the Earth while toroidal modes do not. There are $2l+1$ spheroidal oscillations associated with a given eigenfrequency ${}_n\omega_l^S$. They are, therefore, referred to as $2l+1$ -fold degenerated. They form a multiplet, and each eigenfunction within a multiplet is referred to as a singlet. These singlets are identified by the azimuthal order m . Similarly, there are $2l+1$ toroidal modes that share the same degenerate eigenfrequency ${}_n\omega_l^T$. Besides the degeneracy, another important property of these free oscillations is their orthogonality: the $2l+1$ eigenfunctions defined by 2.17 and 2.18 constitute an orthogonal basis in a $2l+1$ -dimensional space.

2.2 Perturbation of a reference Earth model

The type of model described in the previous section (spherically symmetric, non-rotating, elastic and (transversely) isotropic) is generally taken as a reference and the effect of asphericities, rotation and ellipticity are accounted for using perturbation theory. If asphericities, rotation and ellipticity are considered to be slight perturbations of the reference model, Rayleigh's variational principle can be used to compute the resulting perturbations in the eigenfrequency of a particular mode (Dahlen, 1972; Woodhouse and Dahlen, 1978). This has the effect of removing the degeneracy of the eigenfrequencies and gives rise to multiplet splitting. In other words, the $2l+1$ singlets of a multiplet have slightly different eigenfrequencies ${}_n\omega_l^m$.

In the framework of perturbation theory, each multiplet is considered to be isolated from other multiplets. This assumption, which is valid only when their degenerate frequencies do not overlap, is the basis of the degenerate perturbation theory. In that case, the eigenfrequencies ${}_n\omega_l^m$ of the perturbed Earth model are seen as perturbations of the degenerate eigenfrequencies ${}_n\omega_l$:

$${}_n\omega_l^m = {}_n\omega_l + \delta_n \omega_l^m \quad (2.19)$$

and the eigenfunctions are linear combinations of the eigenfunctions of the reference model (which constitute an orthogonal basis). When the frequencies of two (or more)

multiplets are close together, coupling between the multiplets has to be taken into account. This involves a quasi-degenerate perturbation theory. Coupling can occur through asphericities, ellipticity and because of Earth's rotation (through the Coriolis force). Selection rules describe which modes can couple in the different cases. Accounting for coupling is computationally more expensive, but coupled modes have the advantage of being sensitive to both even and odd degree structure, as opposed to isolated multiplets from which only even degree structure can be retrieved (see section 2.2.3). In the next sections, equations are first given in the general case of normal mode coupling, after which the limit of isolated multiplets is taken.

2.2.1 Rotation and ellipticity

The effect of rotation and ellipticity on normal mode splitting is well known and can be calculated exactly. The perturbation, $\delta_n \omega_l^m$, of the eigenfrequency of toroidal modes is given by

$$\delta_n \omega_l^m = m\beta\Omega + \alpha\epsilon_h\omega \left[1 - 3\frac{m^2}{l(l+1)} \right] \quad (2.20)$$

with the Coriolis splitting parameter $\beta = 1/l(l+1)$ and α the ellipticity splitting parameter. The perturbation for spheroidal modes is given by

$$\begin{aligned} \delta_n \omega_l^m &= m\beta\Omega + (\alpha\epsilon_h\omega + \alpha'\Omega^2/\omega) \left[1 - 3\frac{m^2}{l(l+1)} \right] \\ &+ [1 - l(l+1)\beta]\Omega^2/3\omega \end{aligned} \quad (2.21)$$

Expressions for α and α' are given in Woodhouse and Dahlen (1978).

As mentioned before, rotation can also cause coupling between multiplets. The selection rules show that Coriolis coupling can only occur between

1. spheroidal and toroidal modes that differ by one angular order : ${}_n S_l$ and ${}_{n'} T_{l\pm 1}$
2. spheroidal modes with the same angular order : ${}_n S_l$ and ${}_{n'} S_l$

Furthermore, ellipticity causes coupling between

1. two spheroidal or two toroidal modes whose angular orders differ by two : ${}_n S_l$ and ${}_{n'} S_{l+2}$ or ${}_n T_l$ and ${}_{n'} T_{l+2}$
2. spheroidal modes or toroidal modes with the same angular order : ${}_n T_l$ and ${}_{n'} T_l$ or ${}_n S_l$ and ${}_{n'} S_l$.

2.2.2 Aspherical structure : general case of the elastic tensor

When dealing with three-dimensional perturbations in Earth's structure it can be shown that the $2l + 1$ eigenfrequencies of the perturbed model are the eigenvalues of an Hermitian matrix H with dimension $(2l + 1) \times (2l + 1)$. The elements $H_{mm'}$ of this matrix depend linearly on perturbations in the model parameters through sensitivity kernels that are related to the unperturbed eigenfunctions. Woodhouse and Dahlen (1978) gave the general equations relating perturbations in the eigenfrequencies to slight perturbations in the Earth model (perturbations $\delta\rho_0(\mathbf{r})$ in the density, $\delta\Phi_0(\mathbf{r})$ in the gravitational potential, $\delta\mathbf{T}_0$ in the initial stress tensor, perturbations $h(\mathbf{r})$ in the location of discontinuities and perturbations δC_{ijkl} in the elastic tensor). The application of Rayleigh's principle shows that the perturbation in the eigenfrequencies can be written as the sum of individual contributions.

The case of perturbations in the elastic tensor was treated by Tanimoto (1986) and Mochizuki (1986). If the elastic tensor \mathbf{C} is perturbed by an infinitesimal quantity $\delta\mathbf{C}$, the corresponding variation $\delta_n\omega_l^m$ of the eigenfrequencies ${}_n\omega_l$ of a mode is given by the eigenvalues of the following so-called splitting matrix (Woodhouse and Dahlen, 1978):

$$H_{mm'} = \frac{1}{2_n\omega_l I} \int_{\oplus} \nabla \mathbf{s}_m : \delta\mathbf{C} : \nabla \mathbf{s}_{m'}^* dV, \quad (2.22)$$

with the normalisation factor

$$I = \int_{\oplus} \rho_0 \mathbf{s}_i^* \cdot \mathbf{s}_i dV, \quad (2.23)$$

and where the integrations are made over the entire volume \oplus of the Earth. Equation 2.22 can be rewritten as follows (Tanimoto, 1986):

$$H_{mm'} = \frac{1}{2_n\omega_l I} \int_{\oplus} (\mathbf{E}_m)_K : \delta\mathbf{C} : (\mathbf{E}_{m'}^*)_K dV \quad (2.24)$$

\mathbf{E}_m is the strain tensor with azimuthal order m and index K denotes the multiplet (and thus the spherical harmonic order l). These equations are valid to first order and for an isolated multiplet only. In case of coupling of two different multiplets K and K' through three-dimensional perturbations in the elastic tensor equation 2.24 becomes

$$H_{mm'}^{ll'} = \frac{1}{2\omega_l I} \int_{\oplus} (\mathbf{E}_m)_K : \delta\mathbf{C} : (\mathbf{E}_{m'}^*)_{K'} dV \quad (2.25)$$

The introduction of a generalized coordinate system (Phinney and Burridge, 1973) is very useful to evaluate equation 2.25 (see Appendix A). After some algebraic manipulations, the following relations can be derived from equation 2.25 :

$$H_{mm'}^{ll'} = \frac{1}{2\omega_l I} \sum_{s=|N|}^{s_{max}} \sum_{t=-s}^s (-1)^m 4\pi\gamma_l\gamma_{l'} \begin{pmatrix} l & s & l' \\ -m & t & m' \end{pmatrix} \sum_{\alpha\beta\gamma\delta} G_{st}^{\alpha\beta\gamma\delta} \quad (2.26)$$

with $s_{max} = l + l'$ and

$$\begin{aligned} G_{st}^{\alpha\beta\gamma\delta} &= (-1)^{\alpha+\beta} \begin{pmatrix} l & s & l' \\ -\alpha - \beta & N & -\gamma - \delta \end{pmatrix} \int_0^a g_{\gamma-\gamma} g_{\delta-\delta} \delta C_{st}^{\alpha\beta\gamma\delta}(r) \\ &\times (\epsilon_{lm}^{\alpha\beta})^*(r) \epsilon_{l'm'}^{-\gamma-\delta}(r) r^2 dr \end{aligned} \quad (2.27)$$

Here, α, β, γ and δ are indices that can take the value 0, +1 or -1. $N = \alpha + \beta + \gamma + \delta$ and $\gamma_l = \sqrt{(2l+1)/4\pi}$. We also defined $E_{lm}^{\alpha\beta}(r) = \gamma_l \epsilon_{lm}^{\alpha\beta}(r)$. Expressions for $\epsilon_{lm}^{\alpha\beta}(r)$ as a function of the degenerate radial eigenfunctions are listed in Appendix A. Explicit expressions for $G_{st}^{\alpha\beta\gamma\delta}$ of equation 2.27 can be found in Table 2.1.

N	$\delta C_{st}^{\alpha\beta\gamma\delta}$	$\begin{pmatrix} l & s & l' \\ -\alpha - \beta & t & -\gamma - \delta \end{pmatrix}$	Integrand
0	δC_{st}^{0000}	$\begin{pmatrix} l & s & l' \\ 0 & 0 & 0 \end{pmatrix}$	$r^2 U \dot{U}'$
0	δC_{st}^{+-00}	$\begin{pmatrix} l & s & l' \\ 0 & 0 & 0 \end{pmatrix}$	$-r^2 (F \dot{U}' + F' \dot{U})$
0	δC_{st}^{+--+}	$\begin{pmatrix} l & s & l' \\ 0 & 0 & 0 \end{pmatrix}$	$r^2 F F'$
0	δC_{st}^{+0-0}	$\begin{pmatrix} l & s & l' \\ -1 & 0 & 1 \end{pmatrix}$	$r^2 \Omega_l^0 \Omega_{l'}^0 [(X X' + Z Z') (1 + (-1)^{l+l'+s})$ $+ i (1 - (-1)^{l+l'+s}) (X Z' - Z X')]$
0	δC_{st}^{++--}	$\begin{pmatrix} l & s & l' \\ 2 & 0 & -2 \end{pmatrix}$	$\Omega_l^0 \Omega_{l'}^0 \Omega_l^2 \Omega_{l'}^2 [(V V' + W W') (1 + (-1)^{l+l'+s})$ $+ i (1 - (-1)^{l+l'+s}) (W' V - V' W)]$
1	δC_{st}^{+000}	$\begin{pmatrix} l & s & l' \\ -1 & 1 & 0 \\ l & s & l' \\ 0 & 1 & -1 \end{pmatrix}$	$-r^2 \Omega_l^0 (X - iZ) \dot{U}'$ $-r^2 \Omega_{l'}^0 (X' - iZ') \dot{U}$
1	δC_{st}^{++-0}	$\begin{pmatrix} l & s & l' \\ -2 & 1 & 1 \\ l & s & l' \\ 1 & 1 & -2 \end{pmatrix}$	$-r \Omega_l^0 \Omega_{l'}^0 \Omega_l^2 [V X' + W Z' + i(V Z' - W X')]$ $-r \Omega_{l'}^0 \Omega_l^0 \Omega_{l'}^2 [V' X + W' Z + i(V' Z - W' X)]$
1	δC_{st}^{+-+0}	$\begin{pmatrix} l & s & l' \\ 0 & 1 & -1 \end{pmatrix}$	$r^2 \Omega_{l'}^0 F (X' - iZ')$

Table 2.1 Coefficients $G_{st}^{\alpha\beta\gamma\delta}$ of equation 2.27

(continued on next page)

N	$\delta C_{st}^{\alpha\beta\gamma\delta}$	$\begin{pmatrix} l & s & l' \\ -\alpha - \beta & t & -\gamma - \delta \end{pmatrix}$	Integrand
		$\begin{pmatrix} l & s & l' \\ -1 & 1 & 0 \end{pmatrix}$	$r^2 \Omega_l^0 F'(X - iZ)$
-1	δC_{st}^{-000}	$\begin{pmatrix} l & s & l' \\ 1 & -1 & 0 \end{pmatrix}$	$-r^2 \Omega_l^0 \dot{U}'(X + iZ)$
		$\begin{pmatrix} l & s & l' \\ 0 & -1 & 1 \end{pmatrix}$	$-r^2 \Omega_l^0 \dot{U}(X' + iZ')$
-1	δC_{st}^{--0+}	$\begin{pmatrix} l & s & l' \\ 2 & -1 & -1 \end{pmatrix}$	$-r \Omega_l^0 \Omega_{l'}^0 \Omega_t^2 [VX' + WZ' + i(WX' - VZ')]$
		$\begin{pmatrix} l & s & l' \\ -1 & -1 & 2 \end{pmatrix}$	$-r \Omega_l^0 \Omega_{l'}^0 \Omega_t^2 [V'X + W'Z + i(W'X - V'Z)]$
-1	δC_{st}^{+--0}	$\begin{pmatrix} l & s & l' \\ 0 & -1 & 1 \end{pmatrix}$	$r^2 \Omega_{l'}^0 F(X' + iZ')$
		$\begin{pmatrix} l & s & l' \\ 1 & -1 & 0 \end{pmatrix}$	$r^2 \Omega_l^0 F'(X + iZ)$
2	δC_{st}^{++00}	$\begin{pmatrix} l & s & l' \\ -2 & 2 & 0 \end{pmatrix}$	$r \Omega_l^0 \Omega_t^2 (V - iW) \dot{U}'$
		$\begin{pmatrix} l & s & l' \\ 0 & 2 & -2 \end{pmatrix}$	$r \Omega_{l'}^0 \Omega_t^2 (V' - iW') \dot{U}$
2	δC_{st}^{+0+0}	$\begin{pmatrix} l & s & l' \\ -1 & 2 & -1 \end{pmatrix}$	$r^2 \Omega_l^0 \Omega_{l'}^0 [XX' - ZZ' - i(ZX' + XZ')]$
2	δC_{st}^{++++}	$\begin{pmatrix} l & s & l' \\ -2 & 2 & 0 \end{pmatrix}$	$-r \Omega_l^0 \Omega_t^2 (V - iW) F'$
		$\begin{pmatrix} l & s & l' \\ 0 & 2 & -2 \end{pmatrix}$	$-r \Omega_{l'}^0 \Omega_t^2 (V' - iW') F$
-2	δC_{st}^{--00}	$\begin{pmatrix} l & s & l' \\ 2 & -2 & 0 \end{pmatrix}$	$r \Omega_l^0 \Omega_t^2 (V + iW) \dot{U}'$
		$\begin{pmatrix} l & s & l' \\ 0 & -2 & 2 \end{pmatrix}$	$r \Omega_{l'}^0 \Omega_t^2 (V' + iW') \dot{U}$
-2	δC_{st}^{-0-0}	$\begin{pmatrix} l & s & l' \\ 1 & -2 & 1 \end{pmatrix}$	$r^2 \Omega_l^0 \Omega_{l'}^0 [XX' - ZZ' + i(ZX' + XZ')]$
-2	δC_{st}^{----+}	$\begin{pmatrix} l & s & l' \\ 2 & -2 & 0 \end{pmatrix}$	$-r \Omega_l^0 \Omega_t^2 (V + iW) F'$
		$\begin{pmatrix} l & s & l' \\ 0 & -2 & 2 \end{pmatrix}$	$-r \Omega_{l'}^0 \Omega_t^2 (V' + iW') F$

Table 2.1 Coefficients $G_{st}^{\alpha\beta\gamma\delta}$ of equation 2.27

(continued on next page)

N	$\delta C_{st}^{\alpha\beta\gamma\delta}$	$\begin{pmatrix} l & s & l' \\ -\alpha - \beta & t & -\gamma - \delta \end{pmatrix}$	Integrand
3	δC_{st}^{+++0}	$\begin{pmatrix} l & s & l' \\ -2 & 3 & -1 \\ l & s & l' \\ -1 & 3 & -2 \end{pmatrix}$	$-r\Omega_l^0\Omega_{l'}^0\Omega_t^2[VX' - WZ' - i(WX' + VZ')]$ $-r\Omega_l^0\Omega_{l'}^0\Omega_{t'}^2[V'X - W'Z - i(W'X + V'Z)]$
-3	δC_{st}^{---0}	$\begin{pmatrix} l & s & l' \\ 2 & -3 & 1 \\ l & s & l' \\ 1 & -3 & 2 \end{pmatrix}$	$-r\Omega_l^0\Omega_{l'}^0\Omega_t^2[VX' - WZ' + i(WX' + VZ')]$ $-r\Omega_l^0\Omega_{l'}^0\Omega_{t'}^2[V'X - W'Z + i(W'X + V'Z)]$
4	δC_{st}^{++++}	$\begin{pmatrix} l & s & l' \\ -2 & 4 & -2 \end{pmatrix}$	$\Omega_l^0\Omega_{l'}^0\Omega_t^2\Omega_{t'}^2[VV' - WW' - i(WV' + VW')]$
-4	δC_{st}^{----}	$\begin{pmatrix} l & s & l' \\ 2 & -4 & 2 \end{pmatrix}$	$\Omega_l^0\Omega_{l'}^0\Omega_t^2\Omega_{t'}^2[VV' - WW' + i(WV' + VW')]$

Table 2.1: Coefficients $G_{st}^{\alpha\beta\gamma\delta}$ of equation 2.27. Ω_l^n is defined as $\sqrt{(l+n)(l-n+1)}/2$ and $U(r)$, $V(r)$ and $W(r)$ are the degenerate radial eigenfunctions of the mode considered. $F(r) = (2U(r) - l(l+1)V(r))/r$, $X(r) = \dot{V}(r) + (U(r) - V(r))/r$ and $Z(r) = \dot{W}(r) - W(r)/r$. The dot stands for the derivative with respect to the radius r .

To derive these last expressions from equation 2.25 the components of the elastic and strain tensors in the generalized coordinate system have to be decomposed on a generalized scalar spherical harmonic basis (Phinney and Burridge, 1973). The properties of these generalized scalar spherical harmonics $Y_l^{Nm}(\theta, \phi)$ are listed in Appendix B. For the elastic tensor we have

$$\delta C^{\alpha\beta\gamma\delta}(r, \theta, \phi) = \sum_{s=|N|}^{\infty} \sum_{t=-s}^s \delta C_{st}^{\alpha\beta\gamma\delta}(r) Y_s^{Nt}(\theta, \phi) \quad (2.28)$$

The Wigner 3-j symbols (Edmonds, 1960) were introduced to derive the triple integral of equation 2.25 :

$$\begin{aligned} & \int \int Y_s^{Nt}(\theta, \phi) Y_l^{(\alpha+\beta)m}(\theta, \phi) Y_{l'}^{-(\gamma+\delta)m'}(\theta, \phi) d\Omega \\ &= 4\pi(-1)^{\alpha+\beta-m} \begin{pmatrix} l & l' & s \\ -\alpha - \beta & -\gamma - \delta & N \end{pmatrix} \begin{pmatrix} l & l' & s \\ -m & m' & t \end{pmatrix} \quad (2.29) \end{aligned}$$

The properties of these symbols (given in Appendix C) show that equation 2.29 is non-zero if $|l - l'| \leq s \leq l + l'$ and $m = m' + t$. Examples of explicit expressions for $G_{st}^{\alpha\beta\gamma\delta}$

are :

$$G_{st}^{0000} = \begin{pmatrix} l & s & l' \\ 0 & 0 & 0 \end{pmatrix} \int_0^a \dot{U}(r) \dot{U}'(r) \delta C_{st}^{0000}(r) r^2 dr \quad (2.30)$$

and, using the symmetry properties of the elastic tensor, we can show that G_{st}^{+0-0} is given by :

$$G_{st}^{+0-0} = \Omega_l^0 \Omega_{l'}^0 \begin{pmatrix} l & s & l' \\ -1 & 0 & 1 \end{pmatrix} \int_0^a [XX' + ZZ' + i(XZ' - ZX')] \delta C_{st}^{+0-0}(r) r^2 dr \quad (2.31)$$

2.2.3 Particular case of an isolated multiplet

The imaginary parts of the integrands on which $G_{st}^{\alpha\beta\gamma\delta}$ depends characterize normal mode coupling (they are the product of toroidal and spheroidal eigenfunctions). Therefore, they all disappear in the case of an isolated multiplet ($l = l'$), in which case Table 2.1 (hence equation 2.27) becomes much simpler. The resulting $G_{st}^{\alpha\beta\gamma\delta}$ are given in Table 2.2 for toroidal modes and Table 2.3 for spheroidal modes.

It can be demonstrated that all Wigner 3-j symbols of Tables 2.2 and 2.3 are proportional to $\begin{pmatrix} l & s & l \\ 0 & 0 & 0 \end{pmatrix}$ (Mochizuki, 1986), which is non-zero only for even values of s (see equation C.4). This has important consequences : isolated multiplets are sensitive to even degree structure only. The coupling of modes has to be taken into account to get information on the odd degree structure of the Earth. Equation 2.26 can now be written as :

$$H_{mm'} = \frac{1}{2\omega I} \sum_{\alpha\beta\gamma\delta} \sum_{s=|N|}^{2l} \sum_{t=-s}^s (-1)^m (2l+1) \begin{pmatrix} l & s & l \\ -m & t & m' \end{pmatrix} \times \begin{pmatrix} l & s & l \\ 0 & 0 & 0 \end{pmatrix} c_{st} \quad (2.32)$$

where $N = \alpha + \beta + \gamma + \delta$ and

$$c_{st} = \int_0^a \delta C_{st}^{\alpha\beta\gamma\delta}(r) K_s^{\alpha\beta\gamma\delta}(r) dr \quad (2.33)$$

Functions $K_s^{\alpha\beta\gamma\delta}(r)$ are the sensitivity kernels of a given mode for model perturbation $\delta C_{st}^{\alpha\beta\gamma\delta}(r)$. These kernels are listed in Table 2.4 for toroidal modes and in Table 2.5 for spheroidal modes, in the most general case of anisotropy. Different modes have different sensitivity kernels : they “see” Earth’s structure in their own way. Examples are given below for the case of radial anisotropy (Figures 2.1 and 2.2). The sensitivity kernels and the radial eigenfunctions become more oscillatory and penetrate deeper if the overtone number n increases (at fixed angular order l). Overtones ($n \neq 0$) are thus, in general,

sensitive to deeper parts of the Earth than fundamental modes. At fixed overtone number, if l (hence the frequency) increases, the sensitivity will become more and more concentrated at shallow depths. In the high frequency limit, that is when $l \gg s$, normal modes correspond to surface waves (see section 2.3 for more details). For degrees $s \neq 0$, the c_{st} are called structure coefficients. At degree zero there is no actual splitting but a shift of the degenerate eigenfrequency of the multiplet. Coefficients c_{st} can be seen as the degree s and order t spherical harmonic component of a “splitting function” $\eta(\theta, \phi)$ which can be retrieved from free oscillation spectra. It is defined on the surface of the Earth as follow :

$$\eta(\theta, \phi) = \sum_{s=0}^{2l} \sum_{t=-s}^{t=s} c_{st} Y_s^t(\theta, \phi) \quad (2.34)$$

This splitting function represents a local radial average of Earth’s structure underneath a point at the surface of the Earth. It can be seen as the normal mode equivalent of phase velocity maps.

In the most general anisotropic medium the elastic tensor has 21 independent coefficients. However, in practice, when modelling seismic anisotropy, the number of model parameters is reduced by assuming some symmetries. The simplest case of anisotropy is called transverse isotropy or polarization isotropy. It involves only five independent elastic parameters. If the axis of symmetry is aligned in the radial direction it is called radial anisotropy. In that case, the independent elastic parameters are the five coefficients $\delta C^{\alpha\beta\gamma\delta}$ for which $\alpha + \beta + \gamma + \delta = 0$. They are related to the well-known Love coefficients A, C, L, N, F (Love, 1927) as follow :

$$\delta C^{0000} = \delta C \quad (2.35)$$

$$\delta C^{++--} = 2\delta N \quad (2.36)$$

$$\delta C^{+-+-} = \delta A - \delta N \quad (2.37)$$

$$\delta C^{+-00} = -\delta F \quad (2.38)$$

$$\delta C^{+0-0} = -\delta L \quad (2.39)$$

Coefficients A and C (N and L) are related to the velocity of P-waves (S-waves) travelling horizontally and vertically, respectively. If radial anisotropy is assumed, spheroidal mode structure coefficients ($s \neq 0$) and central frequency shifts ($s = 0$) are given by :

$$\begin{aligned} c_{st} = & \int_0^a [\delta A_{st}(r) K_{A_s}(r) + \delta C_{st}(r) K_{C_s}(r) \\ & + \delta N_{st}(r) K_{N_s}(r) + \delta L_{st}(r) K_{L_s}(r) + \delta F_{st}(r) K_{F_s}(r)] dr \end{aligned} \quad (2.40)$$

with

$$K_{A_s}(r) = (2U - l(l+1)V)^2 \quad (2.41)$$

$$K_{C_s}(r) = (r\dot{U})^2 \quad (2.42)$$

$$K_{N_s}(r) = \frac{1}{2}[2l^2(l+1)^2 - 4l(l+1) - 4l(l+1)s(s+1) + s^2(s+1)^2 + 2s(s+1)]V^2 - (2U - l(l+1)V)^2 \quad (2.43)$$

$$K_{L_s}(r) = [l(l+1) - \frac{1}{2}s(s+1)](r\dot{V} + U - V)^2 \quad (2.44)$$

$$K_{F_s}(r) = 2r\dot{U}(2U - l(l+1)V) \quad (2.45)$$

Figure 2.1 gives examples of kernels for three spheroidal modes. Only the sensitivity to $\delta L(r)$ is shown for the case $s = 0$. For toroidal modes

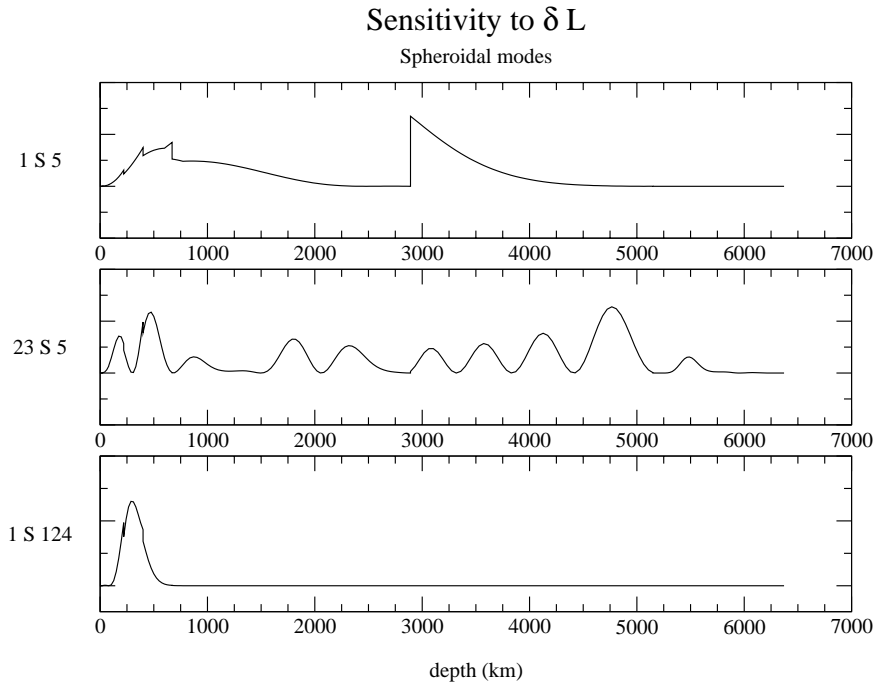


Figure 2.1: Sensitivity to $\delta L(r)$ for different spheroidal modes for the case $s = 0$. N.B. : the vertical scale (not shown here) is not the same for all modes.

$$c_{st} = \int_0^a [\delta N_{st}(r) K_{N_s}(r) + \delta L_{st}(r) K_{L_s}(r)] dr \quad (2.46)$$

with

$$K_{N_s}(r) = \frac{1}{2} [2l^2(l+1)^2 - 4l(l+1) - 4l(l+1)s(s+1) + s^2(s+1)^2 + 2s(s+1)] W^2 \quad (2.47)$$

$$K_{L_s}(r) = [l(l+1) - \frac{1}{2}s(s+1)] (r\dot{W} - W)^2 \quad (2.48)$$

Figure 2.2 shows the sensitivity of three toroidal modes to $\delta N(r)$ for $s = 0$. Thus, central

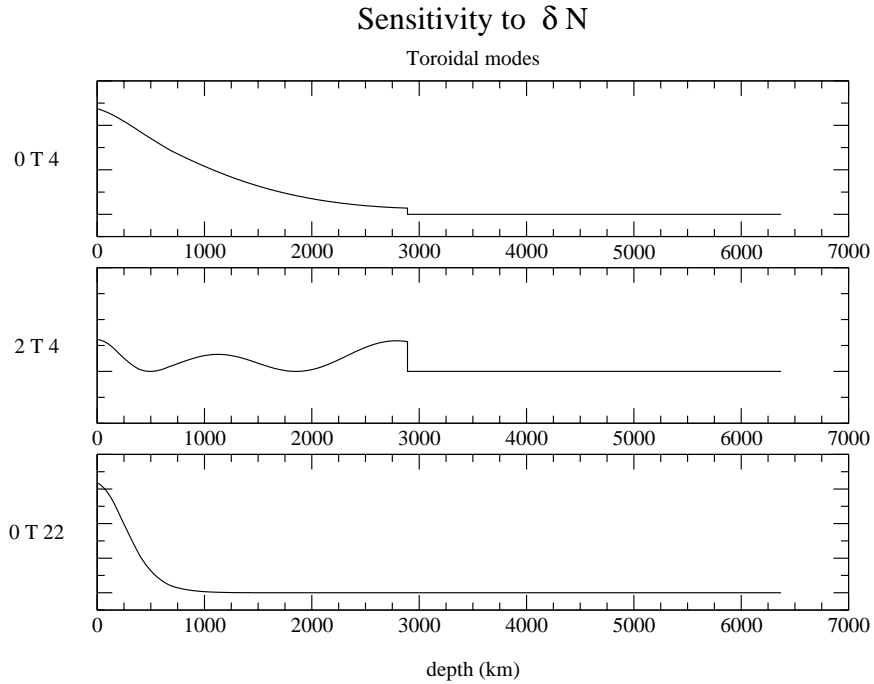


Figure 2.2: Sensitivity to $\delta N(r)$ for different toroidal modes for the case $s = 0$. N.B. : the vertical scale (not shown here) is not the same for all modes.

frequency shifts give constraints on spherically averaged radial anisotropy and structure coefficients can constrain its lateral variations. Equations 2.40 and 2.46 can be rewritten

in various ways, depending on the chosen parameterization (e.g. δV_{pv} , δV_{ph} , δV_s , δV_{sh} and $\delta\eta$, with $\eta = F/(A - 2L)$, or $\delta\phi$, $\delta\xi$, $\delta\eta$, δL and δA , with $\phi = C/A$ and $\xi = N/L$), and the corresponding sensitivity kernels change accordingly. Note that the anisotropic parameter η defined here is different from the splitting function $\eta(\theta, \phi)$ defined in equation 2.34.

Another particular case is the case of an isotropic medium, which has only two independent elastic parameters : μ and κ (or μ and λ with $\kappa = (3\lambda + 2\mu)/3$). In the generalized coordinate system of Phinney and Burridge (1973) the two coefficients are related to $\delta C^{\alpha\beta\gamma\delta}$ by the following relations :

$$\delta\mu = \delta L = \delta N = -\delta C^{+0-0} = \frac{1}{2}\delta C^{++--} \quad (2.49)$$

$$\delta A = \delta C = \delta\kappa - \frac{4}{3}\delta\mu = \delta C^{0000} \quad (2.50)$$

$$\delta F = \delta\kappa - \frac{2}{3}\delta\mu = \delta C^{+-00} \quad (2.51)$$

$$\delta\kappa + \frac{1}{3}\delta\mu = \delta C^{+--+} \quad (2.52)$$

The structure coefficients for spheroidal modes are thus

$$\begin{aligned} c_{st} = & \int_0^a r^2 [\delta\kappa_{st}(Y + \dot{U})^2 + \delta\mu_{st}[\frac{1}{3}(2\dot{U} - Y)^2 \\ & + X^2(l(l+1) - s(s+1)) + \frac{V^2}{r^2}(l(l+1)(l(l+1) - 2) \\ & - s(s+1)(2l(l+1) - \frac{s}{2}(s+1) - 1))] dr \end{aligned} \quad (2.53)$$

For toroidal modes we have :

$$\begin{aligned} c_{st} = & \int_0^a r^2 \delta\mu_{st} [Z^2(l(l+1) - \frac{1}{2}s(s+1)) \\ & + \frac{W^2}{r^2}l(l+1)[l(l+1) - 2 - 2s(s+1)] \\ & + \frac{1}{2}\frac{s(s+1)}{l(l+1)}(2 + s(s+1))] dr \end{aligned} \quad (2.54)$$

with

$$Y(r) = \frac{1}{r}(2U(r) - l(l+1)V(r)) \quad (2.55)$$

$$X(r) = \dot{V}(r) + \frac{1}{r}(U(r) - V(r)) \quad (2.56)$$

$$Z(r) = \dot{W}(r) - \frac{W(r)}{r} \quad (2.57)$$

The dot stands for the derivative with respect to r and $U(r)$, $V(r)$ and $W(r)$ are the radial eigenfunctions of a given mode (see equations 2.17 and 2.18). Note that function $Y(r)$ is

usually named $F(r)$, but we renamed it in this section to avoid any confusion with elastic parameter F . However, the usual notation was kept in Tables 2.1 to 2.5. Note again that, by using the relations $V_s = \sqrt{\mu/\rho}$ and $V_p = \sqrt{(\kappa + 4\mu/3)/\rho}$, the equations for the isotropic case can also be written in terms of velocity and density perturbations instead of perturbations in the elastic parameters.

N	$\delta C_{st}^{\alpha\beta\gamma\delta}$	$\begin{pmatrix} l & s & l' \\ -\alpha - \beta & t & -\gamma - \delta \end{pmatrix}$	Integrand
0	δC_{st}^{+0-0}	$\begin{pmatrix} l & s & l \\ -1 & 0 & 1 \end{pmatrix}$	$2r^2\Omega_l^0\Omega_l^0Z^2$
0	δC_{st}^{++--}	$\begin{pmatrix} l & s & l \\ 2 & 0 & -2 \end{pmatrix}$	$2\Omega_l^0\Omega_l^0\Omega_l^2\Omega_l^2W^2$
1	δC_{st}^{+++0}	$\begin{pmatrix} l & s & l \\ -2 & 1 & 1 \end{pmatrix}$	$-2r\Omega_l^0\Omega_l^0\Omega_l^2WZ$
-1	δC_{st}^{---+0}	$\begin{pmatrix} l & s & l \\ 2 & -1 & -1 \end{pmatrix}$	$-2r\Omega_l^0\Omega_l^0\Omega_l^2WZ$
2	δC_{st}^{+0+0}	$\begin{pmatrix} l & s & l \\ -1 & 2 & -1 \end{pmatrix}$	$-r^2\Omega_l^0\Omega_l^0Z^2$
-2	δC_{st}^{-0-0}	$\begin{pmatrix} l & s & l \\ 1 & -2 & 1 \end{pmatrix}$	$-r^2\Omega_l^0\Omega_l^0Z^2$
3	δC_{st}^{++++0}	$\begin{pmatrix} l & s & l \\ -2 & 3 & -1 \end{pmatrix}$	$2r\Omega_l^0\Omega_l^0\Omega_l^2WZ$
-3	δC_{st}^{----0}	$\begin{pmatrix} l & s & l \\ 2 & -3 & 1 \end{pmatrix}$	$2r\Omega_l^0\Omega_l^0\Omega_l^2WZ$
4	δC_{st}^{+++++}	$\begin{pmatrix} l & s & l \\ -2 & 4 & -2 \end{pmatrix}$	$-\Omega_l^0\Omega_l^0\Omega_l^2\Omega_l^2W^2$
-4	δC_{st}^{-----}	$\begin{pmatrix} l & s & l \\ 2 & -4 & 2 \end{pmatrix}$	$-\Omega_l^0\Omega_l^0\Omega_l^2\Omega_l^2W^2$

Table 2.2: Coefficients $G_{st}^{\alpha\beta\gamma\delta}$ of equation 2.27 for isolated toroidal multiplets ($l = l'$ and s is even). To derive these relations from Table 2.1, one has to use the symmetry properties of the 3-j symbols (Appendix C). Ω_l^n is defined as $\sqrt{(l+n)(l-n+1)}/2$, $W(r)$ is the degenerate radial eigenfunction of the mode considered and $Z(r) = \dot{W}(r) - W(r)/r$. The dot stands for the derivative with respect to the radius r .

N	$\delta C_{st}^{\alpha\beta\gamma\delta}$	$\begin{pmatrix} l & s & l' \\ -\alpha-\beta & t & -\gamma-\delta \end{pmatrix}$	Integrand
0	δC_{st}^{0000}	$\begin{pmatrix} l & s & l \\ 0 & 0 & 0 \end{pmatrix}$	$r^2 U \dot{U}$
0	δC_{st}^{+-00}	$\begin{pmatrix} l & s & l \\ 0 & 0 & 0 \end{pmatrix}$	$-2r^2 F \dot{U}$
0	δC_{st}^{+--+}	$\begin{pmatrix} l & s & l \\ 0 & 0 & 0 \end{pmatrix}$	$r^2 F^2$
0	δC_{st}^{+0-0}	$\begin{pmatrix} l & s & l \\ -1 & 0 & 1 \end{pmatrix}$	$2r^2 \Omega_l^0 \Omega_l^0 X^2$
0	δC_{st}^{++++}	$\begin{pmatrix} l & s & l \\ 1 & 0 & -1 \end{pmatrix}$	$2\Omega_l^0 \Omega_l^0 \Omega_l^2 \Omega_l^2 V^2$
1	δC_{st}^{+000}	$\begin{pmatrix} l & s & l \\ -1 & 1 & 0 \end{pmatrix}$	$-2r^2 \Omega_l^0 X \dot{U}$
1	δC_{st}^{+++0}	$\begin{pmatrix} l & s & l \\ -2 & 1 & 1 \end{pmatrix}$	$-2r \Omega_l^0 \Omega_l^0 \Omega_l^2 V X$
1	δC_{st}^{+-+0}	$\begin{pmatrix} l & s & l \\ 0 & 1 & -1 \end{pmatrix}$	$2r^2 \Omega_l^0 F X$
-1	δC_{st}^{-000}	$\begin{pmatrix} l & s & l \\ 1 & -1 & 0 \end{pmatrix}$	$-2r^2 \Omega_l^0 \dot{U} X$
-1	δC_{st}^{---+0}	$\begin{pmatrix} l & s & l \\ 2 & -1 & -1 \end{pmatrix}$	$-2r \Omega_l^0 \Omega_l^0 \Omega_l^2 V X$
-1	δC_{st}^{+---0}	$\begin{pmatrix} l & s & l \\ 0 & -1 & 1 \end{pmatrix}$	$2r^2 \Omega_l^0 F X$
2	δC_{st}^{++00}	$\begin{pmatrix} l & s & l \\ -2 & 2 & 0 \end{pmatrix}$	$2r \Omega_l^0 \Omega_l^2 V \dot{U}$

Table 2.3 Coefficients $G_{st}^{\alpha\beta\gamma\delta}$ of equation 2.27 for isolated spheroidal multiplets
(continued on next page)

N	$\delta C_{st}^{\alpha\beta\gamma\delta}$	$\begin{pmatrix} l & s & l' \\ -\alpha - \beta & t & -\gamma - \delta \end{pmatrix}$	Integrand
2	δC_{st}^{+0+0}	$\begin{pmatrix} l & s & l \\ -1 & 2 & -1 \end{pmatrix}$	$r^2 \Omega_l^0 \Omega_l^0 X^2$
2	δC_{st}^{++++-}	$\begin{pmatrix} l & s & l \\ -2 & 2 & 0 \end{pmatrix}$	$-2r \Omega_l^0 \Omega_l^2 V F$
-2	δC_{st}^{---00}	$\begin{pmatrix} l & s & l \\ 2 & -2 & 0 \end{pmatrix}$	$2r \Omega_l^0 \Omega_l^2 V \dot{U}$
-2	δC_{st}^{-0-0}	$\begin{pmatrix} l & s & l \\ 1 & -2 & 1 \end{pmatrix}$	$r^2 \Omega_l^0 \Omega_l^0 X^2$
-2	δC_{st}^{----+}	$\begin{pmatrix} l & s & l \\ 2 & -2 & 0 \end{pmatrix}$	$-2r \Omega_l^0 \Omega_l^2 V F$
3	δC_{st}^{++++0}	$\begin{pmatrix} l & s & l \\ -2 & 3 & -1 \end{pmatrix}$	$-2r \Omega_l^0 \Omega_l^0 \Omega_l^2 V X$
-3	δC_{st}^{----0}	$\begin{pmatrix} l & s & l \\ 2 & -3 & 1 \end{pmatrix}$	$-2r \Omega_l^0 \Omega_l^0 \Omega_l^2 V X$
4	δC_{st}^{+++++}	$\begin{pmatrix} l & s & l \\ -2 & 4 & -2 \end{pmatrix}$	$\Omega_l^0 \Omega_l^0 \Omega_l^2 \Omega_l^2 V^2$
-4	δC_{st}^{-----}	$\begin{pmatrix} l & s & l \\ 2 & -4 & 2 \end{pmatrix}$	$\Omega_l^0 \Omega_l^0 \Omega_l^2 \Omega_l^2 V^2$

Table 2.3: Coefficients $G_{st}^{\alpha\beta\gamma\delta}$ of equation 2.27 for isolated spheroidal multiplets ($l = l'$ and s is even). To derive these relations from Table 2.1 one has to use the symmetry properties of the 3-j symbols (Appendix C). Ω_l^n is defined as $\sqrt{(l+n)(l-n+1)/2}$. $U(r)$ and $V(r)$ are the degenerate radial eigenfunctions of the mode considered. $F(r) = (2U(r) - l(l+1)V(r))/r$ and $X(r) = \dot{V}(r) + (U(r) - V(r))/r$. The dot stands for the derivative with respect to the radius r .

N	$\delta C_{st}^{\alpha\beta\gamma\delta}$	$K_s^{\alpha\beta\gamma\delta}(r)$
0	δC_{st}^{+0-0}	$-[l(l+1) - \frac{1}{2}s(s+1)](r\dot{W} - W)^2$
0	δC_{st}^{++--}	$\frac{1}{4}[2l^2(l+1)^2 - 4l(l+1) - 4l(l+1)s(s+1) + s^2(s+1)^2 + 2s(s+1)]W^2$
1	δC_{st}^{++-0}	$-\frac{1}{2}\sqrt{\frac{s(s+1)}{2}}[3l(l+1) - s(s+1)]W(r\dot{W} - W)$
-1	δC_{st}^{--+0}	$-\frac{1}{2}\sqrt{\frac{s(s+1)}{2}}[3l(l+1) - s(s+1)]W(r\dot{W} - W)$
2	δC_{st}^{+0+0}	$-\frac{1}{2}l(l+1)\sqrt{\frac{s(s+1)}{(s+2)(s-1)}}(r\dot{W} - W)^2$
-2	δC_{st}^{-0-0}	$-\frac{1}{2}l(l+1)\sqrt{\frac{s(s+1)}{(s+2)(s-1)}}(r\dot{W} - W)^2$
3	δC_{st}^{+++0}	$-\frac{1}{2}l(l+1)\sqrt{\frac{s(s+1)(s+3)(s-2)}{2(s+2)(s-1)}}W(r\dot{W} - W)$
-3	δC_{st}^{---0}	$-\frac{1}{2}l(l+1)\sqrt{\frac{s(s+1)(s+3)(s-2)}{2(s+2)(s-1)}}W(r\dot{W} - W)$
4	δC_{st}^{++++}	$-\frac{1}{4}(l-1)l(l+1)(l+2)\sqrt{\frac{s(s+1)(s+3)(s-2)}{(s+2)(s-1)(s-3)(s+4)}}W^2$
-4	δC_{st}^{----}	$-\frac{1}{4}(l-1)l(l+1)(l+2)\sqrt{\frac{s(s+1)(s+3)(s-2)}{(s+2)(s-1)(s-3)(s+4)}}W^2$

Table 2.4: Sensitivity kernels of equation 2.33 for toroidal isolated multiplets ($l = l'$ and s is even). The only non-zero degenerate radial eigenfunction is $W(r)$. The dot stands for the derivative with respect to the radius r . To derive these expressions from table 2.2 one has to use the properties of the 3-j symbols (Appendix D, equations D.22 to D.29).

N	$\delta C_{st}^{\alpha\beta\gamma\delta}$	$K_s^{\alpha\beta\gamma\delta}(r)$
0	δC_{st}^{0000}	$(r\dot{U})^2$
0	δC_{st}^{+-00}	$-2r\dot{U}(2U - l(l+1)V)$
0	δC_{st}^{+--+}	$(2U - l(l+1)V)^2$
0	δC_{st}^{+0-0}	$-[l(l+1) - \frac{1}{2}s(s+1)](r\dot{V} + U - V)^2$
0	δC_{st}^{++--}	$\frac{1}{4}[2l^2(l+1)^2 - 4l(l+1) - 4l(l+1)s(s+1) + s^2(s+1)^2 + 2s(s+1)]V^2$
1	δC_{st}^{+000}	$\sqrt{\frac{s(s+1)}{2}}(r\dot{V} + U - V)r\dot{U}$
1	δC_{st}^{+--+0}	$-\sqrt{\frac{s(s+1)}{2}}(r\dot{V} + U - V)(2U - l(l+1)V)$
1	δC_{st}^{++-0}	$-\frac{1}{2}\sqrt{\frac{s(s+1)}{2}}[3l(l+1) - s(s+1)]V(r\dot{V} - V)$
-1	δC_{st}^{-000}	$\sqrt{\frac{s(s+1)}{2}}(r\dot{V} + U - V)r\dot{U}$
-1	δC_{st}^{+--0}	$-\sqrt{\frac{s(s+1)}{2}}(r\dot{V} + U - V)(2U - l(l+1)V)$
-1	δC_{st}^{--+0}	$-\frac{1}{2}\sqrt{\frac{s(s+1)}{2}}[3l(l+1) - s(s+1)]V(r\dot{V} - V)$
2	δC_{st}^{++00}	$\frac{1}{2}\sqrt{\frac{s(s+1)}{(s+2)(s-1)}}[(s+2)(s-1) - 2l(l+1)]r\dot{U}V$
2	δC_{st}^{+++--}	$-\frac{1}{2}\sqrt{\frac{s(s+1)}{(s+2)(s-1)}}[(s+2)(s-1) - 2l(l+1)](2U - l(l+1))V$
2	δC_{st}^{+0+0}	$-\frac{1}{2}l(l+1)\sqrt{\frac{s(s+1)}{(s+2)(s-1)}}(r\dot{V} + U - V)^2$
-2	δC_{st}^{--00}	$\frac{1}{2}\sqrt{\frac{s(s+1)}{(s+2)(s-1)}}[(s+2)(s-1) - 2l(l+1)]r\dot{U}V$
-2	δC_{st}^{----+}	$-\frac{1}{2}\sqrt{\frac{s(s+1)}{(s+2)(s-1)}}[(s+2)(s-1) - 2l(l+1)](2U - l(l+1))V$

Table 2.5 Sensitivity kernels for spheroidal isolated multiplets (continued on next page)

N	$\delta C_{st}^{\alpha\beta\gamma\delta}$	$K_s^{\alpha\beta\gamma\delta}(r)$
-2	δC_{st}^{-0-0}	$-\frac{1}{2}l(l+1)\sqrt{\frac{s(s+1)}{(s+2)(s-1)}}(r\dot{V} + U - V)^2$
3	δC_{st}^{+++0}	$\frac{1}{2}l(l+1)\sqrt{\frac{s(s+1)(s+3)(s-2)}{2(s+2)(s-1)}}V(r\dot{V} + U - V)$
-3	δC_{st}^{---0}	$\frac{1}{2}l(l+1)\sqrt{\frac{s(s+1)(s+3)(s-2)}{2(s+2)(s-1)}}V(r\dot{V} + U - V)$
4	δC_{st}^{++++}	$\frac{1}{4}(l-1)l(l+1)(l+2)\sqrt{\frac{s(s+1)(s+3)(s-2)}{(s+2)(s-1)(s-3)(s+4)}}V^2$
-4	δC_{st}^{----}	$\frac{1}{4}(l-1)l(l+1)(l+2)\sqrt{\frac{s(s+1)(s+3)(s-2)}{(s+2)(s-1)(s-3)(s+4)}}V^2$

Table 2.5: Sensitivity kernels of equation 2.33 for spheroidal isolated multiplets ($l = l'$ and s is even). $U(r)$ and $V(r)$ are the degenerate radial eigenfunctions of the mode considered. $F(r) = (2U(r) - l(l+1)V(r))/r$ and $X(r) = \dot{V}(r) + (U(r) - V(r))/r$. The dot stands for the derivative with respect to the radius r . To derive these expressions from table 2.3 one has to use the properties of the 3-j symbols (Appendix D, equations D.22 to D.29).

2.3 Limit towards surface waves

Although no synthetic seismogram was computed in this thesis, we present some related equations in the next section because it constitutes a good starting point to derive the high frequency limit of free oscillations, i.e. the effect of anisotropy on surface waves (see section 2.3.2). Equations given in section 2.3.1 were taken from Woodhouse (1996), to whom the reader is referred for more details and literature references. Papers by Tanimoto (1986), Romanowicz and Snieder (1988) and Montagner (1996) are particularly relevant for section 2.3.2 where Rayleigh-Love coupling is neglected.

2.3.1 Synthesizing seismograms

Long-period seismograms and spectra can be computed by normal-mode summation. Since the singlet eigenfunctions ${}_n s_l^m$ described in section 2.1 form an orthonormal basis, any response of the Earth to an earthquake in a spherically symmetric Earth model can be expressed as a superposition of normal modes :

$$\mathbf{u}(\mathbf{x}_r, t) = \sum_k a_k(t) \mathbf{s}_k(\mathbf{x}), \quad (2.58)$$

where k denotes the multiplet. It can be shown that, in the case of a point-source, $a_k(t)$ depends on the source moment tensor M . Woodhouse and Girnius (1986) rewrote the previous equation in terms of the individual singlets composing each multiplet :

$$\mathbf{u}(\mathbf{x}_r, t) = \sum_k \sum_{m=-l}^l S_k^m(\mathbf{x}_s) \mathbf{s}_k^m(\mathbf{x}_r) e^{i\tilde{\omega}_k t}, \quad (2.59)$$

where the complex frequency $\tilde{\omega}_k$ is defined by $\tilde{\omega}_k = \omega_k(1 + i/2Q_k)$, Q_k being the quality factor, \mathbf{x}_r is the position of the receiver, \mathbf{x}_s is the position of the source, and $S_k^m(\mathbf{x}_s)$ depends on the source moment tensor. A particular seismogram is then obtained by operating the “instrument vector” \mathbf{v} to the displacement \mathbf{u} .

$$\mathbf{v} \cdot \mathbf{u} = \sum_{k,m} S_k^m(\theta_s, \phi_s) R_k^m(\theta_r, \phi_r) e^{i\tilde{\omega}_k t} \quad (2.60)$$

\mathbf{v} is a unit vector in the direction of motion sensed by the instrument. $S_k^m(\theta_s, \phi_s)$ and $R_k^m(\theta_r, \phi_r)$ involve the source and the receiver, respectively, and are given by :

$$S_k^m(\theta_s, \phi_s) = \sum_{N=-2}^2 S_{kN} Y_l^{Nm}(\theta_s, \phi_s) \quad (2.61)$$

$$R_k^m(\theta_r, \phi_r) = \sum_{N=-2}^2 R_{kN} Y_l^{Nm}(\theta_r, \phi_r) \quad (2.62)$$

Complete expressions for S_{kN} and R_{kN} can be found in Woodhouse and Girnius (1986).

An isolated multiplet in an aspherical Earth is characterized by a splitting matrix $H_{mm'}^k$, and the eigenfunctions of the aspherical Earth model are given by a superposition of the eigenfunctions \mathbf{s}_k of the unperturbed model. It was shown by Woodhouse and Girnius (1986) that the perturbed seismogram is then given by :

$$\mathbf{v} \cdot \mathbf{u} = \sum_{k,m} A_k^m(t) R_k^m(\theta_r, \phi_r) e^{i\tilde{\omega}_k t} \quad (2.63)$$

$A_k^m(t)$ is a function whose time-derivative is expressed as :

$$\frac{d}{dt} A_k^m(t) = i \sum_{m'} H_{mm'}^k A_k^{m'}(t) \quad (2.64)$$

with the initial condition that $A_k^m(t=0) = S_k^m(\theta_s, \phi_s)$. The splitting of the spectrum of the seismogram in the frequency domain results from this time dependence. In the “short time approximation”, Woodhouse and Girnius (1986) expanded $A_k^m(t)$ into

$$A_k^m(t) = S_k^m(\theta_s, \phi_s) + it \sum_{m'} H_{mm'}^k A_k^{m'}(t) \quad (2.65)$$

which yields

$$\mathbf{v} \cdot \mathbf{u} = \sum_{k,m} S_k^m(\theta_s, \phi_s) R_k^m(\theta_r, \phi_r) (1 + i\lambda_k t) e^{i\tilde{\omega}_k t} \quad (2.66)$$

with

$$\lambda_k = \frac{\sum_{m,m'} R_k^m(\theta_r, \phi_r) H_{mm'}^k S_k^{m'}(\theta_s, \phi_s)}{\sum_m R_k^m(\theta_r, \phi_r) S_k^m(\theta_s, \phi_s)} \quad (2.67)$$

λ_k , first introduced by Jordan (1978), is called the location parameter. It expresses the amount by which the frequency of a mode is shifted due to the effect of heterogeneities. This shift of the average frequency of a multiplet is a function of source-receiver geometry. In the asymptotic limit of high frequency it is the average of the local perturbation in the eigenfrequency over the great circle path defined by the source and the receiver. This subject will be treated in the next section.

The contribution of three-dimensional perturbations in the elastic tensor to this shift can be written as :

$$\lambda_k = \delta\omega = \sum_{\alpha,\beta,\delta,\gamma} \delta\omega^{\alpha\beta\delta\gamma} \quad (2.68)$$

with

$$\delta\omega^{\alpha\beta\delta\gamma} = \frac{1}{2\omega ID} \sum_{m,m'} R_k^m S_k^{m'} \sum_{s,t} (-1)^m (2l+1) \begin{pmatrix} l & s & l \\ -m & t & m' \end{pmatrix} G_{st}^{\alpha\beta\gamma\delta} \quad (2.69)$$

and

$$D = \sum_m R_k^m(\theta_r, \phi_r) S_k^m(\theta_s, \phi_s) \quad (2.70)$$

I was defined in equation 2.23.

2.3.2 High frequency limit

In the asymptotic limit $l \gg s$, the sensitivity kernels of an isolated multiplet for which $N = \alpha + \beta + \gamma + \delta$ is odd become an order of magnitude smaller than the other kernels. Indeed, the kernels of Tables 2.2 and 2.3 with odd values of N can all be shown to be proportional to s/l (Tanimoto, 1986). As mentioned in section 2.2.3, the remaining 3-j symbols (with N even) are all proportional to $\begin{pmatrix} l & s & l \\ 0 & 0 & 0 \end{pmatrix}$. At the limit $l \gg s$

$$\begin{pmatrix} l & s & l \\ 0 & 0 & 0 \end{pmatrix} \simeq (-1)^l \frac{1}{\sqrt{2l+1}} P_s(0) = (-1)^l \frac{1}{\sqrt{2l+1}} P_s^{00}(0) \quad (2.71)$$

and

$$\begin{pmatrix} l & s & l \\ -m & t & m' \end{pmatrix} \simeq (-1)^{l+m'} \frac{1}{\sqrt{2l+1}} \sqrt{\frac{(s-t)!}{(s+t)!}} P_s^t(\cos \beta) \quad (2.72)$$

where P_s and P_s^{Nt} are Legendre and generalized associated Legendre polynomials as defined in Phinney and Burridge (1973), P_s^t are associated Legendre polynomials and $\cos \beta \simeq (m+m')/(2l+1)$. $P_s^t(\cos \beta)$ is proportional to $P_s^{0t}(\cos \beta) = Y_s^{0t}(\beta, 0)$. All the $\delta\omega^{\alpha\beta\delta\gamma}$ are therefore related to $\sum_{m,m'} R_k^m S_k^{m'} Y_s^{0t}(\beta, 0)$. After introducing equations 2.71 and 2.72 into equation 2.69 and Tables 2.4 and 2.5, it can be demonstrated that $\delta\omega^{\alpha\beta\delta\gamma}$ depends only on $\sum_{s,t,m,m'} P_s^{N0}(0) R_k^m S_k^{m'} Y_s^{0t}(\beta, 0)$, multiplied by depth integrals of the three-dimensional Earth's structure at degree s and order t . To do so, one has to use the symmetry properties of the generalized associated Legendre polynomials given in Phinney and Burridge (1973) (e.g. $P_s^{Nt}(x) = (-1)^{N+t} P_s^{tN}(x)$), and the following relations :

$$P_s(0) = P_s^{00}(0) \quad (2.73)$$

$$P_s^{20}(0) = -\sqrt{\frac{s(s+1)}{(s-1)(s+2)}} P_s^{00}(0) \quad (2.74)$$

$$P_s^{40}(0) = -\sqrt{\frac{s(s+1)(s+3)(s-2)}{(s-1)(s+2)(s-3)(s+4)}} P_s^{00}(0) \quad (2.75)$$

Finally, it can be shown (Jordan, 1978) that $\sum_{m,m'} R_k^m S_k^{m'} Y_s^{0t}(\beta, 0) = Y_s^{0t}(\Theta, \Phi)$, where (Θ, Φ) denotes the pole of the great circle path defined by the source and receiver. Further algebraic manipulations (Tanimoto, 1986) allow us to write the total eigenfrequency shift, for a particular source-receiver pair in the limit $s/l \ll 1$, as :

$$\delta\omega = \frac{1}{2\pi} \int_{(\Theta, \Phi)} \sum_{\alpha, \beta, \delta, \gamma} \delta\omega_{local}^{\alpha\beta\delta\gamma}(\theta, \phi, \psi) dl \quad (2.76)$$

ψ represents the azimuth of the great circle path, as defined by Tanimoto (1986). $\delta\omega_{local}^{\alpha\beta\delta\gamma}$ are depth integrals over $\delta C^{\alpha\beta\gamma\delta}(\theta, \phi, \psi)$ multiplied by sensitivity kernels which are independent of s (the functions of s in Tables 2.4 and 2.5 are "absorbed" in P_s^{Nt} , as shown by relations 2.73 to 2.75).

The location parameter can also be expressed as a surface integral of the product of the splitting function $\eta(\theta, \phi)$ (equation 2.34) and two-dimensional sensitivity kernels. We do not give detailed algebraic manipulations here. The reader is referred to Woodhouse and Girnius (1986) or Tanimoto (1986) instead. The two-dimensional sensitivity kernels present a peak that is more and more concentrated along the great circle path as the angular order l increases (see examples in Woodhouse and Girnius (1986)). For large values of l , $\delta\omega$ is thus the great circle average of the splitting function, which in turn expresses the change in eigenfrequency corresponding to the local radial structure at each point of the globe.

A recombination of the terms in the sum over $\alpha, \beta, \gamma, \delta$ can yield the following well-known relation for perturbation $\delta c/c$ in the local phase velocity of Love and Rayleigh waves ($\delta c/c$ is related to $\delta\omega/\omega$ through the ratio between the phase and group velocities in the reference model) :

$$\delta c/c(\theta, \phi, \psi) = A_1 + A_2 \cos 2\psi + A_3 \sin 2\psi + A_4 \cos 4\psi + A_5 \sin 4\psi \quad (2.77)$$

with

$$A_i(\theta, \phi) = \sum_{\alpha, \beta, \gamma, \delta} \int_0^a \delta C^{\alpha\beta\gamma\delta}(r, \theta, \phi) K^{\alpha\beta\gamma\delta}(r) dr \quad (2.78)$$

The A_i differ for spheroidal modes (or normal mode Rayleigh waves) or toroidal modes (normal mode Love waves). A_1 does not depend on ψ (it corresponds to the average over all azimuths) and results from terms for which $N = \alpha + \beta + \gamma + \delta$ is zero. It involves the five elastic coefficients that describe radial anisotropy. Expression for A_1 can easily be obtained simply by taking equations 2.40 to 2.48 for $s = 0$. The other terms ($i \neq 0$) describe the effect of azimuthal anisotropy. The $2 - \psi$ terms depend on three parameters, B, G and H which describe the $2 - \psi$ azimuthal variations of the Love parameters A, L and F . An example of sensitivity to these parameters is given in Figure 2.3. The $4 - \psi$ terms depend on one parameter, E , which gives the $4 - \psi$ azimuthal variations of N . Love waves are only sensitive to G and E , while Rayleigh waves are sensitive to all four parameters. The $\cos 2\psi$ -terms are related to the following parameters :

$$B_c = -2(\delta C^{----+} + \delta C^{+++ -}) = \delta C_{\phi\phi\phi\phi} + \delta C_{\theta\theta\theta\theta} \quad (2.79)$$

$$G_c = \delta C^{0+0+} + \delta C^{0-0-} = (\delta C_{\theta r\theta r} - \delta C_{\phi r\phi r})/2 \quad (2.80)$$

$$H_c = \delta C^{--00} + \delta C^{++00} = \delta C_{\theta\theta r r} - \delta C_{\phi\phi r r} \quad (2.81)$$

The $\sin 2\psi$ -terms are related to :

$$B_s = -i(\delta C^{----+} - \delta C^{+++ -}) = -(\delta C_{\theta\theta\theta\phi} + \delta C_{\theta\phi\phi\theta}) \quad (2.82)$$

$$G_s = i(\delta C^{0+0+} - \delta C^{0-0-})/2 = \delta C_{\theta r\phi r} \quad (2.83)$$

$$H_s = -i(\delta C^{--00} - \delta C^{++00})/2 = \delta C_{\theta\phi r r} \quad (2.84)$$

The $\cos 4\psi$ -term is related to

$$E_c = (\delta C_{\theta\theta\theta\theta} + \delta C_{\phi\phi\phi\phi})/8 - \delta C_{\theta\theta\phi\phi}/4 - \delta C_{\theta\phi\theta\phi}/2 \quad (2.85)$$

and $\sin 4\psi$ -term is related to

$$E_s = (\delta C_{\theta\theta\theta\phi} - \delta C_{\theta\phi\phi\theta})/2 \quad (2.86)$$

We also have $2E_c + 2iE_s = \delta C^{++++} = \delta C^{----}$. For Love waves, kernels for G_c and G_s are given by $-l(l+1)Z^2$ and kernels for E_c and E_s are $-(l(l+1))^2 W^2$.

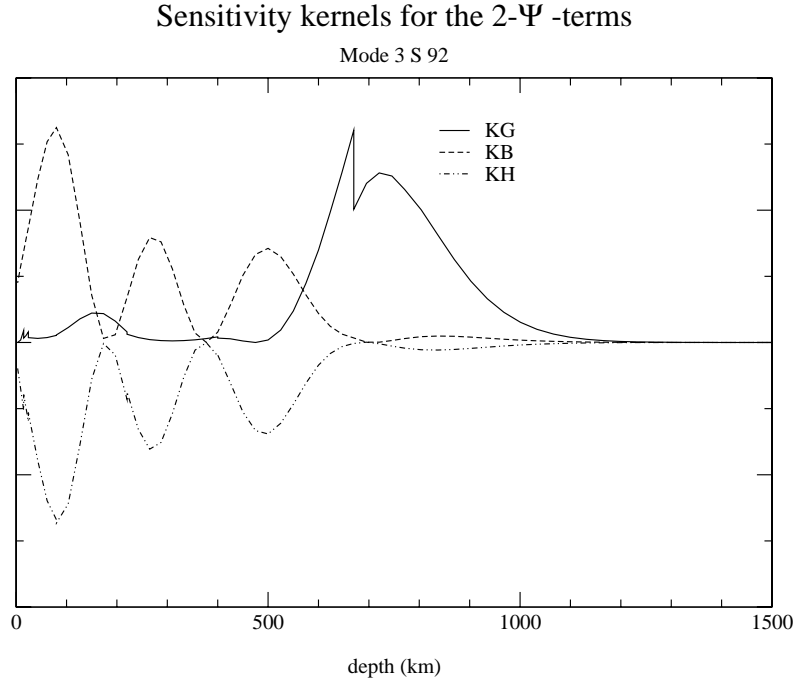


Figure 2.3: Sensitivity to G , B and H for mode ${}_3S_{92}$

2.4 Conclusion

We saw in sections 2.2.3 and 2.3.2 that the equations relating Earth's structure to normal mode structure coefficients (equation 2.33) and to perturbations in phase velocities of Love or Rayleigh waves (equation 2.78) are very similar, which facilitates the simultaneous use of the two types of data. Earth's structure at degree s and order t can be constrained by normal mode structure coefficients and by the corresponding spherical harmonic coefficient of phase velocity maps.

Equations such as 2.40 and 2.46 are employed in most chapters of this thesis. In Chapter 3 we focus on degree two isotropic structure in the whole mantle. Therefore, we have $\delta A_{st} = \delta C_{st}$, $\delta L_{st} = \delta N_{st}$ and $\delta F_{st} = \delta A_{st} - 2\delta L_{st}$. Kernels for normal modes are calculated for $s = 2$, while kernels for the phase velocity maps are independent of s (and correspond to normal mode kernels for which $s = 0$). In Chapter 4, we search for radial anisotropy in reference Earth models, which implies that equations 2.40 and 2.46

are used for degree zero structure. In that case, the sensitivity kernels are identical for normal mode and phase velocity data. Chapters 5 and 6 deal with lateral variations in radial anisotropy in the mantle, up to degree $s = 8$. The sensitivity kernels are identical for each degree because the data set used is the isotropic part of azimuthally anisotropic surface wave phase velocity maps (Coefficient A_1 in equation 2.78). Chapter 7 is a study of azimuthal anisotropy at degree two using the $2 - \Psi$ part of phase velocity maps for Love waves, which gives constraints on elastic parameter G . Finally, transverse isotropy is also assumed in the study of inner core anisotropy with normal modes (Chapter 8), and therefore only five independent elastic coefficients need to be considered. However, because of the symmetry of the problem (cylindrical symmetry about Earth's rotation axis), the equations employed differ from equations 2.40 and 2.46. It can be shown (Tromp, 1995a) that degree zero structure coefficients give constraints on the radial dependence of two elastic parameters, degree two structure coefficients constrain two other parameters, and degree four depends on the fifth parameter. The data used in that study (degrees two and four structure coefficients) are therefore related to only three variables that describe the depth dependence of seismic anisotropy in the inner core (see section 8.2 for details).

Chapter 3

P and S tomography using normal mode and surface wave data with a Neighbourhood Algorithm

Abstract

Traditionally P and S wave tomography is based on the inversion of data which are sensitive to the desired Earth structure, and model covariance is estimated from imperfect resolution and data error propagation. This analysis ignores the usually large null-spaces, and hence significant non-uniqueness of the solution, encountered in seismic tomography problems. Here, we performed a model space search for P- and S-velocity structure to find acceptable fits to recent normal mode splitting and fundamental mode phase velocity data. The survey of the model space employed the Neighbourhood Algorithm of Sambridge which preferentially samples the good data-fitting regions. A Bayesian approach was used subsequently to extract robust information from the ensemble of models. We particularly focussed on posterior marginal probability density functions and covariances for the various model parameters. The covariance matrix obtained is very useful in providing insights on the trade-offs between the different variables and the uncertainties associated with them. We stay in the framework of perturbation theory, meaning that our emphasis is on the null-space of the linear inverse problem rather than the neglected non-linearity. The whole model space (including the null-space) was sampled within reasonable parameter bounds, and hence the error bars were determined by all fitting models rather than

The content of this chapter was published in Beghein, C., Resovsky, J. & Trampert, J., *Geophysical Journal International*, **149**, 646-658 (2002)

subjective prior information. We estimated P and S models for spherical harmonic degree two only. The uncertainties are quite large and corresponding relative errors can exceed 100 % in the mid-mantle for V_p . We found a good correlation between our most likely S model and previous models, with some small changes in amplitude. Our most likely P model differs quite strongly from the recent P model SB10L18 and the correlation between our most likely P and S models is small. However, among all the good data-fitting models, many have a significant $V_p - V_s$ correlation. We computed $d \ln V_s / d \ln V_p$ from those models that correlate significantly. We found an increase with depth in the top 1500 kilometres. Deeper in the mantle, normal mode data prefer modest values compared to travel time data.

3.1 Introduction

Several tomographic models of the Earth's mantle were produced over the past 15 years, using different kinds of data, parameterizations and inversion techniques. Although there are some robust patterns, the models present large discrepancies (Resovsky and Ritziwoller, 1999b). This is partly due to the propagation of data errors through the inversion operator and imperfect resolution. Tomographic inverse problems are generally ill-posed (uneven and inadequate sampling of the Earth and inadequate model parameterization) and ill-conditioned (small errors in the data can lead to large variations in the model estimation owing to very small eigenvalues), resulting in large data and model null-spaces. These null-spaces are usually dealt with by employing some kind of regularisation, i.e. choosing one particular model out of many which are compatible with the data. Different authors use different regularisation schemes and hence produce discrepancies in the obtained models. We propose to sample the model space to have an overview of all models compatible with the data rather than choosing one by some subjective regularisation.

An example of how a model null-space component can change the resulting model was shown by Deal et al. (1999). They were able to incorporate additional, independent information in a tomographic image without affecting the misfit. They added a thermal model of a subducting plate to a high-resolution, three-dimensional tomographic study of the Tonga-Fiji region. Since the thermal model did not fit the seismic data, they added only the component of the theoretical slab insensitive to the seismic data using their null-space shuttle. Vectors of the null-space having no effect on the data prediction, the new tomographic model was in equally good agreement with the data. Unless the employed regularisation is derived from true physical information, it can add artefacts to the tomographic model.

A second advantage of mapping the model space concerns error analysis. Most linearized inversions give a posterior model covariance smaller or equal to the prior covariance by construction (Tarantola, 1987). If the cost function to be minimized has a large valley, i.e. there is a large model null-space, the posterior covariance can be seriously underestimated, depending on the prior covariance (Trampert, 1998). We argue that the width of the valley in the cost function is a realistic representation of the error bars in the

absence of true physical prior information.

We propose, here, to use a forward modelling approach to explore the model space, including the null-space. We suppose that perturbation theory is valid for our forward modelling. This means that the estimated error bars take the null-space of the linear inverse problem into account, but cannot account for the neglected non-linearity in the forward problem. Since we do not make an inversion, our results are not biased by the introduction of damping or any other non-physical *a priori* information, and since we stay within the linear theory the starting model is irrelevant. We applied the Neighbourhood Algorithm (hereafter referred to as NA) developed by Sambridge (1999a,b) to survey the parameter space and to find an ensemble of mostly “good” data-fitting models. This method is a novel direct search technique, conceptually very simple and able to exhibit a self-adaptive behaviour by sampling preferentially the regions of lower misfit. Once the survey of the parameter space is achieved, robust information on the ensemble can be extracted using a Bayesian approach, giving valuable indications on the errors and correlation of the model parameters. We applied this method to recent normal mode splitting measurements and fundamental mode surface wave phase velocity maps. The normal modes provide constraints on the long-wavelength structure of the Earth for compressional and shear wave anomalies in the mantle. Fundamental mode Rayleigh waves were included to constrain the upper mantle. The main purpose of this work is to establish the feasibility of our approach to mantle tomography. As a consequence we concentrate only on degree two structure.

An ensemble of “good” data-fitting joint shear and compressional wave velocity models were produced with the present set of normal mode and phase velocity data, and probabilistic information was retrieved. Error bars were then assigned to tomographic models. Having obtained most likely $dlnV_s$, $dlnV_p$ models and their respective error bars, we examined their correlation and their ratio, a quantity widely discussed in the mineral physics community and which is of particular interest for geodynamists.

3.2 Data and parameterization

The data set we used was composed of normal mode splitting functions and fundamental mode phase velocity models, corrected with the crustal model CRUST5.1 (Mooney et al., 1998). The free oscillations of a spherically symmetric, nonrotating and (transversely) isotropic Earth model have specific degenerate frequencies. The addition of asphericities and slight general anisotropy (under the conditions of application of perturbation theory) generates the splitting of multiplets into singlets with eigenfrequencies close to the degenerate eigenfrequency. Let us represent these three-dimensional model perturbations $\delta\mathbf{m}(r, \theta, \phi)$ from the reference model in terms of spherical harmonic components :

$$\delta\mathbf{m}(r, \theta, \phi) = \sum_{s=0}^{s_{max}} \sum_{t=-s}^s \delta\mathbf{m}_s^t(r) Y_s^t(\theta, \phi) \quad (3.1)$$

where Y_s^t are fully normalised and orthogonal spherical harmonics as defined in Edmonds (1960), with harmonic degree s and azimuthal order t . The structure coefficients ${}_k c_s^t$ of a particular isolated multiplet (denoted by k) characterize the way the eigenfrequencies split. If we neglect boundary perturbations, except for the crustal correction, we are left to first order with a single linearized relation between Earth structure and structure coefficients :

$${}_k c_s^t = \int_0^a \delta \mathbf{m}_s^t(r) {}_k \mathbf{M}_s(r) r^2 dr \quad (3.2)$$

where a is the radius of the Earth and ${}_k \mathbf{M}_s(r)$ is the volumetric structure kernel for perturbation $\delta \mathbf{m}_s^t$ (with respect to PREM (Dziewonski and Anderson, 1981)). For more details about normal modes theory, the reader is referred to chapter 2 of this thesis or to Woodhouse and Dahlen (1978) or Dahlen and Tromp (1998).

Normal mode splitting measurements below 3mHz were recently made by Resovsky and Ritzwoller (1998) for coupled and uncoupled multiplets with good sensitivity to S and P velocity anomalies everywhere in the mantle. In addition to structure coefficients, they also estimated corresponding error bars using Monte Carlo simulations of the effect of theoretical errors and noise. The structure coefficient measurements were used to create synthetic seismograms that were first perturbed with “errors” and noise of the appropriate statistical characteristics, and then inverted for new coefficient estimates. The results of multiple calculations was observed to produce approximately Gaussian coefficient distributions whose widths provided the uncertainties. Also, the coefficients of different angular and azimuthal orders were observed to vary independently. Both measurements and estimated error bars can be found on the internet (<http://physgeophys.colorado.edu/geophysics/nm.dir/>). We used their degree two structure coefficients, determined from uncoupled normal mode multiplets, but we excluded modes with sensitivity to the inner core. We kept measurements for 82 uncoupled mode multiplets, in particular 51 spheroidal modes and 31 toroidal modes.

To constrain the uppermost mantle, we added eight fundamental mode Rayleigh wave phase velocity models between periods of 40 and 275 seconds. For periods between 40 and 150 seconds, the models and errors are the average and standard deviation obtained from different studies : Trampert and Woodhouse (1995, 1996, 2001), Ekström et al. (1997), Laske and Masters (1996), Wong (1989) and van Heijst and Woodhouse (1999). For larger periods, we used the models of Wong (1989). Three dimensional models of phase velocity perturbations $\delta c/c$ (δc is the phase velocity perturbation relative to a reference phase velocity c , PREM in this case) can be expanded into spherical harmonics and their coefficients $\frac{\delta c_s^t}{c}$ are related to the Earth’s three dimensional structure in a way similar to structure coefficients :

$${}_l \left(\frac{\delta c_s^t}{c} \right) = \int_0^a \delta \mathbf{m}_s^t(r) {}_l \mathbf{K}(r) r^2 dr \quad (3.3)$$

Note that kernels for phase velocity perturbations are independent of degree s (they all correspond to kernels with $s = 0$), unlike the kernels relative to structure coefficients,

and neither of them depends on t . l is an index that discriminates between different frequencies.

Unlike for normal mode splitting data, error bars on phase velocity maps are hard to obtain. Trampert and Woodhouse (2001) showed that the quality of published phase velocity models vary widely with the period. At each selected period, we took all existing models, averaged each spherical harmonic coefficient and estimated its standard deviation. This should account for different measuring techniques of phase velocity, different data coverage and different regularisation-schemes in the construction of the maps. The error bars determined for normal mode structure coefficients by Resovsky and Ritzwoller (1998) have the characteristic of being almost constant at a given degree. There is not much variation between the different orders of spherical harmonic coefficient. By analogy, we decided to assign average uncertainties to $l(\frac{\delta c_s^t}{c})$ independent of the order t of spherical harmonic and defined by :

$$\sigma_l^2 = \frac{1}{2s+1} \sum_{t=1}^{2s+1} l \sigma_s^{t^2} \quad (3.4)$$

where s is the degree of the spherical harmonic (degree two in this study) and $l \sigma_s^{t^2}$ is the variance estimated for one particular spherical harmonic coefficient. Fig. 3.1 shows σ_l as a function of the period of the surface waves considered. It appears that the error decreases almost linearly between 40 and 100 seconds and the curve flattens between 100 and 150 seconds. We decided thus to assign a constant uncertainty to models with periods between 150 and 275 seconds, the value computed at 150 seconds (the model of Wong (1989) being the only one available to us at longer periods). We assumed, for convenience, that the errors have a Gaussian distribution, but there are far too few models to test this hypothesis.

To implement the first part of the NA (sampling the parameter space), we need to define the fit of a model to the data. We chose the χ^2 misfit, which is a measure of the average data misfit compared to the size of the error bar. It is defined by

$$\chi^2 = \frac{1}{N} \left[\sum_{k=1}^{N_m} \frac{(k C_s^{t,th} - k C_s^{t,obs})^2}{\sigma_k^2} + \sum_{l=1}^{N_s} \frac{(l(\frac{\delta c_s^t}{c})^{th} - l(\frac{\delta c_s^t}{c})^{obs})^2}{\sigma_l^2} \right] \quad (3.5)$$

where N is the total number of data, N_m is the number of normal mode data, N_s is the number of surface wave data. The upper index “ th ” stands for theoretical structure coefficients and phase velocity perturbations, predicted by equations 3.2 and 3.3, and “ obs ” refers to the measurements. σ_k (σ_l) is the estimated error bar corresponding to the k th (l th) data.

We parameterized our models with independent isotropic perturbations of the elastic coefficients δA and δL (with $A = \kappa + \frac{4}{3}\mu = \rho V_p^2$ and $L = \mu = \rho V_s^2$) with respect to PREM. Where PREM is transversely anisotropic (at depths between 24 and 220 kilometres), we used the equivalent isotropic PREM. The notation A and L was introduced

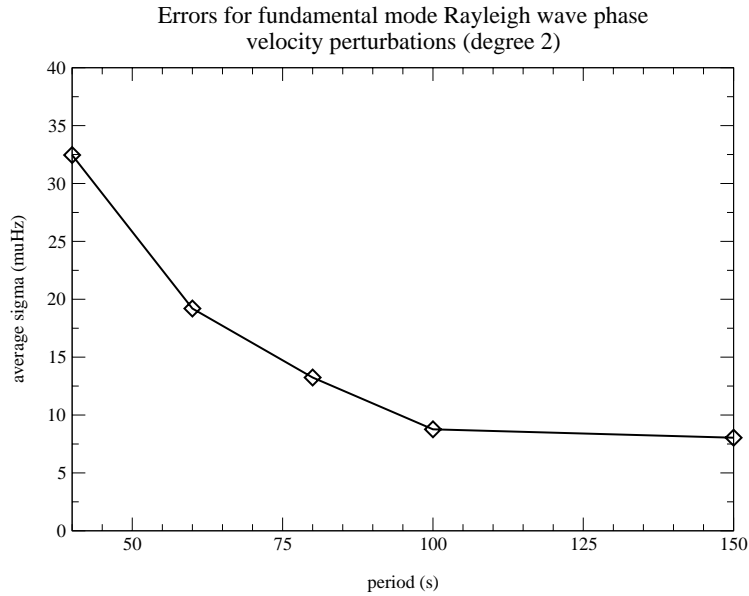


Figure 3.1: Estimated errors for degree two fundamental mode Rayleigh wave phase velocity perturbations.

by Love (1927) and is usually used to describe radially anisotropic medium. The corresponding anisotropic sensitivity kernels are given in section 2.2.3 of this thesis (see also Tanimoto (1986), Mochizuki (1986) or Dahlen and Tromp (1998)), and were combined to derive the appropriate isotropic kernels. Finally $\delta\mathbf{m}$ corresponds to $(\delta A, \delta L, \delta\rho)$. However, with the present set of normal mode data, it is not possible to resolve 3-D density perturbations in the mantle. Several authors have confirmed this (Resovsky and Ritzwoller (1999c), Romanowicz (2001), Resovsky and Trampert (2002)). Instead of taking density as one of our model parameters, we decided to scale density anomalies $\delta\rho$ and shear wave velocity perturbations using $d\ln V_s/d\ln\rho = 2.5$ (Anderson et al., 1968). This constraint, together with the size of the model space, introduces some prior information in the problem. Our models were parameterized radially in 7 layers. The bottom and top depths of these layers are, in kilometres, (2891, 2609), (2609, 2018), (2018, 1526), (1526, 1001), (1001, 670), (670, 220), (220, 24). They correspond to radial knots of PREM and are based on the layers defined in Resovsky and Ritzwoller (1998), which in turn are based on a Backus-Gilbert style resolution analysis (Backus and Gilbert, 1968). We gathered some of their layers into one new layer in order to decrease the number of

variables. Equation 3.2 reduces consequently to a sum over these seven layers :

$${}_k C_s^t = \sum_{i=1}^7 \delta \bar{\mathbf{m}}_s^{t,i} {}_k \bar{\mathbf{M}}_s^i \quad (3.6)$$

with

$${}_k \bar{\mathbf{M}}_s^i = \int_{r_i^{inf}}^{r_i^{sup}} {}_k \mathbf{M}_s(r) r^2 dr \quad (3.7)$$

r_i^{inf} and r_i^{sup} are the lower and upper radii respectively of layer i and $\delta \bar{\mathbf{m}}_s^{t,i}$ is an average perturbation of parameter \mathbf{m}_s^t on layer i . A similar relation holds for fundamental mode phase velocity perturbations (equation 3.3). The lateral parameterization is in spherical harmonics :

$$\delta A(r, \theta, \phi) = \sum_{s=0}^{s_{max}} \sum_{t=-s}^s \delta A_s^t(r) Y_s^t(\theta, \phi) \quad (3.8)$$

$$\delta L(r, \theta, \phi) = \sum_{s=0}^{s_{max}} \sum_{t=-s}^s \delta L_s^t(r) Y_s^t(\theta, \phi) \quad (3.9)$$

These expansions allow us to solve the problem spherical harmonic coefficient by spherical harmonic coefficient. Because of the scaling relationship between $d \ln V_s$ and $d \ln \rho$, we were left with only two parameters in each layer, thus 14 model components for each structure coefficient or phase velocity coefficient.

3.3 Results

3.3.1 Sampling and appraisal

We applied the NA using a linearized forward problem (equations 3.2 and 3.3). We wanted to survey the model space to find combinations of parameters $\delta A_s^t(r)$ and $\delta L_s^t(r)$ that give an acceptable fit to the data (equation 3.5). Because there is assumed to be no covariance among the data of different angular or azimuthal order, each of the five spherical harmonic coefficients at degree two could be treated independently. In other words, we could explore five parameter spaces separately, with 14 unknowns in each of them.

First, we had to fix the boundaries of the model space. We computed the equivalent degree two parameters $\delta L_s^t(r)$ for six different S models (MM2-L12D8 (Resovsky and Ritzwoller, 1999b), SKS12-WM13 (Su et al., 1994), S20RTS (Ritsema et al., 1999), SAW12D (Li and Romanowicz, 1996), S16B30 (Masters et al., 1996) and SB10L18 (Masters et al., 2000)). In each layer, we chose to search twice the range of the largest absolute amplitude obtained from those six models. Because model SB10L18 is a joint P and S model, we had a P model we could use to fix the range of parameter $\delta A_s^t(r)$.

We compared the amplitude of the coefficient $\delta A_s^t(r)$ corresponding to model SB10L18 and those obtained by scaling (factor of two) the other S models. We fixed our range for parameter δA_s^t as twice the absolute amplitude of the largest δA_s^t found. The final result depends on the chosen range (even if the model space is completely sampled, because there is a possibility that a good fitting model exists outside the range), but because of fear of violating perturbation theory, we decided not to increase the range any further. At the same time, we ensured that these six S models were included in the model space we sample, as well as their corresponding P models. Fixing the boundaries is equivalent to taking a boxcar function as prior density probability distribution. This introduces boundary effects and the posterior probability density function is not necessarily Gaussian when the most likely model is close to the edge.

We refer the reader to Sambridge (1999a,b) for details about the NA. The first stage of the algorithm, the sampling, makes use of a geometrical construct, the Voronoi cells, to approximate the misfit function and to drive the search towards the best data-fitting regions while continuing to sample a relatively wide variety of different models. It is relatively easy to tune since only two parameters have to be set : n_s , the number of models generated at each iteration, and n_r the number of “best” data-fitting Voronoi cells in which random walks are performed at each iteration. We were careful with the choice of these values, since it is very important to have a good initial sampling in order to make a meaningful Bayesian interpretation (which is the second stage of the NA). We had to avoid directing the search towards a local minimum and we had to sample the posterior probability density (PPD) with the highest possible accuracy, to sample all the good fitting regions of the model space. A way to do so is by increasing the values of the tuning parameters. As both tuning parameters increase together, the algorithm is more explorative as a sampler but also less efficient at mapping details of the most important (the best fitting) parts of the model space. It is not possible to draw general conclusions on the tuning parameters since every problem is different and requires specific parameters. We had to find their most appropriate values by trial and error. Sambridge explained that the minimum sample size required is very sensitive to the dimension of the problem (Sambridge, 1998). His experiments showed that, to get a good enough approximation of the posterior probability density, the required sample sizes have to be increased when the dimension of the problem becomes larger. We decided to have n_s equal to n_r , which is the minimum value n_s can take, in order to broaden the survey. We started to sample the model space with some relatively low values of n_s and n_r (10 or 20), and we increased the tuning parameters successively and compared the different results. For some variables, we got different results if we used such small values. This indicates that for these tuning parameters, the results are not independent of the tuning. The chosen values of n_r are not large enough to identify all the models compatible with the data. After some trials with n_r ranging up to 200, we decided to use $n_r = 50$. It was the smallest value above which the results appeared to be independent of the tuning and that explored all the good fitting regions. The algorithm is very effective in finding the regions of lowest misfit. To choose the number of iterations, we looked at the evolution of the misfit with time. χ

decreased very rapidly, the sampling being directed towards the cells having the best fit. We decided to stop the survey when the misfit has “flattened”, and the model distribution was observed to approximate a likelihood sampling. The latter condition indicates that the sampling is adequate for analysis using the NA Bayesian resampling (see below). When n_r is increased, more models must be generated and hence the survey requires more time. The sampling was completed in about two hours on a SUN Ultrasparc machine (400 MHz) for $n_r = 200$ and 300 iterations and it only took half an hour for $n_r = 50$ and 600 iterations.

Models generated by the Neighbourhood Algorithm

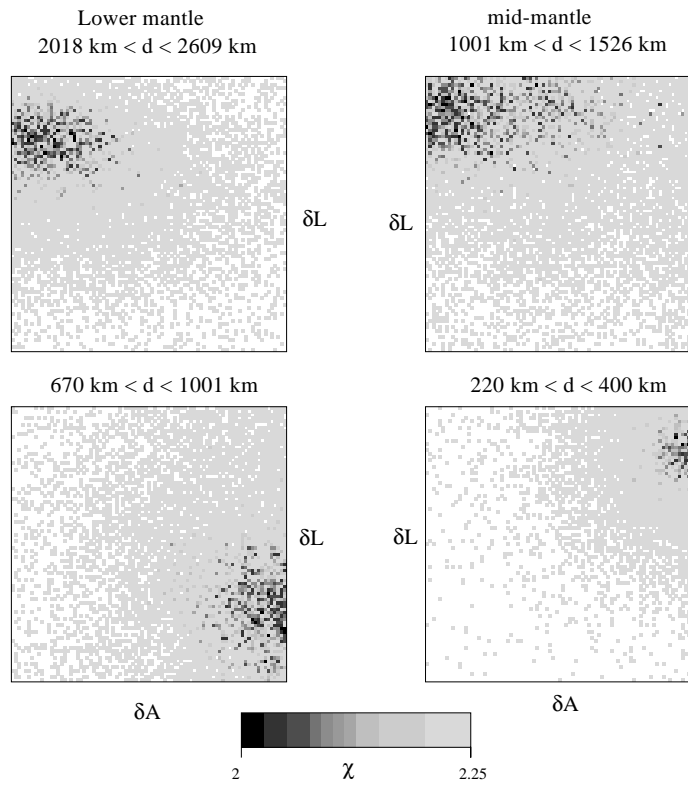


Figure 3.2: Results of the sampling using the real part of c_2^1 ($\delta c_2^1/c$). The scale represents the χ misfit as defined in equation 3.5. Parameters on the horizontal axis correspond to perturbations in elastic coefficient A ($= \delta(\rho V_p^2)$) and parameters on the vertical axis correspond to perturbations in L ($= \delta\mu = \delta(\rho V_s^2)$), with respect to PREM. The full range of the models space is shown.

As an example, we show in Fig. 3.2 the result using the real part of c_2^1 in four of our seven layers. It is a way to depict the shape of the model space with regions of higher misfit (light grey) and regions of better fit (dark), where the sampling density is larger. We see that there is a clear global minimum in the upper mantle. For some other variables, the best fitting region is more elongated. This shows that, within the boundaries of our model space, a large range of values for these variables are compatible with the data. It is the case of perturbations in $\delta A = \delta(\rho V_p^2)$ in the mid-mantle and deeper in the mantle. Several variables have their global minimum situated at the edges of the model space. Increasing the range of the survey has the effect of reducing the minimum misfit somewhat but, because of the trade-offs among the model parameters (visible in the correlation matrix, Fig. 3.3), moving the global minimum of one of them implies that other variables move as well and may, in turn, be directed towards the edge. Therefore we believe that, as long as there are trade-offs between model parameters, the model space cannot be surveyed guaranteeing that no solution is on the edge of the model space. This is not a major problem though, because we can quantify the trade-offs as explained below. Further, increasing the range of search substantially will violate perturbation theory and require a complete new set-up of the problem.

We then needed to extract quantitative information on the models previously generated. Sambridge (1999b) provides an approach to the appraisal problem, based on a Bayesian point of view. This is the second stage of the algorithm. This appraisal of the ensemble is the most time-consuming part of the algorithm. In most model space search techniques, inferences are drawn from the good fitting part of the ensemble only, and sometimes even from a single member. What is new in this algorithm is that the entire ensemble is used, the “bad” data-fitting models as well as the “good” ones, and an efficient summary of the sampled models is provided. In a Bayesian approach, the information contained in the models is represented by a posterior probability density function (PPD). In the absence of restrictive prior information on the models, the model that maximizes the PPD is the model with the best data fit. The PPD can be used to compute quantities such as the posterior mean model, the posterior model covariance matrix and marginal posterior probability density functions. An integration over the parameter space is performed using a “likelihood sampling” whose density corresponds to the PPD. To do this, the algorithm uses the misfit of the sampling to create a likelihood sampling. This requires a new ensemble of points to be generated (the “resampled” ensemble) whose distribution follows the approximate PPD. This is one of the main factors influencing the computation time. Once the resampling is done, computing the Bayesian integrals requires only simple averages over the resampled ensemble.

For the resampling of the model space, tuning parameters have to be set : the number of random walks to perform and the number of steps per random walk. Finding the parameters that optimize the coverage of the Gibbs sampler is a trial and error process, which is time-consuming but it is characteristic to every direct search technique. It is preferable to use multiple random walks instead of a single one, and the number of steps per walk must be large enough to insure the convergence. After each trial, convergence

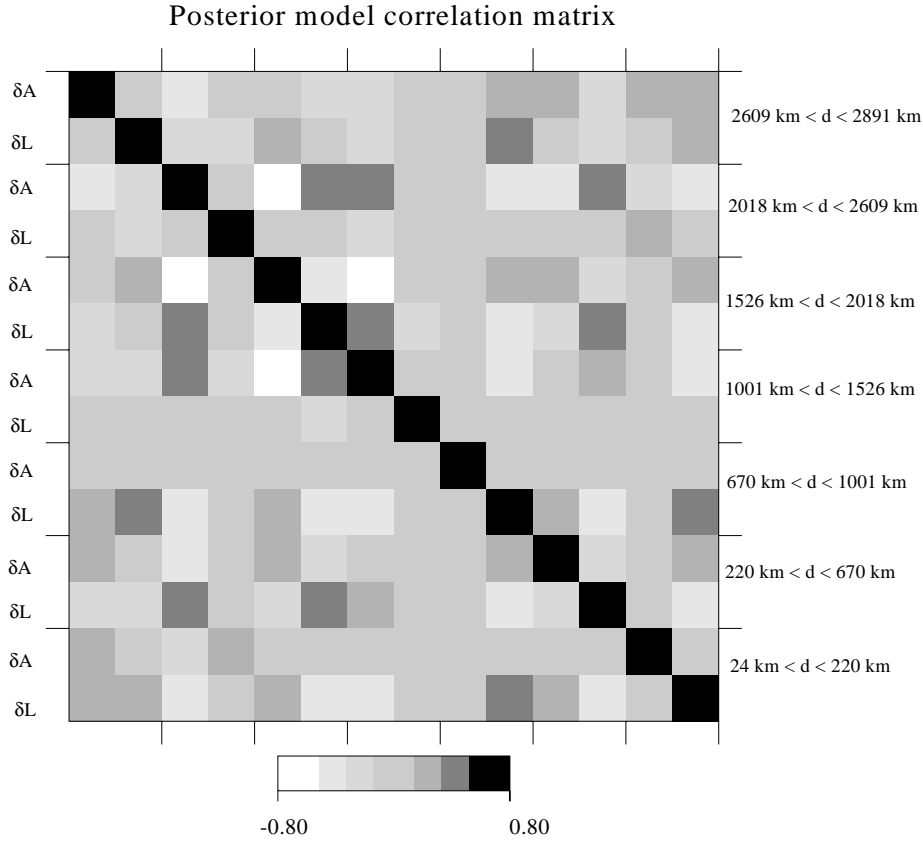


Figure 3.3: Correlation matrix corresponding to the real part of $c_2^1 (\delta c_2^1 / c)$.

can be checked, numerical errors evaluated and the length and number of random walks can be adjusted accordingly. For ensembles generated with 50 cells and 600 iterations, we needed between 6000 and 10000 steps per walk, depending on the coefficient treated, and four to six walks in order to achieve the convergence of the integrals. It took approximately seven hours on a SUN Ultrasparc (400 MHz) to compute 1-D marginals, 2-D marginals and the correlation matrix. We also computed Bayesian integrals for some of the ensembles generated with 200 cells, to make sure the results were the same as the ones obtained with 50 cells. Since their sampling required more iterations, more points were needed for the computation of the integrals. The appraisal then required three to four days.

When the PPD is Gaussian, the trade-off between model parameters can be represented by the correlation matrix, which is derived from the off-diagonals of the posterior

model covariance matrix. The correlation matrix corresponding to our problem is different for each spherical harmonic coefficient. The one obtained for the real part of c_2^1 is represented in Fig. 3.3. We can see that variables of the mid-mantle and lower mantle are highly correlated to one another. They are also correlated to model parameters of the upper mantle, for instance δA between 2018 and 2609 km of depth (layer 2) with δL in the uppermost layer. There are, to some extent, trade-offs among all the model parameters. In order to improve these results, we would need to add independent data sensitive to one or the other of a given pair of correlated model parameters. The correlation matrix is an excellent tool to see what is actually resolvable and what additional data is most desirable.

The covariance matrix can also be used to get the variances of the model parameters (obtained from its diagonals). However, the use of a covariance matrix only makes sense when the PPDF is a Gaussian distribution. A more general way of looking at variances and trade-offs is given by marginal distributions. A one-dimensional marginal is the probability of each value of a particular model parameter, given all possible variations of the others. The width of those posterior marginals gives a further indication on the constraint we have on each variable, and can be assimilated to error bars. A two-dimensional marginal shows the likelihood of each combination of values for a pair of model parameters. Computing the joint marginal of two model parameters implies an integration over all the other parameters. Fig. 3.4 shows 2-D marginals of some pairs of variables for the real part of c_2^1 . These marginals are a robust way to look at model parameter trade-offs. The diagonal elongated shape observed for some pairs of variables shows the trade-off between them. For instance, the top-left marginal of Fig. 3.4 shows a trade-off between δA in the lowermost layer (layer 1) and the layer above (layer 2, between 2018 and 2609 kilometres of depth) and the bottom middle marginal shows a trade-off between P anomalies (δA) in layer 4 (between 1000 and 1526 kilometres of depth) and S anomalies (δL) in layer 3 (at depths between 1526 and 2018 km). Even with the additional constraints provided by surface waves, the upper and the lower mantle are not completely independent. The bottom-left marginal shows a trade-off between δL in the upper mantle (layer 7) and δA between 2018 and 2609 kilometres of depth (layer 2). We also show two pairs of model parameters that almost do not correlate in Fig 3.3 : δA and δL between 2018 and 2609 kilometres of depth (bottom-right) and δA and δL at depths between 670 and 1000 km (top-right). Neither shows the elongated diagonal pattern characterizing a trade-off.

In Fig. 3.5, we show the 1-D marginals for a few model parameters. δA at depths between 2018 and 2609 kilometres can take a large range of values compatible with the data. The width of the 1-D marginal is large. In this particular case, the sign of the perturbation is barely constrained. On the contrary, in the upper layers, between 220 and 1000 km of depth, both P and S anomalies are better determined. If we compare the 1-D marginal and Fig. 3.2 for δA between 1000 and 1526 km of depth, we observe a difference. From Fig. 3.2, one could expect a wide range of possible values for that parameter and thus a 1-D marginal with a shape similar to the one obtained for δA between 2018 and 2609

kilometres of depth. Its width is relatively large but it clearly peaks towards the edge, at a positive value. This difference between the sampling and the Bayesian interpretation of this sampling comes from the resampling of the ensemble that has to be made in order to evaluate an approximate PPD. These marginals also show that all the parameters in the model space do not exactly have a Gaussian distribution. When a most likely parameter is located towards the edge of the model range, boundary effects destroy the Gaussian shape. Another strong influence on the Gaussian distribution comes from the null-space. If the model parameters are Gaussian distributed, the PPD is Gaussian. In the presence of a null-space the PPD will show an elongated valley and appear non-Gaussian. Away

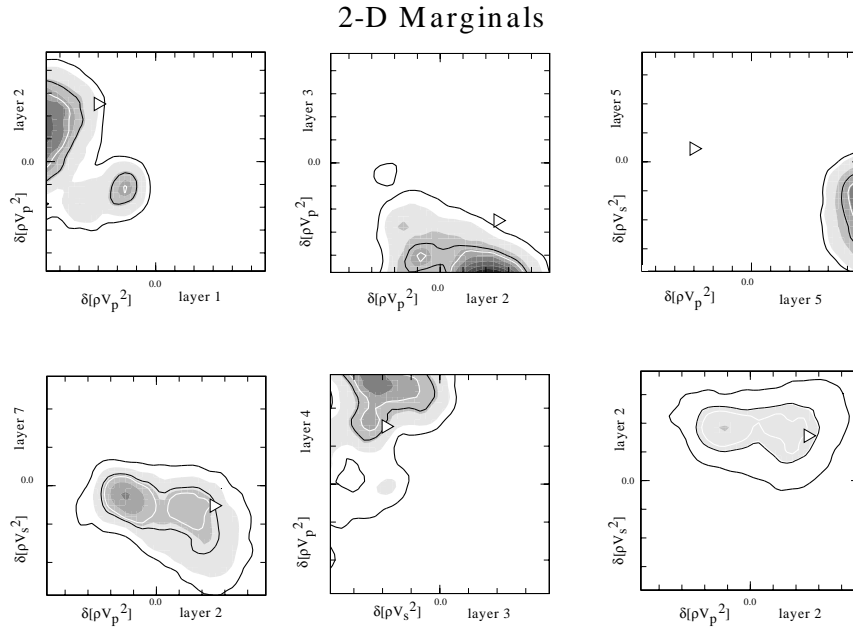


Figure 3.4: 2-D marginals corresponding to the real part of c_2^1 ($\delta c_2^1/c$). The white triangle denotes the values for model SB10L18. and 90 % (blue) confidence levels. Going from inside towards the edges, the solid lines represent the 30 % (white), 50 % (grey) and 90 % (black) confidence levels. Parameters on the horizontal axis correspond to perturbations in elastic coefficient A ($= \delta(\rho V_p^2)$) and parameters on the vertical axis correspond to perturbations in L ($= \delta\mu = \delta(\rho V_s^2)$), with respect to PREM. The full range of the models space is shown. Layer 1 corresponds to the deepest layer and layer 7 represents the range 24-220 km depth.

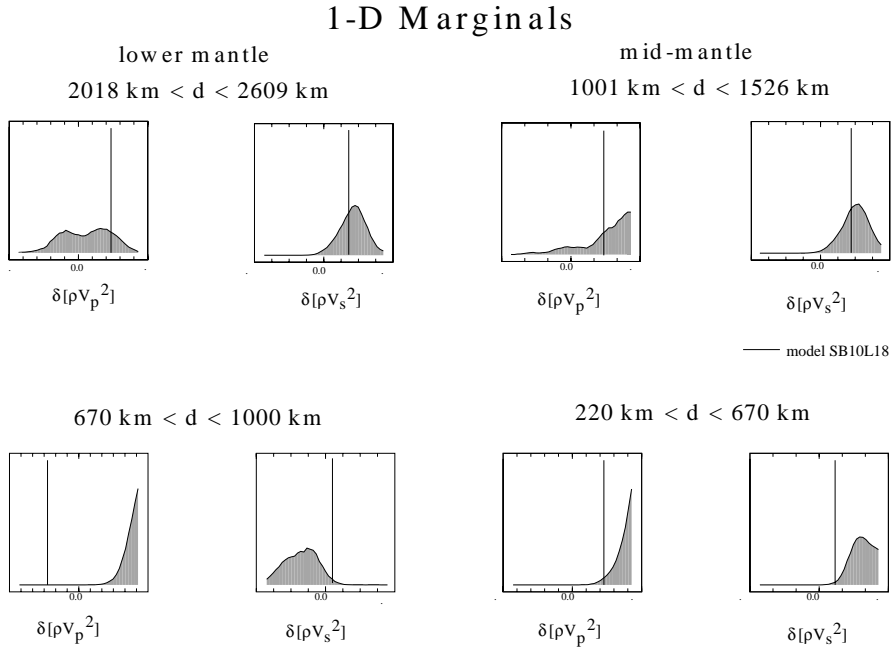


Figure 3.5: 1-D marginals corresponding to the real part of c_2^1 ($\delta c_2^1/c$). The vertical black line is the position of model SB10L18. The full range of the models space is shown.

from the edges of our sampling range, the 1-D marginals are thus a measure of the size of the null-space. The 2-D marginals and the off-diagonal elements of the correlation matrix compare qualitatively well, but the amplitudes of the correlations are affected by large non-Gaussian distributions. Using a Gaussian assumption for the PPD will underestimate the posterior uncertainties on the model parameters in the presence of a large null-space.

We did not test different parameterizations. Choosing another parameterization would probably slightly modify the results since, as shown by the correlation matrix, all model parameters are to some extent correlated to one another. The layers we chose were based on those of Resovsky and Ritzwoller (1998), which approximate the optimal depth layers that can be resolved for the given depth kernels. Modifying the layers would thus only degrade the posterior covariance. The important point is that the results should only be considered with the correlation matrix.

3.3.2 Shear and compressional wave velocity models and error bars

This section, deals mainly with the most likely models. These are the models corresponding to the maximum of the 1-D marginals and not the mean model as calculated directly by the NA. The reason for this is that the mean model is only meaningful when the PPD is Gaussian and it is not exactly the case for all the parameters in the model space, as discussed in section 3.3.1. For the same reason, we preferred estimating the width of the 1-D marginals instead of reading them directly in the covariance matrix. We took this width as the largest distance where the amplitude of the most likely models has decreased by a factor $1/e$. It usually gives slightly larger variances than those read in the covariance matrix.

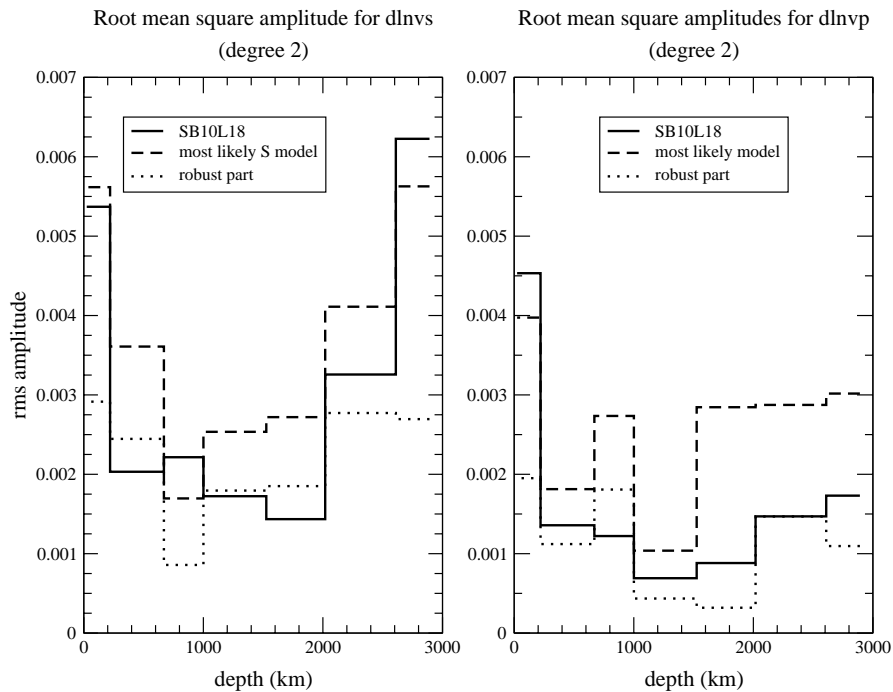


Figure 3.6: Root mean square amplitudes of our most likely models, their robust part and model SB10L18 as a function of depth. Fig. 3.6a (left) corresponds to S anomalies. Fig. 3.6b (right) corresponds to P anomalies.

In Fig. 3.6, we compare the root mean square (rms) amplitude of our most likely velocity models, their robust part (the most likely model from which we subtract the uncertainties) and the rms of model SB10L18, as a function of depth. SB10L18 is a joint P and S model derived from the inversion of body waves, surface waves and normal mode splitting data. The rms of the robust part of our models corresponds to a lower limit for S and P model amplitudes. The size of the anomalies in SB10L18 and in our most likely model is similar. They differ the most between 220 and 670 km depth and in below 1000 km for V_s . For V_p , the amplitudes are close in the top 670 kilometres and between 1000 and 1526 kilometres of depth. The differences are partly due to the presence of body wave data in SB10L18.

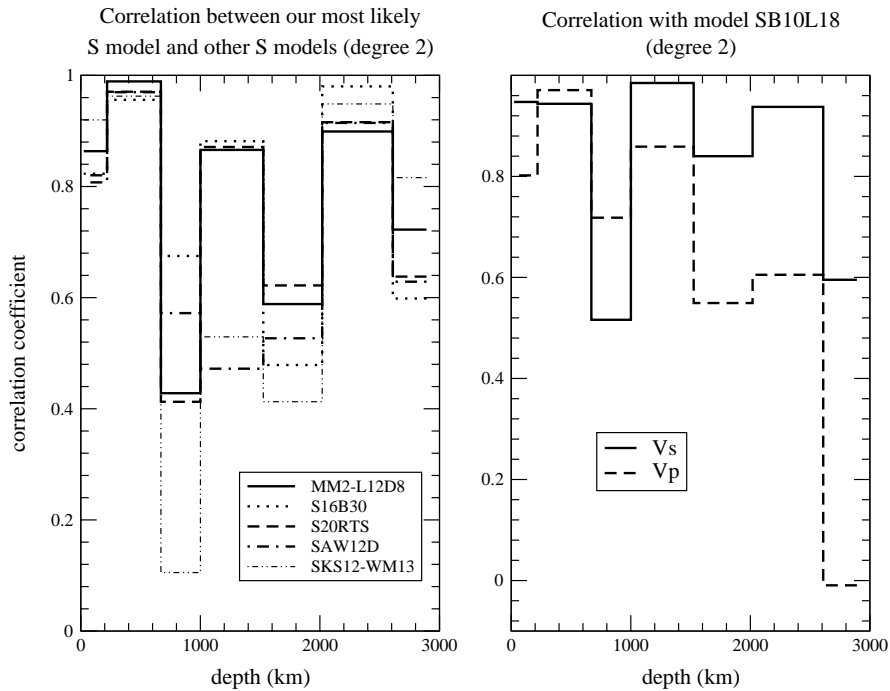


Figure 3.7: Correlation coefficient between our most likely models and other models as a function of depth. Fig. 3.7a (left) represents the correlation between our most likely S model with 5 other S models. Fig. 3.7b (right) represents the correlation between our most likely models with the joint P and S model SB10L18.

We show in Fig. 3.7a the geographical correlation of our $dlnV_s$ model with other S models (degree two) : MM2-L12D8 (Resovsky and Ritzwoller, 1999b), SKS12-WM13 (Su et al., 1994), S20RTS (Ritsema et al., 1999), SAW12D (Li and Romanowicz, 1996) and S16B30 (Masters et al., 1996). These models were derived from linearized inversions. For most models, in some layers, the correlation is above the 90 % confidence level for degree two maps (corresponding to a correlation coefficient of 0.73 (Eckhardt, 1984)) and there are two layers, in the mid-mantle, where the correlation is very low, with any other model. One could expect it to be better for models MM2-L12D8 and S20RTS that incorporated the same set of normal mode data as we used. This poor correlation is related to the trade-off between V_p and V_s in the mid-mantle (Fig. 3.3). We searched for a joint P and S model, whereas MM2-L12D8 and S20RTS assume a scaling between $dlnV_p$ and $dlnV_s$. These very different constraints on V_p lead to different V_p models and, in the mid-mantle, the trade-offs imply that V_s can also be very different. Fig. 3.7b shows the geographical correlation for degree two of our most likely models with model SB10L18, for both P and S since SB10L18 is a joint P and S model. It is interesting to see that the correlation coefficient between our S model and the S model of SB10L18 is above the 90 % confidence level in most layers. For the P models, the correlation is not as good, especially in the lowermost mantle where the correlation coefficient is close to zero. They correlate reasonably well between depths of 220 and 670 kilometres and between 1000 and 1526 km.

In Fig. 3.8, we plotted the maps corresponding to our most likely degree two S and P models in the seven layers we used. A robust feature from all tomographic models to date is that the degree two structure dominates the two lowermost layers ($2609 \text{ km} \leq d \leq 2891 \text{ km}$ and $2018 \text{ km} \leq d \leq 2609 \text{ km}$) and in the transition zone (Resovsky and Ritzwoller, 1999b). These maps are thus good approximations to complete tomographic models only at those depths. As we see from the correlation coefficient in Fig. 3.7b, both S models agree quite well at most depths. On the contrary, the two P models differ much more.

In Fig. 3.9 we plotted the correlation between our most likely P and S models. The correlation is significantly high (above the 90 % confidence level) only between depths of 220 and 670 km. The lowest correlations are situated in the lowermost and uppermost layers. This is not representative in the uppermost mantle because degree two structure is not dominant there. On the contrary, the lowermost mantle is believed to be dominated by that degree. We cannot, however, conclude directly that there is no correspondence between P and S anomalies in the lowermost mantle. One of the advantages of using the NA is that it provides error bars on the models. Within these error bars, there may be models compatible with the data that have a higher $dlnV_s - dlnV_p$ correlation. Thus, a better way to look at that correlation is by taking into account the uncertainties on the models.

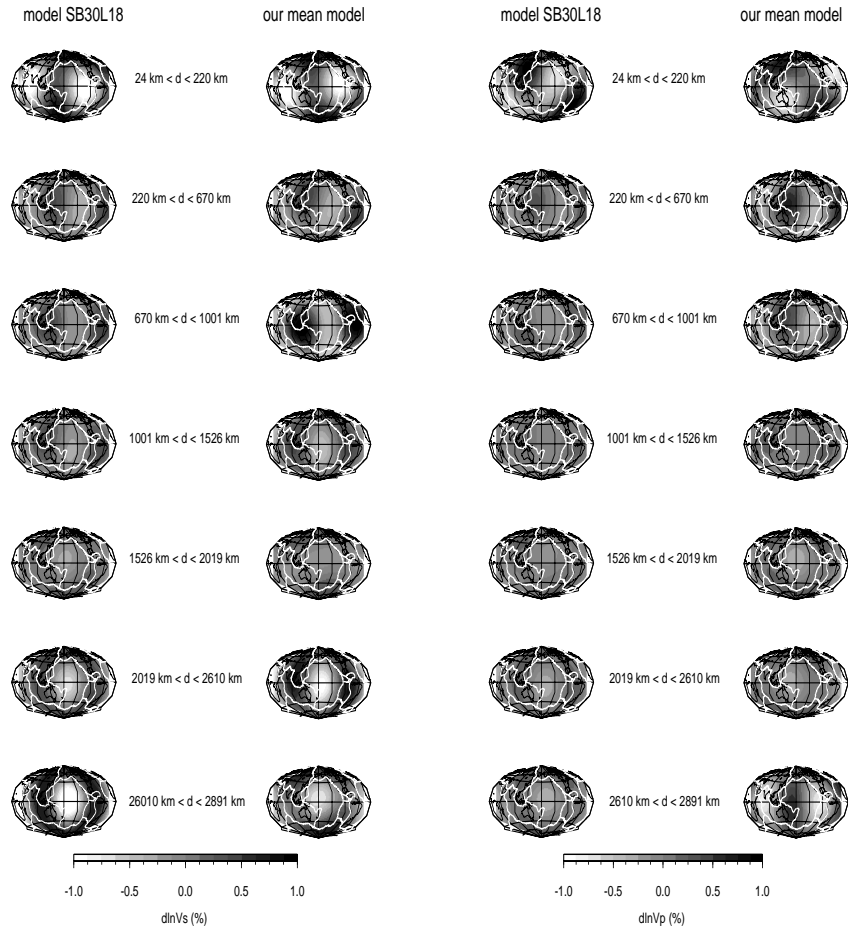


Figure 3.8: Degree two maps of our most likely S (left) and P (right) models compared to degree two maps of models SB10L18.

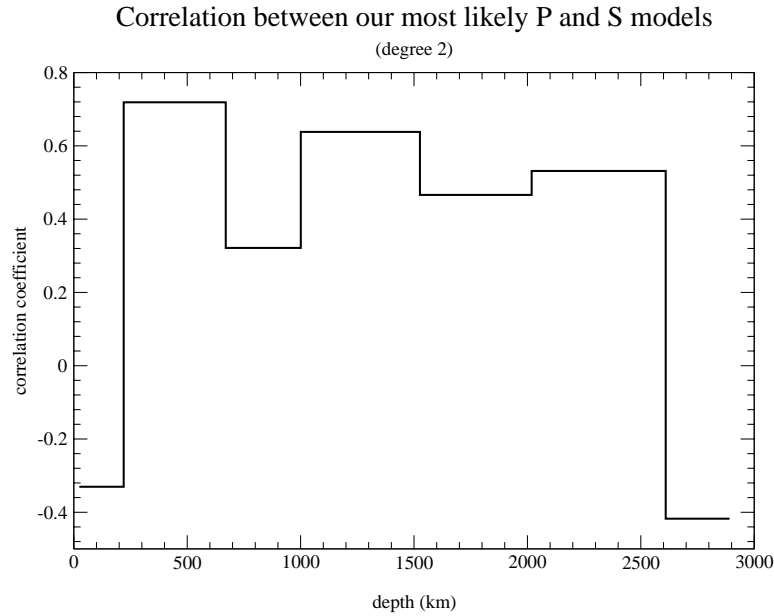


Figure 3.9: S-P correlation as a function of depth.

To take into account all the models, we sampled $\delta A_s^t(r)$ and $\delta L_s^t(r)$ within their estimated error bars with a random number generator, we deduced the corresponding $d \ln V_{s_s}^t(r)$ and $d \ln V_{p_s}^t(r)$ and we computed the correlation coefficient for all the models generated. Note that we can easily compute $d \ln V_{s_s}^t(r)$ and $d \ln V_{p_s}^t(r)$ from $\delta A_s^t(r)$ and $\delta L_s^t(r)$, because we imposed a scaling relationship between $\delta \rho$ and δV_s . The distributions of correlation values can be plotted as histograms. It is interesting to note that the histograms are largely independent on how we sampled the models (uniformly, Gaussian or corresponding to the actual 1-D marginals). We took the median of the correlation coefficient and we estimated its uncertainty. The uncertainty of the median was obtained by computing its scaled median absolute deviation (SMAD) (Bevington, 1969). We used the SMAD as uncertainty on the overall correlation coefficient. In Table 3.1 are listed the median correlation coefficients and their uncertainty at different depths, and Fig. 3.10 gives the histograms for different depths. In our lowermost layer, where our most likely P and S models do not correlate (the correlation coefficient was -0.417), we see that that the median value is also very low (-0.45) and lots of models are anticorrelated. The uncertainty is, however, very large and there are a few models compatible with the data that correlate well. There are models, in the layers above, that correlate well and some that correlate

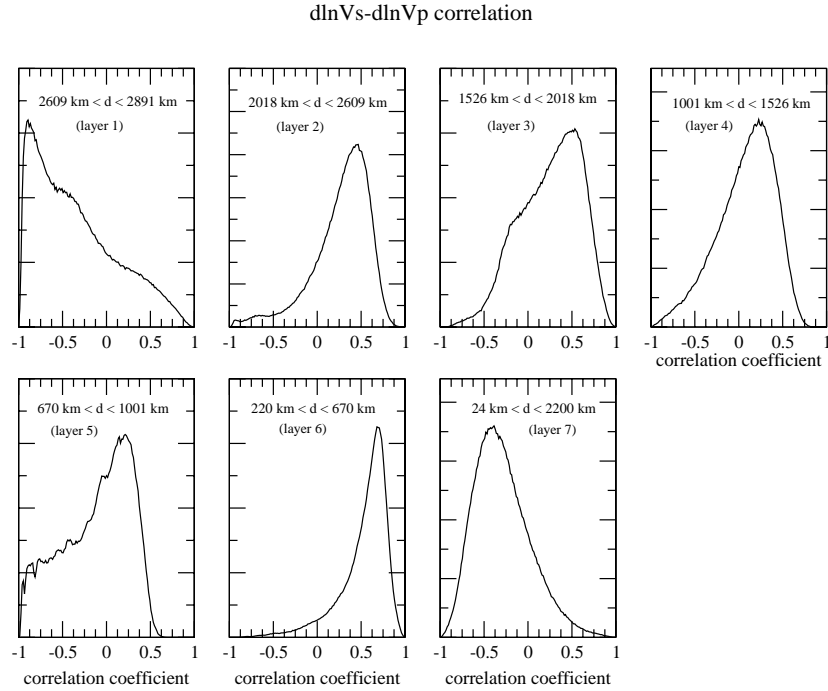


Figure 3.10: Distribution of $d\ln V_s - d\ln V_p$ correlation coefficient between all the models compatible with the data as a function of depth.

significantly. In the uppermost layer, correlation is poor again, but there, degree two is far from dominant. This is one illustration of the importance of error bars in tomographic models.

Error bars on the spherical harmonic components of $d\ln V_s$ and $d\ln V_p$ can easily be derived from those on dA_s^t and dL_s^t because of the scaling between $d\ln \rho$ and $d\ln V_s$. In Fig. 3.11, we show the relative error bars for the rms amplitude, $d(rms)/rms$, for both shear and compressional wave velocities. This represents the size of the error bars on the rms relative to the size of the most likely model. The error bars are large, especially for V_p . These uncertainties are mainly due to the large null-space associated with our problem. It shows what can be determined by the data alone. Prior information can of course reduce the nullspace, but we argue that choosing a model should be based on

Depth (km)	median	SMAD
$2609 < d < 2891$	-0.535	0.425
$2018 < d < 2609$	0.36	0.30
$1526 < d < 2018$	0.205	0.36
$1001 < d < 1526$	0.20	0.27
$670 < d < 1001$	0.003	0.42
$220 < d < 670$	0.62	0.18
$24 < d < 220$	-0.29	0.36

Table 3.1: Correlation between all models generated within their error bars. The second column gives the median of the distribution and the third column gives its robustness.

physical information rather than a subjective damping parameter. Unless such a physical prior information exists, it is preferable to consider all models compatible with the data. Another way to reduce the size of the null-space is of course by adding more data. We expect that including body wave data will significantly reduce the uncertainties.

Perturbations in V_s are believed to be larger than perturbations in V_p . The value of their ratio $R = d \ln V_s / d \ln V_p$ is commonly used as a diagnostic whether the heterogeneities in the mantle have a chemical or thermal origin. The value of R in the deep mantle is still a controversy. A low ratio could be explained by a thermal origin of the anomalies and a high value (above 2.5) could indicate a chemical component in the heterogeneities. Looking at various studies, there is a large variety of values for R . A good review on the subject can be found in Masters et al. (2000). Because different authors compute R in different ways, Masters et al. (2000) recalculated a spherical averaged R for various models. Generally, studies using body wave travel time data only prefer a high value of R in the lowermost mantle. Robertson and Woodhouse (1996) used ISC data and found a ratio slowly increasing from 1.7 to 2.5 for depth between 600 and 2000 km of depth. Bolton (1996) used long period body waves data and his results also showed an increase of R with depth up to a value slightly below 3.5 at the bottom of the mantle. Both studies were constrained inversions, i.e. a perfect proportionality between P and S anomalies at every depth was imposed but R was allowed to change. Su and Dziewonski (1997) used ISC data, long period body wave data and surface wave data to perform an unconstrained inversion for bulk sound and shear wave speed. They obtained a value of R of almost 3.5 in the lowermost mantle. Saltzer et al. (2001) employed ISC data to produce P and S models of the mantle. They distinguished between regions where there has been subduction in the last 120 million years and where there has not. They found a peak value of $R = 3$ around 2200 km of depth in non-slab regions and a ratio smaller than 2 at all depths in slab regions. There are two models using ISC data that show a low ratio at all depths. These are the models of Vasco and Johnson (1998) and Kennett et al. (1998). Their values of R are smaller than 1.5, and even smaller than 1 for Vasco and Johnson (1998). When normal modes are included in the data set, the tendency observed in joint

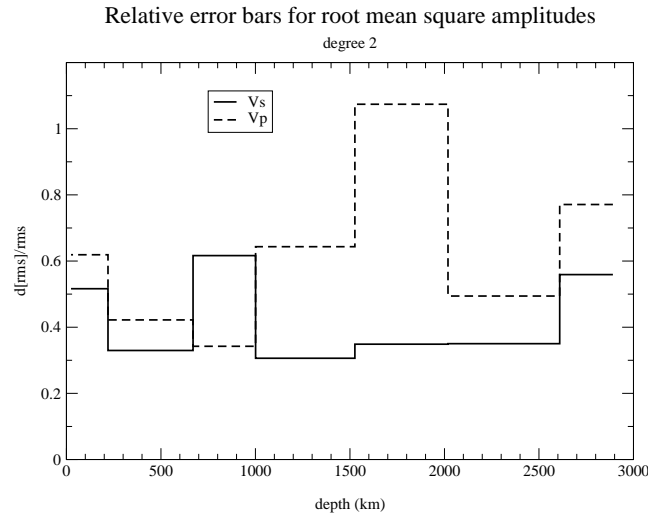


Figure 3.11: Relative uncertainties for the root mean square amplitude of our most likely S model (dashed line) and our most likely P model (solid line) as a function of depth.

inversions is to have a more modest ratio in the lowermost mantle (model SB10L18), except for Romanowicz (2001) who found a value between 1 and 2 everywhere but at depths greater than 2000 km where R is larger than 2.5. Model SB10L18 was obtained from the joint inversion for bulk sound and shear wave speed, whereas Romanowicz (2001) performed inversions for V_p and V_s directly. In their paper, Masters et al. (2000) also observed that constrained inversions for bulk sound and shear wave speed usually give P and S models that correlate significantly, while there is less correlation in inversions for V_p and V_s .

We computed R on a $10^\circ \times 10^\circ$ grid. We took into account all the models obtained for V_s and V_p , in the same way we did to compute the correlation between all our P and S models. We generated a series of values of $\delta A_s^t(r)$ and $\delta L_s^t(r)$ within their estimated error bars, recombined the five spherical harmonic coefficients to get $\delta A(\theta, \phi)$ and $\delta L(\theta, \phi)$ on each grid point, and we computed the corresponding $d \ln V_s(\theta, \phi)$, $d \ln V_p(\theta, \phi)$ and R for all the possible combinations. The distributions obtained expressed the variation of R for various (θ, ϕ) and various models generated within the posterior model uncertainties. We determined the median of these distributions, which we took as the spherically averaged estimate of R . The SMAD is used to derive the uncertainty on R (as in Masters et al. (2000)). We found that R takes modest values in the lowermost mantle (see Fig. 3.12, dotted line). The question is whether R is low in the lowermost mantle (where degree two

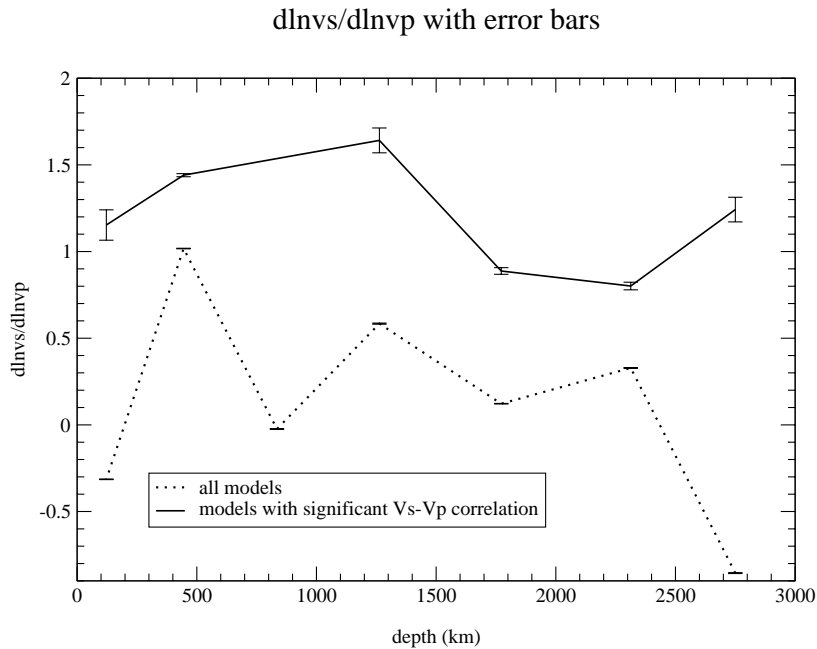


Figure 3.12: Ratio between degree two $dlnvs$ and $dlnvp$ as a function of depth.

structure is dominant) because the correlation is low or because the normal mode data generally prefer a lower ratio. To answer that, we computed R by only taking the models which correlate significantly (above 0.73) in one particular layer. The values are plotted in Fig. 3.12 (solid line). We observe an increase of R with depth in the top 1500 km of the mantle, taking values between 1 and 1.75, and modest values in the lowermost mantle. This shows that normal mode data favour low values for R in the deeper mantle, in contradiction with Romanowicz (2001), who found R up to 3.5 at depths > 2000 km, using degree two normal mode splitting data and a layered parameterization. The possible reasons for this difference are that Romanowicz does not include surface wave measurements in her data and introduces strong prior information in the inversions (the damping was chosen so that $dlnV_s/dlnV_p$ matches the range 1.5 - 2 in the top 1500 km, slightly higher than what we find).

3.4 Conclusion

The aim of this paper was to explore a model space with a direct search method to identify good data-fitting isotropic Earth models. We used the Neighbourhood Algorithm developed by Sambridge (1999a,b), which is a new derivative-free direct search technique that preferentially samples the good data-fitting regions of a model space. A Bayesian approach was used subsequently in order to extract robust information from the ensemble of models generated. We examined the posterior marginal probability density functions, the variances of the various model parameters and the correlations among them. The whole model space, including the null-space, was sampled within reasonable bounds, and the error bars are consequently more realistic than traditional inversion error estimates. This new technique appears to be very efficient in finding the best data-fitting regions in a high dimensional space (provided the size of the model space has been established). It is easy to tune since there are only two tuning parameters but they have to be chosen carefully to avoid the search being trapped in a local minimum and to importance sample the entire parameter space, while not reducing the efficiency of the algorithm. The optimal values have to be found by trial and errors. The subsequent use of the Bayesian algorithm does not require any further solutions of the forward problem. The parameter space is resampled instead, using only information from the initial survey of the model space. The accuracy of the Bayesian integrals will depend on the way the model space was initially sampled.

We applied the Neighbourhood Algorithm to the search of isotropic mantle shear and compressional wave velocity models, using recent normal mode splitting measurements and fundamental mode phase velocity data. We found an ensemble of joint P and S models (spherical harmonic degree two only) for which posterior marginal probability density functions, correlation and covariances were computed. 1-D marginals give information on how well a parameter is constrained, and show whether it is Gaussian distributed or not. They are used to infer error bars on the various model parameters. 2-D marginals show the trade-offs among pairs of model parameters. The posterior covariance matrix obtained under a Gaussian assumption gives fair representation of the correlation, although error bars may be underestimated in case of strong non-Gaussian distribution. The uncertainties and correlations constitute essential information in order to make meaningful analysis of the models obtained. We see, for instance, that there is a correlation between parameters of the lower mantle and parameters of the upper mantle. This implies that we could improve our models by adding data, sensitive exclusively to either the upper or lower mantle in order to decorrelate those parameters. Our most likely S model is highly correlated with other S models, such as MM2-L12D8, SKS12-WM13, S20RTS, SAW12D or S16B30, except where there is a high trade-off between P and S perturbations. The correlation with the recent S model SB10L18 is very high at most depths, but our most likely P model is very different from the P model of SB10L18 in most layers. Degree two error bars on the rms velocity perturbations of our mean models are quite large, especially for P. The correlation between our most likely P and S model is low but among all the

models generated and compatible with the data, there are some that have a high $V_p - V_s$ correlation. We calculated the ratio $R = d \ln V_s / d \ln V_p$, and we found an increase with depth in the top 1500 kilometres up to a value of 1.75. Deeper in the mantle, there is a decrease and R oscillates between 0.8 and 1.3. Many models using body wave data alone seem to find a high value for R in the deep mantle. This is, however, not always the case, as shown by the ratios found by Saltzer et al. (2001) in slab regions. Our study, for which only surface wave and normal mode data have been employed, tends to favour low values. The model of Masters et al. (2000) obtained from surface waves, normal mode and body wave data gives an intermediate ratio at these depths.

We have a powerful new tool to explore a model space, including the null-space, and to estimate ranges of “good” data-fitting models. In the absence of true physical information, we prefer considering the full range of models consistent with the data. Correlations between model parameters can be computed and give valuable indications on what kind of independent data should be added to constrain the models better. Because our problem can be solved spherical harmonic coefficient by spherical harmonic coefficient, it is trivial to parallelize the procedure resulting in huge timesavings for computing a full tomographic model.

Chapter 4

Radial anisotropy in mantle reference models

Abstract

The Neighbourhood Algorithm of Sambridge was applied to normal mode and surface wave phase velocity data to determine the likelihood of radial anisotropy in mantle reference models. This full model space search technique provides probability density functions for each model parameter, and therefore reliable estimates of resolution and uncertainty, without having to introduce unnecessary regularization on the model space. Our results show a fast decrease of S-wave anisotropy (described by parameter ξ) and of intermediate parameter η in the top 220 km of the mantle, and they do not seem to deviate significantly from PREM at any depth. The data do not require strong deviations from PREM for P-wave anisotropy except in the lowermost mantle and between 220 and 400 km depth, which indicates that P-wave anisotropy extends deeper than S- or η -anisotropy. The sign change in the anisotropic parameters across the 670-discontinuity found by other authors is not warranted by our data. Because of the trade-off between P-wave related parameters and density anomalies, it is important to resolve density to make reliable assessments on P-wave anisotropy from traditional inversions. S-wave anisotropy and η are less affected by density. A well-resolved negative density anomaly was found in the uppermost mantle, and a density excess was observed in the transition zone and the lowermost mantle.

The content of this chapter was submitted in Beghein,C., Trampert,J. & van Heijst,H.-J., *Geophysical Journal International*, 2003

4.1 Introduction

It is now commonly accepted that the Earth's uppermost mantle is anisotropic. Laboratory experiments show that the most abundant minerals in the uppermost mantle possess high intrinsic anisotropy, and seismology reveals that anisotropy is present at these depths. This indicates the existence of an efficient mechanism capable of aligning uppermost mantle minerals over large scales. Seismological evidence for radial anisotropy at these depths was first inferred from the discrepancy between isotropic Love and Rayleigh wave phase velocity maps (Anderson, 1961). This was confirmed by many other seismological studies. PREM (Dziewonski and Anderson, 1981) was the first reference model to incorporate radial anisotropy in the top 220 km of the mantle. Spherically averaged radial anisotropy was also found at larger depths by Montagner and Kennett (1996), in an attempt to reconcile body-wave and normal mode observations. They derived a new reference model that contained a small amount of radial anisotropy down to 1000 km depth and in the lowermost mantle. The rest of the lower mantle appears to be devoid of any seismic anisotropy, although both experimental (Chen et al., 1998; Mainprice et al., 2000) and theoretical studies (Oganov et al., 2001a,b; Wentzcovitch et al., 1998) demonstrate that lower mantle minerals are highly anisotropic. This can be understood in terms of superplastic flow (Karato, 1998), since deformation by diffusion creep does not result in any preferred orientation of minerals.

To reconcile body-wave and normal mode data, Montagner and Kennett (1996) inverted free oscillation data for attenuation, density and three of the five parameters characterizing radial anisotropy, using V_p and V_s from body wave models as constraints on the two other parameters. The inclusion of attenuation in the inversion helped reduce the discrepancy between the two types of data, but remained insufficient. The addition of radial anisotropy down to 1000 km depth diminished this difference a lot. On the contrary, releasing the constraint on V_p and V_s improved the fit to the eigenperiods, but it was at the expense of a degradation of the fit to the travel-time data. Their final one-dimensional mantle models contained a few percents of anisotropy down to a depth of 1000 km, and they reported a possible change in the sign of the anisotropic parameters at the 670-discontinuity. Karato (1998) interpreted these sign changes as the signature of a horizontal flow above the discontinuity and a vertical flow in the top of the lower mantle. Clearly, the presence or absence of global radial anisotropy at large depths has large consequences for our understanding of geodynamics and mineralogy, and it should be investigated more thoroughly.

The goal of the present research is to assess the robustness of this 1-D anisotropy and to determine whether it is constrained by the current normal mode and surface wave data. We did not want to fix any model parameter, such as V_p or V_s , because the possible trade-offs with other parameters could affect the results for anisotropy. We did not include attenuation in the parameterization, or any prior information coming from body-waves. The Neighbourhood Algorithm (NA) (Sambridge, 1999a,b) was used to survey the parameter space and to find an ensemble of good data-fitting 1-D models of the man-

tle. This method provides posterior probability density functions (PPDFs) for each model parameter and returns valuable indications on their resolution and trade-offs. Since the entire model space, including the model null-space, is sampled and since we do not perform an inversion, our results are not biased by the introduction of damping or any other unnecessary *a priori* information on the model space. Another advantage of this technique, compared to inversions, is that a much larger part of the valley of the cost function is explored, yielding reliable posterior model variances. The method was applied to a large data set composed of normal mode central frequency shifts and to the degree zero of surface wave phase velocity maps for fundamental and higher modes.

4.2 Data

Phase velocity maps can be expanded into spherical harmonics and, like normal mode central frequency shifts, their degree zero can be linearly related to perturbations in the one-dimensional structure of the Earth. The relation between Earth's structure and these data is given by (Dahlen and Tromp, 1998) :

$${}_k df = \int_0^a \delta \mathbf{m}(r) {}_k \mathbf{K}(r) r^2 dr \quad (4.1)$$

where ${}_k df$ represents normal mode central frequency shift measurements or the degree zero of a phase velocity maps, k discriminates between different surface wave frequencies or different multiplets and a is the radius of the Earth. ${}_k \mathbf{K}(r)$ is the volumetric structure kernel for perturbation $\delta \mathbf{m}(r)$ with respect to PREM (Dziewonski and Anderson, 1981).

The data we used included the degree zero of various surface wave phase velocity maps and central frequency shift measurements of mantle-sensitive normal modes obtained from the Reference Earth Model Website (<http://mahi.ucsd.edu/Gabi/rem.html>). They constitute a large set of published and unpublished measurements for various types of motion (Rayleigh and Love waves, spheroidal and toroidal modes) for fundamental modes and for the first few overtone branches. Error estimates were also available with the measurements. We added eight fundamental mode Rayleigh and Love wave phase velocity models for periods between 40 and 275 seconds. At each selected period between 40 and 150 s, the models and assigned errors resulted from the averaged degree zero coefficient and its standard deviation calculated from different phase velocity maps (Trampert and Woodhouse, 1995, 1996, 2001; Ekström et al., 1997; Laske and Masters, 1996; Wong, 1989; van Heijst and Woodhouse, 1999). This should account for different measuring techniques of phase velocity, different data coverage and different regularisation-schemes in the construction of the maps at these periods. The models obtained by Wong (1989) were used for periods larger than 150 s. The obtained errors for Love and Rayleigh wave data decrease almost linearly between 40 and 100 seconds and the curves flatten between 100 and 150 seconds, as shown in Chapter 3 (Figure 3.1) for degree two Rayleigh wave phase velocity maps. The model of Wong (1989) being the only one available to us at longer periods, we decided to assign a constant uncertainty to models with periods greater

than 150 seconds. We assumed for convenience that the errors have a Gaussian distribution, but there were far too few models to test this hypothesis. Finally, we added the degree zero of the overtone surface wave measurements made by van Heijst and Woodhouse (1999) for toroidal modes up to overtone number $n = 2$ and spheroidal modes up to overtone number $n = 5$. Owing to the absence of corresponding variance estimates, we used the same error bars as those estimated for the fundamental mode surface wave phase velocity maps as a function of frequency.

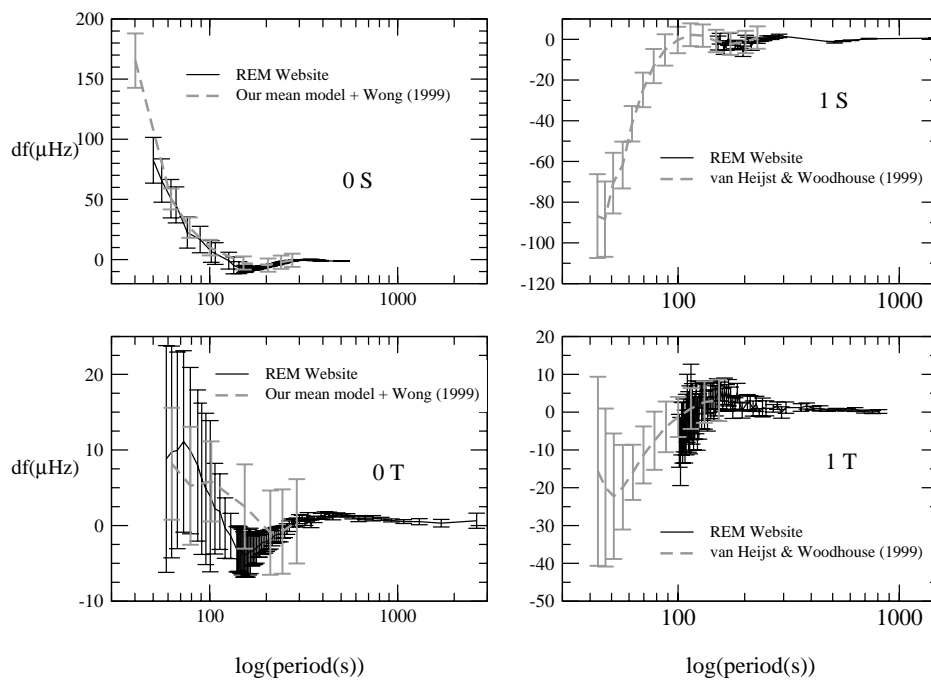


Figure 4.1: Ensemble of data (without the crust) and estimated errors for the fundamental surface wave and normal mode data (left) and for the first overtone branche (right) at different periods. The horizontal axis is a logarithmic scale.

As displayed in Fig. 4.1 for the fundamentals and the first overtone branche, an analysis of the entire data set, error bars included, showed a good agreement between the data published on the Reference Earth Model Website, our averaged degree zero phase velocity data and the overtone measurements. In total, the data set employed was composed of 237 measurements for Rayleigh waves and spheroidal modes and 294 measurements for Love waves and toroidal modes. All data were corrected with the crustal model of Mooney et al. (1998).

4.3 Parameterization and method

An anisotropic medium with hexagonal symmetry is characterized by five independent elastic coefficients A , C , N , L and F , in the notation of Love (1927). Radial anisotropy occurs when the symmetry axis points in the radial direction. This type of anisotropy is usually described by three anisotropic parameters ($\phi = 1 - C/A$, $\xi = 1 - N/L$ and $\eta = 1 - F/(A - 2L)$) and one P and one S velocity. Note that these definitions vary from author to author. The elastic coefficients are related to the wavespeed of P-waves travelling either vertically ($V_{PV} = \sqrt{C/\rho}$) or horizontally ($V_{PH} = \sqrt{A/\rho}$), and to the wavespeed of vertically or horizontally polarized S-waves ($V_{SV} = \sqrt{L/\rho}$ or $V_{SH} = \sqrt{N/\rho}$, respectively). Parameter F is related to the speed of a wave travelling with an intermediate incidence angle. We parameterized the models with perturbations of these five elastic coefficients and perturbations of density with respect to PREM (Dziewonski and Anderson, 1981). The corresponding sensitivity kernels are given in Tanimoto (1986), Mochizuki (1986) and Dahlen and Tromp (1998). The relation between the data ${}_k df$ and the structure of the Earth is then :

$${}_k df = \int_{r_{cmb}}^a [{}_k K_A(r) \delta A(r) + {}_k K_C(r) \delta C(r) + {}_k K_L(r) \delta L(r) + {}_k K_N(r) \delta N(r) + {}_k K_F(r) \delta F(r) + {}_k K_\rho(r) \delta \rho(r)] r^2 dr \quad (4.2)$$

In this equation, r_{cmb} is the radius of the core-mantle boundary and a is the radius of the Earth. The mantle is radially divided in six layers. The bottom and top depths of these layers are, in kilometres, (2891, 2609), (2609, 1001), (1001, 670), (670, 400), (400, 220), (220, 24). This coarse parameterization was dictated by computational resources and, consequently, the results should be seen as an indication of the presence of anisotropy rather than a detailed model. Conservation of the mass of the Earth and its moment of inertia was imposed following Montagner and Kennett (1996).

In the first stage of the NA, the model space is surveyed to identify the regions that best fit the data. A measure of the data fit must therefore be defined. We chose the χ^2 misfit which measures the average data misfit compared to the size of the error bar. The NA iteratively drives the search towards promising regions of the model space and simultaneously increases the sampling density in the vicinity of these good data-fitting areas. One of the characteristics of the NA, which makes it different from usual direct search

approaches, is that it keeps information on all the models generated in the first stage, not only the “good” ones, to construct an approximate misfit distribution. This distribution of misfit is used as an approximation to the real PPDF and as input for the second stage of the NA, where an importance sampling of the distribution is performed. It generates a resampled ensemble which follows the approximate PPD and which is integrated numerically to determine the likelihood associated with each model parameter and the trade-offs. Parameters have to be tuned for each stage of the NA. The optimum values of these tuning parameters have to be found by trial and error as explained below. The two tuning parameters required for the first stage of the algorithm are n_s , the total number of new models generated at each iteration, and n_r , the number of best data-fitting cells in which the new models are created (the model space is divided into Voronoi cells). We chose $n_s = n_r$ to broaden the survey as much as possible. Tuning parameters have also to be chosen to insure the convergence of the Bayesian integrals in the second stage.

The degree zero of the five elastic coefficients were perturbed up to 5 % of their amplitude in PREM. Because our problem is linearized we have to stay within the framework of perturbation theory, which implies that we should not take too large perturbations of the elastic coefficients. On the other hand, we do not want these perturbations to be too small to avoid excluding possible anisotropic good mantle models. Two sets of experiments were performed : one where no density variations were allowed and one where we searched for degree zero density anomalies up to 2 % in addition to perturbations in the five elastic coefficients.

4.4 Results

In the first experiment, we fixed the density anomalies $\delta\rho$ to zero in each layer, and in the second experiment we released the constraint on density and performed a model space search for perturbations of the five elastic coefficients that describe radial anisotropy and density. In this second case we assumed that the layer situated between 1001 and 2609 km depth, which constitutes most of the lower mantle, is isotropic. This assumption was mainly motivated by computational resources, but we believe it to be reasonable because, so far, seismic anisotropy has never been observed at these depths.

We thus studied a 30-dimensional model space in the first experiment and a 33-dimensional model space in the second experiment. The limit of the NA on a single processor is reached with approximately 24 parameters (Sambridge, 1999b). Otherwise, it becomes highly time-consuming. The most reliable way to use the NA is by successively increasing the tuning parameters n_s and n_r (kept equal to broaden the search) in the first stage of the NA, computing the corresponding likelihoods associated with each model parameter, and comparing the different results. Stability is achieved once the solution is independent of the way the model space was sampled. It is also a way to obtain all the models compatible with the data, without being trapped in a local minimum. However, we could not afford to run the NA with high tuning parameters within reasonable time. Instead, we performed several surveys with relatively small tuning parameters (by

resampling between 5 and 20 best data-fitting cells at each iteration). By comparing the results of the different small size surveys, we could determine which parameters were well-constrained and which were not.

Although the decrease of the χ misfit was very slow, the NA found best data-fitting models with $\chi \simeq 1.5$ in all experiments, while the highest misfit found could be as high as 15 when density was included and 20 to 25 when $\delta\rho$ was zero. Fig. 4.2 shows examples of how the data are explained by one of the best data-fitting models. Data are plotted with the corresponding error estimates for some of the fundamental modes and the first and second overtone branches. Fundamental modes and the first overtone branches are well explained for both Rayleigh and Love wave phase velocity anomalies (most predictions fall within data errors, except for a few low period data), but the second overtone branches present more discrepancies between predictions and observations.

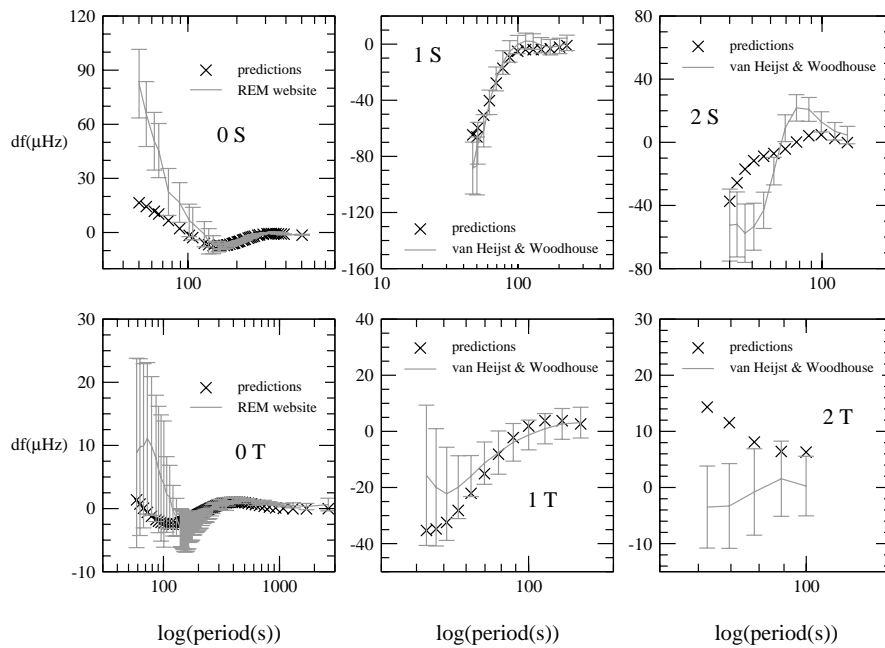


Figure 4.2: Predicted and observed frequency shifts and degree zero phase velocity perturbations (without the crust) for fundamental modes and the first two overtone branches.

From the individual distributions of ξ , ϕ , η and $\delta\rho$ obtained with $n_s = n_r = 15$, we deduced a mean model and a standard deviation. Fig. 4.3 displays the depth variation of the mean perturbation $d\xi = \xi - \xi_{prem}$, together with two standard deviations, which represent about 95 % of the acceptable models (the distributions were approximately Gaussian). Table 4.1 gives the probability, in each layer, that $d\xi$ is negative, based on the integration of the normalized likelihoods. These results for S-wave anisotropy are reasonably independent of the tuning parameters employed, even though small changes occurred in δL and δN . Our models show no significant deviation from PREM in S-wave anisotropy required by the data at any depth. The probability of a departure from PREM is small in every layer, as shown in Table 4.1.

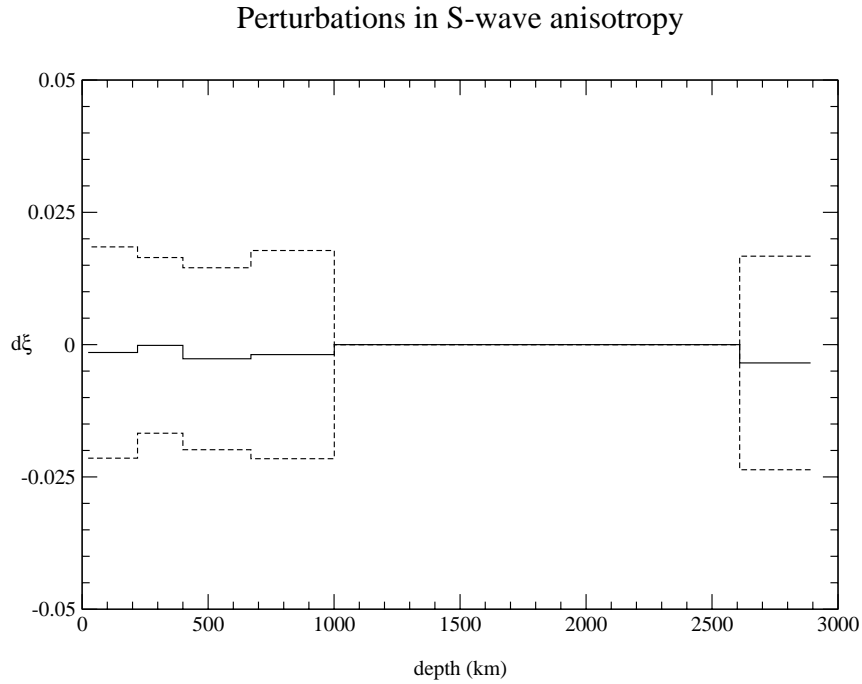


Figure 4.3: Range of $d\xi$ models compatible with the data. The solid line represents the mean model and the two surrounding dotted lines correspond to two standard deviations.

Our results are also robust with respect to density anomalies (they did not strongly depend on the presence of $\delta\rho$ in the model space) except in the lowermost mantle. The signal for

$d\xi$ was clearly negative at these depths when density anomalies were neglected, but it shifted towards zero when $\delta\rho$ was part of the unknowns (the changes occurred in elastic parameter δN and not in δL). In the first experiment, where $\delta\rho$ was zero, anisotropy was allowed in the bulk of the lower mantle (in the depth range 1001-2609 km), but no S-wave anisotropy was detected.

Parameter p	Depth (km)	$P(p > p_{prem})$
$\xi = N/L$	$24 < d < 220$	0.52
	$220 < d < 400$	0.53
	$400 < d < 670$	0.64
	$670 < d < 1001$	0.59
	$2609 < d < 2891$	0.65
$\phi = C/A$	$24 < d < 220$	0.44
	$220 < d < 400$	0.80
	$400 < d < 670$	0.51
	$670 < d < 1001$	0.62
	$2609 < d < 2891$	0.74
$\eta = F/(A - 2L)$	$24 < d < 220$	0.52
	$220 < d < 400$	0.68
	$400 < d < 670$	0.69
	$670 < d < 1001$	0.44
	$2609 < d < 2891$	0.57

Table 4.1: Probability of having more anisotropy than in PREM

P-wave anisotropy was more affected by the introduction of density in the model space than S-wave anisotropy, indicating a higher trade-off between P-wave related parameters and $\delta\rho$. Fig. 4.4 shows that the mean $d\phi$ model, obtained including density variations in the parameterization, does not significantly deviate from PREM in the top layer (from 24 to 220 km depth) or between 400 and 1000 km depth. However, there is a strong probability of $d\phi > 0$ between 220 and 400 km and $d\phi < 0$ in the lowermost mantle (Table 4.1), similarly to what Montagner and Kennett (1996) found. This means that we can expect about 1 % of P-wave anisotropy in these two layers, and that P-wave anisotropy extends deeper than S-wave anisotropy. The trade-off with density is, however, high in the two top layers, since the sign of $d\phi$ changed according to the presence or absence of density anomalies in the model space. A high trade-off was also observed in the transition zone between $d\phi$ and $\delta\rho$. Fig. 4.4 does not display any change in $d\phi$ with respect to PREM in the depth range 400-670 km, but when no density variations were allowed we obtained a clear $d\phi > 0$, which corresponds to the results of Montagner and Kennett (1996) if their models are expressed in our parameterization. This could be an indication that their ϕ

models were contaminated by unresolved density anomalies at these depths.

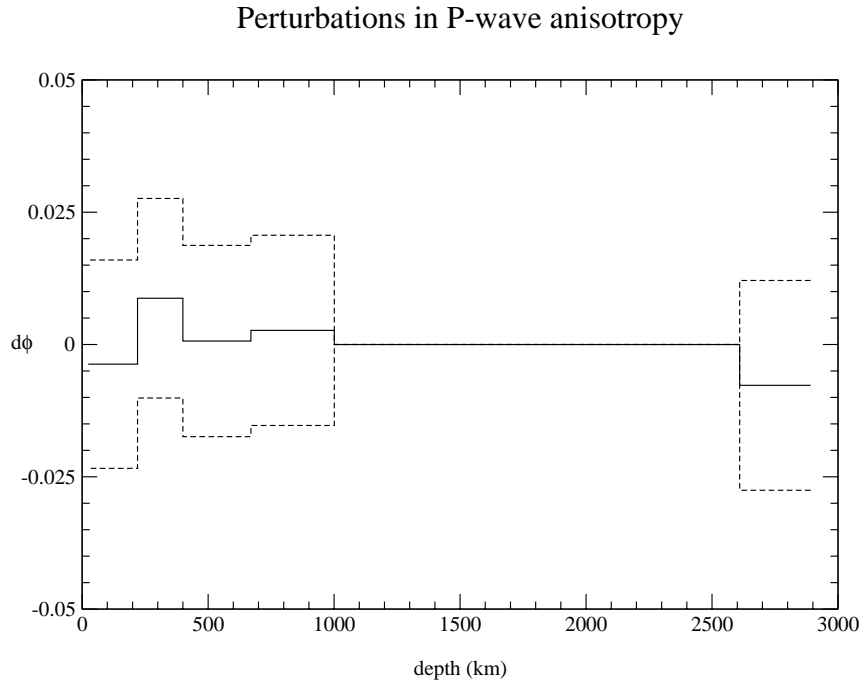


Figure 4.4: Range of $d\phi$ models compatible with the data. The solid line represents the mean model and the two surrounding dotted lines correspond to two standard deviations.

Similarly, our results do not show any significant P-wave anisotropy in the top of the lower mantle, but its presence is not completely unlikely (Table 4.1). We also noticed that $d\phi$ was more clearly positive at these depths when no density anomalies were included (not shown here). In the first experiment, we obtained a high probability (0.86) of $d\phi > 0$ between 1001 and 2609 km depth, but the amplitude was very small (around 0.5 %). Keeping in mind that the trade-off between P-wave related parameters and density was high, this reinforces the validity of the assumption of isotropy in that layer, imposed in the second experiment. The results for $d\phi$ in the lowermost mantle did not reveal a high trade-off with density. The amplitude of the mean $d\phi$ was higher when no density anomalies were included, but the sign did not change.

The η models (Fig. 4.5) were generally not as highly affected by $\delta\rho$ as models of

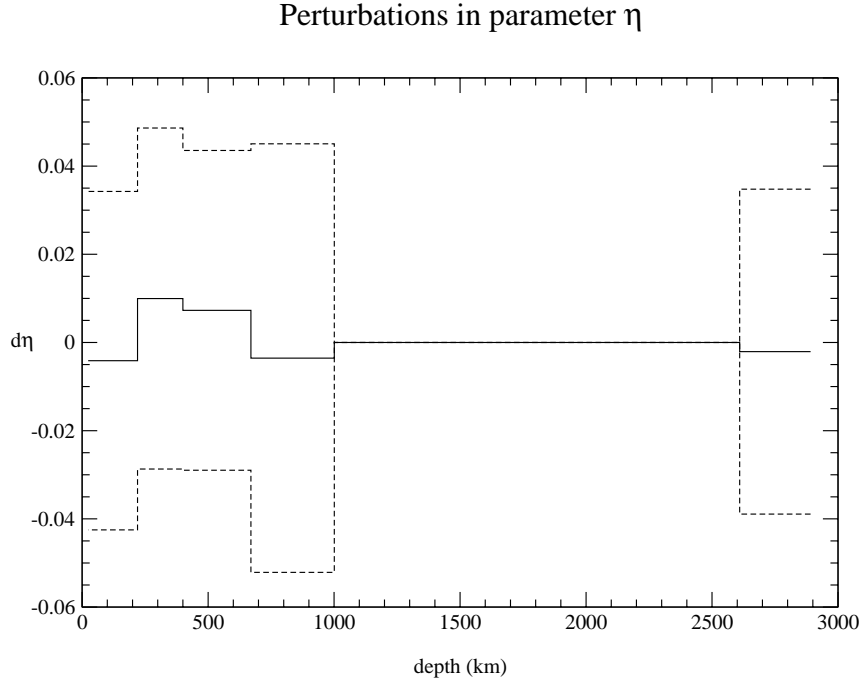


Figure 4.5: Range of $d\eta$ models compatible with the data. The solid line represents the mean model and the two surrounding dotted lines correspond to two standard deviations.

P-wave anisotropy. The NA produced $\eta \simeq \eta_{prem}$ at most depths. The most likely places where we could have $d\eta > 0$ are between 220 and 400 km depth and in the transition zone. The probability is small because the distributions are wide, but their peaks are close to 1 %, similar to model AK135-F of Montagner and Kennett (1996). These two layers are also where the strongest trade-off with density was detected. When we imposed $\delta\rho = 0$, $d\eta$ was clearly centred on zero at these depths. The introduction of density seems to push the signal towards slightly positive values, but the robustness of these perturbations in η is not easy to assess. Also, with $\delta\rho = 0$ we obtained a positive $d\eta$ between 1001 and 2609 km depth but the amplitude was so small that we believe the assumption $d\eta = 0$ imposed in the second experiment is valid.

The sensitivity tests of Resovsky and Trampert (2002) suggest that the data we employed can resolve the density variations correctly. Given the existing trade-offs with

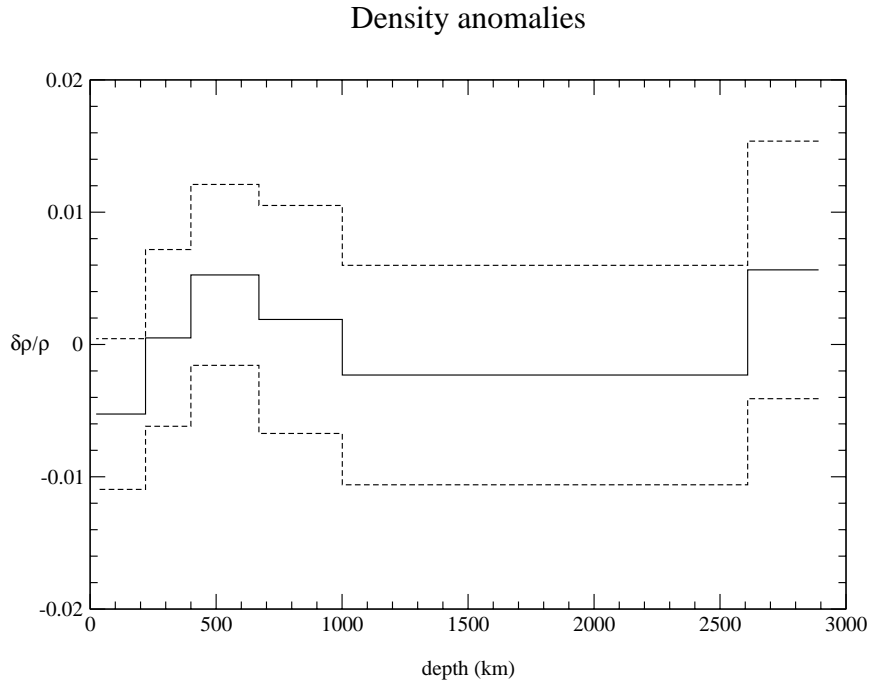


Figure 4.6: Range of relative density perturbation models compatible with the data. The solid line represents the mean model and the two surrounding dotted lines correspond to two standard deviations.

density, we believe that our anisotropic models shown here including density are the closest to reality. The models of density anomalies we obtained (Fig. 4.6, Table 4.2) clearly show a smaller density than in PREM in the top 220 km (-0.5%) and an increase in $\delta\rho$ in the transition zone and in the lowermost mantle. At other depths, no significant departure from PREM is required by the data, but $\delta\rho$ is not quite as well resolved in the depth ranges 220-400 km and 670-1000 km, as shown by the individual likelihoods (not displayed here). The negative perturbation in density in the uppermost mantle is inconsistent with Montagner and Kennett (1996). They, however, found a signal close to ours in the lowermost mantle. The equivalent isotropic $d\ln V_s$ and $d\ln V_p$ were computed as well, but no strong deviations from PREM were required by the data, as the probability of positive $d\ln V_s$ and $d\ln V_p$ was close to 0.5 in all layers.

Depth (km)	$P(\delta\rho/\rho > 0)$
$24 < d < 220$	0.28
$220 < d < 400$	0.50
$400 < d < 670$	0.71
$670 < d < 1001$	0.57
$1001 < d < 2609$	0.40
$2609 < d < 2891$	0.72

Table 4.2: Probability of having positive density anomalies.

4.5 Discussion and conclusion

A direct search method was applied to normal mode central frequency shift measurements and to the degree zero of surface wave phase velocity maps to assess the likelihood of radial anisotropy and density anomalies in one-dimensional mantle models. A high trade-off was found between P-wave related parameters and density perturbations in most of the mantle, but S-wave or η -anisotropy were less affected by the presence of density anomalies in the parameterization.

Where appropriate, we compare the solutions with independent studies which employ fundamental mode data (see Chapter 5 for the method) and overtone data (see Chapter 6) alone. We did not find any significant deviation from PREM in shear-wave anisotropy anywhere in the mantle, which questions the results of Montagner and Kennett (1996). Their models showed a few percents of anisotropy down to 1000 km depth, with a change of sign in parameter ξ across the 670-discontinuity and possibly at 410 km depth. Although their models are not totally incompatible with our range for ξ , they do not correspond to our most likely solution. From our probabilities, we conclude that the changes of sign in ξ below and above the transition zone are not constrained by the data. The trade-off we observed between ξ and density might be responsible for the anisotropy found by Montagner and Kennett (1996) in the lowermost mantle. A finer parameterization, as in Montagner and Kennett (1996), will of course show more details, but because we find all models compatible with the data, the averages from our thick layers are representative of the finer details. Indeed, in Chapter 5, a thinner parameterization of the uppermost mantle was employed and a positive degree zero $d\xi$ was found in the upper 100 km and $d\xi < 0$ between 100 and 220 km depth. This results in a decrease of S-wave anisotropy with depth within the uppermost mantle, with slightly less anisotropy than in PREM in the top 100 km and a little more anisotropy than in PREM below, as predicted by Montagner and Kennett (1996). Our results here simply average over these two layers and overall there is no perturbation.

A strong trade-off was observed between P-wave related parameters and density anomalies at most depths. Departure from PREM in P-wave anisotropy is required by the data between 220 and 400 km depth, with $d\phi > 0$, and in the lowermost mantle, with $d\phi < 0$.

This indicates deeper P-wave anisotropy than S-wave anisotropy. It is worth noting that this feature is not constrained by the overtone data of van Heijst and Woodhouse (1999) but by the normal mode data (comparison with the degree zero obtained in the study of Chapter 6). The negative $d\phi$ in the lowermost mantle was also found by Montagner and Kennett (1996), but it is the only signal of P-wave anisotropy compatible with ours. The change of sign in ϕ observed by Montagner and Kennett (1996) across the 670-discontinuity is not confirmed by our data.

Parameter η did not deviate strongly from PREM, except maybe between 220 and 670 km depth, where the probability of $d\eta > 0$ is close to 0.7 (Table 4.1). This might indicate that η -anisotropy goes deeper than P-wave or S-wave anisotropy, but this is not supported by the overtone data alone (study of Chapter 6, degree zero). We did not find any clear sign of η -anisotropy in the lowermost mantle, but the uncertainty is very large.

It was demonstrated by several authors that inversions of normal mode and surface wave data do not produce reliable lateral variations in density anomalies, due to poor resolution (Resovsky and Ritzwoller, 1999c; Resovsky and Trampert, 2002; Romanowicz, 2001). In addition, damped inversions generally underestimate model amplitudes, the more so if the sensitivity is small. In such cases, the NA is the best tool to put robust bounds on density anomalies inside the Earth. Resovsky and Trampert (2002) clearly showed that our data set could resolve density variations using the NA. The density models we obtained were very different from those derived by Montagner and Kennett (1996), and, because of trade-offs with the other parameters, differences in the models of anisotropy were produced. We obtained a clear deficit in density in the uppermost mantle and an excess of density in the transition zone and the lowermost mantle. An increase of density with respect to PREM (Dziewonski and Anderson, 1981) will result in an increase of Bullen's parameter η_B , which is a measure of the deviation from the Adams-Williamson equation, i.e. from adiabaticity and homogeneity. In PREM (Dziewonski and Anderson, 1981), η_B is smaller than unity in the upper mantle, which is indicative of a large temperature gradient (Anderson, 1989). Our results for the uppermost mantle suggest thus an even larger temperature gradient at these depths. The PREM value of η_B is close to unity in the lowermost mantle. The excess of density obtained in the deep mantle corresponds therefore to $\eta_B > 1$ and could be related to the compositionally distinct dense layer proposed by Kellogg et al. (1999). In the transition zone, η_B is already greater than 1 in PREM. This departure from unity at these depths could be caused by phase transitions of material more compressible than in homogeneous adiabatic conditions (Anderson, 1989), but we speculate that it could also be the global signature of slabs deflected in the transition zone as observed by van der Hilst and Kárason (1999) (see also the review by Fukao et al. (2001)).

The minimum χ misfit found by the NA was close to 1.5, which shows that on average the data employed are relatively well explained, without requiring radial anisotropy in the transition zone, a change of sign in the anisotropic parameters across the 670-discontinuity or attenuation.

Chapter 5

Probability density functions for radial anisotropy in the uppermost mantle

Abstract

We applied Sambridge's Neighbourhood Algorithm to degree eight fundamental mode Love and Rayleigh wave phase velocity maps between 40 and 150s to find models of radial anisotropy in the upper 220 km of the mantle. The Neighbourhood Algorithm is a powerful tool to explore a multi-dimensional model space and to retrieve an ensemble of models from which statistical inferences (posterior probability density functions and trade-offs) can be made. We sought solutions for density anomalies and perturbations in the five elastic coefficients that describe transverse isotropy. We found robust departures from PREM in S-wave anisotropy (ξ) under cratons and oceans alike, with a clear change of sign in the anomalies with respect to the reference model at about 100 km depth. No significant difference was observed between cratons and oceans, both in the amplitude and depth variation of ξ . The signal within continents is clearly age-related, with platforms and tectonically active regions characterized by a rapid decrease in ξ with depth, while cratons display a more constant signal. A similar age dependence in S-wave anisotropy is also observed beneath oceans with a strong and rapidly decreasing anisotropy for young oceans and a more constant anisotropy for older oceans. Perturbations in P-wave anisotropy (ϕ) are small and limited to the shallowest part of the continents. A small age-dependent signal for ϕ is observed beneath oceans. Anomalies in intermediate parameter η are similar to those in ϕ , but the deviation from PREM is

The content of this chapter was submitted in Beghein, C. & Trampert, J., *Geophysical Journal International*, 2003

stronger for η than for ϕ . A similar depth dependence is observed for η and for ξ in various age related regions. The two parameters show a rapid decrease with depth in young oceanic and young continental areas while older regions display a more constant signal. η and ξ also share the same behaviour in the top 100 km, since their values increase from old to young continental and oceanic lithosphere. Cratons appear to be devoid of any η -anisotropy in the top 100 km. There is no obvious global correlation between deviations in ϕ and deviations in ξ , and the ratio between $d\eta$ and $d\xi$ is clearly regionally variable, which cautions against the use of commonly used proportionality factors between these variables in inversions. In all regions, we found a good correlation between the equivalent isotropic P- and S-wave velocity anomalies, with a ratio $d\ln V_s/d\ln V_p$ close to 1. The density anomalies obtained with fundamental mode data alone are likely to be not robust, but did not influence the results for anisotropy.

5.1 Introduction

Upper mantle seismic anisotropy can be observed using different kinds of seismological data : body waves, normal modes and surface waves. Direct observations of anisotropy are provided by body waves through shear wave birefringence and through the azimuthal dependence of propagation of P_n waves, first observed by Hess (1964) in the Pacific ocean. The dispersion of surface waves can also be used to study azimuthal anisotropy (Forsyth, 1975), but it also provides information on radial anisotropy. Radial anisotropy, or polarization anisotropy, describes the anisotropic behaviour of a cylindrically symmetric medium whose symmetry axis is in the radial direction. Its observation is not direct. It was first introduced by Anderson (1961) to explain the incompatibility between isotropic Rayleigh and Love phase velocity maps, known as the Love-Rayleigh discrepancy. There is now a general agreement that upper mantle anisotropy is due to the preferred alignment of olivine crystals, a highly anisotropic mineral very abundant at these depths, which is possibly oriented by a plastic flow in the oceans (Tanimoto and Anderson, 1984) and orogenic deformation in continents (Silver and Chan, 1991).

It is clear that surface waves require the uppermost mantle to be radially anisotropic on average (e.g. PREM (Dziewonski and Anderson, 1981)), but lateral variations are found in many studies. Oceanic regions appear highly anisotropic as shown by L ev eque et al. (1998) for the Indian Ocean, by Silveira and Stutzmann (2002) for the Atlantic Ocean and by L ev eque and Cara (1983), Nataf et al. (1984), Montagner (1985, 2002), Nishimura and Forsyth (1989), Montagner and Nataf (1988) and Ekstr om and Dziewonski (1998) for the Pacific. Radial anisotropy under continents was also observed for Africa (Hadjouche et al., 1989), North America (Cara et al., 1980), Australia (Debayle and Kennett, 2000) and Western Europe (L ev eque and Cara, 1983). A global study (Montagner and Tanimoto, 1991), based on the inversion of surface wave data, showed an upper mantle anisotropy more pronounced beneath oceans than beneath continents. In a simultaneous waveform inversion of surface waves, overtones and body waves, Gung et al. (2003) recently confirmed the existence of anomalous radial anisotropy under the Pacific ocean, as

observed by Ekström and Dziewonski (1998), but they also showed significant variations of anisotropy under the Indian ocean and under most continents. This seems to indicate that deviations of upper mantle anisotropy from PREM are not confined to the Pacific Ocean, as previously claimed (Ekström and Dziewonski, 1998). The precise depth extent of this anisotropy is still not fully clear, although its amplitude appears to decrease with depth. Differences among the various studies could simply arise from different resolutions and different inversion schemes. The strength of anisotropy could vary both laterally and with depth and it could be a signature of the depth extent of continental roots, as first mentioned by Montagner and Tanimoto (1991).

The robustness of these models is difficult to assess. Some result from the difference between two tomographic models obtained from separate inversions (e.g. Ekström and Dziewonski (1998)). As explained by Lévêque and Cara (1983) separate inversions generally provide models that average Earth's properties in different ways (with different resolution kernels). It is therefore quite dangerous to make inferences about the anisotropic properties of the Earth simply by subtracting two models. Problems also arise in inversions made simultaneously for several parameters. It is well-known that inverse problems are generally non-unique, which means that the model parameters cannot be uniquely determined by observations. Imposing a regularisation is a way to reduce the ensemble of possible solutions or to choose a particular solution among all the models compatible with the data. However, this introduces many hidden problems that can make both the interpretation and the uncertainty assessment of tomographic models less straightforward than usually assumed (Trampert, 1998). Several levels of regularisation are involved when solving inverse problems. The physical variables used to describe the Earth are, strictly speaking, continuous functions of position, and should be expanded in a complete set of basis functions. The choice of these basis functions should not matter as long as the expansion is complete. However, for practical reasons, they have to be truncated and this implies some level of regularisation. More implicit regularisation is introduced through the choice of the cost function that is minimized to find a solution (e.g. a χ^2 misfit and/or a model norm term). A general form of the cost function is (Tarantola, 1987) :

$$C_\lambda = \Delta_{\mathcal{D}}(\mathbf{d}, \mathbf{A}\mathbf{m}) + \lambda\Delta_{\mathcal{M}}(\mathbf{m}, \mathbf{m}_0) \quad (5.1)$$

where $\Delta_{\mathcal{D}}$ and $\Delta_{\mathcal{M}}$ are measures of the distance between observation \mathbf{d} and prediction $\mathbf{A}\mathbf{m}$ in the data space and between the solution \mathbf{m} and a reference model \mathbf{m}_0 in the model space, respectively. The choice of these norms is arbitrary and is some kind of *a priori* information. Common examples are :

$$\Delta_{\mathcal{D}}(\mathbf{d}, \mathbf{A}\mathbf{m}) = (\mathbf{d} - \mathbf{A}\mathbf{m})^\dagger \mathbf{C}_d^{-1} (\mathbf{d} - \mathbf{A}\mathbf{m}) \quad (5.2)$$

and

$$\Delta_{\mathcal{M}}(\mathbf{m}, \mathbf{m}_0) = (\mathbf{m} - \mathbf{m}_0)^\dagger \mathbf{C}_m^{-1} (\mathbf{m} - \mathbf{m}_0) \quad (5.3)$$

\dagger stands for the transpose of a matrix. \mathbf{C}_d and \mathbf{C}_m are data and model covariance operators, respectively, and \mathbf{m}_0 is a reference model. By minimizing the cost function, one

simultaneously tries to reduce the data misfit and some information in the model space. A compromise between these two properties is reached by choosing an optimum (arbitrary) value for the trade-off parameter λ . The data covariance matrix \mathbf{C}_d is often reduced to a diagonal matrix containing estimates of data uncertainties. The model covariance matrix \mathbf{C}_m should be chosen using independent prior information on the model space (Tarantola, 1987). The choice of λ , \mathbf{C}_d , \mathbf{C}_m and the reference model \mathbf{m}_0 are explicit regularisation on both the model space and the data space. Many levels of regularisations are thus implicitly and explicitly introduced when solving an inverse problem. It is, therefore, easily understandable that the resulting model could be dominated by such prior information.

Despite the choice of model parameterization, norms and data errors, the solution of inverse problems is still highly non-unique. This is why additional constraints on the model parameters need to be introduced. In studies of lateral variations of mantle anisotropy from surface wave data, only two (S-wave related) parameters can be resolved reasonably well from inversions. Two approaches are then usually taken to reduce the number of parameters : introducing scaling relations between the different unknowns or neglecting the parameters whose partial derivatives have the smallest amplitude. The first approach (e.g. Gung et al. (2003) or Montagner and Tanimoto (1991)) makes use of petrological considerations (Montagner and Anderson, 1989) to choose the scalings between the parameters describing seismic anisotropy. However, the ratios between these parameters vary among the different studies (Nataf et al., 1986; Montagner and Tanimoto, 1991). Authors also often introduce the assumption that thermal effects are dominant in the mantle by imposing a (positive) scaling between density and equivalent isotropic velocity perturbations. In the second approach (Montagner, 1985, 2002; Montagner and Nataf, 1988; Silveira and Stutzmann, 2002), three of the six model parameters are not taken into account, which introduces errors in the amplitude of the models recovered, but might also have stronger effects, more difficult to see.

Direct search approaches offer a way to obtain robust information on Earth's properties without having to introduce unnecessary *a priori* information on the model parameters (i.e. $\lambda = 0$ and equation 5.3 is not used). Here, we applied the Neighbourhood Algorithm (NA) (Sambridge, 1999a,b) to the isotropic part of azimuthally anisotropic phase velocity maps for fundamental Love and Rayleigh modes (Trampert and Woodhouse, 2003) to find models of radial anisotropy in Earth's upper mantle. With the NA, all the models compatible with a given data set are found and robust probabilistic information on the model parameters (probability density functions and trade-offs) are obtained. We did not assume any scaling between the model parameters or neglect parameters whose sensitivity kernels have small amplitudes. This research was, first and foremost, aimed to determine whether lateral variations of upper mantle anisotropy are constrained by the data and statistically robust. In addition, we could verify whether seismological data are compatible with traditional scalings between model parameters.

5.2 Data and parameterization

The data set was composed of the isotropic part of fundamental mode Rayleigh and Love wave phase velocity maps at 40, 50, 60, 70, 80, 90, 100, 115, 130 and 150 seconds (Trampert and Woodhouse, 2003), corrected for the crustal model of Mooney et al. (1998). These phase velocity models were developed on a spherical harmonic (SH) basis up to degree 40. A local perturbation $\delta c/c(\theta, \phi)$ in the phase velocity, with respect to a spherically symmetric reference model, is given by a depth average of perturbations in the Earth's structure (e.g. Dahlen and Tromp (1998)) :

$${}_k \left(\frac{\delta c}{c} \right) (\theta, \phi) = \int_0^a \delta \mathbf{m}(r, \theta, \phi) {}_k \mathbf{K}(r) r^2 dr \quad (5.4)$$

where a is the radius of the Earth, (θ, ϕ) is a point at the surface of the Earth and ${}_k \mathbf{K}(r)$ is the partial derivative, also called sensitivity kernel, for model parameter $\mathbf{m}(r)$. k discriminates between different surface wave frequencies. Both the phase velocity maps and the perturbations of the model parameters are developed on a spherical harmonic basis (Edmonds, 1960) :

$${}_k \left(\frac{\delta c}{c} \right) (\theta, \phi) = \sum_{s=0}^{s_{max}} \sum_{t=-s}^s {}_k \left(\frac{\delta c}{c} \right)_s^t Y_s^t(\theta, \phi) \quad (5.5)$$

$$\delta \mathbf{m}(r, \theta, \phi) = \sum_{s=0}^{s_{max}} \sum_{t=-s}^s \delta \mathbf{m}_s^t(r) Y_s^t(\theta, \phi) \quad (5.6)$$

and therefore

$${}_k \left(\frac{\delta c}{c} \right)_s^t = \int_0^a \delta \mathbf{m}_s^t(r) {}_k \mathbf{K}(r) r^2 dr \quad (5.7)$$

We used degrees 0 to 8 only. The reason for this limitation is that the derivative damping chosen by Trampert and Woodhouse (2003) hardly affects the lower degrees.

To determine the fit of a model to the data, we decided to use a χ^2 misfit (equation 5.2), which measures the average data misfit compared to the size of the error bar. An estimate of uncertainties on the phase velocities was thus needed. The same approach as in Chapter 3 was used here. Models from different studies were employed for periods of 40, 60, 80, 100 and 150 seconds : Trampert and Woodhouse (1995, 1996, 2001, 2003), Ekström et al. (1997), Laske and Masters (1996), Wong (1989) and van Heijst and Woodhouse (1999). At each selected period, a standard deviation was estimated for every SH coefficient. By analogy to error bars determined for normal mode structure coefficients (Resovsky and Ritzwoller, 1998), we decided to assign averaged uncertainties to ${}_k \left(\frac{\delta c}{c} \right)_s^t$ independent of the azimuthal order t and defined by :

$${}_k \sigma_s^2 = \frac{1}{2s+1} \sum_{t=-s}^s {}_k \sigma_s^{t^2} \quad (5.8)$$

where s is the degree of the spherical harmonic and ${}_k\sigma_s^{t^2}$ is the variance estimated for one particular SH coefficient. This should account for different measuring techniques of phase velocity, different data coverage and different regularisation-schemes in the construction of the maps between 40 and 150 seconds. At intermediate periods, we made a simple interpolation of the uncertainties obtained at 40, 60, 80, 100 and 150 seconds. We assumed, for convenience, that the errors were Gaussian distributed, but there were too few models to test this hypothesis.

Radial anisotropy is described by five independent elastic coefficients, A , C , N , L and F in the notation of Love (1927). In seismology the following five parameters are often used to represent this anisotropy: $\phi = 1 - C/A$, $\xi = 1 - N/L$, $\eta = 1 - F/(A - 2L)$ and one P and one S velocity. Note that the definitions of the first three parameters vary from author to author. The elastic coefficients are related to the wavespeed of P-waves travelling either vertically ($V_{PV} = \sqrt{C/\rho}$) or horizontally ($V_{PH} = \sqrt{A/\rho}$), and to the wavespeed of vertically or horizontally polarized S-waves ($V_{SV} = \sqrt{L/\rho}$ or $V_{SH} = \sqrt{N/\rho}$, respectively). Thus, ϕ describes P-wave anisotropy and ξ describes S-wave anisotropy. Parameter η describes the anisotropy of waves travelling with an intermediate incidence angle. We parameterized the models as perturbations of the Love parameters and perturbations of density with respect to PREM (Dziewonski and Anderson, 1981). The corresponding sensitivity kernels are given in Tanimoto (1986), Mochizuki (1986) or Dahlen and Tromp (1998). The model parameters are expanded on a spherical harmonic basis, as in equation 5.6. The relation between the data and the structure of the Earth is then :

$${}_k\left(\frac{\delta C}{c}\right)_s^t = \int_{r_{cmb}}^a [{}_kK_A(r)\delta A_s^t(r) + {}_kK_C(r)\delta C_s^t(r) + {}_kK_N(r)\delta N_s^t(r) + {}_kK_L(r)\delta L_s^t(r) + {}_kK_F(r)\delta F_s^t(r) + {}_kK_\rho(r)\delta\rho_s^t(r)]r^2 dr \quad (5.9)$$

where r_{cmb} is the radius of the core-mantle boundary and a is the radius of the Earth. The problem thus naturally separates into individual SH components. We could have chosen a parameterization in terms of velocity perturbations δV_{PV} , δV_{PH} , δV_{SH} , δV_{SV} instead of A , C , N and L , or in terms of $\delta\phi$, δV_{PV} , $\delta\xi$, δV_{SV} and $\delta\eta$, but the choice of the parameterization does not matter when using the NA, since the entire model space is explored and all the models compatible with the data are represented in the end. In case of an inversion, if no special care is taken, different parameterizations can lead to inconsistent results (L ev eque and Cara, 1983; Tarantola, 1987). With the NA, any information on the trade-offs among the model parameters, which changes the results of a classical linear inversion, is directly available through correlation matrices and two-dimensional posterior probability functions, as described by Sambridge (1999a,b). Examples specific to long wavelength tomography can also be found in Resovsky and Trampert (2002) and Beghein et al. (2002) (or Chapter 3).

No relation was assumed between $\delta\rho$ and equivalent isotropic shear-wave velocity perturbations, or between $\delta\phi$, $\delta\xi$ and $\delta\eta$. We further did not use any explicit regulari-

sation in the model space via the cost function (no $\Delta_{\mathcal{M}}(\mathbf{m}, \mathbf{m}_0)$ term in equation 5.1). We employed a layered parameterization, with layers delimited by 24 and 100 km depth, 100 and 220 km depth and 220 and 670 km depth. The choice of this layered division was not based on the depth resolution of the data, but was mainly motivated by computational resources. Our parameterization is still sufficient to analyze the robustness of the anisotropic signal. Earlier studies showed that upper mantle radial anisotropy decreases rapidly with depth and the sensitivity of fundamental mode surface waves at depths larger than 220 km is relatively small. The deepest layer was thus assumed to be isotropic. This is a strong assumption, but the correlation matrices obtained from the NA showed *a posteriori* that it did not have a large effect on the solution at depths shallower than 220 km (there were very little trade-offs among the different model parameters). We finally had a total of 15 model parameters.

5 % deviation for the elastic coefficients and 2 % deviation for density were allowed from PREM. The choice of these boundaries is arbitrary and constitutes, together with the layered parameterization and the assumption of isotropy in the deepest layer, the only prior information introduced in the model space. However, because the problem is linearized, we have to stay within the framework of perturbation theory, which implies that perturbations in the model parameters should not be too large. On the other hand, we do not want these perturbations to be too small, since it would exclude possible “good” models. This is a trial and error part of the algorithm where the stability of results needs to be checked by changing the boundaries.

5.3 Method

Sambridge’s Neighbourhood Algorithm was employed to identify the regions of the model space that best fit the data. For details about the method, the reader is referred to the two original papers (Sambridge, 1999a,b). Different from usual direct search approaches, the NA characterizes the whole range of models contained in the model space (defined by its bounds) instead of searching for one “best” region. The NA is a two-stage procedure. The first stage consists in an efficient survey of the model space to identify the “good” data fitting regions. The interpolation in the model space using the Voronoi cells makes this algorithm self-adaptative and it allows a complete survey of the model space, provided the right tuning parameters have been chosen. Another advantage is that it can also sample several promising regions simultaneously. During this survey, the sampling density increases in the surroundings of the good models, without losing information on the models previously generated (even the “bad” ones). The second stage of the NA makes use of the entire ensemble of models generated in the first stage to construct an approximate posterior probability density (PPD) function. This approximate PPD is then integrated to obtain statistical inferences on all the model parameters (1-D, 2-D marginals, etc). PPD functions can be associated with each parameter, giving an estimate of their likelihood, and the trade-offs among the different parameters are readily available.

Each stage of the NA requires the tuning of parameters whose optimum values have

to be found by trial and error. Their influence on the survey of the model space and on the Bayesian interpretation of the results was described by Sambridge (1999a,b) in general and by Resovsky and Trampert (2002) in a normal mode problem. To broaden the survey as much as possible, the two tuning parameters required for the first stage of the algorithm were kept equal. These two parameters are n_s , the total number of new models generated at each iteration, and n_r , the number of best data-fitting cells in which the new models are created. The NA was applied to each SH coefficient of the selected phase velocity maps up to degree eight (81 coefficients). After a few tests, we took $n_s = n_r = 100$ and the number of iterations varied between 300 and 700, depending on the SH coefficient treated. For the second stage of the NA, a few random walks of about 6000 steps were enough to insure the convergence of the integrals. In total, solving the problem for one SH coefficient took about one day.

The application of the NA to each SH component of the phase velocity maps provided PPD functions for each SH component δm_s^t of the model parameters : δA_s^t , δC_s^t , δN_s^t , δL_s^t , δF_s^t and $\delta \rho_s^t$ in the top layers, and δA_s^t , δN_s^t and $\delta \rho_s^t$ in the third layer. Random values of these δm_s^t were generated, according to their exact PPD functions, to get random three-dimensional models of δA , δC , δN , δL , δF and $\delta \rho$ using equation 5.6. Data-compatible tomographic maps of the anisotropic parameters ϕ , ξ and η , density anomalies and perturbations in the equivalent isotropic S- and P-wave velocities were then generated. Rather than representing the thousands of tomographic models created, we decided to look at them from a statistical point of view. Histograms were computed to determine whether the seismological data employed can put robust constraints on radial anisotropy and density anomalies, under continents and oceans. To look at the distribution of parameter δm over a given area \mathcal{A} , we divided this area into N cells of area \mathcal{A}_i and integrated δm over each cell, for all the models generated :

$$\delta m_i = \int \int_{\text{celli}} \delta m(\theta, \phi) d\Omega \quad (5.10)$$

The δm_i were then added to one another and the resulting sum was divided by the total area \mathcal{A} to get :

$$\overline{\delta m} = \frac{1}{\mathcal{A}} \sum_{i=1}^N \delta m_i \quad (5.11)$$

Histograms were constructed by accumulating the average $\overline{\delta m}$ obtained for each model. These distributions represent thus the range of data-compatible values of δm , averaged over area \mathcal{A} , and do not account for variations within the area considered.

5.4 Results

Fig. 5.1 shows the likelihoods for the spherically averaged ξ , ϕ and η obtained with the NA for the top layers. Shear-wave anisotropy deviates significantly from PREM

(Dziewonski and Anderson, 1981) in the uppermost layer, with less anisotropy than in PREM, and there is slightly more S-wave anisotropy than in PREM between 100 and 220 km depth. Some changes in η are also visible in the two layers, showing a little more anisotropy than in the reference model. This is in agreement with the results of Chapter 4 where more data were employed.

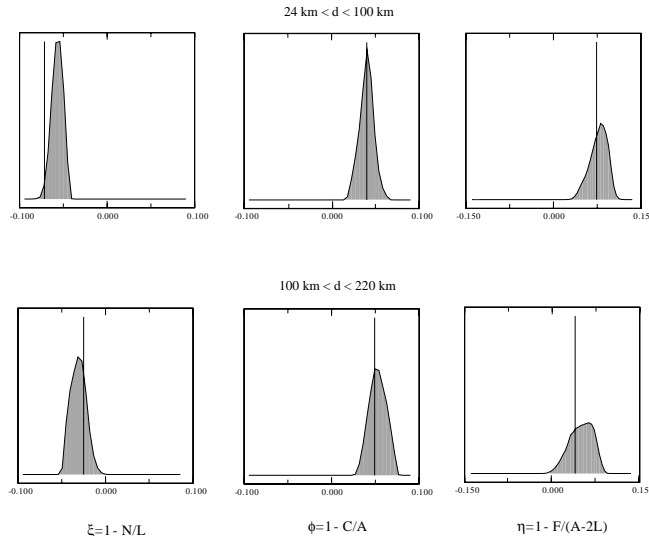


Figure 5.1: Likelihoods for the spherically averaged ξ , ϕ and η . The vertical line represents the value of PREM averaged over our layers.

Fig. 5.2 to 5.4 show the distribution of values for parameter ξ in the two upper layers, obtained by randomly sampling each δL_s^t and δN_s^t according to their PPD functions, and averaging the resulting ξ over a selected region. The histograms have been normalized to 1 to represent PPD functions. The distinction between continents and oceans was made using the 3SMAC model (Nataf and Ricard, 1996). The vertical lines correspond to the PREM values of ξ , averaged over our layers. Fig. 5.2 displays the PPD functions of the average ξ under the Pacific, the Atlantic and the Indian Ocean, and under all the oceans combined. From these PPD functions, we computed the probability of having less S-wave anisotropy in absolute value than in PREM in the different areas (Table 5.1). The distributions for the Pacific, the Atlantic and the Indian Ocean are very similar, and their peaks show a very slight decrease of ξ with depth, except maybe under the Atlantic. This rather uniform S-wave anisotropy had already been observed by Montagner and Tanimoto (1991). A robust feature also visible is that ξ is smaller than PREM between 24 and 100 km depth and larger than PREM between 100 and 220 km depth. This shows that the variation of S-wave anisotropy with depth beneath oceans is not as strong as in the reference model. This characteristic, well resolved by our data, was observed earlier by

Ekström and Dziewonski (1998) under the Pacific Ocean, but we show that this departure from PREM is typical of other oceans as well.

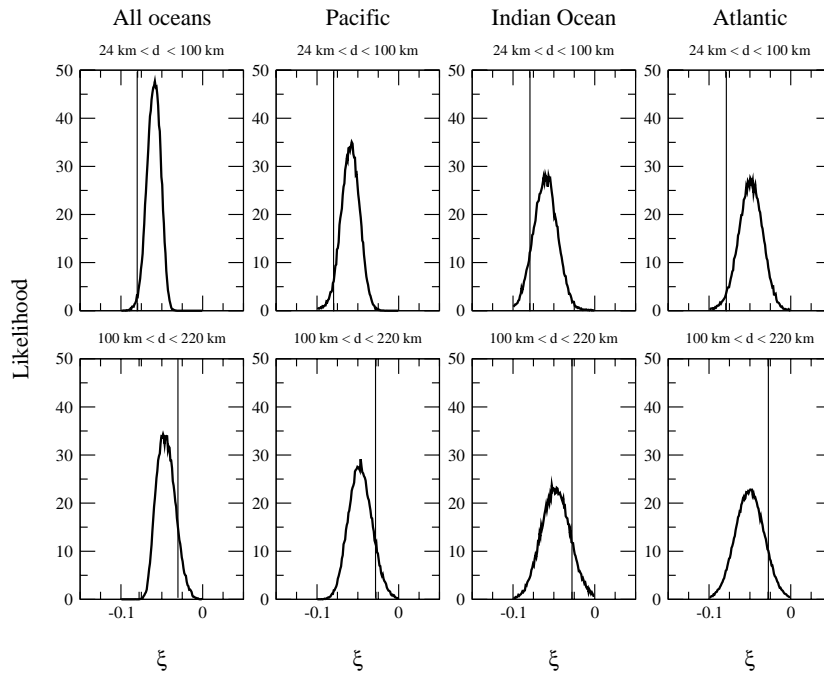


Figure 5.2: Likelihood of S-wave anisotropy beneath oceans. The vertical line indicates the value of ξ in PREM. The upper and the lower panels have the same scale.

Model 3SMAC (Nataf and Ricard, 1996) allows to distinguish oceans according to their age. Montagner (1985) observed an increase of the depth extent and of the strength of shear-wave anisotropy with the age of the ocean floor. Nishimura and Forsyth (1989) also observed an increase of ξ with age in the Pacific and reported a transition, situated at 20 Ma, between young and old oceans, with older regions characterized by a sort of equilibrium. Our lateral resolution of degree eight is not sufficient to make such a precise age distinction. Therefore, we generated histograms of ξ for oceans younger than 50Ma, for oceans aged between 50 and 100 Ma, and for oceans older than 100 Ma. Inspection of Fig. 5.3 reveals a clear departure from PREM for ξ beneath oceans older than 50 Ma, in the two layers, with a change of sign as observed in Fig. 5.2. A similar signal is

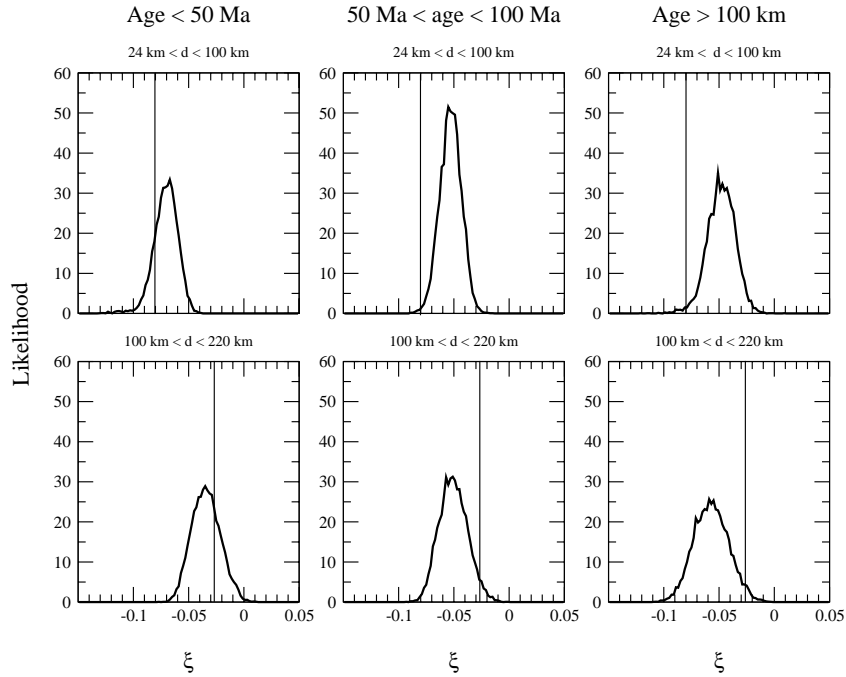


Figure 5.3: Likelihood of S-wave anisotropy beneath oceans according to their age. The vertical line indicates the value of ξ in PREM. The upper and the lower panels have the same scale.

observed for young oceans, but the deviation from PREM is not as strong as for older oceans. There is no observable difference between oceans older than 100 Ma and oceans situated in the age range 50-100 Ma, similar to the observations of Nishimura and Forsyth (1989). However, both Montagner (1985) and Nishimura and Forsyth (1989) obtained ξ increasing with the age of the sea floor, while our models show a decrease in the top 100 km. Between 100 and 220 km depth, we find results in closer agreement with theirs. The probability that ξ is smaller than PREM in absolute value is given in Table 5.1. We find, in the top layer, a probability of 0.84 for oceans younger than 50 Ma, and a probability of 0.99 both for oceans aged between 50 and 100 Ma and for oceans older than 100 Ma. The deviation from PREM has thus a slightly smaller probability for young oceans than for older ones. The same is true for the deeper layer.

Fig. 5.4 displays the values of ξ under continents. No significant deviation in S-wave

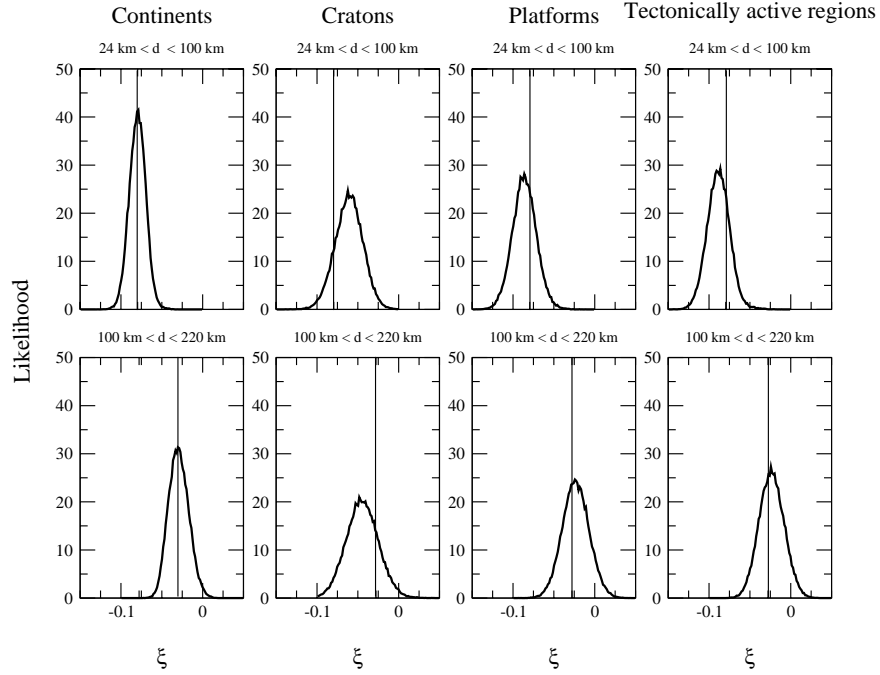


Figure 5.4: Likelihood of S-wave anisotropy beneath continents. The vertical line indicates the value of ξ in PREM. The upper and the lower panels have the same scale.

anisotropy from PREM was observed under continents taken as a whole. However, we found a clear age-related signal (see also Table 5.1). Platforms and tectonically active regions are similar, and moderate change relative to PREM is observed. On the contrary, cratons display less S-wave anisotropy than the world average in the top 100 km, and more anisotropy at depths between 100 and 220 km, like most oceans. The strength of the anisotropy beneath cratons does not change much with depth, similarly to what is observed beneath old oceans. This is very different for younger continental lithosphere where the depth variation is rather strong. S-wave anisotropy is therefore most likely the strongest beneath young continental lithosphere in the top 100 km. It is also less pronounced beneath cratons and old oceans than in young oceanic lithosphere.

Our data do not have as much sensitivity to P-wave related parameters (δC_s^t and δA_s^t) as to S-wave related parameters. If the data were to be inverted, the resulting δC and

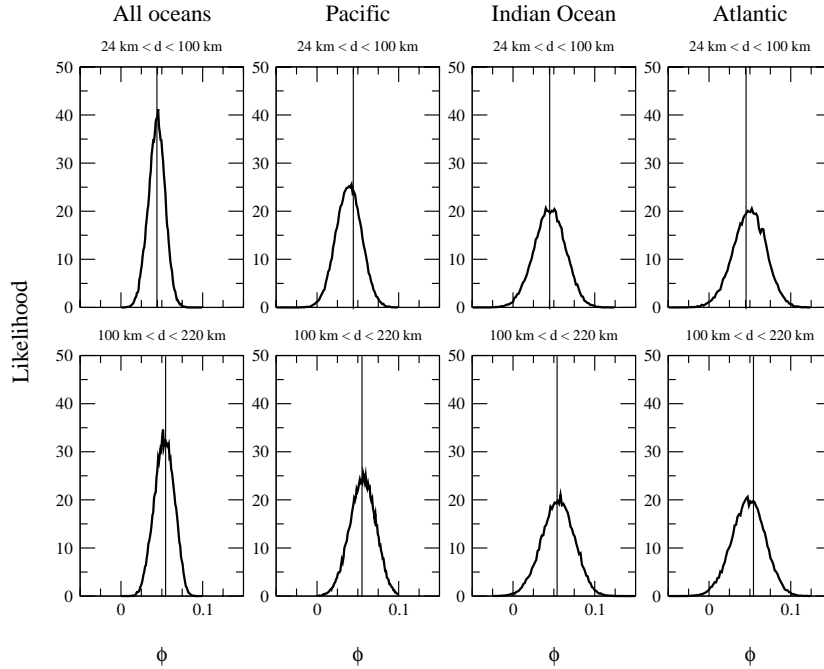


Figure 5.5: Likelihood of P-wave anisotropy beneath oceans. The vertical line indicates the value of ϕ in PREM. The upper and the lower panels have the same scale.

δA models would be highly coupled by regularisation. Using the NA and imposing no explicit regularisation in the model space, we found all models compatible with the data, independent of the sensitivity. Inspection of the posterior covariance matrices (not displayed here) showed, indeed, little trade-offs between parameters with high and small sensitivity. To show the P-wave anisotropy signal, we computed the overall distribution of ϕ , by randomly resampling the PPD functions associated with each δC_s^t and δA_s^t , as described earlier. The PPD functions obtained do not show any significant departure from PREM under oceans (Fig. 5.5 and Table 5.1), but there seems to be a slight age-dependence (Fig. 5.6 and Table 5.1). In the top 100 km, the deviation from PREM goes from positive values for young oceans towards negative values for older oceans, and opposite in the deepest layer. The upper 100 km beneath continents are characterized by a smaller P-wave anisotropy than in PREM (Fig. 5.7 and Table 5.1). No clear age related

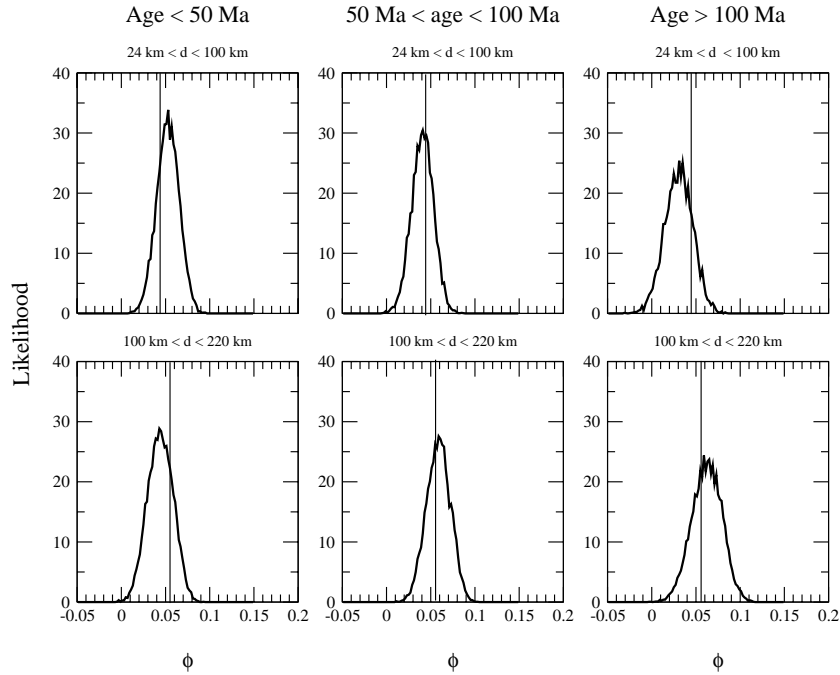


Figure 5.6: Likelihood of P-wave anisotropy beneath oceans according to their age. The vertical line indicates the value of ϕ in PREM. The upper and the lower panels have the same scale.

signal is seen. The PPD functions for parameter η do not show any significant deviation from PREM under oceans as a whole (Fig. 5.8 and Table 5.1), but a clear age dependence is visible in Fig. 5.9 and Table 5.1. Like for ξ , young oceanic lithosphere shows a rapid decrease of η with depth while older oceans are characterized by a more constant η . It is also interesting to note that, like for S-wave anisotropy, old oceans are most likely characterized by less η -anisotropy than young oceans in the top 100 km. The PPDs of Fig. 9 clearly display less anisotropy than in PREM under continents in the top 100 km (see also Table 5.1). It is also most likely that cratons do not have any η -anisotropy in the uppermost layer (we computed $P(\eta > 0) = 0.52$), and that the level of η -anisotropy increases for younger continental lithosphere, similarly to what was observed for oceanic lithosphere. There might be some positive departure from PREM for η beneath cratons in the depth range 100-220 km, but the signal is weak. Elsewhere, PREM gives a good

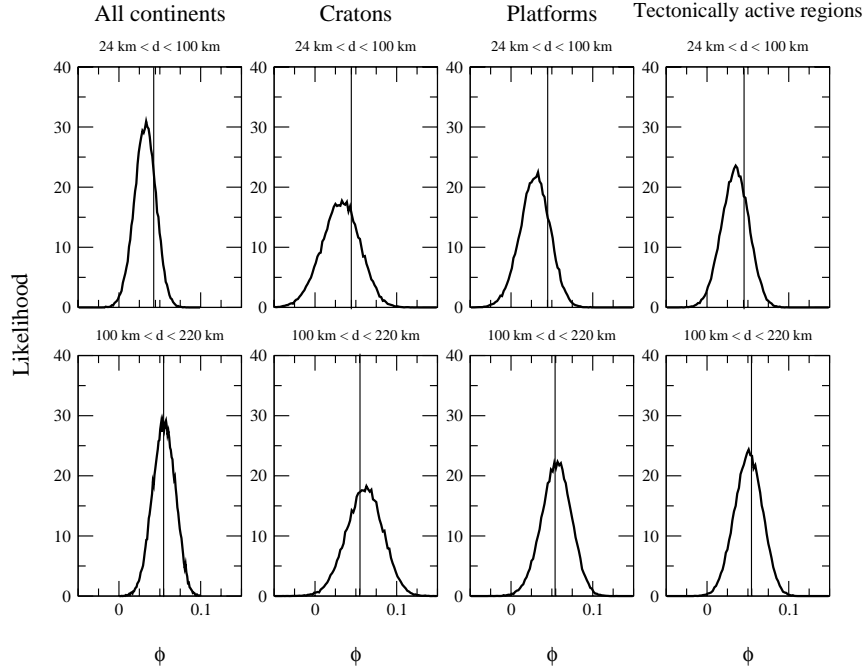


Figure 5.7: Likelihood of P-wave anisotropy beneath continents. The vertical line indicates the value of ϕ in PREM. The upper and the lower panels have the same scale.

approximation for η .

Montagner and Anderson (1989) investigated the correlations between parameters ϕ , ξ , η for two different petrological models (pyrolite and piclogite). They found strong correlation between $N/L - 1$ ($-\xi$ in our notation) and η and between $1 - C/A$ (our ϕ) and $N/L - 1$, independent of the two petrological models employed. They proposed to use these correlations to derive scaling factors between $d\xi$, $d\phi$ and $d\eta$, in order to reduce the number of parameters in inversions of seismological data. They also noticed that most seismological models of upper mantle anisotropy do not fall within their estimates of ξ , ϕ and η , and that there were large regional variations among these models. They proposed that scaling relationships from petrological models should be used as *a priori* constraints in tomographic inversions. Our study provides unbiased and independent constraints on the regional variations of the three parameters ξ , ϕ and η . We computed the overall corre-

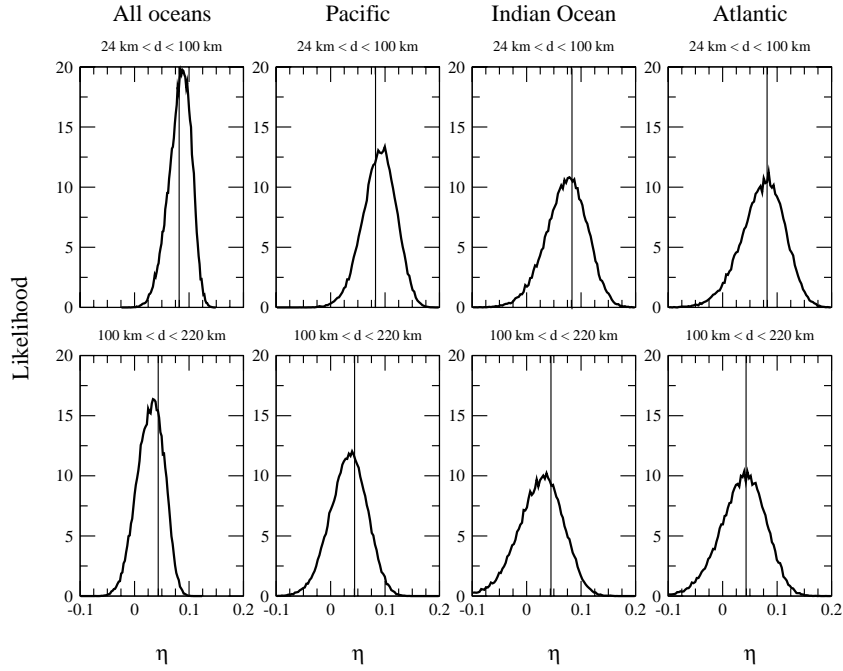


Figure 5.8: Likelihood of η -anisotropy beneath oceans. The vertical line indicates the value of η in PREM. The upper and the lower panels have the same scale.

lation between $d\xi = \xi - \xi_{preM}$ and $d\phi = \phi - \phi_{preM}$, but it did not see any significant correlation or anticorrelation (Fig. 5.11) between the two variables. The distributions are centred on zero, which is easily understandable, since either ϕ or ξ shows no deviation from PREM for a given tectonic province. The overall correlation between $d\xi$ and $d\eta = \eta - \eta_{preM}$ is slightly negative (around -0.3) in the two layers. These correlations are indeed small and do not necessarily justify an overall scaling between these parameters. To make a more regional analysis of the behaviour of $d\phi$ relative to $d\xi$ we computed the distribution of their ratios beneath oceans, cratons, platforms and tectonically active regions. Fig. 5.12 shows the PPD functions for the ratios of the average $d\phi$ over the average $d\xi$ (not the average of $d\phi/d\xi$). The ratio is slightly negative beneath cratons (the peak is situated around -0.5) and slightly positive (around 0.5) beneath platforms and tectonically active regions, in the upper 100 km of the mantle. At larger depths the distributions

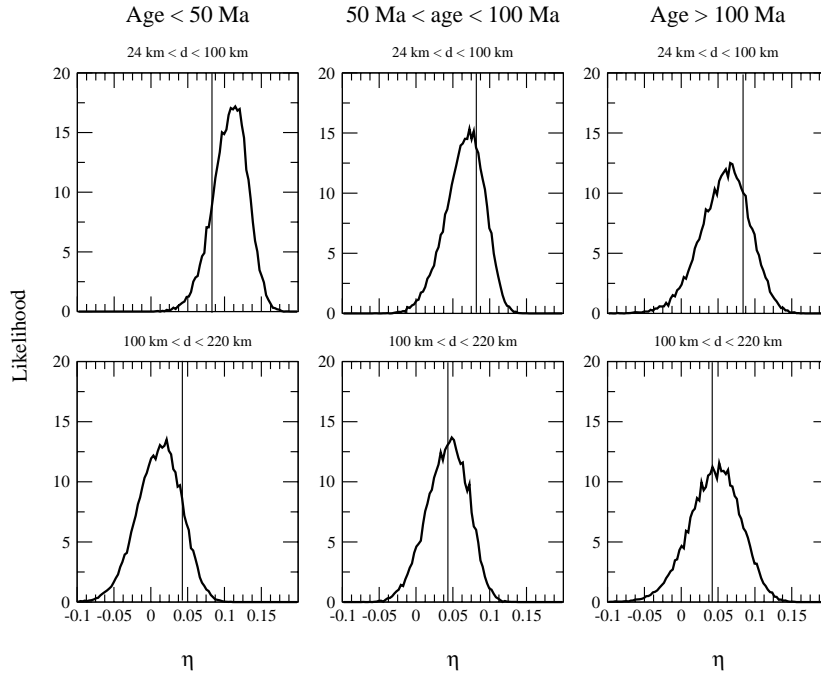


Figure 5.9: Likelihood of η -anisotropy beneath oceans according to their age. The vertical line indicates the value of η in PREM. The upper and the lower panels have the same scale.

are centred on zero. The ratios of the averaged $d\eta$ over the averaged $d\xi$ (Fig. 5.13) are clearly age-related beneath continents in the depth range 24-100 km and suggest more lateral variations in parameter η than in S-wave anisotropy. The ratio is negative beneath cratons in the top layer, with a peak at -2.5. It is positive beneath platforms (around 2) and no significant signal is observed for tectonically active regions and oceans. Between 100 and 220 km depth the distributions of ratios are more uniform, slightly negative for cratons, and centred on zero elsewhere. All distributions are wide, and most commonly used scalings ($-1.5 \leq d\phi/d\xi \leq -0.5$ and $-2.5 \leq d\eta/d\xi \leq -1.75$) fall within our PPD functions (sometimes meaningfully). However, if we believe that the seismological data contain information on these parameters, and one might be better off neglecting $d\phi$ and $d\eta$ altogether in inversions with the risk of biasing the uppermost mantle beneath continents through η . Our preferred approach would be to use the PPD functions of Fig. 11 and 12

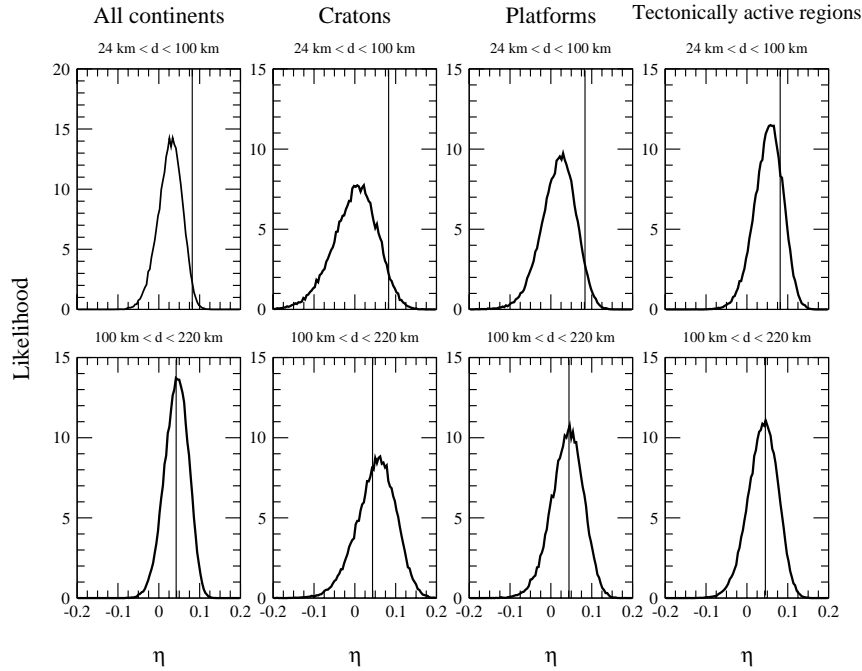


Figure 5.10: Likelihood of η -anisotropy beneath continents. The vertical line indicates the value of η in PREM. The upper and the lower panels have the same scale.

together with the method of Montagner and Anderson (1989) to put bounds on regional petrological variations.

The models obtained for the equivalent isotropic perturbations in S- and P-wave velocity ($d\ln V_s$ and $d\ln V_p$) in the two upper layers are very similar to those usually found : continents are fast and oceans are slow on average. There is a good correlation between S and P anomalies down to 220 km depth, as demonstrated in Fig. 5.14. This figure shows distributions of correlations between $d\ln V_s$ and $d\ln V_p$ in the top two layers. Models for $d\ln V_s$ and $d\ln V_p$ were randomly generated from the PPD functions of each model parameter, as described earlier, and the correlation between S and P anomalies was computed for each model, yielding the PPDs of Fig. 5.14. The same procedure can be applied to get ratios between $d\ln V_s$ and $d\ln V_p$. The ratios peaked at $d\ln V_s/d\ln V_p = 1$, but some of the distributions are sufficiently large that they cannot be used to discriminate between ther-

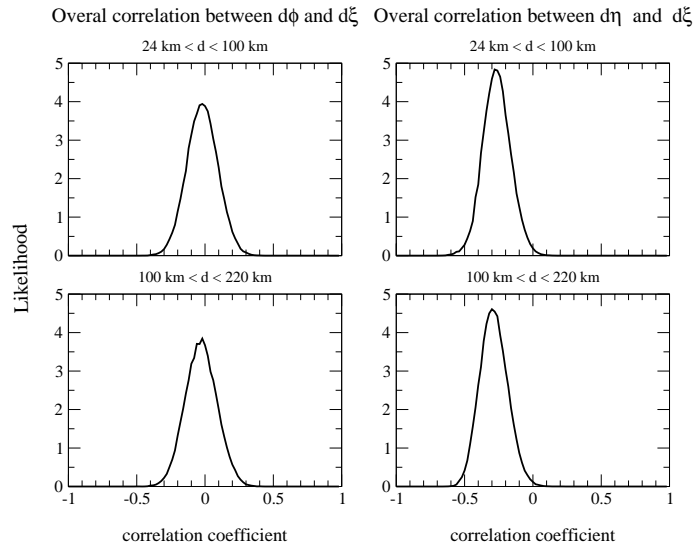


Figure 5.11: Likelihood of correlation between $d\phi$ and $d\xi$ (left) and between $d\eta$ and $d\xi$ (right). The upper and the lower panels have the same scale.

mal or compositional effects (see Chapter 6 for a little more details). Fig. 5.15 displays the variation of $dl n V_s$ with the age of the ocean floor. There is a clear age dependence in the two top layers beneath oceans. As first observed by Zhang and Tanimoto (1991), while young oceans display slow velocity anomalies, older oceans are characterized by fast velocities. The time variation in the top layer appears to correspond to the $t^{1/2}$ law proposed by Zhang and Tanimoto (1991), where t is the age of the ocean floor, but the age dependence seems more linear deeper.

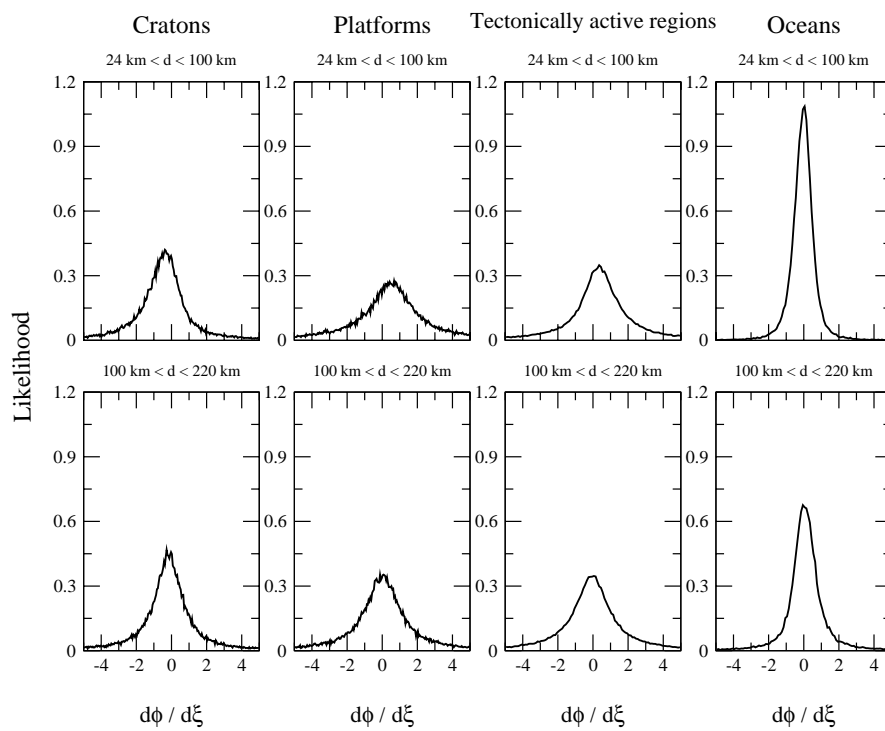


Figure 5.12: Likelihood of $d\phi/d\xi$ in various tectonic regions. The upper and the lower panels have the same scale.

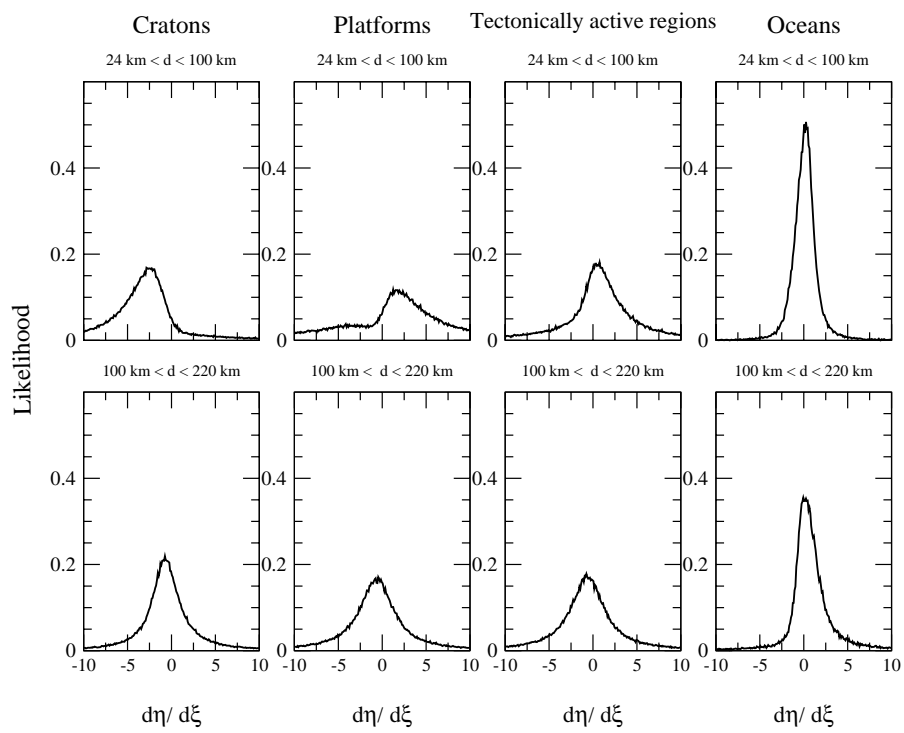


Figure 5.13: Likelihood of $d\eta/d\xi$ in various tectonic regions. The upper and the lower panels have the same scale.

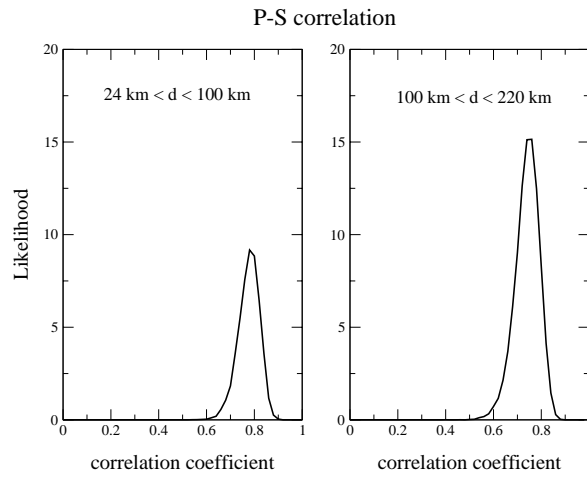


Figure 5.14: Likelihood of P-S correlation.

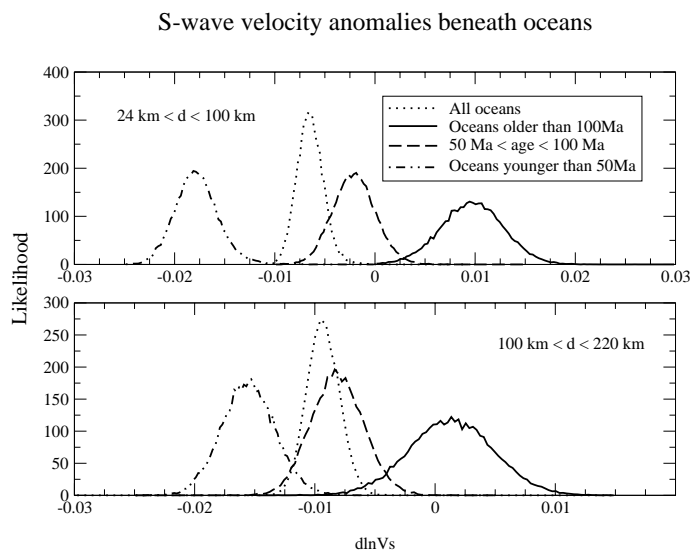


Figure 5.15: Likelihood of $d\ln V_s$ in the top layers for oceans according to the age of the ocean floor. Note that the degree zero perturbation was not included here.

Parameter p	Area	Depth (km)	$P(p < p_{prem})$
$\xi = 1 - N/L$	All oceans	$24 < d < 100$	0.99
		$100 < d < 220$	0.06
	Pacific	$24 < d < 100$	0.96
		$100 < d < 220$	0.10
	Indian Ocean	$24 < d < 100$	0.90
		$100 < d < 220$	0.13
	Atlantic	$24 < d < 100$	0.98
		$100 < d < 220$	0.09
	All oceans younger than 50Ma	$24 < d < 100$	0.69
		$100 < d < 220$	0.31
	All oceans 50 < age < 100Ma	$24 < d < 100$	0.87
		$100 < d < 220$	0.18
	All oceans older than 100Ma	$24 < d < 100$	0.83
$100 < d < 220$		0.19	
All continents	$24 < d < 100$	0.49	
	$100 < d < 220$	0.46	
All cratons	$24 < d < 100$	0.86	
	$100 < d < 220$	0.20	
All platforms	$24 < d < 100$	0.32	
	$100 < d < 220$	0.61	
All tectonically active regions	$24 < d < 100$	0.26	
	$100 < d < 220$	0.61	
$\phi = 1 - C/A$	All oceans	$24 < d < 100$	0.52
		$100 < d < 220$	0.55
	Pacific	$24 < d < 100$	0.63
		$100 < d < 220$	0.45

Table 5.1 Probability of having less anisotropy than in PREM (*continue on next page*)

Parameter p	Area	Depth (km)	$P(p < p_{prem})$
	Indian Ocean	$24 < d < 100$	0.48
		$100 < d < 220$	0.48
	Atlantic	$24 < d < 100$	0.42
		$100 < d < 220$	0.63
	All oceans younger than 50Ma	$24 < d < 100$	0.27
		$100 < d < 220$	0.81
	All oceans $50 < \text{age} < 100\text{Ma}$	$24 < d < 100$	0.56
		$100 < d < 220$	0.35
	All oceans older than 100Ma	$24 < d < 100$	0.74
		$100 < d < 220$	0.33
	All continents	$24 < d < 100$	0.83
		$100 < d < 220$	0.50
	All cratons	$24 < d < 100$	0.73
		$100 < d < 220$	0.39
All platforms	$24 < d < 100$	0.80	
	$100 < d < 220$	0.49	
All tectonically active regions	$24 < d < 100$	0.68	
	$100 < d < 220$	0.60	
$\eta = 1 - F/(A - 2L)$	All oceans	$24 < d < 100$	0.46
		$100 < d < 220$	0.73
	Pacific	$24 < d < 100$	0.98
		$100 < d < 220$	0.42
	Indian Ocean	$24 < d < 100$	0.93
		$100 < d < 220$	0.53
	Atlantic	$24 < d < 100$	0.78

Table 5.1 Probability of having less anisotropy than in PREM (continue on next page)

Parameter p	Area	Depth (km)	$P(p < p_{prem})$
		$100 < d < 220$	0.54
	All oceans younger than 50Ma	$24 < d < 100$	0.14
		$100 < d < 220$	0.87
	All oceans $50 < \text{age} < 100\text{Ma}$	$24 < d < 100$	0.70
		$100 < d < 220$	0.47
	All oceans older than 100Ma	$24 < d < 100$	0.75
		$100 < d < 220$	0.45
	All continents	$24 < d < 100$	0.99
		$100 < d < 220$	0.51
	All cratons	$24 < d < 100$	0.98
		$100 < d < 220$	0.42
	All platforms	$24 < d < 100$	0.93
		$100 < d < 220$	0.53
	All tectonically active regions	$24 < d < 100$	0.78
		$100 < d < 220$	0.54

Table 5.1: Probability of having less anisotropy than in PREM (*continued*)

A last parameter is density. Most density models were anticorrelated to the velocities, and our mean $dln\rho$ model was very similar to Ishii and Tromp (2001)'s model at the corresponding depths. The signal clearly showed a negative ratio $dln\rho/dlnV_s$, in all regions, especially beneath old oceans and cratons, indicative of strong chemical heterogeneities, but this signal might not have any physical meaning. Indeed, while Resovsky and Trampert (2002) demonstrated that NA applied to a data set composed of fundamental and overtone surface waves and normal modes can resolve lateral variations in density anomalies, more tests are needed here to know whether fundamental mode surface waves alone can resolve density. However, we ran tests which showed that the results for density do not affect the results for anisotropy. For several SH coefficients, we did not allow any density anomaly (i.e. $\delta\rho_s^t = 0$), and we did not observe any significant change in the other model parameters, that is to say the five elastic coefficients. This indicates a low trade-off between elastic coefficients and density anomalies.

5.5 Discussion and conclusion

The application of the NA to degree eight fundamental mode Love and Rayleigh wave phase velocity maps allowed us to retrieve robust information on the lateral variations of radial anisotropy in the upper 220 km of the mantle. The method employed was a derivative-free model space search technique which presents the advantages of not requiring any unnecessary regularisation on the model space. The results showed that ξ was negative in the two layers down to 220 km, below oceans and below continents, which means that horizontally polarized shear waves travel faster than vertically polarized shear waves ($V_{SH} > V_{SV}$).

Cratons can be distinguished from younger continental regions using the depth variation of S-wave anisotropy. Our results showed that S-wave anisotropy is almost constant beneath cratons down to at least 220 km depth, as opposed to platforms and tectonically active regions where a strong decrease of ξ was observed with depth. This could be associated with the depth of continental roots, with a continental lithosphere thicker in old regions than young regions. Our results also suggest that cratons have somewhat less S-wave anisotropy than younger continental regions in the top 100 km, and the departure from PREM is generally stronger beneath cratons. No significant age-dependence was observed within continents for P-wave anisotropy. η appears to be most likely zero beneath cratons in the top 100 km and increases for younger continental regions, similarly to ξ . No changes relative to PREM was visible in the deepest layer, both for ϕ and for η .

S-wave anisotropy beneath oceans is rather uniform (no difference was observed from one ocean to another) and similar to the signal for cratons. The data clearly require less S-wave anisotropy than in PREM in the top 100 km beneath oceans and cratons, and more anisotropy in the depth range 100-220km. A strong age-related signal is, however, observed in oceanic lithosphere, similar to the age-dependent signal in continental lithosphere. S-wave anisotropy decreases with depth beneath young oceans, while older oceans display less depth variation, suggesting deeper anisotropy and possibly thicker lithosphere in old oceanic regions. From the point of view of S-wave anisotropy, this means that cratons and old oceans are much more alike than commonly thought. Young continental and young oceanic lithospheres have a similar depth pattern of S-wave anisotropy, within the limits of our layered parameterization. The depth dependence of ξ beneath oceans is compatible with Gung et al. (2003)'s general observation of $V_{SH} > V_{SV}$ between 80 and 200 km depth under ocean basins and down to at least 200 km depth under cratons. Parameter η follows a similar age-dependence as ξ within oceans, with less anisotropy beneath old oceanic lithospheres than beneath younger ones in the top 100 km. The trend is reversed between 100 and 220 km depth. We also observe an age variation of $d \ln V_s$ in the upper 100 km of the oceans that could correspond to the $a + bt^{1/2}$ law proposed by Zhang and Tanimoto (1991), but we do not have enough points to confidently estimate a and b . A more linear age-related signal is observed deeper. These observations for $d \ln V_s$ in the oceans are compatible with a thickening of oceanic lithosphere with age, more rapid for young oceans than older ones. Parameter ξ could,

therefore, characterize the depth extent of the oceanic lithosphere, although the layered parameterization we adopted does not allow us to make a precise interpretation of our results in term of lithosphere-asthenosphere. Karato (1992) proposed that the Lehmann discontinuity results from a change in the deformation mechanism. This means that the depth of the discontinuity varies locally and could be detected by a change in anisotropy. Our results are compatible with such a proposition and the depth dependence of our S-wave anisotropy is largely in agreement with the discontinuity observation of Deuss and Woodhouse (2002).

P-wave anisotropy shows little deviation from PREM. With the NA, we have been able to retrieve valuable information on these two parameters that is lost in traditional inversions. We propose that the distribution obtained for ξ , ϕ and η could be used as constraints on the mineralogical composition of the uppermost mantle.

The correlations and ratios between $d\phi$ and $d\xi$ and between $d\eta$ and $d\xi$ were computed for different regions to test the assumption of proportionality between these variables commonly used in inversions. Our results showed that fundamental mode surface wave data do not favour any particular ratio between perturbations in P-wave and S-wave anisotropy. The ratio $d\eta/d\xi$ is highly dependent on the regions considered. It is different for oceans and for continents and it is clearly age-related within continents. This information should be used to constrain the mineralogy regionally, rather than prescribe global proportionality factors in inversions.

Lateral variations in the location of the 220-discontinuity were neglected in this study. They can be related to phase velocity perturbations through boundary factors that are derived from a linearized perturbation theory approximation. However, we believe that the effect of the crust is more important for the fundamental mode phase velocity data employed here. Levshin and Ratnikova (1984) showed that, if not accounted for properly, large scale inhomogeneities can give rise to apparent anisotropic signals such as shear wave splitting or Love-Rayleigh discrepancy. In this work, we accounted for the effect of the crust in the most precise way possible with exact non-linear computations rather than a linearized perturbation theory. In addition, the type of data used here puts weak constraints on the internal discontinuities (e.g. Ishii and Tromp (2001) or Resovsky and Trampert (2003)), which would probably translate in terms of flat posterior distributions with the NA. More tests would be needed to verify this.

Chapter 6

Probability density functions for radial anisotropy in the upper 1200 km of the mantle

Abstract

The presence of radial anisotropy in the upper mantle, transition zone and the top of the lower mantle is investigated using a model space search technique with Rayleigh and Love wave phase velocity models constructed from overtone measurements. Probability density functions are obtained for S-wave anisotropy, P-wave anisotropy, intermediate parameter η , V_p , V_s and density anomalies. Shear wave anisotropy with $V_{SH} > V_{SV}$ is found down to the transition zone, most likely occurring beneath oceans (and stronger for young oceanic areas than for old ones) and not beneath continents. P-wave anisotropy and η are similar : they both change sign below 220 km depth beneath old oceans and continental regions. For young oceans the positive signal for ϕ and η observed in the uppermost mantle extends slightly deeper than beneath older oceans. The ratio $R = d\ln V_s / d\ln V_p$ suggests that there is good evidence that a chemical component is responsible for the anomalies in most places at depths greater than 220 km. More tests are needed to infer the robustness of the results for density, but they did not affect the results for anisotropy.

The content of this chapter was submitted in Beghein, C. & Trampert, J., *Earth and Planetary Science Letters*, 2003

6.1 Introduction

Radial anisotropy in the uppermost mantle was first proposed to simultaneously explain fundamental Love and Rayleigh wave phase velocity maps (Anderson, 1961). PREM (Dziewonski and Anderson, 1981) was the first reference model to include this type of anisotropy in the upper 220 km of the mantle. Isotropy was assumed deeper. Since then, numerous surface wave studies showed that this anisotropy varies laterally (Montagner and Tanimoto, 1991; Cara et al., 1980; L ev eque et al., 1998; Debayle and Kennett, 2000; Silveira and Stutzmann, 2002) and might extend slightly deeper than 220 km in some areas (Montagner and Tanimoto, 1991; L ev eque et al., 1998), but the exact depth extent is still not clear. It is usually believed that radial anisotropy decreases rapidly with depth. Its presence in the transition zone and in the top of the lower mantle is, however, not excluded, as shown from normal mode data (Montagner and Kennett, 1996) and in a regional study based on shear-wave splitting measurements (Wookey et al., 2002; Chen and Brudzinski, 2003). Higher mode data appear to require radial anisotropy down to about 300 km depth beneath the Indian ocean (L ev eque et al., 1998) and the Pacific (Montagner, 1985), but not deeper than 220 km depth beneath the Atlantic ocean (Silveira and Stutzmann, 2002). Some level of shear-wave anisotropy was also detected in the range 200-400 km depth beneath cratons and 80-200 km under ocean basins in a global study (e.g. Gung et al. (2003)).

Current models of radial anisotropy are usually derived from the inversion of surface wave data (fundamental and higher modes). Because these problems are highly non-unique, additional constraints on the model parameters need to be introduced. The number of unknowns is often reduced by either neglecting model parameters to which the data have the least sensitivity and inverting only for two S-wave related parameters and density (Montagner, 1985), or by imposing global scalings between perturbations in the different anisotropic parameters (Gung et al., 2003).

In this chapter, we investigate lateral variations in radial anisotropy in global models using the Neighbourhood Algorithm (NA) (Sambridge, 1999a,b). The method is applied to surface wave phase velocity maps constructed from overtone measurements (van Heijst and Woodhouse, 1999), which have sensitivity down to approximately 1200 km depth. The NA does not require neglecting parameters or scaling relations and returns probability density functions for all model parameters with reliable uncertainty estimates.

6.2 Method

The NA (Sambridge, 1999a,b) is a direct search approach from which robust information on Earth's properties can be obtained without having to introduce unnecessary *a priori* information in the model space. The NA consists of two stages. During the first stage, the model space is surveyed and regions that best fit the data are identified. Provided the right tuning parameters, the NA finds all models compatible with the data. One can explore different parts of the model space simultaneously and there is always a possibility

to move towards more promising regions. The number of models generated automatically increases in the vicinity of the good fitting areas. After the sampling of the model space, a “misfit map” is obtained, and models of high misfit are associated with a small likelihood, while models with lower misfit are associated with a higher likelihood. An importance sampling of this ensemble of models is then performed in the second stage of the NA to generate a resampled ensemble whose distribution follows the distribution of misfit previously obtained. This resampled ensemble is integrated numerically to compute the likelihood, or 1-D marginal, associated with each model parameter and the covariance matrix that gives the trade-offs among the different variables. Because the second stage is highly time-consuming, the NA limits the size of the model space that can be studied in a reasonable amount of time. It can, however, be easily applied to phase velocity maps as they can be expanded into spherical harmonics. The inverse problem is then solved separately for each spherical harmonic (SH) coefficient of Earth’s structure.

6.3 Data

The data set employed is composed of the isotropic part of azimuthally anisotropic phase velocity maps constructed from higher mode measurements (van Heijst and Woodhouse, 1999) for Rayleigh and Love waves of overtone number $n = 1$ and $n = 2$. The technique to obtain these phase velocity maps is described by Trampert and van Heijst (2002) and Trampert and Woodhouse (2003). The isotropic part of the phase velocity models were developed on a spherical harmonic basis up to degree 40 and coefficients up to degree eight are employed here to constrain Earth’s structure. It can be shown that the degree s and order t of the phase velocity perturbation ${}_k \left(\frac{\delta c}{c} \right)_s^t$ is linearly related to perturbations in Earth’s structure at degree s and order t :

$${}_k \left(\frac{\delta c}{c} \right)_s^t = \int_0^a \delta \mathbf{m}_s^t(r) {}_k \mathbf{K}(r) r^2 dr \quad (6.1)$$

where k discriminates between different surface wave frequencies, a is the radius of the Earth and ${}_k \mathbf{K}(r)$ is the partial derivative, or depth sensitivity kernel, for model parameter $\delta \mathbf{m}_s^t(r)$.

Errors in phase velocity models are best evaluated by comparing different models. Due to the lack of other overtone phase velocity maps, data errors are assumed to be identical to errors previously determined for fundamental Love and Rayleigh wave phase velocity maps at the corresponding periods (see Chapter 3). The study of Chapter 4 showed that this assumption is reasonable for degree zero. We assume here that it is also valid for other SH coefficients. For periods of 40, 60, 80, 100 and 150 seconds, fundamental mode surface wave phase velocity models from different studies (van Heijst and Woodhouse, 1999; Trampert and Woodhouse, 1995, 1996, 2001, 2003; Ekström et al., 1997; Laske and Masters, 1996; Wong, 1989) were averaged and a standard deviation was computed for each SH coefficient. As in previous chapters, data uncertainties at degree

s and azimuthal order t are assumed to be independent of t , and an average over t is calculated. At intermediate periods, we made a simple interpolation of the uncertainties obtained at 40, 60, 80, 100 and 150 seconds. At periods higher than 150 seconds, we imposed the same error as the one estimated at 150 seconds (see Chapter 3, section 3.2, for explanations).

The data are corrected with the crustal model CRUST5.1 (Mooney et al., 1998). Since the size of the model space that can be surveyed with the NA is limited, we reduced the number of unknowns by further correcting the data with models of radial anisotropy previously obtained for the uppermost mantle (Chapter 5). These models were derived by applying the NA to fundamental mode Love and Rayleigh wave phase velocity models to constrain radial anisotropy in the top 220 km of the mantle. The likelihoods obtained for each model parameter, at each SH coefficient up to degree eight, were resampled to compute distributions of predictions of overtone measurements for the uppermost mantle (UUM). From each distribution (approximately Gaussian) we calculated a mean contribution \mathbf{d}^{UUM} and a standard deviation σ^{UUM} which were employed to correct the data :

$$\mathbf{d}^{\text{res}} = \mathbf{d}^0 - \mathbf{d}^{\text{CRUST5.1}} - \mathbf{d}^{\text{UUM}} \quad (6.2)$$

$$\sigma^{\text{res}} = \sigma^0 + \sigma^{\text{UUM}} \quad (6.3)$$

\mathbf{d}^0 and σ^0 represent the original data and data uncertainty. $\mathbf{d}^{\text{CRUST5.1}}$ represents the contribution of the crust. Original errors were incremented to account for the uncertainties on the models of uppermost mantle anisotropy. We thus inverted residual data \mathbf{d}^{res} and associated errors σ^{res} with the NA to find models of radial anisotropy between 220 and 1200 km depth.

6.4 Parameterization

Radial anisotropy can be described by five independent elastic coefficients A , C , N , L and F (Love, 1927). C and A are related to the wavespeed of P-waves travelling vertically and horizontally, respectively. L and N give the wavespeed of vertically and horizontally polarized S-waves and F describes waves travelling with an intermediate incidence angle. We parameterized the models as perturbations of the Love parameters and perturbations of density with respect to PREM (Dziewonski and Anderson, 1981). The model parameters are expanded on a spherical harmonic basis, and the relation between the data and the structure of the Earth is :

$$\begin{aligned} {}_k \left(\frac{\delta c}{c} \right)_s^t = \int_{r_{cmb}}^{r_{220}} [& {}_k K_A(r) \delta A_s^t(r) + {}_k K_C(r) \delta C_s^t(r) \\ & + {}_k K_N(r) \delta N_s^t(r) + {}_k K_L(r) \delta L_s^t(r) \\ & + {}_k K_F(r) \delta F_s^t(r) + {}_k K_\rho(r) \delta \rho_s^t(r)] r^2 dr \end{aligned} \quad (6.4)$$

where the integration is done between the core-mantle boundary (r_{cmb} is the radius of core-mantle boundary) and 220 km depth. A layered parameterization is adopted with

three layers delimited by the following depths : 220-400 km, 400-670 km and 670-1230 km. We therefore have 18 model parameters (six parameters in three layers) for each SH component. The choice of this layered division was not based on the depth resolution of the data but it was mainly motivated by computational resources. Our parameterization is still sufficient to analyze the robustness of the anisotropic signal, but a detailed geodynamical interpretation will clearly need a more refined analysis.

6.5 Retrieving anisotropy, velocity and density anomalies

The same procedure as in Chapter 5 is applied. The NA provides PPD functions associated with each SH component of the model parameters : δA_s^t , δC_s^t , δN_s^t , δL_s^t , δF_s^t and $\delta \rho_s^t$. Random values of these δm_s^t are generated, using to their exact PPD functions, and the SH coefficients are recombined to get $\delta m(r, \theta, \phi)$. The parameters describing radial anisotropy are then recovered by computing $\xi = 1 - N/L$, $\phi = 1 - C/A$ and $\eta = 1 - F/(A - 2L)$ at each point (r, θ, ϕ) in the Earth. Parameter ξ describes the anisotropy of shear waves, ϕ P-wave anisotropy and η intermediate anisotropy. Equivalent isotropic P-wave and S-wave velocity anomalies, together with density anomalies, are also calculated at (r, θ, ϕ) . Histograms are then computed by repeating the procedure described above several thousand times and, for every model generated, the function of interest (anisotropy, velocity or density anomalies) is averaged over a particular area (e.g. continents, oceans,...). The distributions represent thus the range of data-compatible values of this function averaged over a certain area, and they do not account for structure variations within the area considered.

6.6 Results

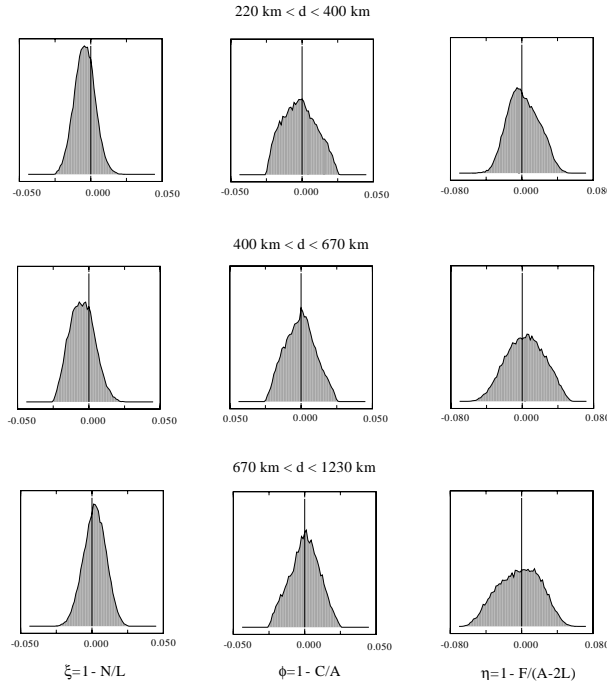


Figure 6.1: Likelihoods for the spherically averaged ξ , ϕ and η . The vertical line represents the value of PREM (zero at these depths).

Figure 6.1 gives the likelihoods obtained for the spherically averaged ξ , ϕ and η . It shows that these parameters do not significantly deviate from PREM (Dziewonski and Anderson, 1981) in the three layers. This is in agreement with the results of the whole mantle study of Chapter 4, where more data were employed, but not with ϕ between 220 and 400 km depth. The presence of normal mode data in Chapter 4 favoured slightly positive values for this parameter at these depths.

Figures 6.2 to 6.7 represent the likelihoods for parameter ξ , ϕ and η in various tectonic regions, selected with model 3SMAC (Nataf and Ricard, 1996). Note that the degree zero perturbation of the elastic coefficients was included in the calculation of the anisotropic parameters. On top of the three layers employed here, we plotted the results obtained in a previous study for the uppermost mantle (Chapter 5). Table 6.1 displays the probability that a given parameter is negative, computed by integration of the normalized likelihoods. Different tests showed that anomalies in S-wave related parameters (L and N) have very little trade-offs with other model parameters and that they are well re-

solved (narrow marginals) by the data, indicating the robustness of the results for S-wave anisotropy. More caution is necessary for the other model parameters since not all SH coefficients are well constrained (wide marginals) for δA , δC , δF and $\delta \rho$.

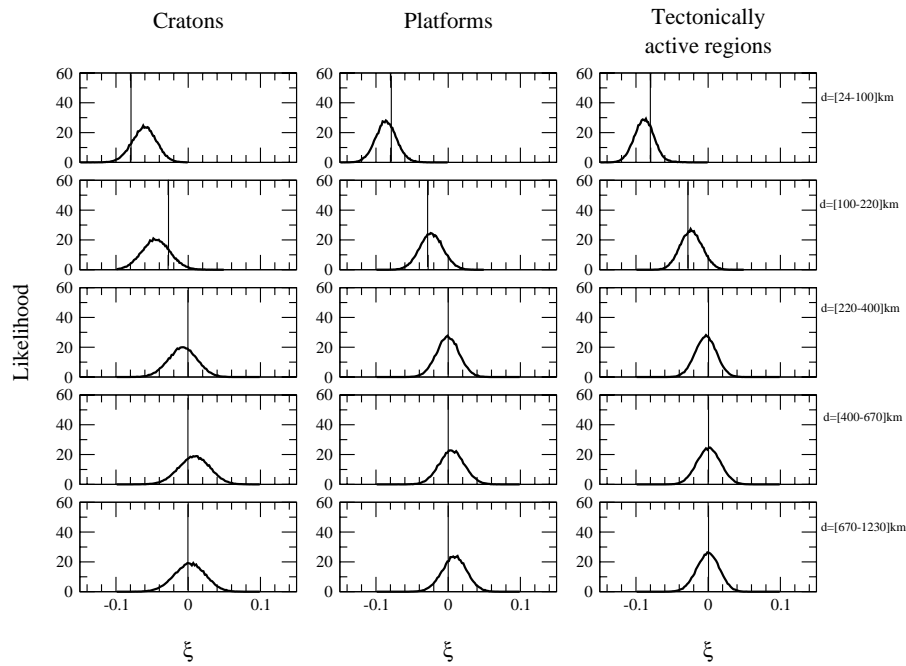


Figure 6.2: Likelihood of S-wave anisotropy beneath continents. The vertical line represents the value of PREM averaged over the layers.

Figure 6.2 shows the likelihood of S-wave anisotropy in the different layers, beneath continents. The data do not require S-wave anisotropy below 220 km depth in most continental regions, except maybe beneath cratons where the probability to have $\xi < 0$ is 0.65 between 220 and 400 km depth (see Table 6.1). This possibly indicates that shear-wave anisotropy, with fast horizontally polarized shear waves, extends a little deeper than the Lehmann discontinuity in PREM (Dziewonski and Anderson, 1981) beneath cratons, but not beneath younger continental areas. There is further a small probability that ξ becomes positive in the transition zone beneath cratons.

The signal is much clearer beneath oceans, as shown in Figure 6.3 where oceanic regions are separated according to the age of the overlying ocean floor. We see that there

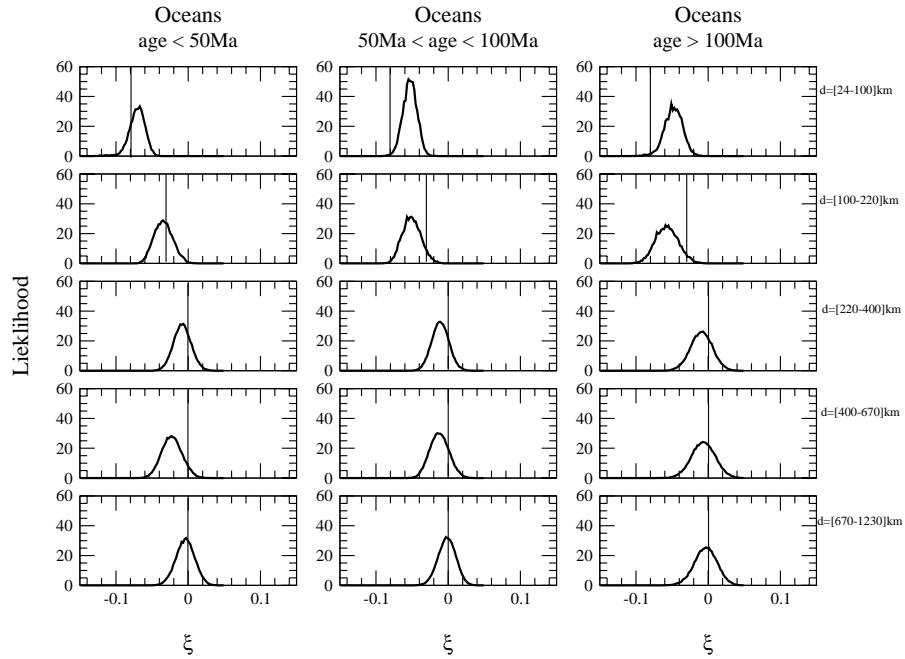


Figure 6.3: Likelihood of S-wave anisotropy beneath oceans. The vertical line represents the value of PREM averaged over the layers.

is a strong probability of $V_{SH} > V_{SV}$ between depths of 220 and 400 km and in the transition zone. The anisotropy between 220 and 400 km depth is smaller than on top, but its presence is still likely (see also Table 6.1). In the transition zone, we clearly observe $\xi < 0$, therefore $V_{SH} > V_{SV}$, beneath young oceans, with amplitudes comparable to the ones obtained between 100 and 220 km depth. An age-dependent signal is also detected in the transition zone since the probability of $\xi < 0$ decreases towards older oceanic regions.

Figures 6.4 and 6.5 give the likelihoods associated with P-wave anisotropy beneath continents and oceans, respectively. There is a high probability of ϕ negative beneath continents in the depth range 220-400 km and possibly in the transition zone. This corresponds to fast vertically travelling P-waves ($V_{PV} > V_{PH}$) and indicates a change of sign in ϕ with respect to the uppermost mantle. An age-related signal is observed for oceanic regions, between 220 and 400 km depth. ϕ seems most likely positive beneath young oceans and it tends to become most likely positive in older regions. $\phi < 0$ also appears to extend in the transition zone beneath old and intermediate oceans, but not as clearly as at shallower depths.

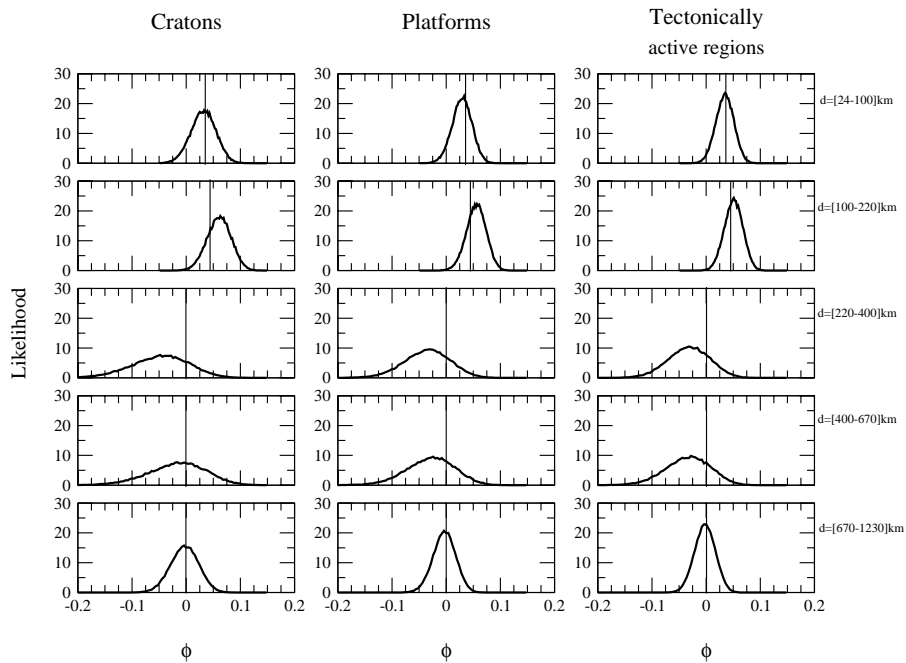


Figure 6.4: Likelihood of P-wave anisotropy beneath continents. The vertical line represents the value of PREM averaged over the layers.

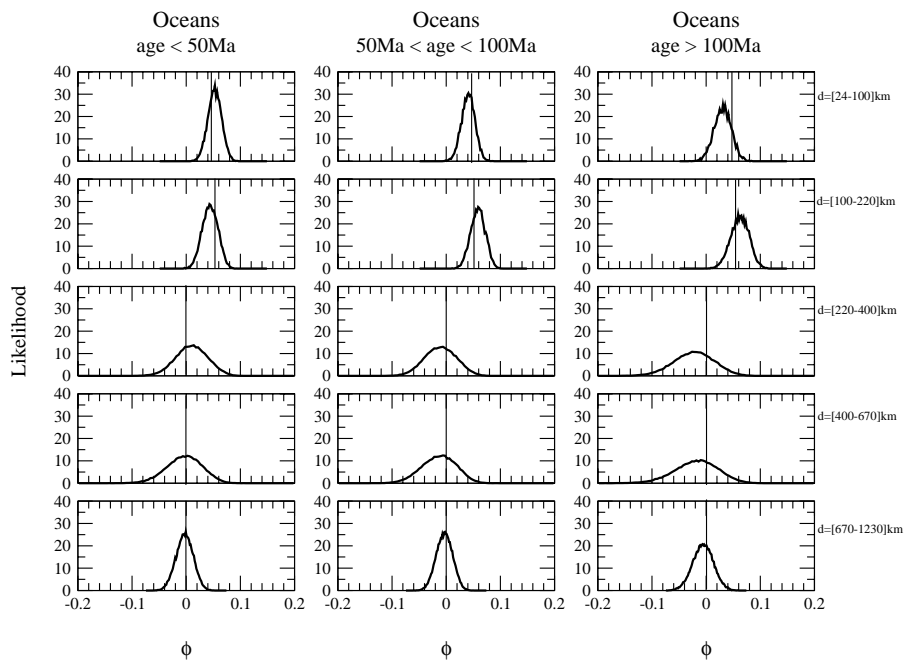


Figure 6.5: Likelihood of P-wave anisotropy beneath oceans. The vertical line represents the value of PREM averaged over the layers.

In Figure 6.6, η clearly changes sign between the uppermost mantle and larger depths, in continental areas. It stays negative down to 1230 km depth beneath platforms and tectonically active regions, and maybe beneath cratons but with a smaller probability. Similar to ϕ , parameter η is most likely positive beneath young oceans and becomes most likely negative in old regions (Figure 6.7). A strong signal with $\eta < 0$ is also observed at depths between 670 and 1230 km. However, as mentioned above, parameters δA , δC and δF are less well determined (wider marginals) than δL and δN . The likelihoods obtained for ϕ and η by recombining individual likelihoods for different elastic parameters could therefore be dominated by only a few well resolved SH coefficients.

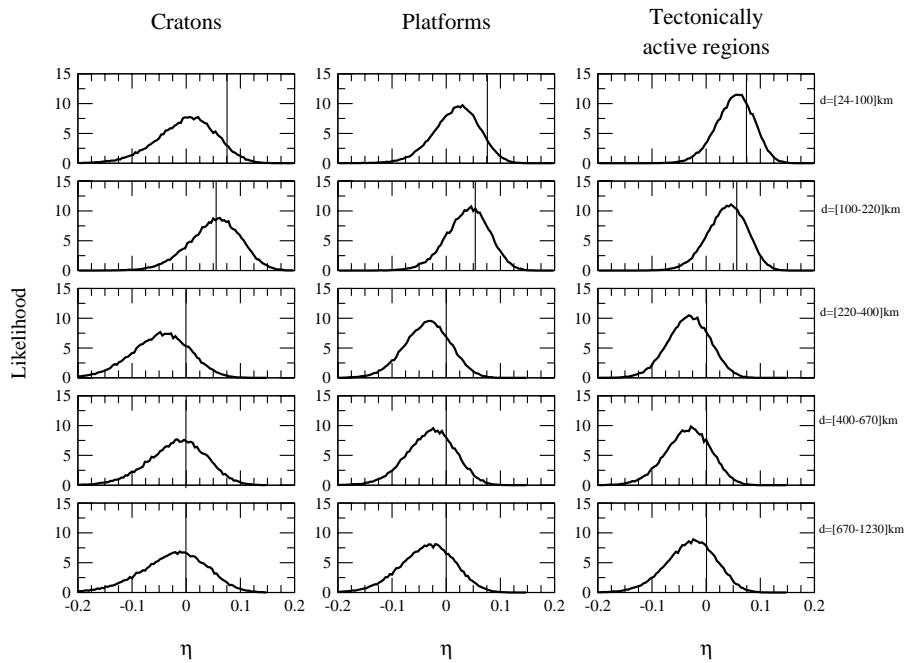


Figure 6.6: Likelihood of η -anisotropy beneath continents. The vertical line represents the value of PREM averaged over the layers.

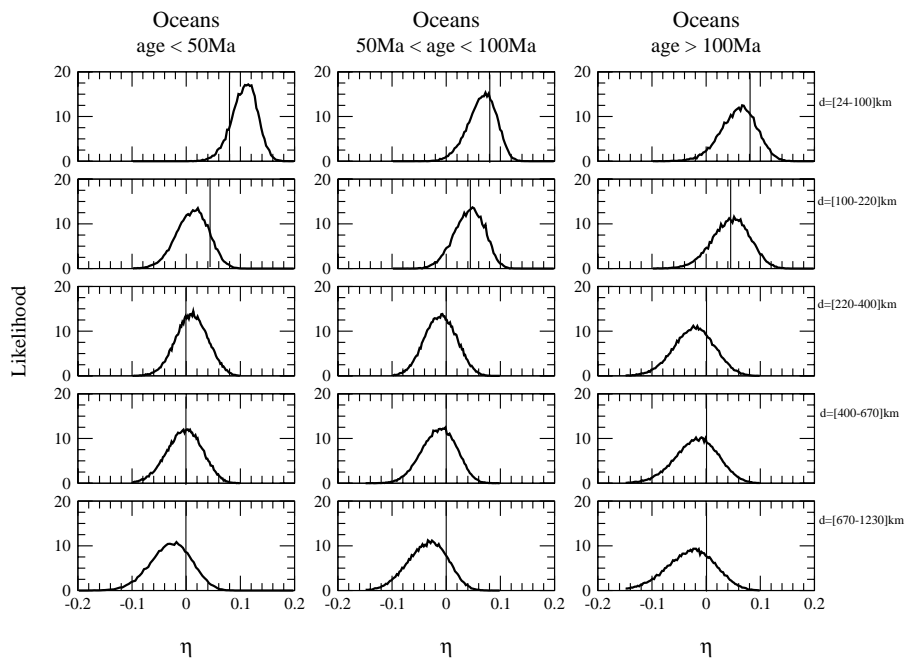


Figure 6.7: Likelihood of η -anisotropy beneath oceans. The vertical line represents the value of PREM averaged over the layers.

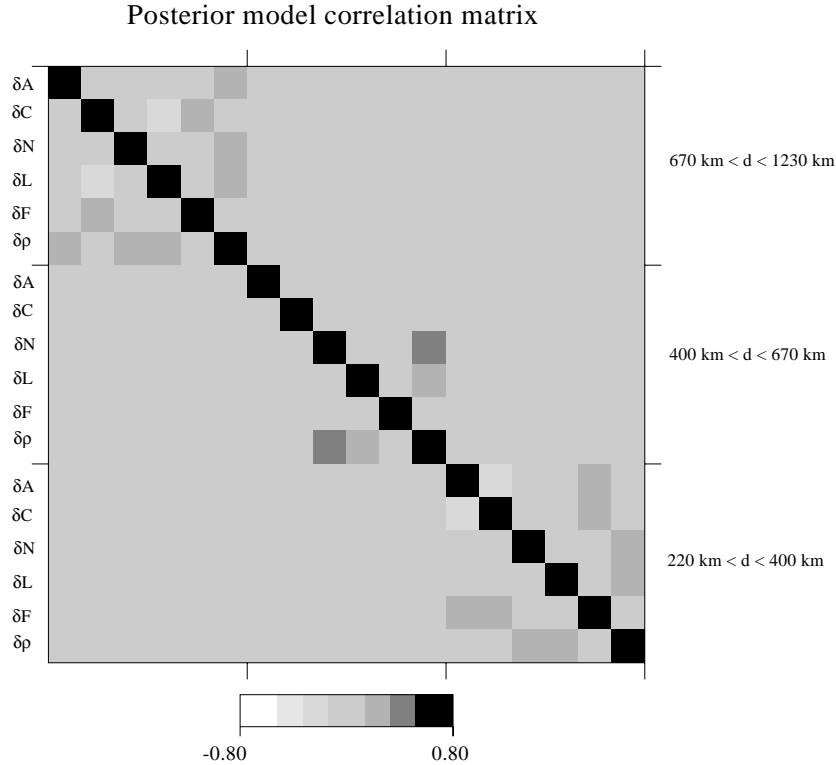


Figure 6.8: Correlation matrix corresponding to the imaginary part of $\left(\frac{\delta c}{c}\right)_4^2$.

Figure 6.8 shows the correlation matrix for the imaginary part of $\left(\frac{\delta c}{c}\right)_4^2$. It demonstrates that there is a low trade-off between the different layers, indicative of a depth resolution approximately equal to the width of the layers.

Histograms for the likelihood of correlation between $d \ln V_p$, $d \ln V_s$ and $d \ln \rho$ were also computed and showed a good global correlation between $d \ln V_p$ and $d \ln V_s$, but poor correlation between density and velocity anomalies in the three layers. Resovsky and Trampert (2002) demonstrated with synthetic tests that density anomalies could be recovered using normal mode data, overtone and fundamental surface wave data together. Further tests are needed to see whether fundamental mode and overtone phase velocity data alone can determine density. We thus refrain here from a further interpretation of density results. Importantly, extensive tests showed that density did not influence any elastic parameter in this study. If the anomalies in $d \ln V_s$ and $d \ln V_p$ would be thermal in origin, one would expect the highest probability for $d \ln V_s / d \ln V_p$ to be between 1 and 2 (Karato and Karki, 2001). This is clearly not the case below 220 km depth (Tables 6.2 and 6.3), and in most places in the uppermost mantle. We therefore suggest that a chemical

component is responsible for the observed signal.

Depth (km)	Area	$P(\xi < 0)$	$P(\phi < 0)$	$P(\eta < 0)$
$220 < d < 400$	All cratons	0.65	0.79	0.79
$400 < d < 670$		0.35	0.60	0.60
$670 < d < 1230$		0.46	0.55	0.63
$220 < d < 400$	All platforms	0.54	0.79	0.79
$400 < d < 670$		0.39	0.60	0.75
$670 < d < 1230$		0.31	0.60	0.77
$220 < d < 400$	All tectonically active regions	0.59	0.80	0.80
$400 < d < 670$		0.48	0.77	0.77
$670 < d < 1230$		0.52	0.61	0.72
$220 < d < 400$	All oceans younger than 50 Ma	0.71	0.37	0.38
$400 < d < 670$		0.93	0.53	0.53
$670 < d < 1230$		0.62	0.59	0.78
$220 < d < 400$	All oceans 50 Ma < age < 100 Ma	0.80	0.62	0.65
$400 < d < 670$		0.83	0.65	0.66
$670 < d < 1230$		0.54	0.57	0.84
$220 < d < 400$	All oceans older than 100 Ma	0.73	0.72	0.75
$400 < d < 670$		0.66	0.66	0.66
$670 < d < 1230$		0.58	0.61	0.73

Table 6.1: Probability of having negative $\xi = 1 - N/L$, $\phi = 1 - C/A$ and $\eta = 1 - F/(A - 2L)$

Depth (km)	Area	$P\left(\frac{dlnV_s}{dlnV_p} < 0\right)$	$P\left(0 < \frac{dlnV_s}{dlnV_p} < 1\right)$	$P\left(1 < \frac{dlnV_s}{dlnV_p} < 2\right)$	$P\left(\frac{dlnV_s}{dlnV_p} > 2\right)$
24 < d < 100	All cratons	0.0	0.0	0.49	0.51
100 < d < 220		0.0	0.0	0.74	0.26
220 < d < 400		0.34	0.23	0.21	0.22
400 < d < 670		0.16	0.37	0.29	0.18
670 < d < 1230		0.23	0.38	0.20	0.19
24 < d < 100	All platforms	0.0	0.0	0.32	0.68
100 < d < 220		0.0	0.0	0.69	0.31
220 < d < 400		0.29	0.08	0.22	0.41
400 < d < 670		0.19	0.32	0.29	0.20
670 < d < 1230		0.24	0.44	0.23	0.09
24 < d < 100	All tectonically active regions	0.25	0.58	0.15	0.02
100 < d < 220		0.14	0.46	0.34	0.06
220 < d < 400		0.36	0.26	0.20	0.18
400 < d < 670		0.23	0.32	0.23	0.22
670 < d < 1230		0.18	0.40	0.19	0.23

Table 6.2: Probabilities for $dlnV_s/dlnV_p$ beneath continents. The results of Chapter 5 are also displayed for the uppermost mantle. Velocity anomalies were calculated for degrees 1 to 8 with respect to PREM (Dziewonski and Anderson, 1981).

Depth (km)	Area	$P\left(\frac{dlnV_s}{dlnV_p} < 0\right)$	$P\left(0 < \frac{dlnV_s}{dlnV_p} < 1\right)$	$P\left(1 < \frac{dlnV_s}{dlnV_p} < 2\right)$	$P\left(\frac{dlnV_s}{dlnV_p} > 2\right)$
$24 < d < 100$	All oceans	0.06	0.44	0.43	0.07
$100 < d < 220$	younger than 50 Ma	0.0	0.0	0.57	0.43
$220 < d < 400$		0.70	0.08	0.12	0.10
$400 < d < 670$		0.19	0.28	0.31	0.22
$670 < d < 1230$		0.23	0.43	0.27	0.07
$24 < d < 100$	All oceans	0.0	0.0	0.21	0.79
$100 < d < 220$	50 Ma < age < 100 Ma	0.0	0.0	0.80	0.20
$220 < d < 400$		0.25	0.23	0.23	0.29
$400 < d < 670$		0.21	0.38	0.33	0.08
$670 < d < 1230$		0.21	0.46	0.21	0.12
$24 < d < 100$	All oceans	0.0	0.0	0.29	0.71
$100 < d < 220$	older than 100 Ma	0.0	0.0	0.79	0.21
$220 < d < 400$		0.20	0.42	0.28	0.10
$400 < d < 670$		0.19	0.43	0.27	0.11
$670 < d < 1230$		0.23	0.44	0.25	0.08

Table 6.3: Probabilities for $dlnV_s/dlnV_p$ beneath oceans. The results of Chapter 5 are also displayed for the uppermost mantle. Velocity anomalies were calculated for degrees 1 to 8 with respect to PREM (Dziewonski and Anderson, 1981).

6.7 Discussion and conclusion

Our results suggest an age-related anisotropic signal beneath oceanic areas going as deep as the transition zone. Indeed, we observe shear wave anisotropy with horizontally polarized shear waves faster than vertically polarized shear waves down to 670 km beneath oceans. The anisotropy in the transition zone is stronger and more likely beneath young oceans than beneath older ones. It is also characterized by a minimum between 220 and 400 km depth for oceans younger than 50 Ma, and P-wave anisotropy and η display an age-dependent signal. A depth pattern similar to the one observed for ξ beneath young oceans was found for azimuthal anisotropy by Trampert and van Heijst (2002). Both η and ϕ are positive in the uppermost mantle and in the depth range 220-400 km beneath young oceans with amplitudes decreasing with depth, whereas a clear change of sign is observed for old oceans and continents between the uppermost mantle and the underlying layers. While no S-wave or P-wave anisotropy is detected below the transition zone, η appears to be most likely negative between 670 and 1230 km depth, but caution is required here since the signal might be dominated by only a few well-resolved parameters. There is no systematic relation between perturbations in parameters η , ϕ and ξ , as sometimes assumed in inversions (e.g. Gung et al. (2003)), which implies that the data do not support any particular scaling relationship between $d\eta$, $d\phi$ and $d\xi$.

The fact that the anisotropy varies with the age of the ocean floor in the transition zone, and that the anisotropic signal observed in the uppermost mantle seems to extend deeper beneath young oceans but not beneath old ones, could be an indication that ridges have some deep connection. This connection is most likely chemical in origin as inferred from Table 6.3. A better resolution of the anomalies at these depths is, however, required to draw more robust conclusions.

No strong S-wave anisotropy is required by the data beneath continents. There is, however, some evidence for shear-wave anisotropy (with $\xi < 0$) deeper than 220 km beneath cratons, but not beneath platforms or tectonically active regions. The signals for P-wave anisotropy and for η are stronger and they display a change of sign between the uppermost mantle and the deeper layers down to the transition zone. This could be a strong indication of a change of mechanical behaviour of the materials beneath continents and the oldest oceans.

Interpreting this deep anisotropy in terms of flow is delicate. Upper mantle anisotropy can be related to horizontal or vertical flow through the sign of ξ because anisotropy at these depths is believed to result from the lattice preferred orientation (LPO) of olivine crystals (Karato, 1989). However, at larger depth there is no *a priori* reason to favour LPO over shape preferred orientation of inclusions (SPO). Among all phases present in the transition zone wadsleyite has the largest intrinsic anisotropy and it is therefore the most likely candidate for seismic anisotropy due to LPO at these depths. Other phases such as majorite or ringwoodite are nearly isotropic at transition zone conditions (Mainprice et al., 2000). SPO with $V_{SH} > V_{SV}$ can occur at large scale in horizontally laminated structures or in partially molten rocks (Karato, 1998). While partial melting is considered

unlikely in most of the mantle, horizontal layering could be partly responsible for the detected anisotropy in the transition zone if the contrast in elastic moduli between the different phases is large enough. However, it would not result in the observed azimuthal anisotropy (Trampert and van Heijst, 2002).

Chapter 7

Azimuthal anisotropy down to 1200 km depth from Love wave overtone measurements

Abstract

The presence of azimuthal anisotropy from the top of the mantle down to 1200 km depth is investigated with the Neighbourhood Algorithm. The data employed is the $2 - \psi$ terms of Love wave phase velocity maps constructed from measurements for the first and second overtone branches. We focus on the degree two of parameter G , which describes the azimuthal dependence of V_{SV} . The likelihoods obtained show that the models resulting from an independent study using a Backus-Gilbert inversion scheme are very close to the most likely model found by the Neighbourhood Algorithm. This is especially visible in the top 100 km of the mantle, where G is best resolved. At larger depth the distributions are wider, showing the difficulty to constrain the amplitude of azimuthal anisotropy from Love wave phase velocity models alone.

7.1 Introduction

Azimuthal anisotropy is commonly observed from shear-wave splitting and from the azimuthal dependence of Rayleigh and Love wave phase velocities. Shear-wave splitting is the most unambiguous manifestation of azimuthal anisotropy. It is widely used in seismology but it has the disadvantage of providing poor depth resolution (see Savage (1999) for a review). Surface waves have a better vertical but less lateral resolution than body waves. Numerous surface wave studies have revealed the presence of azimuthal anisotropy in the uppermost mantle, both at the regional scale (Lévêque et al., 1998; Silveira and Stutz-

mann, 2002; Simons et al., 2002) and in global models (Tanimoto and Anderson, 1985; Montagner and Tanimoto, 1990, 1991). On the other hand, only a few studies have found evidence for azimuthal anisotropy in the transition zone. It was inferred in a few regional studies from body wave data (Fouch and Fischer, 1996; Vinnik and Montagner, 1996; Vinnik et al., 1998) and the first global model of azimuthal anisotropy at these depths was recently derived by Trampert and van Heijst (2002). They constructed azimuthally anisotropic phase velocity models for Love waves along the first and second overtone branch, and using a Backus-Gilbert approach (Backus and Gilbert, 1968) they inverted the anisotropic part of these maps to make a depth interpretation of azimuthal anisotropy.

In this chapter, we aimed to determine the probability of azimuthal anisotropy in the transition zone using the same azimuthally anisotropic Love wave phase velocity maps as those used by Trampert and van Heijst (2002). We employed the Neighbourhood Algorithm (NA) of Sambridge (Sambridge, 1999a,b) to obtain likelihoods for parameter G at degree two.

7.2 Data and method

Azimuthally anisotropic phase velocity maps can be written as the sum of five terms as follow (e.g. Smith and Dahlen (1973)) :

$$\frac{\delta c}{c}(\theta, \phi, \psi) = A_1 + A_2 \cos 2\psi + A_3 \sin 2\psi + A_4 \cos 4\psi + A_5 \sin 4\psi \quad (7.1)$$

where $\delta c/c$ is the relative phase velocity perturbation with respect to PREM (Dziewonski and Anderson, 1981) at a point (θ, ϕ) at the surface of the Earth and ψ is the azimuth of propagation. A_1 is the isotropic part of the phase velocity map. It is linearly related to the five elastic parameters that describe radial anisotropy. The other terms describe azimuthal anisotropy.

We applied the NA to the degree two of the $2 - \psi$ terms of the azimuthally anisotropic phase velocity maps constructed by Trampert and van Heijst (2002) for toroidal mode surface waves with overtone number $n = 1$ and $n = 2$. These data are only sensitive to parameter $G = \sqrt{G_c^2 + G_s^2}$, which describes the $2 - \psi$ variation of vertically polarized shear wave velocity. The relation between data and unknowns is then :

$$A_2(\theta, \phi) = \int_0^a G_c(r, \theta, \phi) K_G(r) dr \quad (7.2)$$

$$A_3(\theta, \phi) = \int_0^a G_s(r, \theta, \phi) K_G(r) dr \quad (7.3)$$

$$(7.4)$$

where $K_G(r)$ are sensitivity kernels computed in a spherical Earth. These kernels were averaged over five layers delimited by the following bottom depths : 100 km, 220 km, 400 km, 670 km and 1200 km. The phase velocity maps were expanded on a basis of

generalized spherical harmonics, as explained by Trampert and Woodhouse (2003). We applied the NA to the first 10 spherical harmonic coefficients corresponding to the degree two only of the $2 - \psi$ maps. 5-dimensional model spaces were surveyed to identify the regions of best data-fit for each coefficient. Likelihoods were obtained for each model parameter in the second stage of the NA, as explained in previous chapters and by Sambridge (1999b).

The misfit chosen to drive the model space search is the χ^2 misfit, which requires an estimate of data uncertainties. Due to the lack of other azimuthally anisotropic overtone phase velocity maps, we could not determine data errors by comparing different models. We therefore assumed the errors were identical to those previously determined for degree two fundamental Love and Rayleigh wave phase velocity maps at the corresponding periods (see, for instance, Chapter 6, section 6.2, for details). The assigned errors were much larger than the data (sometimes a factor 10) but this is not completely unrealistic. Indeed, to obtain the azimuthal terms of the phase velocity maps, Trampert and van Heijst (2002) adopted a conservative point of view and chose the smallest significant amount of azimuthal anisotropy required by the data. The full procedure of obtaining azimuthally anisotropic phase velocity maps is described in Trampert and Woodhouse (2003). We believe that taking large uncertainties for these terms is reasonable. No crustal correction was applied to the data since it was demonstrated by Trampert and Woodhouse (2003) and Trampert and van Heijst (2002) that it does not affect the azimuthally anisotropic part of the phase velocity maps.

7.3 Results

Figures 7.1 and 7.2 represent the 1-D marginals (or likelihoods) obtained for the ten spherical harmonic coefficients of parameter G at degree two in generalized spherical harmonics. The top 100 km are obviously better resolved than deeper layers and the solution obtained by Trampert and van Heijst (2002) is always close to the most likely solution (the peak of the distributions), which shows the efficiency of the Backus-Gilbert method. At larger depths, we see that the range of possible values for G is wide, which confirms the difficulty to determine the amplitude of the anisotropy with phase velocity data, as explained by Trampert and Woodhouse (2003) for fundamental mode surface waves. However, although the distributions are large, a slight peak is usually visible, and in most cases the solution of Trampert and van Heijst (2002) is situated nearby.

A factor that could influence the obtained likelihoods is data uncertainties. We chose to impose large data errors because of the incapacity of inversions to constrain the amplitude of azimuthally anisotropic terms in phase velocity maps (Trampert and Woodhouse, 2003). We tested the influence of data uncertainties on the solution by dividing all data errors by five. This number was chosen arbitrarily but it should give an idea of how much change more confidence in the data would bring to the models. Modifying all data errors in the same way does not affect the sampling stage of the NA since the survey of the model space made to identify the regions of acceptable data-fit is driven by the relative χ^2 misfit

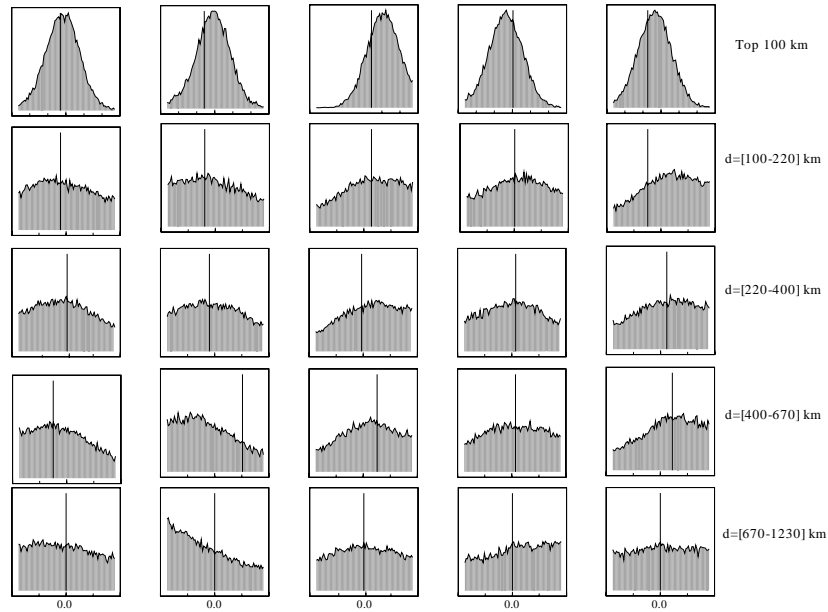


Figure 7.1: Likelihoods obtained for the first five spherical harmonic coefficients of parameter G at degree two. The vertical lines in the top four layers represent the values obtained by Trampert and van Heijst (2002). Between 670 and 1230 km, the reference value was set to zero.

between two models. On the contrary, the likelihoods obtained from the second stage of the NA might change because the Bayesian interpretation of the model space search is being done with the absolute values of the misfit. If the misfit values of two adjacent models is not very different, as it might occur when data errors are large, these models are seen by the NA as two equivalent solutions, with similar likelihoods. If data errors are smaller the difference in misfit between the two models is clearer and different likelihoods will be associated with them. Reducing all data errors did not modify the position of the peak or the shape of the likelihoods obtained for the top 100 km of the mantle but changed the likelihoods obtained at greater depths (Figure 7.3). However, it either produced multiple peaks instead of rather flat distributions or produced narrower peaks centred on the slight peaks observed in Figures 7.1 and 7.2. This is particularly visible in Figure 7.3 in the transition zone, where the main peak narrowed around the solution found by Trampert and van Heijst (2002).

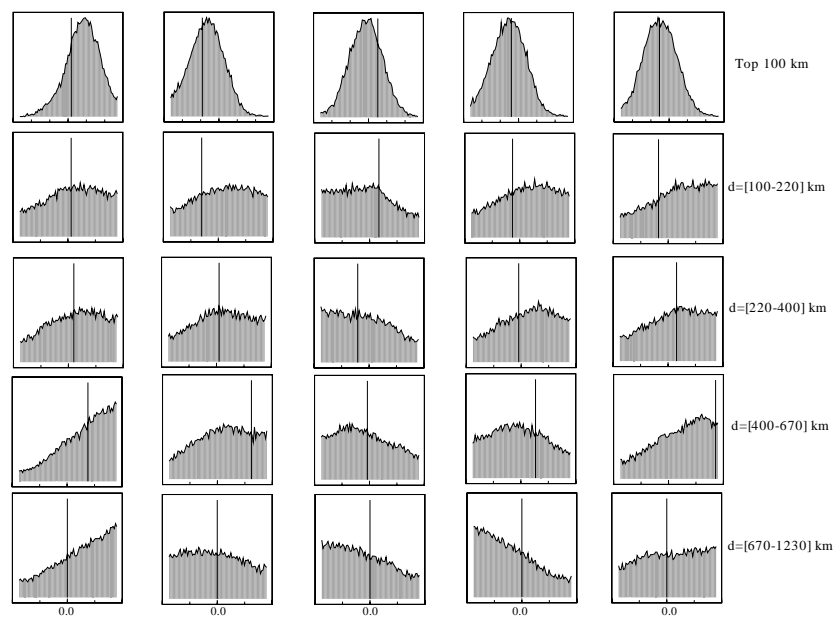


Figure 7.2: Likelihoods obtained for the last five spherical harmonic coefficients of parameter G at degree two. The vertical lines in the top four layers represent the values obtained by Trampert and van Heijst (2002). Between 670 and 1230 km, the reference value was set to zero.

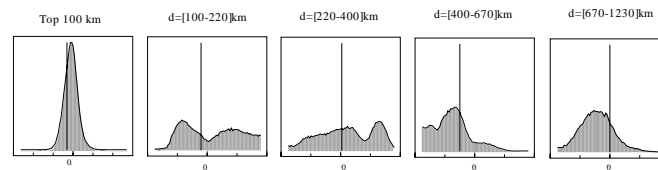


Figure 7.3: Likelihoods obtained for the first spherical harmonic coefficient of parameter G at degree two with smaller data errors. The vertical lines in the top four layers represent the values obtained by Trampert and van Heijst (2002). Between 670 and 1230 km, the reference value was set to zero.

7.4 Concluding remarks

From this first study of azimuthal anisotropy with the application of the NA to overtone Love wave phase velocity maps, we can conclude that the Backus-Gilbert inversion technique employed by Trampert and van Heijst (2002) can find solutions very close to the most likely model found by the NA, even when the peak of the likelihood is only slightly visible. Assessments of azimuthal anisotropy would certainly benefit from better data uncertainties, hence the need for more overtone measurements.

Chapter 8

Inner core anisotropy

Abstract

Discrepancies among existing seismological models of inner core anisotropy could be introduced by the regularisation of the inverse problem, needed to force a solution in the presence of non-uniqueness. The influence of regularisation, mantle correction and data quality on the models of inner core anisotropy resulting from the inversion of anomalous normal mode measurements was first tested. We found that regularisation and data quality had a significant influence on the final model, while the chosen mantle model was less crucial. Second, a full model space search technique was applied to recent measurements of anomalously split normal modes, to obtain all possible models of inner core anisotropy compatible with free oscillation data, and to circumvent regularisation. The models obtained show a robust pattern of P-wave and S-wave anisotropy in the inner core. The parameter describing P-wave anisotropy changes sign around a radius of 400 km, while S-wave anisotropy is small in the upper two-thirds of the inner core and becomes negative at greater depths. Our results agree with observed travel time anomalies of rays travelling at epicentral distances varying from 150° to 180° . The models may be explained by progressively tilted hexagonal close-packed iron in the upper half of the inner core, but could suggest a different iron phase in the centre.

8.1 Introduction

The concept of inner core anisotropy is generally accepted as an explanation for the directional dependence of PKIKP travel-times and the anomalous splitting of core-sensitive free oscillations (Morelli et al., 1986; Woodhouse et al., 1986). Masters and Gilbert (1981) were the first to measure modes sensitive to the inner core that were split much

The content of this chapter was published in Beghein, C. & Trampert, J., *Science*, **299**, 552-555 (2003)

more than predicted from Earth's rotation, ellipticity or any three-dimensional mantle model. These modes are qualified as anomalous. Poupinet et al. (1983) observed that PKIKP body waves propagating along paths parallel to Earth's spin axis were faster than waves travelling along equatorial paths. Inner core anisotropy was advanced to explain these observations for the first time by Morelli et al. (1986) and by Woodhouse et al. (1986), who simultaneously proposed a cylindrically symmetric model, with the fast direction aligned with the rotation axis.

Several models have tried to explain both kinds of data, but the amplitude and depth dependence of the anisotropy is still a matter of debate (Morelli et al., 1986; Woodhouse et al., 1986; Tromp, 1993, 1995b; Durek and Romanowicz, 1999; Romanowicz and Bréger, 2000; Creager, 2000). In particular, models derived from the inversion of normal mode data cannot explain the large travel time anomalies observed for body waves travelling at high epicentral distances (Su et al., 1995; Song, 1996; Sun and Song, 2002). Even joint inversions of normal mode and travel time data fail to reconcile all observations (Tromp, 1995b; Durek and Romanowicz, 1999; Ishii and Dziewonski, 2002). Outer core structure was even suggested to explain all existing data but could not account for the strong splitting of modes highly sensitive to inner core structure (e.g. mode ${}_3S_2$) (Romanowicz and Bréger, 2000). Differential travel-times between rays turning in the liquid outer core (PKP(BC) and PKP(AB)) and rays turning in the solid inner core (PKIPK or PKP(DF)) suggest an increase in anisotropy with depth, with a maximum in the innermost 500 km of the inner core (Morelli et al., 1986; Creager, 1999). This is also supported by the large travel-time anomalies observed for rays travelling almost vertically, at epicentral distances of $170^\circ - 180^\circ$ (Vinnik et al., 1994; Su et al., 1995; Song, 1996; Sun and Song, 2002). On the contrary, the top 100 to 250 kilometres of the inner core seem to be isotropic or very slightly anisotropic. This was first shown by Song and Helmberger (1995) from differential travel times, and several studies tend to confirm these observations (Song and Helmberger, 1998; Ouzounis and Creager, 2001; Sun and Song, 2002).

The inner core is believed to be mainly composed of solid iron, with some unknown light elements (Birch, 1964; Stixrude et al., 1997; Mao et al., 2001; Lin et al., 2002; Gessman and Wood, 2002). Although the stable phase of iron at inner core conditions is not known, mineralogical studies tend to favour a hexagonal close-packed (h.c.p.) structure. Nevertheless, the possibility of another stable phase is not excluded, especially in the presence of lighter elements (Lin et al., 2002). Estimates of the elastic properties of h.c.p. iron at high pressure and temperature (Steinle-Neumann et al., 2001) suggest that the basal plane of one third of the crystals would have to be aligned with Earth's spin axis to match travel time observations. It is therefore important to reconcile normal mode and body wave data in term of inner core anisotropy. It would help to shed new light on the phase diagram of iron at inner core conditions.

Discrepancies among existing seismological models of inner core anisotropy could be introduced by the regularisation that stabilizes the inverse problem. Regularization or damping is needed to force a solution in the presence of non-uniqueness, because of bad model sampling or contradictions in the data. It can, however, have a large effect on

the resulting model, and the solution can be largely dominated by subjective, unphysical *a priori* information. In addition, inversions do not provide realistic posterior model uncertainties, because of a complete trade-off between variance and resolution (Backus and Gilbert, 1970). To obtain all possible models of inner core anisotropy compatible with free oscillation data, we employed a forward modelling approach, the Neighbourhood Algorithm (Sambridge, 1999a,b), hereafter referred to as NA. With such a method, the entire model space is explored, no unnecessary regularisation is introduced, and the model parameter uncertainties and correlations can be obtained. Since normal mode data are not only sensitive to the core, but also to the overlying mantle, another possible source of uncertainty is the three-dimensional mantle model used to correct the measurements.

In the first part of this research, we studied the effects of the mantle correction and data quality on the inferred inner core structure, when normal mode data are inverted. The influence of the regularisation on the solution was also investigated. In the second part of the paper, we applied the NA to the latest measurements of anomalously split normal modes, in order to circumvent regularisation and to determine the robust constraints that normal mode data can put on inner core anisotropy. The whole ensemble of models was then tested against travel time data at various epicentral distances.

8.2 Parameterization

The inner core is generally modelled as a cylindrical medium with a symmetry axis parallel to Earth's rotation axis (Woodhouse et al., 1986; Morelli et al., 1986). Such a transverse isotropic medium produces normal mode splitting of isolated spheroidal mode multiplets of angular degree l of the form

$$\delta\omega_m = \omega(a + cm^2 + dm^4) \quad (8.1)$$

where coefficients a , c , d are related to structure coefficients c_{20} and c_{40} and to perturbation c_{00} of the degenerate eigenfrequency ω . m varies between $-l$ and $+l$. In the geometry considered, all expansion coefficients of the elastic tensor with azimuthal order $t \neq 0$ are zero (Tromp, 1995a). Non-zonal terms could be produced by a tilt of the symmetry axis relative to the spin axis, for instance.

A transversely isotropic medium is described by five independent elastic parameters. In the case where the symmetry axis is aligned along Earth's rotation axis, it can be demonstrated (Tromp, 1995a) that degree zero coefficients c_{00} are sensitive to perturbations in two elastic parameters, namely λ_1 and λ_2 . Degree two structure coefficients c_{20} are determined by two other elastic parameters, λ_3 and λ_4 , and c_{40} depends only on the fifth parameter λ_5 .

$$c_{00} = \int_0^b (\delta\lambda_1 K_1(r) + \delta\lambda_2 K_2(r)) dr \quad (8.2)$$

$$c_{20} = \int_0^b (\delta\lambda_3 K_3(r) + \delta\lambda_4 K_4(r)) dr \quad (8.3)$$

$$c_{40} = \int_0^b \delta\lambda_5 K_5(r) dr \quad (8.4)$$

Functions $K_i(r)$ ($i = 1, \dots, 5$) are the sensitivity kernels of a given mode to Earth's structure and b is the radius of the inner core. The five independent elastic parameters λ_i are different from the elastic parameters defined by Love (1927), but they are related by the following relations :

$$\lambda_1 = 6A + C - 4L - 10N + 8F \quad (8.5)$$

$$\lambda_2 = A + C + 6L + 5N - 2F \quad (8.6)$$

$$\lambda_3 = -6A + C - 4L + 14N + 5F \quad (8.7)$$

$$\lambda_4 = A + C + 3L - 7N - 2F \quad (8.8)$$

$$\lambda_5 = A + C - 4L - 2F \quad (8.9)$$

The anisotropic parameters employed for inner core anisotropy are usually defined by $\alpha = (C - A)/A_0$, $\beta = (L - N)/A_0$ and $\gamma = (A - 2N - F)/A_0$, with A_0 the value of $A = \kappa + 4\mu/3$ at the centre of the Earth. α , β and γ describe P-wave anisotropy, S-wave anisotropy and the anisotropy of waves that do not travel along the vertical or horizontal directions, respectively.

It is straightforward to show that λ_3 , λ_4 and λ_5 are functions of α , β and γ only. λ_1 and λ_2 do not share that property and are dependent on all five elastic coefficients A , C , N , L and F . Equations 8.3 and 8.4 can therefore be written as :

$$c_{20} = \int_0^a (\delta\alpha(r)K_\alpha(r) + \delta\beta(r)K_\beta(r) + \delta\gamma(r)K_\gamma(r)) dr \quad (8.10)$$

$$c_{40} = \int_0^a (\delta\alpha(r)K'_\alpha(r) + \delta\beta(r)K'_\beta(r) + \delta\gamma(r)K'_\gamma(r)) dr \quad (8.11)$$

The primed sensitivity kernels depend on $K_5(r)$ only and the unprimed kernels are functions of $K_1(r)$ and $K_2(r)$.

The three model parameters ($\alpha(r)$, $\beta(r)$ and $\gamma(r)$) were expanded on a series of five cubic spline functions with knots equally spaced through the inner core. The anisotropic models are found by inverting or solving the equations 8.10 and 8.11 for the spline coefficients.

8.3 Data

The data consisted of zonal degree two and degree four structure coefficients and their error estimates. No covariance was assumed between degree two and degree four data. Data errors were given by the authors of the measurements, and were assumed to be Gaussian distributed. Two data sets were tested : the first one consisted of older normal mode splitting measurements (Ritzwoller et al., 1988; Widmer et al., 1992) (with 15 degree two and 7 degree four structure coefficients), and the second one consisted of the most recent splitting measurements that followed the great Bolivia and Kuril Islands earthquakes in 1994 (Tromp and Zanzerkia, 1995; He and Tromp, 1996; Resovsky and Ritzwoller, 1998) (with 22 degree two and 16 degree four data). The choice of data set one was based on the modes employed by Tromp (1993) to derive his first model of inner core anisotropy. However, we decided to remove mode ${}_6S_3$, due to a possible overlapping with mode ${}_3S_8$, and ${}_{13}S_2$, since it has been demonstrated (Durek and Romanowicz, 1999) that different splitting functions could explain the spectrum of mode ${}_{13}S_2$ equally well. We also discarded the measurements made by Giardini et al. (1988) because their degree two splitting coefficients were systematically smaller than coefficients determined in other studies (Tromp and Zanzerkia, 1995; He and Tromp, 1996; Resovsky and Ritzwoller, 1998; Ritzwoller et al., 1988; Widmer et al., 1992). In the end, data set one was composed of degree two measurements for modes ${}_2S_3$, ${}_3S_2$, ${}_8S_5$, ${}_9S_3$, ${}_{11}S_4$, ${}_{11}S_5$, ${}_{13}S_3$, ${}_{15}S_3$, ${}_{16}S_6$, ${}_{18}S_4$, ${}_{20}S_5$, ${}_{21}S_6$, ${}_{23}S_5$, ${}_{25}S_2$ and ${}_{27}S_2$; degree four data were modes ${}_2S_3$, ${}_3S_2$, ${}_8S_5$, ${}_9S_3$, ${}_{11}S_4$, ${}_{11}S_5$ and ${}_{13}S_3$. Data set two was composed of degree two measurements for modes ${}_2S_3$, ${}_3S_2$, ${}_5S_3$, ${}_7S_4$, ${}_7S_5$, ${}_8S_1$, ${}_8S_5$, ${}_9S_3$, ${}_{11}S_4$, ${}_{11}S_5$, ${}_{13}S_1$, ${}_{13}S_3$, ${}_{16}S_5$, ${}_{16}S_7$, ${}_{17}S_1$, ${}_{18}S_3$, ${}_{18}S_4$, ${}_{21}S_6$, ${}_{21}S_7$, ${}_{21}S_8$, ${}_{23}S_5$ and ${}_{27}S_1$, and degree four measurements for modes ${}_2S_3$, ${}_3S_2$, ${}_5S_3$, ${}_7S_4$, ${}_7S_5$, ${}_8S_5$, ${}_9S_3$, ${}_{11}S_4$, ${}_{11}S_5$, ${}_{13}S_3$, ${}_{16}S_5$, ${}_{16}S_7$, ${}_{18}S_3$, ${}_{21}S_7$, ${}_{21}S_8$ and ${}_{23}S_4$. Original error bars for degree four data of mode ${}_2S_3$ were increased in data set two to account for discrepancies between the measurements. Modes ${}_3S_8$, ${}_6S_3$ and ${}_{13}S_2$ were discarded as in data set one together with ${}_3S_1$ which is also difficult to measure. All data were corrected with crustal model CRUST5.1 (Mooney et al., 1998).

8.4 Results

8.4.1 Inversions

In this section, inversions by singular value decomposition (Matsu'ura and Hirata, 1982) were performed in various cases. We used different levels of damping and the two sets of data described in the previous section. We also tested several mantle corrections (Resovsky and Ritzwoller, 1999a; Resovsky and Trampert, 2003; Beghein et al., 2002; Masters et al., 1996; Ritsema et al., 1999; Li and Romanowicz, 1996; Masters et al., 2000; Su et al., 1994) to assess their effect on the final model. In two recent studies (Beghein et al., 2002; Resovsky and Trampert, 2003), a model space search technique was employed to find families of mantle models that fit normal mode splitting measurements. These ensembles of mantle models were randomly sampled, according to their associated probability density functions, to correct the data. They gave rise to a family of inner core models, represented by the shaded grey areas in Fig. 8.1 (the limits correspond to two standard deviations). Six mantle models (Resovsky and Ritzwoller, 1999b; Masters et al., 1996; Ritsema et al., 1999; Li and Romanowicz, 1996; Masters et al., 2000; Su et al., 1994) resulting from the inversion of seismological data were also employed, yielding the models represented in colour.

For all data sets, we observed that the choice of the mantle model does not have a profound effect on the solution : it affects the amplitude of the anisotropy, but not the depth pattern. The regularisation, however, changes the models significantly. In general, a higher damping pushes the anisotropic signal into shallower parts of the inner core. We further observed that inversions of the older measurements produced models with the maximum of P-wave anisotropy situated at the top of the inner core, whereas including more recent data shifts this maximum to greater depths. All models obtained by damped inversions showed small amplitudes in the innermost inner core because of the nature of the sensitivity kernels. Therefore, they cannot predict the large travel time anomalies observed for waves travelling in a North-South direction (Su et al., 1995; Song, 1996; Sun and Song, 2002).

The models of inner core anisotropy resulting from those inversions fit the recent normal mode data set with a χ misfit between 3.5 and 5.5 (depending on the mantle model and the damping). For comparison the inner core model obtained by Tromp (1993) gives $\chi \simeq 5.6$ when data are corrected with SKS12WM13 (Su et al., 1994). Without inner core anisotropy the χ misfit varies between 9.1 and 10.9, depending on the mantle model. Without mantle correction and without inner core anisotropy $\chi \simeq 12.2$.

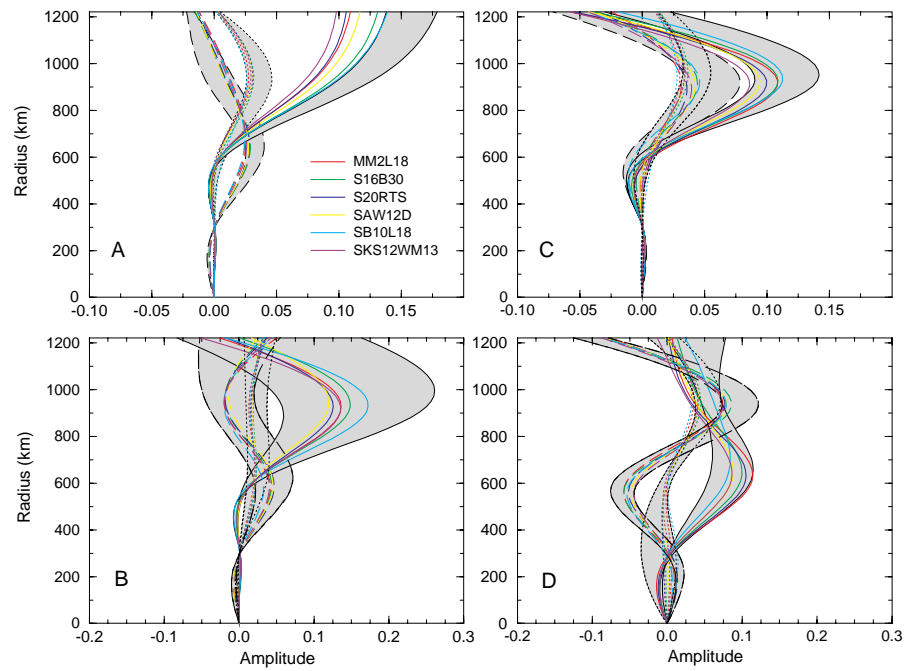


Figure 8.1: Models resulting from the inversion of older data are shown in panels (A) and (B), those resulting from the inversion of recent data are shown in panels (C) and (D). Two levels of damping were applied. The upper panels correspond to highly damped models, the lower panels are models for which the constraint of the damping was lower. The solid lines represent P-wave anisotropy, the dotted lines S-wave anisotropy and the dashed lines parameter γ . Different mantle models were used to correct the data, yielding the inner core models in colour and in the grey areas.

8.4.2 Model space search

The strong dependence of the obtained anisotropic model upon damping indicates the presence of a large model null-space (the part of the model space not constrained by the data). We therefore employed the NA (Sambridge, 1999a,b) to obtain all possible models of inner core anisotropy compatible with free oscillation data. In addition, the NA provides realistic posterior model parameter uncertainties and correlations. Because the free oscillations were best excited by the Bolivia and Kuril Islands earthquakes of 1994, we applied the NA to the most recent anomalous splitting measurements only.

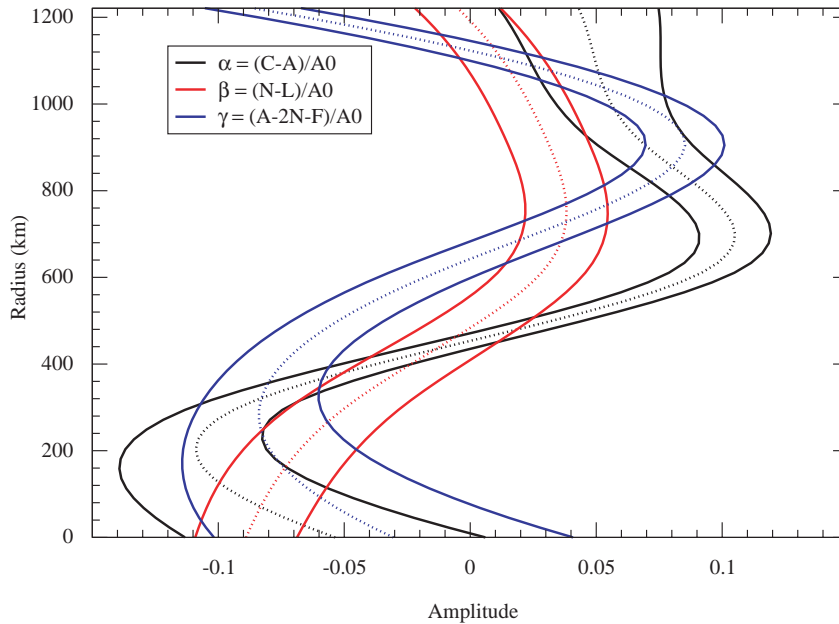


Figure 8.2: Models resulting from the application of the NA, using a mantle model from Resovsky and Trampert (2003). The thin dotted line represents the mean model and the thick surrounding lines correspond to two standard deviations taken from the posterior probability density functions obtained from the NA. A_0 is the value of elastic parameter A at the center of the Earth.

The resulting models of inner core anisotropy are shown in Fig. 8.2. We used differ-

ent mantle corrections : SB10L18 (Masters et al., 2000), SKS12WM13 (Su et al., 1994) and the most likely V_p , V_s and density mantle model derived with the NA (Resovsky and Trampert, 2003). Our results did not strongly depend on the mantle correction. Only for mantle model SKS12WM13 (Su et al., 1994) our analysis produced a significant proportion of inner core models with a negative P-wave anisotropy at the inner core boundary not supported by 150° travel time data. We only show the models obtained using the mantle model of Resovsky and Trampert (2003). It was not derived from an inversion (the solution is, therefore, not contaminated by any regularisation) and, in contrast with most mantle models, no scaling was assumed between density and velocity anomalies.

The results present several robust characteristics (Fig. 8.2). Firstly, for most models, α is positive in the upper half of the inner core (radius $r = 500 - 1200$ km), with amplitude increasing down to the middle of the inner core and becoming negative at greater depths. The fast direction for P-waves is thus along the rotational axis in the middle of the inner core, but becomes parallel to the equatorial plane at greater depths. Secondly, β is small and slightly positive in the upper two-thirds of the inner core and becomes negative in the lower 400 km of the core. Thus, shear waves sampling the innermost inner core are expected to move faster along the rotational axis than along the equatorial plane. Thirdly, γ is negative at the inner core boundary and undergoes two successive changes of sign around $r = 1100$ km and $r = 600$ km. All these features are robust and independent of the mantle correction. The most interesting finding is that many models show an anisotropic signal at large depths, as opposed to inversion results where the damping drives the innermost core anisotropy to zero. There are some features that are not as well constrained : α and γ have much larger error bars at the very bottom of the inner core and their sign is not robust. Their values at large depths are not independently constrained by our data, as can be seen on the correlation matrix (Fig. 8.3).

The models fit the data with a χ misfit slightly lower than 3, regardless of the mantle correction applied. In particular, the fit to the strongly split mode ${}_3S_2$ is remarkably very good, both at degree two and degree four (the observations are explained within data errors). Including complementary measurements of Widmer et al. (1992) didn't change our results. It is interesting to note that removing ${}_3S_2$ from the data does not change the results for α , but does increase the uncertainties on β and γ at a radius of 300 km. We also tested that the introduction of zonal degree two and four density perturbations in the parameterization did not alter the results. The correlation between the anisotropic parameters and the fit to the data did not change either.

We finally tested the compatibility of this family of inner core models with observed differential travel time anomalies. P-wave velocity anomalies associated with inner core anisotropy are given by (Morelli et al., 1986)

$$\frac{\delta v}{v_{eq}} = (2\beta - \gamma) \cos^2 \xi + \left(\frac{1}{2}\alpha - 2\beta + \gamma\right) \cos^4 \xi \quad (8.12)$$

where ξ is the angle between the ray and Earth's rotation axis and v_{eq} is the equatorial velocity. Random deviates were drawn from the marginal posterior probability density functions of each model parameter obtained from the NA to make predictions of travel

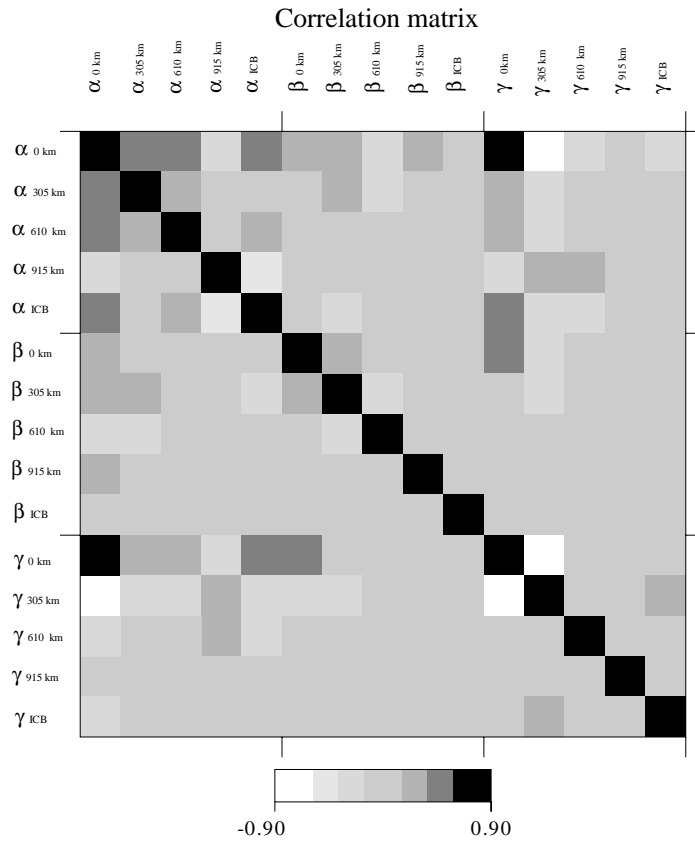


Figure 8.3: Correlation matrix corresponding to the family of models in Fig. 8.2. Indices correspond to the radius of the different spline knots. The off-diagonal elements in the matrix describe how the data link the different model parameters.

time anomalies. One hundred thousands models were randomly generated, and predictions of travel time anomalies were computed for all of them, with different ray angles. We thus had a distribution of predictions for each ray angle, and the width of these distributions, corresponding to 95% of the predictions, was used to plot the range of travel time predictions displayed in Fig. 8.4. Predictions were computed for waves travelling at about 153° epicentral distance, which sample the upper 290 km of the inner core, and for rays travelling at 170° epicentral distance, which turn at a radius of about 350 km. We also computed predictions in the epicentral range $168^\circ - 180^\circ$. All models produced, irrespective of the mantle correction, are compatible with the observed travel time anomalies of rays sampling the upper quarter of the core, and most of them predict anomalies between

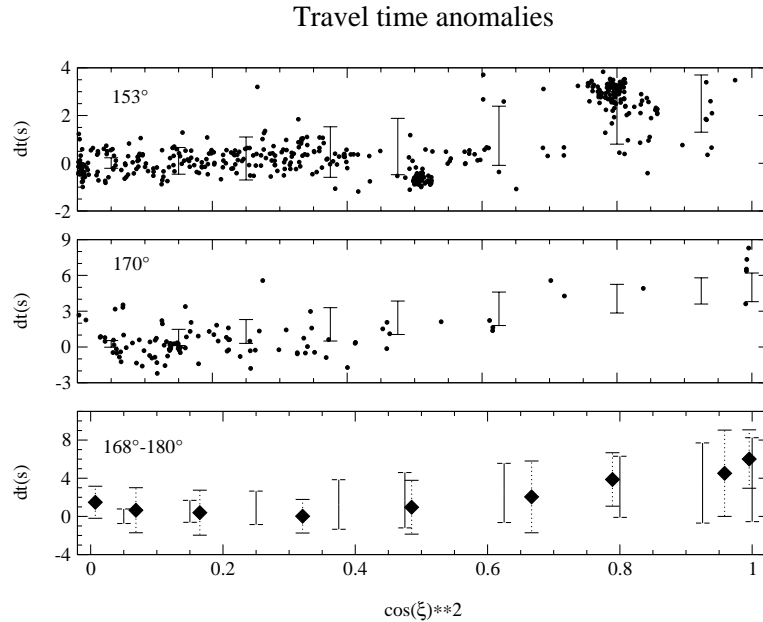


Figure 8.4: Predictions of differential travel time anomalies PKP(BC)-PKP(DF) at epicentral distances of 153° (A) and PKP(AB)-PKP(DF) at 170° (B) and in the range $168^\circ - 180^\circ$ (C). ξ is the angle between Earth's rotation axis and the direction of propagation of the wave. The dots in the upper and lower panels are data points for waves travelling in the epicentral distance range $147^\circ - 153^\circ$ and $167^\circ - 173^\circ$, respectively (Creager, 2000). The diamonds of the third panel are binned AB-DF data between 168° and 180° , with two standard deviations (Sun and Song, 2002). These estimations are based on random predictions from the family of models shown in 8.2. The solid vertical lines represent two standard deviations of our predictions.

four and six seconds for rays travelling in a N-S direction, which confirms the estimates made from mantle corrected travel time data (Sun and Song, 2002). Interestingly, tests including modes ${}_6S_3$ and ${}_{13}S_2$ in the NA produced models that highly degraded the fit to mode ${}_3S_2$ and to travel-time data at high epicentral distances. The splitting measurements for these two modes are, however, controversial: it was shown that the splitting function of mode ${}_{13}S_2$ is highly unstable (Durek and Romanowicz, 1999), and the same seems to apply to mode ${}_6S_3$. This suggests that modes ${}_{13}S_2$ and ${}_6S_3$ are incompatible with other mode data and with travel time data.

8.5 Conclusion

We established that discrepancies among existing seismological models of inner core anisotropy are mainly due to regularisation that stabilizes the inverse problem defined by Equations 8.10 and 8.11. Regularisation and data quality have a significant influence on the final model, whereas the chosen mantle model is less crucial. This high dependence of the results on the regularisation showed the presence of a large model null-space. Moreover, due to the nature of the sensitivity kernels at large depths, inversions of normal mode alone were not capable of reproducing the large travel-time anomalies observed for rays travelling in the N-S direction. The signal was damped towards zero at large depths. The use of a direct search method, however, gave us the possibility to circumvent these problems. The full model space search identified solutions previously unknown from damped inversions and produced models using normal mode data alone, which agree with the observed differential travel time anomalies of rays travelling through the inner core at epicentral distances varying between 150° and 180° . Our results, issued from the latest normal mode splitting measurements applied to the NA, are robust and independent of the mantle model used to correct the data. More detailed than a division between bulk and innermost inner core (Ishii and Dziewonski, 2002), a simple model of radially varying cylindrical anisotropy is sufficient to explain both splitting and travel time data. Also, the ability of our models to fit the high splitting of mode ${}_3S_2$ within data errors shows that outer core structure is not required to explain anomalously split normal modes (Romanowicz and Bréger, 2000).

A comparison with the latest determination of the elasticity of h.c.p. iron at inner core conditions (Steinle-Neumann et al., 2001) shows that some of our models can be explained by progressively tilted h.c.p. iron in the upper half of the inner core, with their symmetry axis oriented at 45° from Earth's rotation axis at radius $r = 900 \text{ km}$ and at 90° in the middle of the inner core. In the deepest inner core ($r = 0 - 400 \text{ km}$), none of our models is compatible with published data of h.c.p. iron. This might suggest the presence of another phase from these depths. Such a phase of iron could indeed be stable in the presence of impurities (Lin et al., 2002).

Summary and Conclusions

In this thesis, we investigated the necessity for seismic anisotropy in global tomographic models using a new technique to solve inverse problems. We adopted the Neighbourhood Algorithm (NA) developed by Sambridge (1999a,b), which is a model space mapping technique that characterizes the entire ensemble of models that fit a given data set. The whole model space can be surveyed, null-space included, and likelihoods can be assigned to each model parameter. Information on the trade-offs among the variables is also directly available. This technique provides more reliable uncertainty estimates than conventional inversions, especially in the presence of a large model null-space or in case of a strongly non-Gaussian likelihoods. The likelihoods can then be used to test different hypotheses (e.g. composition, correlation between variables, etc), and with independent data sets one can try to reduce the range of possible solutions. Although limited by the size of model space that can be surveyed within a reasonable time, the NA is well suited for normal mode problems or for investigating Earth's interior using surface wave phase velocity maps. This is due to the fact that these problems naturally separate into individual inverse problems for each spherical harmonic components of the structure.

After applying the NA to the large scale tomographic problem of obtaining degree two isotropic P and S models of the whole mantle (Chapter 3) we focused on the presence of radial anisotropy inside the Earth. Using the normalized likelihoods obtained with the NA, the probability of having a change in the anisotropic parameters with respect to PREM (Dziewonski and Anderson, 1981) was calculated for various cases, using the normalized likelihoods obtained with the NA. Chapter 4 deals with radial anisotropy in mantle reference models from a large data set of normal modes and surface waves, whereas Chapter 5 and Chapter 6 investigate the likelihood of lateral variations in radial anisotropy down to a 1200 km depth using phase velocity models derived from fundamental and overtone Love and Rayleigh wave measurements. In Chapter 4 we found that the current set of normal mode and surface wave data does not favour any significant deviation from PREM in reference model anisotropy, except for P-wave anisotropy between 220 and 400 km depth and perhaps for parameter η between 220 and 400 km depth and in the transition zone. The probability that the anisotropic parameters change sign across the 670-discontinuity, as observed earlier by Montagner and Kennett (1996), is small. If there are any deviation from PREM in anisotropy, other than the one found in Chapter 4, it cannot be resolved by the data currently available. In this one-dimensional study of the mantle we also found evidence for a deficit of density in the uppermost mantle and an excess of density in the transition zone and in the lowermost mantle, which may be the signature of slabs deflected between 400 and 670 km depth or accumulated atop the core-mantle boundary (see, for instance, van der Hilst and Kárason (1999) and Fukao et al. (2001)). The positive density anomaly above the core-mantle boundary could be associated with the compositionally distinct dense layer proposed by Kellogg et al. (1999).

An alternative explanation to the excess of density in the transition zone is the presence of phase transitions at these depths. Indeed, an increase of density implies that the Bullen parameter is larger than one, which can result from phase transitions of material more compressible than in homogeneous adiabatic conditions (Anderson, 1989). Lateral variations in radial anisotropy were also found in the upper 1200 km of the mantle (Chapters 5 and 6). Clear age-dependent signals were observed in the top 220 km for the various anisotropic parameters, both in oceanic and continental regions. Shear-wave anisotropy and parameter η are characterized by a faster decrease with depth beneath young oceans and young continental areas than beneath old oceans and cratons. Shear-wave anisotropy might extend slightly deeper than 220 km beneath cratons, but not elsewhere in continental areas. S-wave anisotropy with $V_{SH} > V_{SV}$ was also found in the transition zone beneath young oceans but not beneath older ones, which could indicate that ridges have some deep signature. Parameters η and ϕ both change sign at about 220 km depth, and our results suggest P-wave and η -anisotropy between 220 and 400 km depth beneath continents. In general, no particular relation between perturbations in ξ , ϕ or η is favoured by the data and in the uppermost 100 km, the ratio between $d\eta$ and $d\xi$ is clearly laterally variable, which cautions against the use of global ratios in tomographic inversions for radial anisotropy.

Our study of azimuthal anisotropy in Chapter 7 investigated the results from the Backus-Gilbert inversion method employed by Trampert and van Heijst (2002). We showed that it can find the most likely solution of an inverse problem, as found by the NA, even if the likelihood is wide. Finally, the study of inner core anisotropy in Chapter 8 showed that the NA can find solutions to an inverse problem that were previously unknown from conventional inverse methods and which can reconcile different types of data. We found a whole family of models of inner core anisotropy that fit the most recent normal mode measurements and which also predict the observed travel-time anomalies at all epicentral distances. The models obtained present a rather complicated depth pattern and a change of sign in the anisotropic parameters is observed at a radius of about 300-400 km. This could reflect a change of phase of iron at these depths and/or different stages in the history of formation of Earth's core.

The NA is thus a powerful tool to solve small size inverse problems. We obtained probability density functions for seismic anisotropy in different regions and at different depths inside the Earth, which yield better uncertainty estimates than traditional inversions. These probability density functions can be used to calculate probabilities for various anisotropic parameters and for the equivalent isotropic velocities. These probability density functions can now be employed in future research to test compositional models and to investigate how these models of anisotropy relate to mantle flow. The models of inner core anisotropy obtained will help understanding core formation and constraining its mineralogical composition. The limitation imposed by the size of the model space that can be surveyed with the NA could certainly be relaxed by parallelizing the code. It will then become possible to infer Earth's structure by applying the NA directly to normal mode or surface wave spectra rather than inverting "secondary" data such as phase

velocity models or normal mode structure coefficients.

Bibliography

- Anderson, D. L. (1961). Elastic wave propagation in layered anisotropic media. *J. Geophys. Res.*, 66:2,953–2,963.
- Anderson, D. L. (1989). *Theory of the Earth*. Blackwell, Boston.
- Anderson, O., E. Schreiber, R. C. L., and Soga, M. (1968). Upper mantle anisotropy: evidence from free oscillations. *Rev. Geophys.*, 6:491–524.
- Backus, G. E. and Gilbert, F. (1968). The resolving power of gross earth data. *Geophys. J. R. astr. Soc.*, 16:169–205.
- Backus, G. E. and Gilbert, F. (1970). Uniqueness in the inversion of inaccurate gross earth data. *Phil. Trans. R. Soc. London*, A266:123–192.
- Becker, T. W. and Boschi, L. (2002). A comparison of tomographic and geodynamic mantle models. *Geochem. Geophys. Geosyst.*, 3.
- Becker, T. W., Kellogg, J. B., Ekström, G., and O'Connell, R. J. (2003). Comparison of azimuthal seismic anisotropy from surface waves and finite-strain from global mantle-circulation models. *Geophys. J. Int.* in press.
- Beghein, C., Resovsky, J., and Trampert, J. (2002). P and S tomography using normal mode and surface wave data with a neighbourhood algorithm. *Geophys. J. Int.*, 149:646–658.
- Bevington, P. R. (1969). *Data Reduction and Error Analysis for the Physical Sciences*. McGraw-Hill Book Company, USA.
- Birch, F. (1964). Density and composition of mantle and core. *J. Geophys. Res.*, 69:4,377–4388.
- Bolton, H. (1996). *Long period travel times and the structure of the mantle*. PhD thesis, Univ. of Calif. San Diego.
- Cara, M., Necessian, A., and Nolet, G. (1980). New inferences from higher mode data in western Europe and northern Eurasia. *Geophys. J. R. astr. Soc.*, 61:459–478.
- Chen, G., Liebermann, R. C., and Weidner, D. J. (1998). Elasticity of single-crystal MgO to 8 Gigapascals and 1600 kelvin. *Science*, 280:1,913–1,915.
- Chen, W.-P. and Brudzinski, M. R. (2003). Seismic anisotropy in the mantle transition zone beneath Fiji-Tonga. *Geophys. Res. Lett.*, 30(13):1682, doi:10.1029/2002GL016330.
- Creager, K. C. (1999). Large-scale variations in inner core anisotropy. *J. Geophys. Res.*, 104(B10):127–139.
- Creager, K. C. (2000). Inner core anisotropy and rotation. In Karato, S., editor, *Earth's Deep Interior: Mineral Physics and Tomography From the Atomic to the Global Scale, Seismology and Mineral Physics, Geophys. Monogr. Ser.*, volume 117, pages 89–114. AGU, Washington, D.C.
- Dahlen, F. A. (1972). Elastic dislocation theory for a self-gravitating elastic configuration with an initial static stress field. *Geophys. J. R. astr. Soc.*, 28:357–383.
- Dahlen, F. A. (1973). Elastic dislocation theory for a self-gravitating elastic configuration with an initial static stress field II. Energy released. *Geophys. J. R. astr. Soc.*, 31:469–484.
- Dahlen, F. A. and Smith, M. L. (1975). The influence of rotation on the free oscillations of the Earth. *Phil. Trans. R. Soc. London*, A279:583–624.
- Dahlen, F. A. and Tromp, J. (1998). *Theoretical Global Seismology*. Princeton Univ. Press, Princeton, New Jersey.
- Deal, M., Nolet, G., and van der Hilst, R. D. (1999). Slab temperature and thickness from seismic tomography 1. Method and application to Tonga. *J. Geophys. Res.*, 104(12):28,789–28,802.

- Debayle, E. and Kennett, B. L. N. (2000). Anisotropy in the Australasian upper mantle from Love and Rayleigh waveform inversion. *Earth Planet. Sci. Lett.*, 184:339–351.
- Deuss, A. and Woodhouse, J. H. (2002). Systematic search for mantle discontinuities using SS-precursors. *Geophys. Res. Lett.*, 29(8):?–?
- Durek, J. J. and Romanowicz, B. (1999). Inner core anisotropy inferred by direct inversion of normal mode spectra. *Geophys. J. Int.*, 139:599–622.
- Dziewonski, A. M. and Anderson, D. L. (1981). Preliminary reference Earth model. *Phys. Earth Planet. Inter.*, 25:25,297–25,356.
- Eckhardt, D. H. (1984). Correlations between global features of terrestrial fields. *Math. Geol.*, 16:155–171.
- Edmonds, A. R. (1960). *Angular Momentum and Quantum mechanics*. Princeton Univ. Press, Princeton, New Jersey.
- Ekström, G. and Dziewonski, A. M. (1998). The unique anisotropy of the Pacific upper mantle. *Nature*, 394:168–172.
- Ekström, G., Tromp, J., and Larson, E. W. F. (1997). Measurements and global models of surface wave propagation. *J. Geophys. Res.*, 102:8,137–8,157.
- Forsyth, D. W. (1975). The early structural evolution and anisotropy of the oceanic upper mantle. *Geophys. J. R. astr. Soc.*, 43:103–162.
- Forte, A. M., Woodward, R. L., and Dziewonski, A. M. (1994). Joint inversions of seismic and geodynamic data for models of three-dimensional mantle heterogeneity. *J. Geophys. Res.*, 99(B11):21,857–21,877.
- Fouch, M. J. and Fischer, K. M. (1996). Mantle anisotropy beneath northwest Pacific subduction zones. *J. Geophys. Res.*, 101(B7):15,987–16,002.
- Fukao, Y., Widiyantoro, S., and Obayashi, M. (2001). Stagnant slabs in the upper and lower mantle transition zone. *Rev. Geophys.*, 39(3):291–323.
- Gaboret, C., Forte, A. M., and Montagner, J.-P. (2003). The unique dynamics of the Pacific Hemisphere mantle and its signature on seismic anisotropy. *Earth Planet. Sci. Lett.*, 208:219–233.
- Gessman, C. and Wood, B. J. (2002). Potassium in the Earth's core? *Earth Planet. Sci. Lett.*, 200:63–78.
- Giardini, D., Li, X.-D., and Woodhouse, J. H. (1988). Splitting functions of long-period normal modes of the Earth. *J. Geophys. Res.*, 93(B11):13,716–13,742.
- Gung, Y., Panning, M., and Romanowicz, B. (2003). Global anisotropic and the thickness of continents. *Nature*, 422.
- Hadiouche, O., Jobert, N., and Montagner, J.-P. (1989). Anisotropy of the African continent inferred from surface waves. *Phys. Earth Planet. Inter.*, 58:61–81.
- He, X. and Tromp, J. (1996). Normal-mode constraints on the structure of the Earth. *J. Geophys. Res.*, 101(B9):20,053–20,082.
- Hess, H. (1964). Seismic anisotropy of the uppermost mantle under the oceans. *Nature*, 203:629–631.
- Ishii, M. and Dziewonski, A. M. (2002). The innermost inner core of the earth: Evidence for a change in anisotropic behaviour at the radius of about 300 km. *Proc. Natl. Acad. Sci. USA*, 99:14026–14030.
- Ishii, M. and Tromp, J. (2001). Even-degree lateral variations in the Earth's mantle constrained by free oscillations and the free-air gravity anomaly. *Geophys. J. Int.*, 145:77–96.
- Jordan, T. H. (1978). A procedure for estimating lateral variations from low-frequency eigenspectra data. *Geophys. J. R. astr. Soc.*, 52:441–455.
- Jung, H. and Karato, S.-I. (2001). Water-induced fabric transitions in olivine. *Science*, 293:1460–1463.
- Karato, S.-I. (1989). Seismic anisotropy: mechanisms and tectonic implications. In Karato, S. and Toriumi, M., editors, *Rheology of solids and of the Earth*, pages 393–342. Oxford University Press, Oxford.
- Karato, S.-I. (1992). On the Lehmann discon-

- tinuity. *Geophys. Res. Lett.*, 19(22):2,255–2,258.
- Karato, S.-I. (1995). Superplasticity in Earth's lower mantle : evidence from seismic anisotropy and rock physics. *Science*, 270:458–461.
- Karato, S.-I. (1998). Seismic anisotropy in the deep mantle, boundary layers and the geometry of mantle convection. *Pure Appl. Geophys.*, 151:565–587.
- Karato, S.-I. and Karki, B. (2001). Origin of lateral variation of seismic wave velocities and density in the deep mantle. *J. Geophys. Res.*, 106(B10):21,771–21,783.
- Kellogg, L. H., Hager, B. H., and van der Hilst, R. D. (1999). Compositional stratification in the deep mantle. *Science*, 283:1881–1884.
- Kendall, J.-M. and Silver, P. G. (1996). Constraints from seismic anisotropy on the nature of the lowermost mantle. *Nature*, 381:409–412.
- Kennett, B. L., Widiyantoro, S., van der Hilst, R. D., Warren, W. C., Ackland, G. J., and Crain, J. (1998). Joint tomography for bulk sound and shear wave speed in the Earth's mantle. *J. Geophys. Res.*, 103(B6):12,469–12,493.
- Laske, G. and Masters, G. (1996). Constraints on global phase velocity maps from long-period polarization data. *J. Geophys. Res.*, 101:16,059–16,075.
- Lévêque, J.-J. and Cara, M. (1983). Long-period Love wave overtone data in North America and the Pacific Ocean : new evidence for upper mantle anisotropy. *Phys. Earth Planet. Inter.*, 33:164–179.
- Lévêque, J.-J., Debayle, E., and Maupin, V. (1998). Anisotropy in the Indian Ocean upper mantle from Rayleigh- and Love-waveform inversion. *Geophys. J. Int.*, 133:529–540.
- Levshin, A. and Ratnikova, L. (1984). Apparent anisotropy in inhomogeneous media. *Geophys. J. R. astr. Soc.*, 76:65–69.
- Li, X. D., Giardini, D., and Woodhouse, J. H. (1991). Large-scale three-dimensional even-degree structure of the Earth from splitting of long-period normal modes. *J. Geophys. Res.*, 96(B1):551–577.
- Li, X. D. and Romanowicz, B. (1996). Global mantle shear-velocity model developed using nonlinear asymptotic coupling theory. *J. Geophys. Res.*, 101:22,245–22,272.
- Lin, J. F., Heinz, D. L., Campbell, A. J., Devine, J. M., and Shen, G. (2002). Iron-silicon alloy in earth's core? *Science*, 295:313–315.
- Love, A. E. H. (1927). *A Treatise on the Theory of Elasticity*. Cambridge Univ. Press.
- Mainprice, D., Barruol, G., and Ismaïl, W. B. (2000). The seismic anisotropy of the Earth's mantle : from single crystal to polycrystal. In Karato, S., editor, *Earth's Deep Interior: Mineral Physics and Tomography From the Atomic to the Global Scale, Seismology and Mineral Physics, Geophys. Monogr. Ser.*, volume 117, pages 237–264. AGU, Washington, D.C.
- Malvern, L. E. (1969). *Introduction to the mechanics of a continuous medium*. Prentice-Hall, New Jersey.
- Mao, H. K., Xu, J., Struzhkin, V. V., Shu, J., Hemley, R. J., Sturhahn, W., Hu, M. Y., Alp, E. E., Vocadlo, L., Alfè, D., Price, G. D., Gillan, M. J., Schwöerer-Böhning, M., Häusermann, D., Eng, P., Shen, G., Giefers, H., Lübbers, R., and Wortmann, G. (2001). Phonon density of states of iron up to 153 Ggigapascals. *Science*, 292:914–916.
- Masters, G. and Gilbert, F. (1981). Structure of the inner core inferred from observations of its spheroidal shear modes. *Geophys. Res. Lett.*, 8(6):569–571.
- Masters, G., Johnson, S., Laske, G., and Bolton, H. (1996). A shear velocity model of the mantle. *Phil. Trans. R. Soc. London*, 354:1,385–1,411.
- Masters, G., Laske, G., Bolton, H., and Dziewonski, A. M. (2000). The relative behavior of shear velocity, bulk sound speed, and compressional velocity in the mantle: Implications for chemical and thermal structure. In Karato, S., editor, *Earth's Deep Interior: Mineral Physics and Tomography From*

- the Atomic to the Global Scale, Seismology and Mineral Physics, Geophys. Monogr. Ser.*, volume 117, pages 63–87. AGU, Washington, D.C.
- Matsu'ura, M. and Hirata, N. (1982). Generalized least-squares solutions to quasi-linear problems with *a priori* information. *J. Phys. Earth*, 30:451–468.
- McNamara, A. K., van Keken, P. E., and Karato, S.-I. (2002). Development of anisotropic structure in the Earth's lower mantle by solid-state convection. *Nature*, 416:310–314.
- Mochizuki, E. (1986). The free oscillations of an anisotropic and heterogeneous Earth. *Geophys. J. R. astr. Soc.*, 86:167–176.
- Montagner, J.-P. (1985). Seismic anisotropy of the Pacific Ocean inferred from long-period surface waves dispersion. *Phys. Earth Planet. Inter.*, 38:28–50.
- Montagner, J.-P. (1996). Surface waves on a global scale - Influence of anisotropy and anelasticity. In E. Boschi, G. E. and Morelli, A., editors, *Seismic modelling of Earth structure*, pages 81–148. Editrice Compositori, Bologna, Italy.
- Montagner, J.-P. (1998). Where can seismic anisotropy be detected in the Earth's mantle? In boundary layers... *Pure Appl. Geophys.*, 151:223–256.
- Montagner, J.-P. (2002). Upper mantle low anisotropy channels below the Pacific Plate. *Earth Planet. Sci. Lett.*, 202:263–274.
- Montagner, J.-P. and Anderson, D. L. (1989). Petrological constraints on seismic anisotropy. *Phys. Earth Planet. Inter.*, 54:82–105.
- Montagner, J.-P. and Kennett, B. L. N. (1996). How to reconcile body-wave and normal-mode reference Earth models. *Geophys. J. Int.*, 125:229–248.
- Montagner, J.-P. and Nataf, B. L. N. (1988). Vectorial tomography - I.Theory. *J. Geophys. Res.*, 94:295–307.
- Montagner, J.-P. and Nataf, H.-C. (1986). A simple method for inverting the azimuthal anisotropy of surface waves. *J. Geophys. Res.*, 91(B1):511–520.
- Montagner, J.-P. and Tanimoto, T. (1990). Global anisotropy in the upper mantle inferred from the regionalization of phase velocities. *J. Geophys. Res.*, 95(B4):4797–4819.
- Montagner, J.-P. and Tanimoto, T. (1991). Global upper mantle tomography of seismic velocities and anisotropies. *J. Geophys. Res.*, 96(B12):20,337–20,351.
- Mooney, W., Laske, G., and Masters, G. (1998). Crust 5.1 : a global crustal model at 5 deg × 5 deg. *J. Geophys. Res.*, 103(B1):727–747.
- Morelli, A., Dziewonski, A. M., and Woodhouse, J. H. (1986). Anisotropy of the inner core inferred from PKIKP travel times. *Geophys. Res. Lett.*, 13(13):1,545–1,548.
- Nataf, H.-C., Nakanishi, I., and Anderson, D. L. (1984). Anisotropy and shear-velocity heterogeneities in the upper mantle. *Geophys. Res. Lett.*, 11(2):109–112.
- Nataf, H.-C., Nakanishi, I., and Anderson, D. L. (1986). Measurements of mantle wave velocities and inversion for lateral heterogeneities and anisotropy 3. Inversion. *J. Geophys. Res.*, 91(B7):7,261–7,307.
- Nataf, H.-C. and Ricard, Y. (1996). 3SMAC : an a priori tomographic model of the upper mantle based on geophysical modeling. *Phys. Earth Planet. Inter.*, 95:101–122.
- Nishimura, C. E. and Forsyth, D. W. (1989). The anisotropic structure of the upper mantle in the pacific. *Geophysical Journal*, 96:203–229.
- Oganov, A. R., Brodholt, J. P., and Price, D. (2001a). Ab initio elasticity and thermal equation of state of *mgsio₃* perovskite. *Earth Planet. Sci. Lett.*, 184:555–560.
- Oganov, A. R., Brodholt, J. P., and Price, D. (2001b). The elastic constants of *mgsio₃* perovskite at pressures and temperatures of the Earth's mantle. *Nature*, 411:934–937.
- Ouzounis, A. and Creager, K. C. (2001). Isotropy overlying anisotropy at the top of the inner core. *Geophys. Res. Lett.*, 28:4,331–4,334.

- Phinney, R. A. and Burridge, R. (1973). Representation of the elastic-gravitational excitation of a spherical Earth model by generalized spherical harmonics. *Geophys. J. R. astr. Soc.*, 34:451–487.
- Poupinet, G. R., Pillet, R., and Souriau, A. (1983). Possible heterogeneity of the Earth's core deduced from PKIKP travel times. *Nature*, 305:204–206.
- Resovsky, J. S. and Ritzwoller, M. (1998). New and refined constraints on three-dimensional Earth structure from normal modes below 3 mHz. *J. Geophys. Res.*, 103(B1):783–810.
- Resovsky, J. S. and Ritzwoller, M. (1999a). A degree 8 mantle shear velocity model from normal mode observations below 3mHz. *J. Geophys. Res.*, 104(B1):993–1,014.
- Resovsky, J. S. and Ritzwoller, M. (1999b). A degree 8 mantle shear velocity model from normal mode observations below 3mHz. *J. Geophys. Res.*, 104(B1):993–1,014.
- Resovsky, J. S. and Ritzwoller, M. (1999c). Regularization uncertainty in density models estimated from normal mode data. *J. Geophys. Res.*, 26(15):2319–2322.
- Resovsky, J. S. and Trampert, J. (2002). Reliable mantle density error bars : An application of the Neighbourhood Algorithm to normal mode and surface wave data. *Geophys. J. Int.*, 150:665–672.
- Resovsky, J. S. and Trampert, J. (2003). Using probabilistic seismic tomography to test mantle velocity-density relationships. *Earth Planet. Sci. Lett.* in press.
- Ribe, N. (1987). Seismic anisotropy and mantle flow. *J. Geophys. Res.*, 94(B4):4,213–4,223.
- Ritsema, J., van Heijst, H.-J., and Woodhouse, J. H. (1999). Complex shear wave velocity structure imaged beneath africa and iceland. *Science*, 286:1,925–1,928.
- Ritzwoller, M. and Lavelly, E. M. (1995). Three-dimensional seismic models of the Earth's mantle. *Rev. Geophys.*, 33:1–66.
- Ritzwoller, M., Masters, G., and Gilbert, F. (1988). Constraining aspherical structure with low-degree interaction coefficients : application to uncoupled multiplets. *J. Geophys. Res.*, 93(B6):6,369–6,396.
- Robertson, G. and Woodhouse, J. H. (1996). Ratio of relative S to P velocity heterogeneity in the lower mantle. *J. Geophys. Res.*, 101(B9):20,041–20,052.
- Romanowicz, B. (2001). Can we resolve 3d heterogeneity in the lower mantle? *Geophys. Res. Lett.*, 28:1,107–1,110.
- Romanowicz, B. and Bréger, L. (2000). Anomalous splitting of core sensitive modes : a reevaluation of possible interpretations. *J. Geophys. Res.*, 105(B9):21,559–21,578.
- Romanowicz, B. and Snieder, R. (1988). A new formalism for the effect of lateral heterogeneity on normal modes and surface waves-ii : General anisotropic perturbation. *Geophysical Journal*, 93:91–99.
- Saltzer, R., van der Hilst, R. D., and Káráson, H. (2001). Comparing P and S wave heterogeneity in the mantle. *Geophys. Res. Lett.*, 28:1,335–1,338.
- Sambridge, M. (1998). Exploring multidimensional landscapes without a map. *Inverse Problems*, 14:427–440.
- Sambridge, M. (1999a). Geophysical inversion with a neighbourhood algorithm-I. Searching a parameter space. *Geophys. J. Int.*, 138:479–494.
- Sambridge, M. (1999b). Geophysical inversion with a neighbourhood algorithm-II. Appraising the ensemble. *Geophys. J. Int.*, 138:727–746.
- Savage, M. K. (1999). Seismic anisotropy and mantle deformation : what have we learned from shear wave splitting? *Rev. Geophys.*, 37:65–106.
- Silveira, G. and Stutzmann, E. (2002). Anisotropic tomographic of the Atlantic Ocean. *Phys. Earth Planet. Inter.*, 132:237–248.
- Silver, P. G. and Chan, W. W. (1991). Shear wave splitting and subcontinental mantle deformation. *J. Geophys. Res.*, 96:16,419–16,454.
- Simons, F. J., van der Hilst, R. D., Montagner,

- J.-P., and Zielhuis, A. (2002). Multimode Rayleigh wave inversion for heterogeneity and azimuthal anisotropy of the Australian upper mantle. *Geophys. J. Int.*, 151:738–754.
- Smith, M. L. and Dahlen, F. A. (1973). The azimuthal dependence of Love and Rayleigh wave propagation in a slightly anisotropic medium. *J. Geophys. Res.*, 73(17):3,321–3,332.
- Song, X. (1996). Anisotropy in central part of inner core. *J. Geophys. Res.*, 101:16,089–16,097.
- Song, X. and Helmberger, D. V. (1995). Depth dependence of anisotropy of Earth's inner core. *Geophys. Res. Lett.*, 20:2,591–2,594.
- Song, X. and Helmberger, D. V. (1998). Seismic evidence for an inner core transition zone. *Science*, 282:924–927.
- Steinle-Neumann, G., Stixrude, L., Cohen, R. E., and Gülseren, O. (2001). Elasticity of iron at temperature of the Earth's inner core. *Nature*, 413:57–60.
- Stixrude, L., Wasserman, E., and Cohen, R. E. (1997). Composition and temperature of Earth's inner core. *J. Geophys. Res.*, 102(B11):24,729–24,739.
- Su, W.-J. and Dziewonski, A. M. (1997). Simultaneous inversion for 3-D variations in shear and bulk velocity in the mantle. *Phys. Earth Planet. Inter.*, 100:135–156.
- Su, W.-J., Woodward, R. L., and Dziewonski, A. M. (1994). Degree 12 model of shear velocity heterogeneity in the mantle. *J. Geophys. Res.*, 99(B4):6,945–6,980.
- Su, W.-J., Woodward, R. L., and Dziewonski, A. M. (1995). Inner core anisotropy in three dimensions. *J. Geophys. Res.*, 100:9,831–9,852.
- Sun, X. and Song, X. (2002). PKP travel times at near antipodal distances : implications for inner core anisotropy and lowermost mantle structure. *Earth Planet. Sci. Lett.*, 199:429–445.
- Tanimoto, T. (1986). Free oscillations of a slightly anisotropic Earth. *Geophys. J. R. astr. Soc.*, 87:493–517.
- Tanimoto, T. and Anderson, D. L. (1984). Mapping convection in the mantle. *Geophys. Res. Lett.*, 11(4):287–290.
- Tanimoto, T. and Anderson, D. L. (1985). Lateral heterogeneity and azimuthal anisotropy in the upper mantle : Love and Rayleigh waves 100-250 s. *J. Geophys. Res.*, 90(B2):1,842–1,858.
- Tarantola, A. (1987). *Inverse Problem Theory, Methods for Data Fitting and Model Parameter Estimation*. Elsevier, Amsterdam.
- Tikonov, A. N. and Arsenin, V. (1977). *Solutions of ill-posed problems*. John Wiley, New York.
- Tommasi, A. (1998). Forward modeling of the development of seismic anisotropy in the upper mantle. *Earth Planet. Sci. Lett.*, 160:1–13.
- Trampert, J. (1998). Global seismic tomography : the inverse problem and beyond. *Inverse Problems*, 14:371–385.
- Trampert, J. and van Heijst, H. J. (2002). Global azimuthal anisotropy in the transition zone. *Science*, 296:1,297–1,299.
- Trampert, J. and Woodhouse, J. H. (1995). Global phase velocity maps of Love and Rayleigh waves between 40 and 150 seconds. *Geophys. J. Int.*, 122:675–690.
- Trampert, J. and Woodhouse, J. H. (1996). High resolution global phase velocity distributions. *Geophys. Res. Lett.*, 23:21–24.
- Trampert, J. and Woodhouse, J. H. (2001). Assessment of global phase velocity models. *Geophys. J. Int.*, 144:165–174.
- Trampert, J. and Woodhouse, J. H. (2003). Global anisotropic phase velocity maps for fundamental mode surface waves between 40 and 150 seconds. *Geophys. J. Int.*, 154:154–165.
- Tromp, J. (1993). Support for anisotropy of the Earth's inner core from free oscillations. *Nature*, 366:678–681.
- Tromp, J. (1995a). Normal mode splitting due to inner-core anisotropy. *Geophys. J. Int.*, 121:963–968.
- Tromp, J. (1995b). Normal-mode splitting ob-

- servations from the great 1994 Bolivia and Kuril Islands earthquakes : constraints on the structure of the mantle and inner core. *GSA Today*, 5(7):137–151.
- Tromp, J. and Zankerka, E. (1995). Toroidal splitting observations from the great 1994 Bolivia and Kuril earthquakes. *Geophys. Res. Lett.*, 22(16):2,297–2,300.
- van der Hilst, R. D. and Káráson, H. (1999). Compositional heterogeneity in the bottom 1000 kilometers of Earth's mantle : toward a hybrid convection model. *Science*, 283:1,885–1,887.
- van Heijst, H. J. and Woodhouse, J. H. (1999). Global high-resolution phase velocity distributions of overtone and fundamental-mode surface waves determined by mode branch-stripping. *Geophys. J. Int.*, 137:601–620.
- Vasco, D. W. and Johnson, L. R. (1998). Whole earth structure estimated from seismic arrival times. *J. Geophys. Res.*, 103(B2):2,633–2,671???
- Vinnik, L., Farra, F., and Romanowicz, B. (1989). Observational evidence for diffracted SV in the shadow of the Earth's core. *Geophys. Res. Lett.*, 16:519–522.
- Vinnik, L. P., Chevrot, S., and Montagner, J.-P. (1998). Seismic evidence of flow at the base of the upper mantle. *Geophys. Res. Lett.*, 25:1,995–1,998.
- Vinnik, L. P. and Montagner, J.-P. (1996). Shear wave splitting in the mantle p_s phases. *Geophys. Res. Lett.*, 23:2,449–2,452.
- Vinnik, L. P., Romanowicz, B., and Bréger, L. (1994). Anisotropy in the center of the inner core. *Geophys. Res. Lett.*, 21:1,671–1,674.
- Wentzcovitch, R., Karki, B., Karato, S.-I., and Silva, C. R. S. D. (1998). High pressure elastic anisotropy of $mgsio_3$ perovskite and geophysical implications. *Earth Planet. Sci. Lett.*, 164:371–378.
- Widmer, R., Masters, G., and Gilbert, F. (1992). Observably split multiplets-data analysis and interpretation in terms of large-scale aspherical structure. *Geophys. J. Int.*, 111:559–576.
- Wong, Y. K. (1989). *Upper mantle heterogeneity from phase and amplitude data of mantle waves*. PhD thesis, Harvard Univ.
- Woodhouse, J. H. (1996). Long period seismology and the Earth's free oscillations. In E. Boschi, G. E. and Morelli, A., editors, *Seismic modelling of Earth structure*, pages 31–80. Editrice Compositori, Bologna, Italy.
- Woodhouse, J. H. and Dahlen, F. A. (1978). The effect of a general aspherical perturbation on the free oscillations of the Earth. *Geophys. J. R. astr. Soc.*, 53:335–354.
- Woodhouse, J. H., Giardini, D., and Li, X.-D. (1986). Evidence for inner core anisotropy inferred from free oscillations. *Geophys. Res. Lett.*, 13(13):1549–1552.
- Woodhouse, J. H. and Girnius, T. P. (1986). Surface waves and free oscillations in a regionalized Earth model. *Geophys. J. R. astr. Soc.*, 68:653–673.
- Wookey, J., Kendall, J.-M., and Barruol, G. (2002). Mid-mantle deformation inferred from seismic anisotropy. *Nature*, 415:777–780.
- Zhang, Y.-S. and Tanimoto, T. (1991). Global Love wave phase velocity variation and its significance to plate tectonics. *Phys. Earth Planet. Inter.*, 66:160–202.

Appendix A

Strain tensor in generalized coordinates

Phinney and Burridge (1973) introduced a generalized coordinate system, very useful in normal mode theory. This orthogonal basis $(\hat{\mathbf{e}}_-, \hat{\mathbf{e}}_0, \hat{\mathbf{e}}_+)$ is related to the unit vectors $(\hat{\mathbf{e}}_r, \hat{\mathbf{e}}_\theta, \hat{\mathbf{e}}_\phi)$ pointing in the direction (r, θ, ϕ) by :

$$\hat{\mathbf{e}}_- = \frac{1}{\sqrt{2}}(\hat{\mathbf{e}}_\theta - i\hat{\mathbf{e}}_\phi) \quad (\text{A.1})$$

$$\hat{\mathbf{e}}_0 = \hat{\mathbf{e}}_r \quad (\text{A.2})$$

$$\hat{\mathbf{e}}_+ = -\frac{1}{\sqrt{2}}(\hat{\mathbf{e}}_\theta + i\hat{\mathbf{e}}_\phi) \quad (\text{A.3})$$

The corresponding metric is given by

$$g_{\alpha\beta} = 0 \quad \text{if } \alpha + \beta \neq 0 \quad (\text{A.4})$$

$$g_{+-} = g_{-+} = -1 \quad (\text{A.5})$$

$$g_{00} = 1 \quad (\text{A.6})$$

Any vector \mathbf{u} can be expanded into :

$$\mathbf{u} = \sum_{l=0}^{\infty} \sum_{m=-l}^l u_l^{\alpha m} Y_l^{\alpha m} \mathbf{e}_\alpha \quad (\text{A.7})$$

where $Y_l^{\alpha m}$ are generalized spherical harmonics (see Appendix B) and \mathbf{e}_α stands for $\hat{\mathbf{e}}_-, \hat{\mathbf{e}}_0$ and $\hat{\mathbf{e}}_+$, the sum over α being implicit. Similarly, the strain tensor is given by :

$$\mathbf{E} = \sum_{l=0}^{\infty} \sum_{m=-l}^l \mathbf{E}_l^{\alpha\beta m} Y_l^{(\alpha+\beta)m} \mathbf{e}_\alpha \mathbf{e}_\beta \quad (\text{A.8})$$

Its components in the new basis are related to its components in the old basis through :

$$E_{kl} = R_{k\gamma'} R_{l\delta'} (E^{\gamma'\delta'}) \quad (\text{A.9})$$

$$E_{ij}^* = R_{i\alpha'}^* R_{j\beta'}^* (E^{\alpha'\beta'})^* \quad (\text{A.10})$$

with

$$R_{i\alpha} R_{i\alpha'}^* = \delta_{\alpha\alpha'} \quad (\text{A.11})$$

$$R_{i\alpha} R_{i\alpha'} = g_{\alpha\alpha'} \quad (\text{A.12})$$

The * sign stands for the complex conjugate. For the elastic tensor, we have :

$$\delta C_{ijkl} = R_{i\alpha} R_{j\beta} R_{k\gamma} R_{l\delta} \delta C^{\alpha\beta\gamma\delta} \quad (\text{A.13})$$

If we write $E_{lm}^{\alpha\beta}(r) = \gamma_l \epsilon_{lm}^{\alpha\beta}(r)$ with $\gamma_l = \sqrt{(2l+1)/4\pi}$, it can be shown (Phinney and Burridge, 1973; Tanimoto, 1986) that :

$$\epsilon_{lm}^{00}(r) = \dot{U}(r) \quad (\text{A.14})$$

$$\epsilon_{lm}^{++}(r) = \frac{1}{r} \Omega_l^0 \Omega_l^2 (V(r) + iW(r)) \quad (\text{A.15})$$

$$\epsilon_{lm}^{--}(r) = \frac{1}{r} \Omega_l^0 \Omega_l^2 (V(r) - iW(r)) \quad (\text{A.16})$$

$$\epsilon_{lm}^{+-}(r) = \epsilon_{lm}^{-+}(r) = \frac{1}{2} F(r) \quad (\text{A.17})$$

$$\epsilon_{lm}^{0+}(r) = \frac{1}{2} \Omega_l^0 (X(r) + iZ(r)) \quad (\text{A.18})$$

$$\epsilon_{lm}^{0-}(r) = \frac{1}{2} \Omega_l^0 (X(r) - iZ(r)) \quad (\text{A.19})$$

with $\Omega_l^n = \sqrt{\frac{(l+n)(l-n+1)}{2}}$ and $U(r)$, $V(r)$ and $W(r)$ are the radial eigenfunctions of a given mode (see equations 2.17 and 2.18).

Appendix B

Generalized spherical harmonics

The generalized scalar spherical harmonics (Phinney and Burridge, 1973) are defined by :

$$Y_l^{Nm}(\theta, \phi) = P_l^{Nm}(\cos \theta)e^{im\phi} \quad (\text{B.1})$$

with the associated Legendre function

$$\begin{aligned} P_l^{Nm}(x) &= \frac{(-1)^{l-N}}{2^l(l-N)!} \sqrt{\frac{(l-N)!(l+m)!}{(l+N)!(l-m)!}} \\ &\times (1-x)^{-(m-N)/2}(1+x)^{-(m+N)/2} \\ &\times \frac{d^{l-m}}{dx^{l-m}} [(1-x)^{l-N}(1+x)^{l+N}] \end{aligned} \quad (\text{B.2})$$

They are normalised :

$$\int \int Y_l^{Nm}(\theta, \phi) Y_{l'}^{Nm'}(\theta, \phi) d\Omega = \frac{4\pi}{2l+1} \delta_{ll'} \delta_{mm'} \quad (\text{B.3})$$

In the particular case $N = 0$ we have :

$$Y_l^{0m}(\theta, \phi) = \sqrt{\frac{4\pi}{2l+1}} Y_l^m(\theta, \phi) \quad (\text{B.4})$$

with

$$Y_l^m(\theta, \phi) = P_l^m(\cos \theta)e^{im\phi} \quad (\text{B.5})$$

The components of any tensor can be decomposed on a generalized scalar spherical harmonic basis :

$$\Lambda^{\alpha, \beta, \gamma, \dots}(r, \theta, \phi) = \sum_{s=|N|}^{\infty} \sum_{t=-s}^s \Lambda_{st}^{\alpha, \beta, \gamma, \dots}(r) Y_s^{Nt}(\theta, \phi) \quad (\text{B.6})$$

with $N = \alpha + \beta + \gamma + \dots$

Appendix C

Wigner 3-j symbols

The Wigner 3-j symbols (Edmonds, 1960) have the following properties ;

$$\begin{pmatrix} l_1 & l_2 & l_3 \\ m_1 & m_2 & m_3 \end{pmatrix} = \begin{pmatrix} l_2 & l_3 & l_1 \\ m_2 & m_3 & m_1 \end{pmatrix} = \begin{pmatrix} l_3 & l_1 & l_2 \\ m_3 & m_1 & m_2 \end{pmatrix} \quad (\text{C.1})$$

$$\begin{pmatrix} l_1 & l_2 & l_3 \\ m_1 & m_2 & m_3 \end{pmatrix} = (-1)^{l_1+l_2+l_3} \begin{pmatrix} l_2 & l_1 & l_3 \\ m_2 & m_1 & m_3 \end{pmatrix} \quad (\text{C.2})$$

$$= (-1)^{l_1+l_2+l_3} \begin{pmatrix} l_1 & l_2 & l_3 \\ -m_1 & -m_2 & -m_3 \end{pmatrix} \quad (\text{C.3})$$

$$\begin{pmatrix} l_1 & l_2 & l_3 \\ 0 & 0 & 0 \end{pmatrix} \neq 0 \quad \text{if } l_1 + l_2 + l_3 \text{ is even} \quad (\text{C.4})$$

And $\begin{pmatrix} l_1 & l_2 & l_3 \\ -m_1 & m_2 & m_3 \end{pmatrix} \neq 0$ if $l_i \geq |m_i|$, $|l_1 - l_2| \leq l_3 \leq l_1 + l_2$ and $m_1 = m_2 + m_3$.

They are also related to one another by the following recursion relations (Dahlen and Tromp, 1998) :

$$\begin{aligned} & - \sqrt{(l_1 - m_1)(l_1 + m_1 + 1)} \begin{pmatrix} l_1 & l_2 & l_3 \\ -m_1 - 1 & m_2 & m_3 \end{pmatrix} \\ & = \sqrt{(l_2 + m_2)(l_2 - m_2 + 1)} \begin{pmatrix} l_1 & l_2 & l_3 \\ -m_1 & m_2 - 1 & m_3 \end{pmatrix} \\ & + \sqrt{(l_3 + m_3)(l_3 - m_3 + 1)} \begin{pmatrix} l_1 & l_2 & l_3 \\ -m_1 & m_2 & m_3 - 1 \end{pmatrix} \end{aligned} \quad (\text{C.5})$$

$$\begin{aligned}
& - \sqrt{(l_1 + m_1)(l_1 - m_1 + 1)} \begin{pmatrix} l_1 & l_2 & l_3 \\ -m_1 + 1 & m_2 & m_3 \end{pmatrix} \\
& = \sqrt{(l_2 - m_2)(l_2 + m_2 + 1)} \begin{pmatrix} l_1 & l_2 & l_3 \\ -m_1 & m_2 + 1 & m_3 \end{pmatrix} \\
& + \sqrt{(l_3 - m_3)(l_3 + m_3 + 1)} \begin{pmatrix} l_1 & l_2 & l_3 \\ -m_1 & m_2 & m_3 + 1 \end{pmatrix} \tag{C.6}
\end{aligned}$$

Using these recursion relations, we can show the following :

$$\begin{aligned}
\begin{pmatrix} l_1 & l_2 & l_3 \\ -1 & -1 & 2 \end{pmatrix} & = -\sqrt{\frac{(l_1 - 1)(l_1 + 2)}{l_2(l_2 + 1)}} \begin{pmatrix} l_1 & l_2 & l_3 \\ -2 & 0 & 2 \end{pmatrix} \\
& - \sqrt{\frac{(l_3 - 1)(l_3 + 2)}{l_2(l_2 + 1)}} \begin{pmatrix} l_1 & l_2 & l_3 \\ -1 & 0 & 1 \end{pmatrix} \tag{C.7}
\end{aligned}$$

$$\begin{aligned}
\begin{pmatrix} l_1 & l_2 & l_3 \\ -2 & 3 & -1 \end{pmatrix} & = -\sqrt{\frac{(l_1 - 1)(l_1 + 2)}{(l_2 - 2)(l_2 + 3)}} \begin{pmatrix} l_1 & l_2 & l_3 \\ -1 & 2 & -1 \end{pmatrix} \\
& - \sqrt{\frac{l_3(l_3 + 1)}{l_2(l_2 + 1)}} \begin{pmatrix} l_1 & l_2 & l_3 \\ -2 & 2 & 0 \end{pmatrix} \tag{C.8}
\end{aligned}$$

$$\begin{aligned}
\begin{pmatrix} l_1 & l_2 & l_3 \\ -2 & 4 & -2 \end{pmatrix} & = -\sqrt{\frac{(l_1 - 1)(l_1 + 2)}{(l_2 + 4)(l_2 - 3)}} \begin{pmatrix} l_1 & l_2 & l_3 \\ -1 & 3 & -2 \end{pmatrix} \\
& - \sqrt{\frac{(l_3 + 2)(l_3 - 1)}{(l_2 + 4)(l_2 - 3)}} \begin{pmatrix} l_1 & l_2 & l_3 \\ -2 & 3 & -1 \end{pmatrix} \tag{C.9}
\end{aligned}$$

Appendix D

Wigner 3-j symbols : recursion relations for even $l + l' + s$

In this appendix, we treat the case where $l + l' + s$ takes even values. Let us write

$$L = l(l+1) \quad (\text{D.1})$$

$$L' = l'(l'+1) \quad (\text{D.2})$$

$$S = s(s+1) \quad (\text{D.3})$$

$$\alpha(l', s, l) = -\frac{1}{2} \frac{L' + L - S}{\sqrt{LL'}} \quad (\text{D.4})$$

$$\beta(l', s, l) = \frac{(L' + L - S)(L' + L - S - 2) - 2LL'}{2\sqrt{L'(L' - 2)L(L - 2)}} \quad (\text{D.5})$$

$$(\text{D.6})$$

It is easy to see that $\alpha(l', s, l)$ and $\beta(l', s, l)$ are symmetric with respect to permutations between l and l' ($\alpha(l', s, l) = \alpha(l, s, l')$ and $\beta(l', s, l) = \beta(l, s, l')$). We can derive the following identities, using the properties of the 3-j symbols listed in appendix C :

$$\begin{pmatrix} l' & s & l \\ -1 & 0 & 1 \end{pmatrix} = \alpha(l', s, l) \begin{pmatrix} l' & s & l \\ 0 & 0 & 0 \end{pmatrix} \quad (\text{D.7})$$

$$\begin{pmatrix} l' & s & l \\ -2 & 0 & 2 \end{pmatrix} = \beta(l', s, l) \begin{pmatrix} l' & s & l \\ 0 & 0 & 0 \end{pmatrix} \quad (\text{D.8})$$

$$\begin{pmatrix} l' & s & l \\ -1 & 1 & 0 \end{pmatrix} = \begin{pmatrix} l' & s & l \\ 1 & -1 & 0 \end{pmatrix} = \alpha(l', l, s) \begin{pmatrix} l' & s & l \\ 0 & 0 & 0 \end{pmatrix} \quad (\text{D.9})$$

$$\begin{pmatrix} l' & s & l \\ 0 & 1 & -1 \end{pmatrix} = \begin{pmatrix} l' & s & l \\ 0 & -1 & 1 \end{pmatrix} = \alpha(l, l', s) \begin{pmatrix} l' & s & l \\ 0 & 0 & 0 \end{pmatrix} \quad (\text{D.10})$$

$$\begin{pmatrix} l' & s & l \\ -2 & 2 & 0 \end{pmatrix} = \begin{pmatrix} l' & s & l \\ 2 & -2 & 0 \end{pmatrix} = \beta(l', l, s) \begin{pmatrix} l' & s & l \\ 0 & 0 & 0 \end{pmatrix} \quad (\text{D.11})$$

$$\begin{pmatrix} l' & s & l \\ 0 & 2 & -2 \end{pmatrix} = \begin{pmatrix} l & s & l' \\ -2 & 2 & 0 \end{pmatrix} = \beta(l, l', s) \begin{pmatrix} l' & s & l \\ 0 & 0 & 0 \end{pmatrix} \quad (\text{D.12})$$

Let us now define the following functions :

$$\Gamma(l) = \sqrt{(l+2)(l-1)} \quad (\text{D.13})$$

$$\delta(l) = \frac{1}{\sqrt{(l-2)(l+3)}} \quad (\text{D.14})$$

$$\lambda(l) = \frac{1}{\sqrt{(l-3)(l+4)}} \quad (\text{D.15})$$

Using the recursion relations C.7 to C.9, we can show the following :

$$\begin{aligned} \begin{pmatrix} l' & s & l \\ -2 & 1 & 1 \end{pmatrix} &= \begin{pmatrix} l' & s & l \\ 2 & -1 & -1 \end{pmatrix} \\ &= -\frac{\Gamma(l')}{\sqrt{S}} \begin{pmatrix} l & s & l' \\ -1 & 0 & 1 \end{pmatrix} - \frac{\Gamma(l)}{\sqrt{S}} \begin{pmatrix} l & s & l' \\ -2 & 0 & 2 \end{pmatrix} \quad (\text{D.16}) \\ &= -\frac{[\Gamma(l')\alpha(l, s, l') + \Gamma(l)\beta(l, s, l')]}{\sqrt{S}} \begin{pmatrix} l' & s & l \\ 0 & 0 & 0 \end{pmatrix} \end{aligned}$$

$$= -\frac{[\Gamma(l')\alpha(l', s, l) + \Gamma(l)\beta(l', s, l)]}{\sqrt{S}} \begin{pmatrix} l' & s & l \\ 0 & 0 & 0 \end{pmatrix} \quad (\text{D.17})$$

$$\begin{aligned} \begin{pmatrix} l' & s & l \\ -1 & 2 & -1 \end{pmatrix} &= \begin{pmatrix} s & l' & l \\ -2 & 1 & 1 \end{pmatrix} = \begin{pmatrix} s & l' & l \\ 2 & -1 & -1 \end{pmatrix} \\ &= -\frac{[\Gamma(s)\alpha(s, l', l) + \Gamma(l)\beta(s, l', l)]}{\sqrt{L'}} \begin{pmatrix} l' & s & l \\ 0 & 0 & 0 \end{pmatrix} \quad (\text{D.18}) \end{aligned}$$

$$\begin{aligned} \begin{pmatrix} l' & s & l \\ 1 & 1 & -2 \end{pmatrix} &= \begin{pmatrix} l & s & l' \\ -2 & 1 & 1 \end{pmatrix} \\ &= -\frac{[\Gamma(l)\alpha(l', s, l) + \Gamma(l')\beta(l', s, l)]}{\sqrt{S}} \begin{pmatrix} l' & s & l \\ 0 & 0 & 0 \end{pmatrix} \quad (\text{D.19}) \end{aligned}$$

Similarly, it is easy to show that

$$\begin{aligned} \begin{pmatrix} l' & s & l \\ -2 & 3 & -1 \end{pmatrix} &= \begin{pmatrix} l' & s & l \\ 2 & -3 & 1 \end{pmatrix} = -\delta(s)\Gamma(s) \begin{pmatrix} l' & s & l \\ -1 & 2 & -1 \end{pmatrix} \\ &\quad - \delta(s)\sqrt{L} \begin{pmatrix} l' & s & l \\ -2 & 2 & 0 \end{pmatrix} \quad (\text{D.20}) \end{aligned}$$

and

$$\begin{aligned} \begin{pmatrix} l' & s & l \\ -2 & 4 & -2 \end{pmatrix} &= \begin{pmatrix} l' & s & l \\ 2 & -4 & 2 \end{pmatrix} = -\lambda(s)\Gamma(l') \begin{pmatrix} l' & s & l \\ -1 & 3 & -2 \end{pmatrix} \\ &\quad - \lambda(s)\Gamma(l) \begin{pmatrix} l' & s & l \\ -2 & 3 & -1 \end{pmatrix} \end{aligned} \quad (\text{D.21})$$

In the particular case of an isolated multiplet, $l = l'$ and s is even. The following relations can easily be deduced :

$$\begin{pmatrix} l & s & l \\ -1 & 0 & 1 \end{pmatrix} = - \left[1 - \frac{s(s+1)}{2l(l+1)} \right] \begin{pmatrix} l & s & l \\ 0 & 0 & 0 \end{pmatrix} \quad (\text{D.22})$$

$$\begin{aligned} \begin{pmatrix} l & s & l \\ -2 & 0 & 2 \end{pmatrix} &= \frac{1}{2(l+2)(l+1)l(l-1)} [2l^2(l+1)^2 - 4l(l+1) \\ &\quad - 4l(l+1)s(s+1) + s^2(s+1)^2 + 2s(s+1)] \\ &\quad \times \begin{pmatrix} l & s & l \\ 0 & 0 & 0 \end{pmatrix} \end{aligned} \quad (\text{D.23})$$

$$\begin{pmatrix} l & s & l \\ -1 & 1 & 0 \end{pmatrix} = -\frac{1}{2} \sqrt{\frac{s(s+1)}{l(l+1)}} \begin{pmatrix} l & s & l \\ 0 & 0 & 0 \end{pmatrix} \quad (\text{D.24})$$

$$\begin{pmatrix} l & s & l \\ -2 & 1 & 1 \end{pmatrix} = \sqrt{\frac{s(s+1)}{(l+2)(l-1)}} \frac{3l(l+1) - s(s+1)}{2l(l-1)} \begin{pmatrix} l & s & l \\ 0 & 0 & 0 \end{pmatrix} \quad (\text{D.25})$$

$$\begin{pmatrix} l & s & l \\ -1 & 2 & -1 \end{pmatrix} = \sqrt{\frac{s(s+1)}{(s+2)(s-1)}} \begin{pmatrix} l & s & l \\ 0 & 0 & 0 \end{pmatrix} \quad (\text{D.26})$$

$$\begin{aligned} \begin{pmatrix} l & s & l \\ -2 & 2 & 0 \end{pmatrix} &= \frac{1}{2} \sqrt{\frac{s(s+1)}{(s+2)(s-1)(l+2)(l+1)l(l-1)}} \\ &\quad \times [(s+2)(s-1) - 2l(l+1)] \begin{pmatrix} l & s & l \\ 0 & 0 & 0 \end{pmatrix} \end{aligned} \quad (\text{D.27})$$

$$\begin{pmatrix} l & s & l \\ -2 & 3 & -1 \end{pmatrix} = -\frac{1}{2} \sqrt{\frac{(s+3)(s-2)s(s+1)}{(l+2)(l-1)(s+2)(s-1)}} \begin{pmatrix} l & s & l \\ 0 & 0 & 0 \end{pmatrix} \quad (\text{D.28})$$

$$\begin{pmatrix} l & s & l \\ -2 & 4 & -2 \end{pmatrix} = \sqrt{\frac{(s+3)(s-2)s(s+1)}{(s+4)(s-3)(s+2)(s-1)}} \begin{pmatrix} l & s & l \\ 0 & 0 & 0 \end{pmatrix} \quad (\text{D.29})$$

Samenvatting (Summary in Dutch)

In dit proefschrift werd de noodzaak voor seismische anisotropie in globale tomografische modellen onderzocht door middel van een nieuwe inversie techniek. Wij gebruikten het door Sambridge (1999a,b) ontwikkelde Neighbourhood Algorithm (NA). Dit is een zoekalgoritme in de model ruimte dat de modellen karakteriseert die bij een data set passen. De gehele model ruimte, inclusief de model nulruimte, kan doorzocht worden, en waarschijnlijkheden van elke model parameter kunnen berekend worden. Informatie over de trade-offs tussen variabelen is ook per direkt beschikbaar. Dergelijke technieken geven betere schattingen van de onzekerheden dan inversies, vooral in aanwezigheid van een grote model nulruimte, of in het geval van een sterke niet-Gaussische waarschijnlijkheid. De waarschijnlijkheden kunnen gebruikt worden om verschillende hypothesen (bijv. compositie, correlatie tussen variabelen, enz) te testen, en met onafhankelijke data sets kan men proberen het bereik van mogelijke oplossingen te verminderen. Hoewel de grootte van de model ruimte die binnen een redelijke tijd onderzocht kan worden begrensd is, is het NA geschikt voor eigentrillingen problemen en voor het onderzoeken van de aarde met behulp van fase snelheid kaarten. De reden hiervoor is dat deze problemen gescheiden kunnen worden in individuele inversie problemen voor elke sferisch harmonische component van de structuur.

Na een eerste applicatie van het NA aan een tomografisch probleem van graad twee isotropische P en S modellen van de gehele mantel (Hoofdstuk 3), concentreerden wij ons op de aanwezigheid van radiale anisotropie in de aarde. De waarschijnlijkheid van een verandering in de anisotrope parameters met betrekking tot PREM (Dziewonski and Anderson, 1981) werd in verschillende gevallen, met de genormaliseerde waarschijnlijkheden van het NA, uitgerekend. Hoofdstuk 4 behandelt radiale anisotropie in referentie modellen van de mantel met een groot data set van eigentrillingen en oppervlaktegolven. Hoofdstuk 5 en Hoofdstuk 6 onderzoeken de waarschijnlijkheid van laterale variaties in radiale anisotropie tot een diepte van 1200 km met gebruik van snelheids modellen die afgeleid zijn van metingen van fundamentele en boventonen van Love en Rayleigh golven.

Het actuele set van eigentrillingen en oppervlaktegolven geeft geen betekenisvolle afwijking van PREM in referentie model anisotropie, behalve voor de anisotropie van P-golven tussen een diepte van 220 en 400 km, en misschien voor parameter η tussen een diepte van 220 en 400 km en in de transitie zone. De teken verandering voor de anisotrope parameters bij de 670 km discontinuïteit, die eerder door Montagner and Kennett (1996) gevonden werd, wordt niet met een grote waarschijnlijkheid door onze data gesteund. Als er andere afwijkingen van PREM voor de anisotropie zijn, kunnen deze niet door de data die tegenwoordig beschikbaar is opgeslot worden. Naast onze één-

dimensionale studie van de anisotropie, hebben wij een bewijs gevonden voor een tekort aan dichtheid in het bovenste deel van de mantel en een overschot aan dichtheid in de transitie zone en het onderste deel van de mantel. Dit laatste kan verklaard worden door een laag met hoge dichtheid die verschilt in compositie met de rest van de mantel, zoals voorgesteld door Kellogg et al. (1999). Laterale variaties van radiale anisotropie werden ook gevonden in de bovenste 220 km van de mantel. Duidelijke leeftijdsafhankelijke signalen werden in de bovenste 220 km geobserveerd voor de verschillende anisotropie parameters, zoals in de oceanische en in de continentale gebieden. S-golf anisotropie en de parameter η worden gekarakteriseerd door een snellere afname met de diepte onder jonge oceanen en jonge continentale gebieden dan onder oude oceanen en cratons. S-golf anisotropie kan iets dieper zijn dan 220 km onder cratons, maar niet in ander continentaal gebieden. Anisotropie van S-golven met $V_{SH} > V_{SV}$ werd ook in de transitie zone, onder jonge oceanen en niet onder oude oceanen, gevonden. Dit zou een indicatie kunnen zijn voor diepe kenmerken van oceanische ruggen. Zowel parameter η als parameter ϕ hebben een tekenverandering op een diepte van ongeveer 220 km. Onze resultaten suggeren anisotropie voor P-golven en voor η tussen diepten van 220 en 400 km onder continenten. In het algemeen wordt er geen bijzondere relatie tussen afwijkingen in ξ , ϕ of η door de data ondersteund. In de bovenste 100 km is de verhouding tussen $d\eta$ en $d\xi$ duidelijk lateraal variabel. Dit waarschuwt tegen het gebruik van globale verhoudingen in tomografische inversies voor radiale anisotropie.

Onze studie van “azimuthal” anisotropie in Hoofdstuk 7 onderzocht de resultaten van een Backus-Gilbert inversie methode die door Trampert and van Heijst (2002) gebruikt werd. Wij hebben laten zien dat deze methode de meest waarschijnlijke oplossing voor een inversie probleem kan vinden, net als het NA, zelfs als de waarschijnlijkheid breed is. Tot slot, de studie van anisotropie in de binenkern in Hoofdstuk 8 heeft laten zien dat het NA oplossingen kan vinden die eerder onbekend waren met het gebruik van normale inversie methoden, en dat het NA verschillende types van data simultaan kan verklaren. Wij hebben een hele familie modellen van anisotropie in de binenkern gevonden die voldoen aan de meeste recente metingen van eigentrillingen, en die ook onafhankelijk de geobserveerde reistijd anomalieën van alle epicentrale afstandenvoorspelen. De modellen hebben een ingewikkeld patroon in de diepte en een tekenverandering voor de anisotrope parameters op een straal van 300-400 km. Dit zou verklaard kunnen worden door een faseverandering van ijzer op deze dieptes en/of een overgang in de formatie van de kern van de aarde.

Het NA is dus een krachtig gereedschap om kleine inversie problemen op te lossen. Wij hebben “probability density functions” voor seismische anisotropie in verschillende gebieden en diepten in de aarde verkregen die een betere onzekerheid geven van de anisotropie dan traditionele inversies. Deze “probability density functions” kunnen gebruikt worden om waarschijnlijkheden te berekenen voor verschillende anisotrope parameters en voor de equivalente isotropische snelheden. Deze “probability density functions” kunnen nu in andere onderzoeken gebruikt worden om compositie modellen te testen en om te onderzoeken hoe deze anisotropie modellen gerelateerd kunnen worden aan mantel

convectie. De modellen voor anisotropie in de binenkern zullen het begrip van de formatie en compositie van de kern verbeteren. De beperkingen van het NA door de grootte van de model ruimte die onderzocht kan worden kan gereduceerd worden door de code parallel te maken. Het zal dan mogelijk worden om de structuur van de aarde te bestuderen door het NA direct op de spectra van eigentrillingen of oppervlaktegolven te gebruiken in plaats van secundaire data zoals fase snelheid modellen of eigentrillingen structuur coëfficiënten te inverteren.

Résumé (Summary in French)

Le sujet de cette thèse concerne l'anisotropie sismique à l'intérieur de la Terre, c.à.d. la dépendance de la vitesse des ondes sismiques en fonction de leur direction de propagation. Nous avons évalué à quel point il est nécessaire d'introduire de l'anisotropie sismique dans les modèles tomographiques globaux en utilisant une nouvelle technique de résolution des problèmes inverses. La méthode adoptée s'appelle "Neighbourhood Algorithm" (NA) et fut récemment développée par Sambridge (1999a,b). C'est un algorithme qui explore l'espace des modèles et qui caractérise tous les modèles compatibles avec un certain ensemble de données. L'entièreté de l'espace des modèles, espace nul inclus, est échantillonnée et une densité de probabilité peut être associée à chaque inconnue. De plus, des informations sur les corrélations entre les différents paramètres sont fournies directement par l'algorithme. Cette technique présente l'avantage, par rapport aux inversions traditionnelles, de procurer des estimations d'incertitude sur les modèles plus fiables, surtout lorsque l'espace nul est important ou lorsque les densités de probabilité sont fortement non-gaussiennes. Ces densités de probabilité peuvent être employées a posteriori afin de tester différentes hypothèses (p.ex. composition, corrélation entre variables, etc), et il est possible de réduire le nombre de modèles de Terre en utilisant des données indépendantes. Bien que limité par la taille de l'espace des modèles pouvant être exploré en un laps de temps raisonnable, le NA convient bien pour étudier l'intérieur de la Terre à partir de données provenant des oscillations libres de la planète et à partir de cartes de vitesse de phase. Ceci est en effet possible parce que ce type de problèmes peut facilement être divisé en plusieurs problèmes inverses de plus petite taille, par décomposition de la structure en harmoniques sphériques.

Le NA a d'abord été appliqué à un problème tomographique à grande échelle, pour trouver un ensemble de modèles de vitesse d'ondes P et S de degré deux dans le manteau (Chapitre 3). Nous nous sommes ensuite concentrés sur la présence d'anisotropie radiale dans la Terre. Ce type d'anisotropie est décrit par cinq paramètres élastiques indépendants et survient quand un milieu élastique présente un axe de symétrie pointant dans la direction radiale. Le modèle PREM fût le premier modèle de référence (1-D) à inclure de l'anisotropie radiale dans le manteau supérieur jusqu'à une profondeur de 220 km. Nous avons calculé la probabilité pour que les paramètres anisotropes diffèrent de PREM dans différents cas, en intégrant les densités de probabilité obtenues avec le NA. Le Chapitre 4 traite de la présence d'anisotropie radiale dans des modèles de manteau de référence, à partir d'un ensemble de données composé de nombreux modes propres et ondes de surface. Les Chapitres 5 et 6 s'occupent des variations latérales de cette anisotropie jusqu'à une profondeur de 1200 km, en utilisant des cartes de vitesse de phase de mode fondamentaux et d'harmoniques pour des ondes de Rayleigh et de Love. Nous avons trouvé que l'ensemble actuel de données d'ondes de surface et de modes propres ne favorise aucune

déviations significative des paramètres anisotropes par rapport à PREM, dans les modèles de référence, excepté pour les ondes P entre 220 et 400 km de profondeur et, peut-être pour le paramètre η entre 220 et 400 km de profondeur et dans la zone de transition. Les données employées ne cautionnent pas, avec une grande probabilité, les changements de signes des paramètres anisotropes observés précédemment par Montagner et Kennett (Montagner and Kennett, 1996) à 670 km de profondeur. Si des déviations par rapport à PREM, autres que celles décrites dans le Chapitre 4, sont effectivement présentes à l'intérieur de la Terre, elles ne peuvent pas être résolues par les données actuellement disponibles. Dans le Chapitre 4, en plus des résultats pour l'anisotropie, nous avons trouvé un déficit de densité dans les 220 premiers kilomètres du manteau et un excès de densité dans la zone de transition et dans le manteau profond (couche D"). Cet excès de densité dans le manteau profond pourrait correspondre à la couche dense, compositionnellement différente du reste du manteau, proposée par Kellogg et al. (1999). Des variations latérales d'anisotropie radiale ont également été trouvées dans les 1200 premiers kilomètres du manteau. Nous avons observé un signal dépendant clairement de l'âge de la région considérée jusqu'à 220 km de profondeur pour les différents paramètres anisotropes, dans les régions océaniques et dans les régions continentales. L'anisotropie des ondes S et le paramètre η sont tous deux caractérisés par une décroissance en fonction de la profondeur plus rapide sous les "jeunes" océans et les "jeunes" continents que sous les océans plus vieux et sous les cratons. L'anisotropie des ondes S pourrait s'étendre à des profondeurs supérieures à 220 km sous les cratons, mais pas sous les autres régions continentales. De l'anisotropie S, avec $V_{SH} > V_{SV}$, a aussi été détectée dans la zone de transition sous les jeunes océans, mais pas sous les océans plus âgés, ce qui pourrait indiquer que les rides océaniques ont une origine relativement profonde. Aussi bien le paramètre η que le paramètre ϕ changent de signe entre 220 et 400 km de profondeur et nos résultats suggèrent de l'anisotropie P et η non nuls sous les continents, à des profondeurs comprises entre 220 et 400 km. De manière générale, aucune relation préférentielles entre les perturbations de ξ , ϕ ou η n'est soutenue par les données dans les premiers 100 km du manteau et, visiblement, le rapport entre $d\eta$ and $d\xi$ varie latéralement, ce qui devrait inciter à la prudence quant à l'utilisation de facteurs de proportionnalité globaux dans les inversions.

Le Chapitre 7 traite d'anisotropie azimuthale, qui correspond à la dépendance de la vitesse des ondes sismiques en fonction de l'azimuth de propagation. Nous avons comparé nos résultats à ceux obtenus par Trampert et van Heijst (Trampert and van Heijst, 2002) à partir d'une inversion de type "Backus-Gilbert". Nous avons ainsi montré que cette méthode d'inversion est capable de trouver la solution la plus probable d'un problème, telle celle trouvée par le NA, même si la densité de probabilité est large. Enfin, l'étude d'anisotropie dans le noyau interne de la Terre (Chapitre 8) a démontré qu'avec le NA, on peut obtenir des solutions à un problème inverse qui n'avaient encore pu être trouvées par les méthodes traditionnelles d'inversion. Nous avons pu, par la même occasion, réconcilier différents types de données. Nous avons, en effet, trouvé une famille de modèles anisotropes de la graine à partir de mesures de modes propres de la Terre, et ces modèles prédisent indépendamment les temps de trajets d'ondes de volume traversant le

noyau interne à toute distance épacentrale. La dépendance en profondeur des modèles est relativement compliquée, et nous avons obtenu un changement de signe des paramètres anisotropes à un rayon d'environ 300-400 km. Ceci pourrait être expliqué en terme d'un changement de phase du fer à ces profondeurs et/ou refléter l'histoire de la formation du noyau terrestre.

Le NA est donc un outil très puissant pour résoudre des problèmes inverses de petites tailles. Nous avons pu obtenir des densités de probabilité pour l'anisotropie sismique dans différentes régions du globe et à différentes profondeurs, qui procurent de meilleures estimations de l'incertitude sur cette anisotropie que les inversions traditionnelles. Ces densités de probabilité peuvent être utilisées pour calculer des probabilités pour chaque paramètre anisotrope et pour les vitesses isotropes équivalentes. Elles pourront également être employées dans de futures recherches pour tester des modèles de composition de la Terre et pour tenter d'incorporer cette anisotropie dans des modèles de convection. Les modèles d'anisotropie dans le noyau que nous avons trouvés aideront peut-être à comprendre la formation du noyau et à déterminer sa composition. La limitation du NA imposée par la taille de l'espace des modèles qui peut être explorée en un temps raisonnable pourrait être fortement réduite en parallélisant le code. Il sera dès lors possible d'étudier la structure de la Terre en appliquant le NA directement au spectre des modes propres et des ondes de surface plutôt que d'inverser des données "secondaires" telles que des cartes de vitesses de phase ou des coefficients de splitting.

Acknowledgments

Many people contributed to this thesis, directly and indirectly, and I would like to take this opportunity to acknowledge them.

I would like to express my deep gratitude to Jeannot Trampert, my co-promotor, who instigated the subject of this PhD and who offered me the possibility to carry out an interesting and challenging research. I learned a lot from him and I really appreciated his daily guidance, his availability whenever I had a question and his promptness in reading the different chapters of this manuscript. I also thank him for his support during the moments of doubt and stress I encountered for the past four and a half years. Merci beaucoup Jeannot!!

I am grateful to Rob van der Hilst for accepting to become my promotor when he arrived in Utrecht. And thanks for reading my thesis thoroughly at short notice and for the useful comments.

I am indebted to Malcolm Sambridge who developed the Neighbourhood Algorithm and made it available through his well-documented website (<http://rses.anu.edu.au/malcolm/na/na.html>). I hope more people will benefit from it in the future. And it was also a pleasure to finally meet him, after a few email exchanges, at the last EGS-AGU-EUG joint assembly.

I really appreciated Hanneke Paulssen's expertise on body waves when I had to test the models of inner core anisotropy of Chapter 8 against travel-time data. She computed the reference travel times for P-waves inside the inner core, and her little cartoons and explanations were very helpful. As always, they made things look simpler. I also thank her for being there for my first AGU talk in Spring 2001 and for reading the introduction of my thesis.

I sincerely thank Joe Resovsky with whom I shared an office during four years. I benefited from his expertise on normal modes many times. He is the one who introduced me to Malcolm Sambridge's papers on the Neighbourhood Algorithm and our numerous discussions undoubtedly helped understanding the method. Thanks also for the good working atmosphere and for the not-so-scientific talks and laughs. Joe, I wish you and Justa a lot of joy with little Tamar.

I wish to acknowledge the reading committee : Chris Spiers, Jean-Paul Montagner, Michel Cara and Alessandro Forte. The PKP(BC)-PKP(DF) and PKP(AB)-PKP(DF) data and the code giving travel time anomalies as a function of the ray angle for the inner core study were provided by K. C. Creager, and X. Song gave the differential travel time data for the epicentral distance range $168^\circ - 180^\circ$. Hendrik-Jan van Heijst shared his overtone measurements, used in Chapters 4 and 6, and as co-author of the paper presented in Chapter 4 he made useful comments on its content.

I had several opportunities to go to great conferences during the last four years and

to spend some time at Yale University. I would like to thank Jeffrey Park for hosting me there for three weeks and for the dinners with his wife and daughters. I also thank Brian Kennett, David Price and John Woodhouse for the thought-provoking discussions.

Theo van Zessen and Joop Hoofd were always around to help me with computer-related matters, and thanks to Theo's patience my (very) time consuming programs of Chapter 4 could run on PBS. Frederic Deschamps helped me with program 3SMAC, which I used in Chapters 5 and 6. Karin Visser was very nice to help me with the Dutch translation of the summary, and Robbert van Vossen made the last verifications.

I am glad to have met many other nice and interesting people during my stay in Utrecht. Special thanks to Vessa Dimova for her friendship and the (unfortunately too few) moments spent together outside university, at dinners or on a bicycle. Stéphanie Godey gave me useful advices and tips concerning life in Utrecht as a french-speaking foreigner. Thank you to all other PhD students, post-docs and undergraduate students for the nice chats, lunches, dinners and coffee breaks that were most welcome during the last few months : Sergei Lebedev, Dirk kraaijpoel, Tim van Zon, Stefan Carpentier, Jacqueline Landsheer, Arie van Wettum, Kabir Roy-Chowdhury and Henk van Meer. Thanks to Rita Pestana and her great laugh, which I am sure everybody will remember, and to Maisha Amaru, Peter van Thienen, Antonio Villaseñor, Jojanneke van den Berg, Renate Hartog, Sandra Richwalski, Axel Röhm, Jesper Spetzler, Jeroen van Hunen, Paul Meijer, Edith Hafkenscheid, Christine Franke, Annemarie Bos, Luis Martinez, and many others.

I finish by acknowledging my parents, André Beghein and Lina Denée, as well as Monique Sauvage and Jean-Marie Diez for their support. And of course a big "merci" to Bernard Diez who helped me through these years, with encouragements, understanding and love, in the good and the not-so-good moments, and who conscientiously proofread my (almost) whole dissertation.

Curriculum Vitae

May 22, 1975 Born in Rocourt (Liège), Belgium
1981 - 1987 Primary school in Amay, Belgium
1987 - 1993 Secondary school (Athénée Royal) in Huy, Belgium
1993 - 1997 Study of Physics, University of Liège, Belgium
1997 - 1998 Study of Geophysics ("D.E.A."), Institut de Physique
du Globe in Paris, France
1998 - 2003 PhD student at Utrecht University, The Netherlands

